Low Temperature Air Plasmas for Wound Healing Applications

Helen Louise Davies

PhD

University of York

Biology

September 2019

Abstract

Chronic wounds present a huge socio-economic burden across the world. With current treatment strategies remaining inefficient and unreliable, new therapeutics are desperately sought. One potential new therapeutic for chronic wounds is the use of Low Temperature Plasmas (LTPs) which are showing promise in laboratory and clinical trials for chronic wound healing. LTPs are electrically produced, gaseous, chemically reactive environments consisting of electrons, electric fields, photons and Reactive Oxygen and Nitrogen Species (RONS). These are able to synergistically activate biological pathways by mimicking the function of RONS produced physiologically to mediate many processes, including wound healing.

For development of LTP-based treatments, the types and concentrations of RONS delivered to a target site, and their effects on target cells need to be understood. In this work, global modelling is used to understand the time-evolved species densities in atmospheric pressure nitrogen and nitrogen/oxygen discharges, and also to determine the dominant production and destruction reactions for biorelevant species. Development of a new detailed nitrogen chemistry set has identified the importance of vibrationally excited nitrogen in atmospheric pressure discharges. Extension of the nitrogen set to include oxygen species has allowed the process of benchmarking air simulations to experimental data, and shows the dominant production and destruction pathways of the biorelevant species, nitric oxide and ozone. For use in future work, a protocol for correlation of the plasma RONS composition delivered in a particular treatment to skin cells, and the biological effects seen has also been developed. This has been achieved by combining realtime cellular viability assays, and the global modelling methods.

This work is a first step to relating LTP RONS composition to biological effects, and will help inform the future design of LTPs for all purposes, including those for chronic wound therapies.

Contents

List of Tables

List of Figures

Acknowledgements

I am extremely grateful to my supervisors Professor Deborah O'Connell and Dr Marjan van der Woude for all of their help, support and encouragement throughout this project. Without them, it would not have been possible. Thanks are also due to my thesis advisory panel members Professor Timo Gans, and Professor Paul Genever, who have helped to guide both the physics and biology aspects of the project. I am grateful to Dr Kari Niemi and Richard Armitage for their expert scientific and technical advice in the York Plasma Institute laboratories, and to Dr James Fox for all his help with cell culture. I would also like to thank Professor Vasco Guerra for the many helpful discussions relating to this project, the staff in the Biosciences Technology Facility for their technical advice, and the Wellcome Trust for providing financial support.

Being part of the Low Temperature Plasma group has made this whole project all the more enjoyable. I have made friends for life and feel so fortunate to have been part of such a fun, supportive group. Special thanks go to Andrew Gibson for his extremely helpful discussions and guidance throughout the project. As well as the LTP group, I would like to thank the rest of my CIDCATS PhD cohort, Rosie, Shoumit, Steve and Karinna, for being awesome, and the Van der Woude group for all your expert biology help!

Of course, none of this would have been possible without the help and support of my wonderful family. Mum, thank you so much for everything you have done for me, and for helping me to reach this point. Dad, thank you for being a constant support, and for your engineering prowess when experimental things

needed modifying! Finally, Ian, Bro. Ta for being the bestest big brother a girl could ask for! To all three of you, thank you for just being you.

Special thanks finally to all of the 4-legged family, past and present, who have helped to keep me sane throughout this rollercoaster of a journey that is a PhD!

Declaration

I, Helen Davies, declare that this thesis is a presentation of original work and I am the sole author. This work has not previously been presented for an award at this, or any other, University. All sources are acknowledged as References.

Introduction

1.1. Motivation: The Socioeconomic Burden of Chronic Wounds

Thought to affect ≈ 2 % of the developed population, chronic wounds present a huge socioeconomic burden, not only in the UK, but across the world [1, 2]. For the patients, chronic wounds often occur on top of pre-existing conditions, adding to their psychological stress and physical limitations due to pain, odour and ongoing management of non-healing wounds [3]. On top of the direct effects of chronic wounds themselves, non healing wounds that last for decades refusing to heal are one of the biggest reasons for major amputations, and infections and death resulting from chronic wounds are all too common [4]. The estimated cost of chronic wound care and managements varies from ≈ 3-6 % of the budgets of healthcare providers in the UK [5, 6]. Therefore, with the combined burden on patients and healthcare providers, new methods of accelerating wound healing, and optimising wound care are desperately sought.

1.2. Pathophysiology of Chronic Wounds

To understand the pathophysiology of chronic wounds, it is first necessary to understand the affected organ, the skin, and the normal wound healing process. By understanding the normal physiology of wound healing, and how the normal processes become aberrant in chronic wound development, it is easier to identify specific pathways that could be targeted by potential new therapeutics.

1.2.1. The Skin

The skin is the largest organ in the body, consisting of multiple layers of different cell types, in order to provide a functional, protective barrier from the myriad of pathogens and chemical insults that would be harmful if they were to reach the subcutaneous structures [7]. As well as providing a protective barrier to potentially harmful invasion, the skin is important for maintaining homeostasis and fluid balance, and has to be able to withstand a range of mechanical stresses, such as stretching and compression arising when the body moves [8].

The skin is made up of multiple layers, each containing different cell types and structures, which altogether give the skin its abilities of preventing pathogen invasion, excessive water loss and permeation by injurious chemicals and toxins. Of particular importance for the barrier function of the skin is the uppermost layer, termed the epidermis [7]. The epidermis itself is also a layered tissue, of which ≈95 % is made up of layers of specialised skin cells called keratinocytes, that are important for producing cytoskeletal proteins, maintaining the keratinocyte population through proliferation, alerting the immune system to damage, and initiating repair mechanisms [9–11]. Keratinocytes contain intermediate filament proteins called keratins which contribute to the cytoskeleton. The types of keratins produced by keratinocytes indicate their level of differentiation or their activation status [9, 10]. The remaining ≈ 5% of cells in the epidemis are are melanin-producing melanocytes, Langerhans cells (an immune cells specific to the skin) and mechanoreceptors [11].

The epidermal layers are termed, from deep to superficial, the stratum basale, stratum spinosum, stratum granulosum and stratum corneum. The stratum basale is a single layer of keratinocytes, sitting on a basement membrane. These undifferentiated keratinocytes are proliferative, and produce the daughter cells which move upwards through the epidermal layers to the surface, becoming increasingly differentiated. In the stratum spinosum, keratinocytes are tightly connected to each other through desmosomes, strong intercellular attachments which contribute to the physical barrier provided by the skin [7].

The stratum granulosum, or 'granular layer' is so-called due to the accumulation of granules in the keratinocyte cytoplasm. These granules are made up of multiple components, including keratins. As keratinocytes ascend through the stratum granulosum, their keratin production increases, the cellular organelles begin to dissolve, and the cells flatten, indicating that the cells are going through the process of cornification, to become a terminally differentiated keratinocyte, called a corneocyte [7, 11]. Corneocytes also have a cornified envelope surrounding them, which is made up of cross-linked cytosolic proteins, which provides a stable scaffold for the corneocytes and matrix in the stratum corneum. The stratum corneum is the uppermost layer of the epidermis, and is the principle component for the physical barrier of the skin [7]. Corneocytes are joined to each other through cell attachments called corneodesmosomes and are suspended in a matrix containing lots of lipids. Together, the flattened corneocytes and intercellular matrix provide a barrier that can withstand mechanical forces and prevent the entry of pathogens and chemicals into the tissues below, as well as helping to regulate water loss from the body to the environment (the transepidermal water loss, TEWL) [7]. Over time, cells of the stratum corneum are sloughed off and lost, and replaced by new corneocytes that have ascended through the epidermal layers to terminally differentiate in the transition between the stratum granulosum and stratum corneum.

Below the epidermis is the dermis. The dermis is attached to the epidermis via a basement membrane on which the epidermal stratum basale sits. The dermis consists mainly of extracellular matrix components, and fibroblast cells that produce them. It also contains sweat glands, hair follicles and blood vessels [12]. Finally, the hypodermis is below the dermis. This layer consists mainly of fatty tissue to support the layers of skin above it [12].

1.2.2. The Normal Wound Healing Process

Important for all aspects of wound healing are the signalling molecules that orchestrate the different processes, and cellular responses required for repair. There are many different cytokines, growth factors and chemokines involved in

wound healing, with complex interactions, which all lead to successful wound healing [13]. Cytokines are small proteins which are usually released in response to a stimulus. They can act on the signalling cells themselves (autocrine signalling) and neighbouring cells (paracrine signalling), to activate cell surface receptors, signal transduction mechanisms, and ultimately, gene transcription to bring about a cellular response [14]. Chemokines are a subset of cytokines that can attract other cell types with specific receptors to the source of the chemokine. For example, they can draw immune cells to a wound site [14].

There are many important cytokines and chemokines involved in wound healing. For example, the initial damage is signalled in the skin by the cytokine interleukin (IL)-1, which is rapidly released by damaged keratinocytes [10, 15]. This response alerts surrounding keratinocytes and fibroblasts to the damage, and initiates their cellular responses, as well as drawing in other immune cells such as neutrophils and macrophages to the site of damage [15]. Following the IL-1 signalling, this triggers further release of more cytokines from both keratinocytes and other immune cells drawn to the site, such as IL-6 and tumour necrosis factor α (TNF-α) [10, 15]. This rich cocktail of cytokines also begin to, activate endothelial cells to promote the formation of new blood vessels, maintain keratinocytes in an activated state, and activate migration and proliferation of keratinocytes and fibroblasts to allow re-epithelialisation to occur [15].

The process of cutaneous wound healing follows a well defined, highly regulated sequence of events, in order to repair the protective skin layer in an ordered, timely manner. The healing process can be split up into chronological, overlapping categories of coagulation and haemostasis, inflammation, proliferation and remodelling, and will be discussed briefly below [16, 17].

Coagulation and Haemostasis

The immediate aim of this process is to prevent bleeding to death, firstly effected by a reflexive contraction of smooth muscle, to reduce blood loss. As blood enters the wounded tissue, it interacts with extracellular matrix (ECM)

and causes release of clotting factor, which through activation of the clotting cascade, result in the formation of a blood clot [16]. As well as acting to stop blood loss, the blood clot also provides a matrix for infiltration by cells important for the subsequent healing phases [16].

Inflammation

Occurring shortly after injury, the inflammatory phase aims to prevent pathogens entering at the wound site and causing infection. Initially, the innate immune system dominates, by activating the complement cascade and recruiting neutrophils to begin the process of phagocytosis to clear the area of microbes and debris [17]. Over time, the inflammatory response moves to being more macrophage driven [17]. These continue the process of phagocytosis, whilst also activating keratinocytes, fibroblasts and endothelial cells and providing a reservoir of potent tissue growth factors. Macrophages are also important for activating the adaptive immune system to recruit lymphocytes to the wound site, usually by around 72 hours post injury [16].

Proliferation

The proliferative phase of wound healing, begins within days of injury, and lasts for approximately 2 weeks, thus forming the majority fraction of the overall healing process [16].

During this phase, fibroblasts proliferate and migrate into the wound area, depositing abundant new extracellular matrix (ECM), termed granulation tissue. Alongside this, fibroblasts become activated, gain contractile actin bundles and differentiate into myofibroblasts. These myofibroblasts then contract to reduce the wound size. Collagen is also produced in large amounts by fibroblasts, and new blood vessels sprout from the wound margins into the wound to maintain perfusion [16].

Above the newly formed ECM, keratinocytes begin to migrate into the wound to reform an epithelial layer. When the migrating epithelial cells from the

wound margins meet in the middle, they stop proliferating and a basement membrane begins to form [16, 18].

Remodelling

The remodelling phase of wound healing, including the process of scar tissue formation, can take years to complete. Here, the newly produced epithelium is remodelled through careful balance of degradation and synthesis, and any scar tissue is formed. As well as this, helped by wound contraction, collagen production becomes increasingly more well organised over time, to increase the wound strength. As time progresses, the cell density in the wound decreases and the metabolic activity in the area decreases, resulting in healed tissue and a mature scar [16].

1.2.3. Progression of Wounds from Acute to Chronic

As described above, the process of wound healing is strictly regulated and progresses in a timely manner. However, in some cases, wounds can stall in one of the phases, and progress from being an acute wound, which heals properly, to a chronic wound, which does not heal. Types of chronic wound include, but are not restricted to, diabetic ulcers, venous ulcers and pressure ulcers, which are generally attributed to circulatory diseases, prolonged pressure on the skin or nerve damage (neuropathy) [2, 16].

Generally, chronic wounds are found to be in a maintained inflammatory state, characterised by excessive numbers of immune cells, excessive pro-inflammatory signalling cytokines, little neoangiogenesis and very few myofibroblasts [19]. The excess of proinflammatory cytokines results in high, unregulated levels of proteases which in turn causes destruction of the ECM. This not only prevents progression to the proliferative phase, but also ECM breakdown products stimulate the immune system resulting in a vicious cycle of increasing inflammatory response and delayed healing [2].

Alongside the effects of the over activation of the immune response in the

wound, cells found in chronic wounds are often found to be either deficient in number, senescent, or unresponsive to wound healing signals, meaning they are unable to perform their functions as competently as in acute, healing wounds [2]. In fact, the proportion of senescent cells found in chronic wounds has been suggested to be an indicator of whether or not a wound is likely to become hard-to-heal [20].

1.2.4. Wound infections

Infection is a common problem in chronic wounds, with the most common types of wound-colonising bacteria including *Staphylococcus aureus, Pseudomonas aeruginosa* and coagulase-negative staphylococci [1, 21, 22]. However, a chronic wound containing bacteria does not necessarily mean that it is infected. In fact, it is thought that the presence of bacteria in a chronic wound exists as a continuum, from contamination, through colonisation, critical colonisation to infection [1]. Due to the abundance of bacteria on skin and in the environment, all wounds become contaminated with bacteria. However, not all wounds become colonised, defined as having proliferating bacteria but no host response, and there is some evidence suggesting that the bacteria present on the skin may be beneficial to the wound healing process [23].

At a certain point in some wounds, colonisation reaches a critical point, termed critical colonisation, where the bacterial colonisation reaches a level where there is a host response. Infection occurs when the bacterial proliferation overcomes the host response [1, 24]. The notion of critical colonisation, and the point at which the level of bacteria present hinders the healing process is controversial. Though debateable, it is generally thought that a low level of bacteria is not detrimental to the healing process, but above critical colonisation, the bacterial presence is accepted to adversely affect healing [1, 25].

Biofilms present a huge problem in chronic wounds, and form when bacteria proliferate and aggregate, surrounding themselves with extracellular matrix. These are particularly difficult to treat as the matrix is impermeable to antibi-

otics, and they often contain antibiotic resistant bacterial strains, meaning they are less susceptible to certain treatments [1, 26]. The biofilms present in chronic wounds are usually polymicrobial, consisting of many different species of bacteria [26].

1.2.5. Current wound treatment strategies

Currently, the mainstay of treatment for chronic wounds involves the careful debridement of the wound to remove necrotic and/or infected tissue, offloading pressure from the area, and the careful management of the patient as a whole. For example, patients with diabetic ulcers often require better control of their blood glucose to improve their nutritional status and, therefore, their ability to heal naturally. Similarly, those suffering from vascular insufficiencies leading to venous ulcers require treatment for the subsequent ischaemia, to increase perfusion and oxygenation of the wound site, to help promote healing [2]. These are the basic principles for the treatment of chronic wounds of all aetiologies.

For infected wounds, the general course of action is to administer systemic antibiotics [1]. However, the evidence for their effectiveness is lacking, and this adds to the ever increasing problem of antibiotic resistance [25]. The biofilms formed in infected chronic wounds often consist of multiple types of bacteria, including those that are antibiotic resistant, and are frequently unresponsive to topical or systemic antibiotics [26]. The prevalence of infected chronic wounds and the likely presence of antibiotic resistant strains within them, present a huge reservoir for increasing the incidence of antibiotic resistant bacterial infections [26]. Overuse of questionably efficient antibiotics has been studied in [25], showing that 68.3% of patients with a chronic wound had received a course of antibiotics in the year of 2000, compared to just 29.4% of the general population. Without hard evidence that these antibiotics are required and effective, over prescribing systemic antibiotics is just adding to the greater problem of antibiotic resistance.

In terms of physical treatments beside prescription antibiotics, there are many types of wound care options. These range from a vast array of wound dressings, including basic gauze dressings, highly absorbent dressings and micronised collagen dressings. Dressings containing silver can also be used, due to the bacterial reduction abilities of silver [2].

However, beyond dressings, more advanced wound therapies are coming to light, such as:

- **Negative pressure wound therapy** - Application of a vacuum dressing to the wound to aid blood flow, enhance wound drainage, and promote wound closure [27]

- **Hyperbaric oxygen therapy** - The aim of subjecting wounds to high oxygen environments is to promote proliferation of fibroblasts, angiogenesis and immune function. However, in practice, this therapy has not shown any significant advantages over basic therapies [27]

- **Skin Substitutes** - A more advanced type of dressing, where either cellular or acellular tissues are applied to the wound to aid repair [27]

Currently, the overall treatment of chronic wounds is inefficient and unreliable. The ever increasing risk of antibiotic resistance, and the expected rise in chronic wound incidence over the coming years gives a compelling reason for research into novel, effective chronic wound treatments that can reduce infection, and promote healing. One such treatment strategy that has been showing promise in recent years is the use of Low Temperature Plasmas (LTPs) [28].

1.3. Introduction to Atmospheric Pressure Low Temperature Plasmas (LTPs)

Plasma is the fourth state of matter, formed when energy is increased in a gas, causing some of the gas particles to become ionised [29]. The degree of ionisation of a plasma refers to the proportion of gas molecules that are ionised and this depends largely on the energy of the system. The higher the energy,

the greater the degree of ionisation and therefore, the higher the density of free electrons (electron density). The process of ionisation of gases results in free electrons within the plasma region, which gives the plasma its properties. Plasmas are said to be quasi-neutral, meaning that whilst they contain many charged particles, overall, there is no charge to the system.

Plasmas can range from being almost fully ionised, to very weakly ionised. Highly ionised, very hot plasmas, such as the sun, exist at very high overall temperatures. This is due to a state of thermodynamic equilibrium being reached [29]. For this to occur, free electrons are accelerated across a potential difference and gain energy which they then impart to other ions and neutrals through collisions. Due to the large difference in mass, energy transfer between very small electrons and much bigger neutrals and ions is poor. However, if there is sufficient energy in the system, then all the particles within the plasma will end up 'hot', $T_e \approx T_i \approx T_g$ (where T_e is electron temperature, T_i is ion temperature and T_g is gas temperature).

At the other end of the scale are low temperature plasmas. These plasmas are only weakly ionised and therefore have low degrees of ionisation and low electron densities [29]. For these plasmas, thermodynamic equilibrium is never reached due to the poor energy transfer between electrons and bigger ions and neutrals [30]. This results in a state where $T_e >> T_i \approx T_g$ and therefore, overall, the temperature of the plasma remains cool at approximately room temperature. It is this ability to produce plasmas at low temperatures, at atmospheric pressure, that makes them so exciting in the field of biomedicine.

1.3.1. Electron Dynamics in LTPs

Electrons produced in LTPs gain energy by accelerating in response to the applied electric field, and lose energy by colliding with other ions and neutrals in the plasma. The collisionality of LTPs helps to determine the average electron energy, as the higher the number of collisions, the lower the energy of electrons as their time available for acceleration is decreased. Also due to colli-

sion, electrons in LTPs form an energy distribution called the Electron Energy Distribution Function, an illustrated example of which is shown in Figure 1.1.

The electrons in LTPs mediate many different processes, each of which have a role to play in the biomedical application of LTPs. In particular, electrons mediate:

1. **Dissociation** - Electron impact dissociation of background gas and other plasma species results in the formation of highly reactive free radicals and reactive oxygen and nitrogen species (RONS) [31]. LTPs are particularly efficient producers of RONS, and these will discussed in more detail later, due to their extremely important role in biomedical plasmas.

2. **Electronic excitation** - When electrons collide with other plasma species, they can impart energy which can excite the particle to a higher electronic state. These high energy particles can be very short-lived, and decay quickly emitting a photon, hence giving off the visible and ultraviolet light found from LTPs [31]. Alternatively, some electronically excited species can be considered to be metastable species, meaning they have much longer lifetimes and are, therefore, able to mediate other processes, including dissociation and ionisation, through chemical reactions [32].

3. **Ionisation** - If the energy of the electron colliding with another plasma species is sufficient, the electron can ionise that species, thus producing another free electron. During plasma breakdown (when a gas first becomes a plasma), this is known as an electron avalanche, when a single seed electron causes ionisation and production of another electron, both of which can then themselves cause ionisation and so on. Electrons lost to the walls of the plasma, or through recombination reactions, are replaced by electrons produced by ionisation events, hence this is how plasmas are sustained [32].

Besides the electron kinetics in LTPs, chemical reactions between heavy particles are also vitally important for determining the concentrations of different spe-

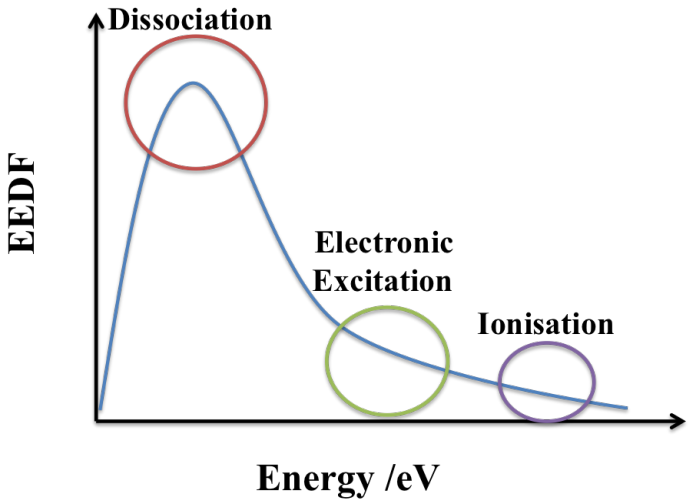

Figure 1.1: Diagram showing a typical plasma EEDF curve and the different processes occurring at different electron energies. There are more lower energy electrons than high energy electrons. The coloured circles indicate the relative energy regions of the EEDF for the different processes.

cies produced [31]. Overall LTPs consist of a rich cocktail of RONS, charged particles, electric fields and photons (including ultraviolet), all of which have a potential for influencing biological targets, hence, there is a growing interest in using LTPs for medical applications.

1.3.2. Different Plasma Geometries

The composition of plasma incident on a target can be influenced by the geometry of the plasma source, for example, the shape and configuration of the electrodes, and their relation to the target itself. There are many different geometries, and some of the most common will be discussed here.

Firstly there are jet-like plasma sources, as shown in Figure 1.2a. Here, a gas flow is passed between two electrodes where plasma forms, then an effluent region is formed as the gas flow carries reactive species towards the target. In cases where the electric field between the electrodes is parallel to the gas flow, the plasma itself can propagate by a so-called streamer mechanism in the effluent to be incident on the target [33–35]. This results in electric fields and charged and neutral RONS being incident on the target. An example of a

plasma jet for use in plasma medicine is the kINPen [36], which is a plasma jet which uses argon as a feed gas. This device will be discussed in more detail later in Section 1.5.1. Alternatively, if the electric field between the electrodes is perpendicular to the gas flow, as in Figure 1.2b, such as in a plane-parallel discharge like the COST jet, then the plasma is confined to the region between the electrodes, and no charged reactive species can escape the electric field [37]. This results in the gas flow carrying only neutral RONS out of the plasma bulk, meaning there is no ion bombardment or electric fields incident on the target. This can be an advantage for sensitive materials, where ions or electric fields can cause damage, but may be a disadvantage if the charged particles and electric fields could be beneficial. An example of a plane parallel discharge is the COST reference microplasma jet, described fully in [37], designed to be a reference source for comparing experimental results across different laboratories by using a standardised source. It uses noble gases, such as helium, as a feed gas, with small admixtures of molecular gases such as oxygen and water.

In contrast to a plasma jet is a volume dielectric barrier discharge (DBD), where there is no gas flow, and the plasma forms in the ambient gas. An example diagram is shown in Figure 1.2c. In this case, there is a powered electrode, and the target is either placed on a ground electrode, or itself acts as the ground (either at a fixed or floating ground potential), to ignite a plasma in direct contact with the target [38–40]. Since the plasma ignites in direct contact with the target, it is exposed to all types of charged and neutral RONS, as well as electric fields and photons that may have an influence. There is interest in whether this type of geometry could be made into a wearable pad for biomedical applications [41].

The choice to use a particular plasma geometry depends on the needs of the experiment. For biomedical purposes, plasma jets can be problematic when trying to determine exact quantities and types of species incident on a biological target, due to mixing of the effluent with ambient air [42]. This mixing results in additional ambient environment gases influencing the chemistry occurring in the plasma effluent, therefore, resulting in alteration of effluent RONS composition. In this way, volume DBDs can be seen as 'simpler' environments to

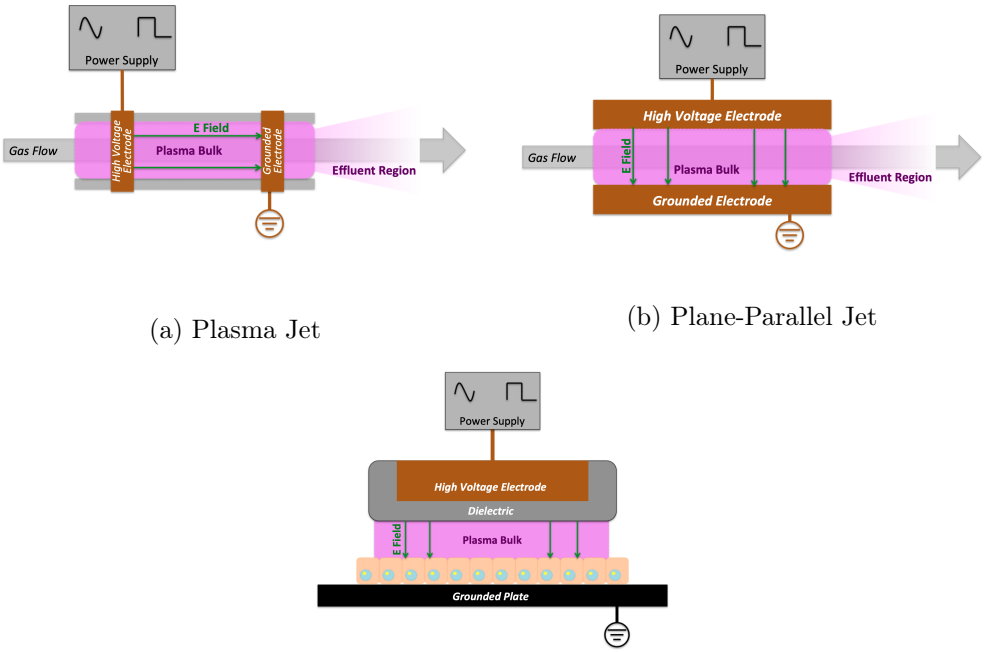

(a) Plasma Jet

(b) Plane-Parallel Jet

(c) Volume Dielectric Barrier Discharge

Figure 1.2: Examples of different types of LTP geometries used for biomedical applications, with the electrode configuration, E field direction and gas flow (if any) direction indicated. 1.2a shows electrodes at either end of an insulated housing, causing an electric field to run parallel to the direction of gas flow. Charged and neutral particles are present in the effluent region, and would reach a target. 1.2b shows two plane parallel electrodes through which a gas flow is passed, with the electric field perpendicular to the gas flow. Charged particles are contained within the plasma bulk region, and only neutral species will be present in the effluent region and able to reach the target. 1.2c shows a high voltage electrode covered in a dielectric, and a ground plate placed below the biological target, such as cells. The electric field is directly incident on the target, and both charged and neutral species will reach the cells. There is no gas flow, the plasma ignites in the ambient air.

characterise, as the plasma is only minimally influenced by the background environment around the source once the plasma is ignited.

1.3.3. The Dielectric Barrier Discharge - Physics Principles

Breakdown

For a plasma to ignite in a DBD, gas is placed in the strong electric field produced by two electrodes, one powered, and one grounded. Occasionally free electrons are produced, for example by cosmic rays, and these electrons can be accelerated by the electric field [43]. As electrons are very small and light in comparison to the heavy, neutral gas particles ($M_e << M_h$, where M_e and M_h are the masses of electrons and heavy particles, respectively), they are able to respond quickly to the electric field and gain energy. As an electron gains sufficient energy, it is able to collide with a neutral gas particle to cause another ionisation event. This process results in two free electrons which can be accelerated, gain energy, and cause further ionisation. This is known as an electron avalanche and results in the breakdown of the gas, to form a plasma. The process of plasma breakdown is explained in detail in Fridman et al. [43].

However, this process is affected by the mean free path of electrons (the average distance an electron will travel before it collides with another particle), which is dependent on the plasma source geometry, the gap between the electrodes and the gas pressure. A high mean free path means electrons can be accelerated by the electric field and gain high energies, as they will collide less frequently than if their mean free path was reduced. Another way of describing this is through the collisionality of a plasma. A plasma with a high collisionality generally has lower energy electrons as they collide frequently and lose energy. Atmospheric pressure plasmas are typically collisional, meaning that large breakdown voltages are required so that electrons can gain sufficient energies for ionisation, even with a short mean free path. The voltages required for breakdown in different gases, as a function of pressure and gap distance, can be determined using a Paschen Curve [29]. An example Paschen Curve is shown in Section 1.3.3, where the breakdown voltage is shown on the vertical axis, and the product of the gap and pressure, pd, is on the horizontal axis. These curves

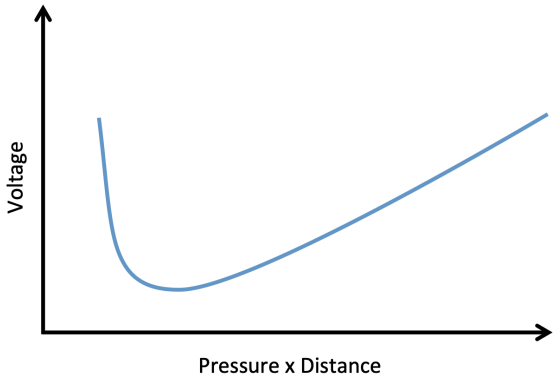

Figure 1.3: An example of a Paschen curve. The product of gas pressure and gap distance, *pd*, is shown on the horizontal axis, while breakdown voltage is shown on the vertical axis.

show that there is an optimal *pd* value where the breakdown voltage is minimal. For a constant gap size, as the gas pressure increases to the right of the optimal *pd* value, there in increase in required breakdown voltage, due to the increased collisionality and decreased mean free path of the electrons. Below, the optimal *pd*, a similar increase in required voltage is needed, due to the fact that there are insufficient particles to ionise, therefore, breakdown is also difficult. Similarly, for a constant pressure, it can be seen using these curves how the gap distance can strongly influence how easy it is to cause breakdown. For atmospheric pressures, the gap sizes required are generally small, on the order of millimetres [44].

Modes of Operation

DBDs can operate in different modes, termed homogeneous and streamer-driven regimes [44]. Homogeneous discharges have a uniform appearance, and are also known as glow discharges. As the name suggests, if treating a surface with a uniform plasma, the treatment is consistent across the whole target. However, streamer-driven plasmas operate as a series of filaments, which propagate between the two electrodes by similar physical principles to lightening occurring in the environment. Filaments concentrate energy into a much smaller area

($\approx$ 50-100 μm radius), and can result in excessive local heating at the target, and cause non-uniform treatments over a whole surface [43, 45]. The power deposition into the plasma can affect which mode a plasma will operate in. This is discussed more in [45], where the mode of operation can be varied by altering the power pulse characteristics, such as rise time and pulse length. It was shown that with shorter rise times and pulse durations on the nanosecond scale, the plasma is uniform. However, if the pulse length and rise time are taken to the microsecond scale, filamentary behaviour is seen instead [45].

1.4. RONS Production by LTPs

One of the main properties of LTPs that is valuable for medical applications is their ability to efficiently produce high concentrations of a wide variety of Reactive Oxygen and Nitrogen Species (RONS) through dissociation of gas particles via electron impact dissociation, or dissociation through collisions with other energetic plasma species [46, 47]. The significance of RONS production by LTPs becomes clearer when the actions of RONS produced natively in the body to mediate many physiological processes are described.

1.4.1. Reactive Oxygen and Nitrogen Species and their Role in Physiology

It is well-documented that there are many reactive oxygen and nitrogen species (RONS) produced endogenously in the body. RONS have a long history of being viewed as purely damaging molecules, promoting the pathophysiological processes driving the development of conditions such as neurodegenerative diseases and atherosclerosis, as well as contributing to the overall process of ageing [48]. Despite their known ability to cause cell membrane damage, lipid peroxidation and DNA damage, in more recent years, it has come to light that RONS are in fact molecules crucial for the normal physiological cellular function, due to many varied roles in a wide range of processes. RONS have been shown to be crucial for processes such as immune responses, growth, proliferation and differentiation [49–51].

RONS that have been shown to have particular biological significance, and known to be present in air plasmas include hydrogen peroxide (H_2O_2), nitric oxide (NO), superoxide (O_2^-), hydroxyl radical ($\cdot OH$) and singlet delta oxygen ($^1O_2$). O_2^- is a highly reactive, short lived radical species, which is rapidly converted to H_2O_2 via the superoxide dismutase (SOD) enzymes. Before it is converted, O_2^- is a signalling molecule, which can interact with certain proteins to increase the cells tolerance to O_2^-, or to promote cell death [50]. O_2^- is also known to be important during the process of phagocytosis, where pathogens are ingested by immune cells and destroyed by a process known as the respiratory burst, which involves killing using RONS. Chronic granulomatous disease is a condition where patients cannot make O_2^- for the respiratory burst, and are subject to multiple, persistent infections [14, 51]. H_2O_2 from the enzymatic destruction of O_2^-, and from other sources, is a relatively long-lived species that can diffuse freely across cell membranes, and is one of the lesser reactive RONS, thus making it a good candidate for a signalling molecule [52]. It is involved in the mediation of cell growth by enhancing the signalling initiated by growth factors, involved in cell fate decisions and contributes to the mounting of an immune response [50, 52]. In mice, it has been shown that low concentrations of H_2O_2 ($\leq$ 0.5 mM) supports wound healing, through acting as a chemoattractant for immune cells, and through inducing the production of factors, such as vascular endothelial growth factor (VEGF), which promotes the vital process of forming new blood vessels [53]. However, at high concentrations ($\geq$ 50 mM), H_2O_2 impairs the healing process, showing how the action of reactive species is dependent on the concentration [53]. Another reactive oxygen species of interest is singlet oxygen, $O_2^1\Delta$. This species is also known to be able to influence signalling pathways such as the AP-1, NK-κB and AP-2 pathways [54], but it has also received much attention in medicine due to its role in Photodynamic Therapy (PDT). For this cancer therapy, a photosensitiser is administered topically or systemically, and when the sensitiser has reached the diseased area, it is stimulated with a particular wavelength of light. This energy from the light activates the photosensitiser and induces production of high doses of singlet oxygen which can disrupt the disease tissue [55]. Finally, NO is a species that

can also diffuse freely across membranes and cytoplasm, with a wide range of useful functions in the body, and has a half life of the order of a few seconds in an aqueous environment [56]. In particular, it is important for regulating vascular tone and blood pressure, neutrotransmission, and like other RONS, the immune response [49].

RONS do not act alone - there are complex interactions between the different species, which add another level of modulation. For example, NO causes relaxation of smooth muscle. O_2^- reacts with NO with the highest rate constant known for NO-involved reactions as follows:

$$NO + O_2^- \rightarrow ONOO^- \tag{1.1}$$

where the reaction rate is 7×10^9 M^{-1} s^{-1} [56]. Not only does this produce a highly toxic peroxynitrite anion, it also reduces the amount of NO available to cause muscle relaxation. Therefore, by regulating superoxide concentrations by SOD expression, muscle tone and blood pressure can be maintained [49].

1.4.2. Mechanisms to Maintain Redox Homeostasis and Prevent Oxidative Stress

RONS are produced by cells through a variety of different processes, as a result of normal cellular functioning. As mentioned above, these RONS have a wide variety of vital functions when present at low levels [49–51]. However, these species need to be maintained at physiological concentrations by carefully balancing their production with a variety of destruction mechanisms to maintain a state of redox homeostasis. To achieve this, cells can reduce the concentration of RONS present through the use of antioxidant scavenging molecules and by reducing further RONS production by activation of feedback loops [57]. Compounds such as glutathione are present in cells and act as basal scavenging molecules of RONS. As well as these, amino acids and proteins also have the ability to counteract RONS and act as scavengers to maintain physiological concentrations. Feedback loops are also important for species such as NO. An increase in NO concentration results in direct inhibition of Nitric Oxide Synthase enzymes, which stops further cellular production of NO [57].

Whilst there are a variety of mechanisms in place to maintain RONS at physiological concentrations, if RONS concentrations rise excessively, a condition called oxidative stress can occur, and can be damaging to cells [58, 59]. As well as regulating the production of RONS in the body to prevent oxidative stress occurring, the body also has many mechanisms in place to protect itself from excessive RONS. Upon exposure to excessive levels of RONS, cells have multiple layers of protection [60]. Firstly, there are stress response pathways such as the nuclear factor E2-related factor 2 (NRF-2), which is an important cellular rescue pathway, regulating several RONS detoxification and antioxidant genes relating to oxidative stress [61, 62]. Included in these genes upregulated during oxidative stress are chaperone proteins which help to stabilise cells during periods of stress, and antioxidants [63].

Alongside these protective mechanisms, cells also have robust mechanisms for quickly repairing damage. Oxidative damage to DNA can cause mutations which can lead to cancer, therefore, cells have multiple important DNA repair mechanisms to limit long-term damage [64].

Failure to protect themselves from stress or repair damage can lead to cell senescence, apoptosis, or in severe cases of stress, necrosis [60].

1.4.3. Reactive Oxygen and Nitrogen Species Produced by LTPs

Depending on the background gas of LTPs, the types of species produced can vary. However, when using air and other molecular gases, either alone or as an admixture to a noble gas, typical RONS produced include nitric oxide (NO), hydrogen peroxide (H_2O_2) and superoxide (O_2^-), all known to mediate aspects of the immune response, cellular proliferation and regulate perfusion [49, 52, 65], as well as other species such as ozone (O_3), atomic nitrogen (N) and oxygen (O). Therefore, the rationale for LTP use is that by externally applying RONS that are important for the process being targeted (such as wound healing), they will be able to mimic the function of the native RONS and carry out the same signalling/mediation processes. The types and concentrations of RONS produced

by LTPs are dependent on the plasma source and operating conditions, and they act in synergy with LTP electric fields and photons, to influence biological pathways [66, 67].

In recent years, there has been growing evidence suggesting a beneficial effect of using LTPs to aid healing of chronic cutaneous wounds, due to the synergistic action of applied RONS and electric fields interacting with important healing-related cellular pathways. Previous laboratory studies using LTPs have shown their ability to positively affect the migration and proliferation of fibroblasts and epithelial cells [67–69], increase expression of wound healing genes [70], increase angiogenesis and collagen production [68, 71, 72] and reduce bacterial wound burden [36, 73]. Success in clinical trials has led to the development of multiple LTP devices, now licensed for medical use on chronic wounds [74–76].

1.5. Evidence for Using LTPs for Wound Healing Applications

The interest in using LTPs for wound healing applications has led to the development of CE-certified LTP devices, classified for medical use. The treatment aim for these devices is to reduce the bacterial load found in chronic wounds, and accelerate the healing process.

1.5.1. Devices Currently in Use and their Evidence of Beneficial Effects

Three of the CE-certified LTP devices classified for medical use are the kINPen, the SteriPlas, and the PlasmaDerm [28]. Each of these devices have undergone series of trials to measure their efficacy and safety, and will be discussed in the following sections, to give an overview of why LTPs are of significant interest to the biomedical community.

It has been well documented over the years that all of these devices are effective for killing a wide range of bacteria in planktonic and biofilm forms (kINPen -[36, 77, 78], SteriPlas - [79, 80], PlasmaDerm - [81]), in the laboratory in dishes,

on skin [36], and in wounds (kINPen - [82, 83], SteriPlas - [73, 84], PlasmaDerm - [76]). When considering the use of LTPs for deactivation of biofilms, it is important to note that works to date are *in vitro*, using biofilm models of single bacterial species. Therefore, the positive results seen by the likes of Matthes et al. [77] and Fricke et al. [78] may not be directly applicable to an *in vivo* setting, or a biofilm in a patient as these are more complex, usually polymicrobial and often contain more resistant bacterial strains.

kINPen

The kINPen is an LTP device, intended for use on non-healing wounds and ulcers in human skin [36], developed in Germany (neoplas tools GmbH, Greifswald, Germany). The kINPen is a plasma jet with a central powered pin/rod electrode inside a quartz capillary. It has a single grounded ring electrode on the outside of the capillary, and uses an argon gas feed. The kINPen is powered by a 2-6 kV, $\approx$ 1 MHz, sinusoidal voltage which is pulsed on and off (1:1 ratio) at $\approx$ 2.5 kHz frequency, and produces a plasma effluent $\approx$ 1 cm long with a diameter of 1 mm [36].

As mentioned in previous sections discussing the aetiology of chronic wounds, infections and bacterial burden is often a problem. The kINPen has been shown to be effective at killing bacteria of many different types, including the common chronic wound pathogens of *Pseudomonas aeruginosa* and *Staphylococcus aureus*, kill bacteria in, and etch away biofilms [36, 77, 78, 81]. On top of this, the kINPen has been tested on wounds in artificial skin models infected with bacteria, and showed improved healing in the plasma treated wounds compared to the non plasma treated ones [85].

Aside from the macroscopic effects of bacterial killing, and improved *in vitro* healing, the kINPen has also been shown to be able to affect the cellular transciptome [86] and proteome [87], to regulate many different proteins, particularly those related to oxidative stress. These include cytoskeletal proteins, such as keratins and chaperone proteins, such as heat shock proteins. Changes in

protein production are thought to be effected by the LTP-induced activation of various different signalling pathways, including, but not restricted to, the NRF-2 pathway and mitogen-activated protein kinase (MAPK) signalling [62, 88]. Combined, results suggest that LTPs can activate cellular repair and defence mechanisms, presumably by influencing cellular signalling pathways by delivery of exogenous RONS.

Treatment of immune cells, including neutrophils, macrophages and lymphocytes, with the kINPen have also been performed *in vitro*. These studies showed that the chance of an LTP treatment being cytotoxic to immune cells depended on the LTP treatment time and the cell type [89, 90]. This is potentially very exciting for the setting of chronic wounds, as being able to affect the nature of the immune response occurring in the chronic inflammatory state of these wounds, could help to restart the healing process.

Besides *in vitro* studies of the kINPen, clinical trials have been performed to determine whether or not beneficial effects are seen in patients. A review of the actions of the kINPen, including data from animal and human clinical trials is found in [36]. The kINPen has been used in clinical trials on leg ulcers to compare the efficacy of LTP treatment compared to antiseptics. Here, it was found that LTP treatment was superior to both combination treatment, and antiseptic treatment alone for reducing the wound size, and was equal for bacterial decontamination [82]. In another study by Vandersee et al. [74], wounds were made on the arms of healthy volunteers, and they were then treated with the kINPen. Following treatment, confocal laser scanning microscopy was used to determine the healing response. In the LTP treatment groups, the initial wound healing process was shown to be accelerated, with an earlier onset of the proliferative wound healing phase. This result suggests a shortened inflammatory phase [36], and therefore, due to the proposed ability to alter the inflammatory phase, gives further evidence for the potential impact of using the kINPen on chronic wounds.

SteriPlas

The SteriPlas (ADTEC, Hunslow, UK) is another plasma jet device which uses an argon feed gas and a microwave frequency (2.46 MHz) power supply. Typically it is powered by 50-100 V voltages [73]. The SteriPlas has undergone *in vitro* studies, mainly to investigate effects in fibroblasts, keratinocytes and endothelial cells. It was shown that keratinocytes and fibroblasts show different tolerance levels to LTP treatment, but both show an enhanced production of certain cytokines and factors important for wound healing, including IL-8 and TGF-βs [91]. Keratinocytes were also shown to produce more defensins, which may contribute to bactericidal abilities of LTP [91]. mRNA for collagen was also increased, suggested collagen production is enhanced by Steriplas LTP treatment, and the collagen arrangement in mouse trials was shown to be superior when SteriPlas treatment had been used [68]. Besides these effects, it is proposed that SteriPlas treatment may be pro-angiogenic, shown by an upregulation of many pro-angiogenic factors following treatment [72].

Currently, clinical trials for SteriPlas have been concerned with monitoring the bacterial burden of wounds. Initial trials using a 5 minute treatment regime, and a two minute treatment regime have been carried out, both showing significantly greater reductions in bacterial loads LTP-treated wounds compared to controls [73, 84]. Wound healing was also investigated retrospectively from clinical trial data where the endpoint was to look at bacterial reduction. Here, the authors compared the differences in wound aetiology and LTP treatment time to see when plasma was effective for promoting healing. They found in groups with the same aetiology (venous ulcers), there was a significant reduction in wound width of lower leg ulcers when SteriPlas treatment was used [75].

PlasmaDerm

Finally, whereas the kINPen and SteriPlas are jet plasmas, the PlasmaDerm (CINOGY GmbH Duderstadt, Germany) is a DBD device, which, as discussed in Section 1.3.2 ignites an LTP in direct contact with the target tissue. The Plas-

maDerm forms an LTP using alternating voltage pulses of > 10 kV and a power density of 120 mW/cm^2 [76]. The bacterial killing ability of the PlasmaDerm has been demonstrated *in vitro* [81], but also in a clinical trial to determine firstly the efficacy of LTP treatment in reducing bacterial load in chronic venous leg ulcers, and secondly, the patient tolerance to treatment [76]. The trial showed significant reduction in bacterial load, and no significant adverse effects in patients receiving PlasmaDerm treatment.

1.5.2. LTPs for Wounds - Summary

In general, plasma seems to be able to effectively kill bacteria, promote angiogenesis, influence signalling pathways to enhance proliferation and/or migration through altering mRNA and subsequent protein production, affect production of cytokines and growth factors, and affect collagen production and arrangement. Together, these biological responses to LTP treatment have shown, through clinical trials, that LTP treatment can reduce the bacterial colonisation of chronic wounds, and accelerate the early wound healing process, giving a potentially enhanced aesthetic result.

Importantly, LTP treatment appears to be safe, and well-tolerated by chronic wound patients and healthy volunteers in clinical trials [76, 92–94].

1.6. Thesis Aims - Tailoring LTPs for Wound Healing Applications

The ultimate aim for any medical treatment is to be able to restore the health of the patient, and for any illness this requires the correct dosage of a particular treatment or drug. The potential use of LTPs is no different and the ultimate goal for therapeutic LTPs is to be able to tailor the specific RONS composition (RONS types and concentrations) to be delivered, in the context of chronic wound treatments, directly to the target wound site. For this to be possible, it is necessary to understand how different species are produced in LTPs, and how they can be controlled through different physical operating conditions, such as the power input, gas feed and LTP geometry. Combined with this, a thorough

understanding of how different compositions of different LTP-produced RONS elicit different biological effects is required. Between these two arms of investigation, it is hoped that specific biological pathways can be accessed by specific LTP treatments. As well as being of interest for future therapeutic intervention, these investigations of correlations between RONS delivery and biological outcome are crucial for ensuring the safety of patients who may be treated with plasmas. First and foremost, medical treatments must be safe, and not cause more harm than good.

The aim of this body of work is to begin the process of correlation between LTP-produced RONS delivery, and biological effects on skin cells. To do this, a combination of experimental and computational plasma diagnostics will be used to investigate the chemical kinetics occurring within low temperature air plasmas, and how these can be controlled.

The work will be conducted using air plasmas, as these are so far underresearched for biomedical applications. Further to this, they are extremely efficient for production RONS, and due to the ubiquitous nature of air around the globe and the reduced need for complex LTP delivery systems, and costly infrastructure associated with bottled gases, it is possible that air LTPs could become potential therapeutics that are accessible in both developed and developing countries.

Aims

The aims of this work are as follows:

1. Develop an air plasma chemistry model for interrogating the chemical kinetics occurring in a low temperature air plasma

2. Investigate how different plasma species can be controlled by adjusting the experimental plasma operating conditions

3. Develop a protocol for future correlation between concentrations of LTP-delivered RONS and the viability of a skin cell line.

These aims will be addressed in the following chapters, to present a novel body of work that will contribute to the progression of development of air LTPs for wound healing applications.

First of all in Chapter 2, the principles of plasma chemistry modelling will be discussed, along with the development of a detailed nitrogen chemistry set used as a first step to the development of an air chemistry set. Next, in Chapter 3, pure nitrogen atmospheric pressure plasmas are modelled, and comparisons made between those studied previously at low pressure and the atmospheric pressure data obtained in this work. The focus is on the complex interactions between vibrationally excited states of nitrogen and other nitrogen species present in the plasma. Subsequently, the experimental and computational characterisation of an air DBD is presented in Chapter 4, where the ability to control plasma chemical kinetics using the physical operating parameters is discussed. Chapter 5 is concerned with the first steps to beginning the corrrelation between LTP-produced RONS concentrations delivered to a skin cell target. The thesis closes with conclusions in Chapter 6 and a discussion of the intended direction of subsequent research efforts in this area.

Plasma Modelling

To be able to understand interactions between LTPs and biological targets, it is important to be able to characterise the LTPs in terms of RONS composition, as these are believed to be the major player in biological influence [46]. Experimental methods of determining RONS concentration range from highly sophisticated methods, such as two-photon absorption laser-induced fluorescence (TALIF) [95] and absorption spectroscopy [96–99], to more basic measurement strategies using commercially available monitors for species such as nitric oxide and ozone (paper in preparation). However, when considering LTPs operating at atmospheric pressure, collisional quenching of reactive species can reduce their lifetimes, to the point that they are extremely challenging to quantify experimentally [42]. For these cases, plasma models can be a highly valuable tool for aiding plasma characterisation. Atmospheric pressure air LTPs fall into this category, therefore, the development of a suitable model is key.

In Section 1.6, the thesis aims of further characterising air LTPs for biomedical applications were outlined. In particular, the overall goal of the computational aspect of this work was to develop a chemistry model for air LTPs, in order to help with the understanding of chemical kinetics and how they can be controlled. This understanding will help to inform the development of biomedical plasma devices in the future. However, as air is a particularly complex mixture comprising of (at least) two molecular gases, as well as a myriad of electronically and vibrationally excited states, this was approached as a two-step process.

Firstly, to model the pure nitrogen situation, then secondly, to extend this to include oxygen and nitrogen/oxygen species.

There has been a significant effort afforded to the simulation of chemical kinetics in molecular gas plasmas, such as N_2, O_2 and air, over the past years. However, these works are largely focussed into two areas. i) Modelling of low pressure pure molecular gas discharges [100–114] and ii) modelling of atmospheric pressure discharges, where the molecular gas is a small admixture to a main noble gas feed gas [96, 115–123]. These studies are able to provide large amounts of data to understand the kinetics occurring in plasmas formed by different gases. However, when translating to pure molecular gas plasmas at atmospheric pressure, there can be issues due to the pressure differences, and the lack of a background noble gas. For example, in nitrogen, there are situations where certain chemical kinetics, such as 3-body reactions, are absent at low pressures, but extremely important as the pressure rises. Similarly, there are large differences in oxygen kinetics at low and high pressures, meaning that to develop a robust air chemistry set for atmospheric pressure, it is important to take into account these differences [99]. This neccessitates a step-wise approach to air chemistry set development, whereby each gas is developed individually first.

Further to this work on low pressure discharges, or molecular admixture plasmas, there have also been studies investigating pure molecular gas plasmas at atmospheric pressures. However, these are often concerned with much higher gas temperatures, for different types of application, where large gas temperatures are not problematic, such as nitrogen fixation into soil [124–126]. This results in simulations of plasmas which generally have much higher energies, and consequently higher ionisation degrees than low temperature situations which would be more applicable to biomedical applications.

In this work, the aim is to investigate low temperature, atmospheric pressure nitrogen and air plasmas. Previous works addressing these plasmas and conditions have been undertaken, for example [100, 127–129], which provide a

useful basis for the development of new reaction schemes suitable for the intended applications. The development of the reaction schemes will be discussed in the following sections. Consistent with all chemical kinetics simulations, one of the main limitations of the work is the lack of reliable reaction rate and cross sectional data. Therefore, it is beneficial to use a variety of validated reaction schemes for different conditions as a starting point for the development of new sets.

There are many different types of plasma models, including particle-in-cell and fluid models, however, many of these are extremely computationally expensive, and do not allow for thorough understanding of chemical kinetics [130]. However, since chemical kinetics are of utmost importance for this work, the use of a global model is more suitable. A comprehensive review of global models, including their advantages and common pitfalls is presented by Hurlbatt et al. [131]. Briefly, global models are able to quickly simulate spatially averaged parameters, over a wide range of plasma operating conditions, by solving particle and energy balance equations and neglecting spatial variations [130]. Large reaction schemes containing hundreds or thousands of reactions can be used, in order to gain insight into chemical kinetics. The ability to calculate densities of a large number of different species in a plasma is vital for considering molecular plasmas, as they are known to contain many different electronically and vibrationally excited species whose kinetics are important for the overall plasma properties [101]. However, global models must be used carefully, and their limitations acknowledged, as they are based on reaction rate data, that are often estimated, unavailable experimentally, or are associated with high levels of uncertainty in their values [132]. However, global models provide an excellent starting point for understanding systems with high levels of chemical complexity, such as air LTPs.

GlobalKin is a global plasma chemistry model developed by Kushner and colleagues, and described in detail in [133]. Specifics relating to the inputs for the code, including the development of a detailed nitrogen chemistry set, will be discussed in this chapter.

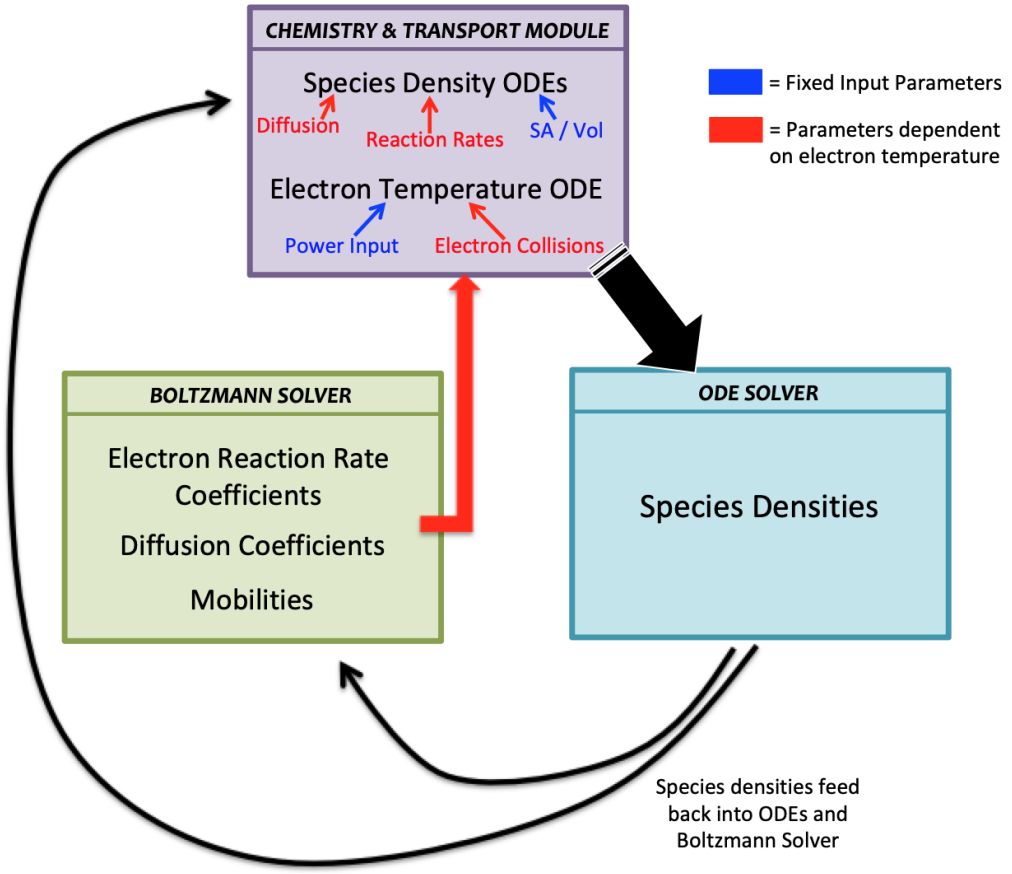

Figure 2.1: Diagram showing how the GlobalKin model works. Firstly, ordinary differential equations, ODEs, for species density and electron temperature are constructed. This takes direct GlobalKin inputs specified by the user, as well as electron reaction rate coefficients, diffusion coefficients and mobilities from the Boltzmann solver. An ODE solver then solves the equations and the new species densities are fed back into the ODEs and Boltzmann solver and densities are recalculated. At user-specified intervals, the Boltzmann solver also updates and new coefficients are fed back into the ODEs for the ODE solver to work with. This results in the time evolution of species densities and electron temperature.

2.1. GlobalKin Model Description

As mentioned above, GlobalKin is a zero-dimensional global plasma chemistry model, which has three main modules which will be discussed in the following sections. An overview of how each of these modules contributes to the GlobalKin running process is shown in Figure 2.1.

2.1.1. Reaction chemistry and transport module

This part of the model takes into account all the species that are present in the plasma, and their influx to and efflux from the plasma by constructing ordinary differential equations (ODEs) for time evolution of species densities and electron temperatures.

For each species included in the plasma, the mass balance continuity equation shown in Equation 2.1 is solved.

$$\frac{dN_i}{dt} = \frac{S}{V}\left(- \frac{D_i N_i \gamma_i}{\gamma_i \Lambda_D + \frac{4D_i}{\nu_{th,i}}} + \sum_j \frac{D_j N_j \gamma_j f_{ji}}{\gamma_j \Lambda_D + \frac{4D_j}{\nu_{th,j}}} \right) + S_i \tag{2.1}$$

where S and V are the surface area and volume of the plasma, respectively, N is the number density of heavy species i, Λ_D is the diffusion distance, D is the diffusion coefficient, γ is the sticking coefficient of species j at the walls, f_{ji} is the fraction of species j that returns from the wall as species i, ν_{th} is the thermal velocity of the particle, and S_i is the source term. γ and f_{ji} will be discussed in more detail in Section 2.2.3.

In Equation 2.1, the term in brackets refers to the loss and gain of species at the walls, and S_i is a source term for a species, which takes into account the reactions producing and consuming it.

The source term is calculated using the following equation:

$$S_i = \sum_j (a_{ij}^{RHS} - a_{ij}^{LHS}) k_j \prod_l N_l^{a_{lj}^{(LHS)}} \tag{2.2}$$

where a is the stoichiometric coefficients of species i in reaction j on the right and left hand side (RHS and LHS, respectively) of the reaction equation and k is the reaction rate coefficient for reaction j. $\prod_l N_l^{a_{lj}^{(LHS)}}$ is a term relating to the interaction of species i with any other species, including electrons and heavy particles.

The electron energy conservation equation is also solved in GlobalKin as follows:

$$\frac{d}{dt}\left(\frac{3}{2}n_e k_B T_e\right) = P_d - \sum_i \frac{3}{2} n_e \nu_{mi}\left(\frac{2m_e}{M_i}\right) k_B (T_e - T_i) + \sum_l n_e k_l N_l \Delta\epsilon_l \qquad (2.3)$$

where n_e is the electron density, T_e is the electron temperature, P_d is the plasma power input, m_e and M_i are the masses of electrons and heavy particles, respectively, ν_{mi} is the collision frequency, k is the reaction rate, N_l is the gas phase collision partner density and $\Delta\epsilon_l$ is the electron energy loss. The first terms on the RHS of the equation corresponds to power deposited into the plasma, and the second two terms describe the energy transfer in elastic and inelastic collisions with heavy particles, respectively [133].

2.1.2. Boltzmann equation solver

GlobalKin has an internal two-term Boltzmann solver to calculate the EEDF. It is called at regular, user-defined time intervals so that the EEDF can evolve over time in response to changing species densities. The Boltzmann solver calculates electron transport parameters for a variety of reduced electric field (E/N, where E is the electric field and N is the neutral particle density) values, which can be used by GlobalKin in the equations above described in Section 2.1.1

2.1.3. Ordinary differential equation (ODE) solver

An ODE solver described in [134] is used to solve Equations 2.1 and 2.3.

2.2. GlobalKin Inputs

There are a number of inputs required for GlobalKin to work. Firstly plasma parameters are needed. In order to be able to relate simulated plasma species densities to a particular experimental situation, certain parameters of the physical plasma setup need to be provided to GlobalKin. In particular, details about

the power input to the plasma, the geometry of the plasma volume, details regarding the gas flow/compositions and gas temperatures.

Alongside this, a detailed chemistry set is required, which outlines all of the plasma species and all the possible reactions and rate coefficients for the plasma.

The required inputs will be discussed in the following sections.

2.2.1. Translation from Experimental Setup

Power Deposition

To determine the energy input into the simulated plasma, GlobalKin requires the user to specify the power input, as a function of time. The power input can either be constant, or pulsed, whereby the pulse shape and power magnitude at different time points are detailed, then the pulse repeats for the specified simulation time, given a particular pulse frequency.

In practical terms, this means that to compare with experimental conditions, the power dissipated into a physical plasma must be determined. This involves measuring the current and voltage waveforms in the setup, then calculating powers using a method appropriate for the type of power input, for example, radio frequency (RF) or pulsed powers. Measuring the power in pulsed plasmas will be discussed in Chapter 4.

Plasma Geometry

GlobalKin works by using a surface area to volume ratio for the plasma. For this, the volume of the plasma is taken to be a cylinder with the gap as the height, and the electrode diameter as the diameter of the cylinder. The surface are of the plasma is the surface area of the same cylinder. Therefore, both of these values are specified. As well as this information, the diffusion distance is also required to calculate the loss of species due to diffusion, for a particular geometry [135]. For cylindrical geometries, with radius r, and length l (the

Table 2.1: Translation of DBD parameters to GlobalKin inputs

Parameter	Value
Radius, r	0.5 cm
Plasma Gap, l	0.2 cm
Pressure	1 atm

distance between electrodes), the diffusion length is calculated as in equation 2.4. This calculation is performed internally in GlobalKin when provided with a radius.

$$\frac{1}{\Lambda^2} = \left(\frac{2.405}{r}\right)^2 + \left(\frac{\pi}{l}\right)^2 \tag{2.4}$$

However, for geometries with a rectangular cross section, the diffusion distance has to be calculated manually and then provided as an input. To calculate the diffusion distance, Equation 2.5 is used.

$$\frac{1}{\Lambda^2} = \left(\frac{\pi}{x}\right)^2 + \left(\frac{\pi}{y}\right)^2 + \left(\frac{\pi}{l}\right)^2 \tag{2.5}$$

Where Λ is the diffusion length, r is the radius of a cylindrical geometry, x and y are the height and width of a rectangular cross section and l is the length of the plasma channel. All dimensions are given in cm.

In the work presented, all simulations have been performed assuming a cylindrical geometry for the plasma volume, following the dimensions of the dielectric barrier discharge (DBD) presented in [40], and currently in use at York Plasma Institute. As shown in Figure 2.2, the cylindrical electrode covered with an aluminium oxide dielectric layer, has a 1 cm diameter, and the electrode is held at a fixed distance from the ground, giving a discharge gap of $\approx$ 1 - 2 mm. The GlobalKin input parameters for this source are given in Table 2.1. This source was chosen as it is suitable for modelling purposes, as well as being appropriate for treating biological samples (see Chapter 5).

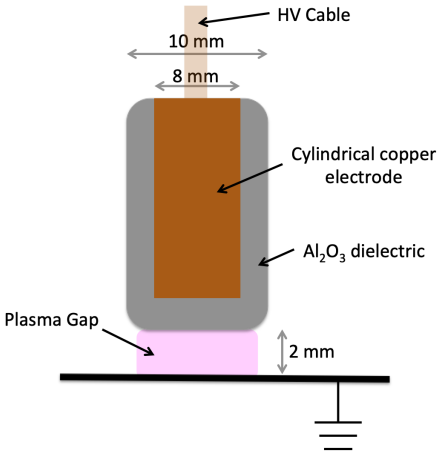

Figure 2.2: Schematic of the dielectric barrier discharge source geometry

Gas Composition

The gas composition used by the plasma is specified as an input of the initial molar fraction (MF) of each particular species. For example, for a pure nitrogen plasma, the initial MF of N_2 would be 1, and the ions and excited species would have a suitably small initial MFs of between $\approx 10^{-10}$ to 10^{-12} (unless otherwise specified). Electrons are assumed to have an initial MF of 10^{-11}.

For gas mixtures, the specific mixtures can be specified using the MFs for the component gases.

2.2.2. Chemistry Set

GlobalKin requires a chemistry set detailing all of the plasma species included in the model, alongside all of the possible reactions and reaction rate coefficients for within the plasma. The main components of a chemistry set are discussed in the following sections, and the development of detailed nitrogen and air chemistry sets will be discussed in Section 2.3 and Section 2.4, respectively.

2.2.3. Species

Every species that is included in the model has to be specified with its enthalpy of formation, charge and molecular weight. As well as this, other parameters are required, such as Lennard Jones parameters (related to the potential between two atoms/molecules) and the characteristics of species interaction with walls. In particular, with respect to density of species i:

- the sticking/disappearance coefficient - the fraction of species i that will be lost through interaction with the wall (γ in Equation 2.1)
- the return branching fraction - the fraction of a different species (species j) that produces species i when it is lost to the walls (f_{ji} in Equation 2.1)
- the return species - the species that species i will produce if it is lost to the wall

Wall losses can often have a large impact on the densities of species present in the plasma. Plasma species can diffuse to the walls, become adsorbed on the surfaces and react either with other adsorbed species, or react with other gas phase species, and contribute to the formation of a different species by re-entering the plasma volume. These processes are affected by many different factors, such as wall surface materials, gas pressure and temperature [136, 137]. The experimental data for wall sticking coefficients, γ, are generally obtained through experiments in low pressure systems. Therefore, there is uncertainty as to whether values of γ are still applicable and reliable when considering atmospheric pressure systems. Generally speaking, negatively charged ions and neutral ground state species are assumed to not react at the plasma walls, therefore $\gamma_n = 0$ and $\gamma_- = 0$ [137]. Negatively charged species are assumed to not diffuse to the walls as they are contained in the positive plasma potential of the plasma bulk [137]. However, for positive ions, electrons and excited states, the general assumption is $\gamma_+ = \gamma_e = \gamma_* = 1$. Positive ions and excited states are assumed to return to the plasma with a returning fraction $f = 1$, uncharged and in their ground state. Electrons, however, do not return to the plasma, therefore

$f = 0$, as they are assumed to recombine with adsorbed species, or contribute to current flows [137]. For species that do not follow this general case, their values of γ and f will be discussed in the following sections.

2.2.4. Reactions

Every reaction taking place in the plasma also has to be specified along with a set of parameters. These are vital for calculation of the reaction rate coefficient and the contribution to gas heating for each individual reaction.

To calculate the rate coefficient, the methods are different for heavy particle reactions and electron reactions. This is because electron reaction rate coefficients have a strong dependence on electron energy and, therefore, the state of the internally calculated EEDF at a particular time point. For heavy species (neutrals and ions) reactions, a specific rate coefficient k in Arrhenius form (Equation 2.6) can be specified, as ion energies do not change much due to their heavy mass.

$$k = A\left(\left(\frac{T_g}{300}\right)^n\right)exp\left(\frac{-E_a}{T_g}\right) \tag{2.6}$$

Where A is the Arrhenius coefficient (in s^{-1}, cm^3s^{-1} or cm^6s^{-1} for 1-, 2- or 3-body reactions, respectively), T_g is the gas temperature in Kelvin and E_a is the activation energy in K.

Whilst the Arrhenius equation can be used for electron impact rate coefficients, with T_g substituted with T_e in eV, and the $\frac{T_g}{300}$ term being replaced just with T_e in eV, electron reaction rate coefficients are more accurate when they are calculated from reaction cross sections. Electron energies can vary greatly (shown by the EEDF), and since their reaction rate coefficients are highly dependent on the electron energy, a constant reaction rate coefficient would not be appropriate. Instead, a reaction cross section is specified. This can be thought of as the effective area around a particle that another particle must be within for a reaction to occur and is dependent on particle energy. The reaction rate coefficient for electron processes can then be calculated in GlobalKin by combining this

specified cross section with the electron energy from the internally calculated, regularly updated EEDF.

The heavy particle reaction rate coefficients are often obtained from published literature. Electron impact cross sections are also found in publications, but also in online databases, such as LXCat [138], and Phys4Entry [139]. For data that is not available in sources such as these, estimates can be made based on data for similar reactions.

As well as the reaction rate, other important information to be specified includes how the reaction contributes to overall gas heating in the system. The user can either specify the amount of energy which is released or consumed by a particular reaction, or GlobalKin can calculate this internally, by using the enthalpies of formation for the species on either side of the reaction equation.

2.3. Nitrogen Chemistry Set Development

Pure nitrogen plasmas have many uses and have been of interest to researchers for many years [113]. The simulation of pure nitrogen plasmas is not a new concept for low pressure discharges, however, accurate modelling of species densities produced in atmospheric pressure nitrogen discharges has not yet been achieved [104, 112].

Here, a new detailed chemistry set for pure nitrogen discharges operating at atmospheric pressure will be outlined. Of particular interest, it contains a full manifold of 58 vibrational states for the ground $N_2(X)$ molecule, known to be vitally important for accurate nitrogen plasma simulations at low pressure. The reaction scheme was developed taking into account those presented in [102, 104, 113, 140], where multiple validation steps were presented alongside the reaction schemes. The pressures investigated in these publications varied from ≈ 1 Torr up to atmospheric pressure, covering most of the required reactions.

2.3.1. Species Included

Included in the reaction mechanism are 72 different species, shown in Table 2.2, and in the energy level diagram in Figure 2.3. Alongside electrons, ground state molecular nitrogen ($N_2(X)$), electronically excited nitrogen ($N_2(A, B, C, a, a', w)$) and molecular nitrogen ions ($N_2^+(X, B)$) are included. The singlet excited states $N_2(a, a', w)$ are included as a single state in GlobalKin, whereas the triplet states of $N_2(A, B, C)$ are considered individually. All 58 vibrational levels for ground state nitrogen, $N_2(X)$, are considered, however, no vibrationally excited levels are included for the electronically excited states. The potential energy levels for each of the vibrational states are from Laporta et al. [141], and the energies of some vibrationally excited states are shown in Figure 2.3. Nitrogen atoms are included in the model in both the ground state $N(^4S)$, and in the electronically excited states $N(^2P)$ and $N(^2D)$. The ions included in the model are $N_2(X)^+$, $N_2(B)^+$ and N_4^+. In low pressure discharges, the $N_2(X)^+$ ion is the dominant positive ion, however, it has been shown that as pressure increases, N_4^+ becomes dominant [113].

With regards to the nomenclature of the different species, the letter and superscript numbers following the element name (N, N_2 etc) denotes the specific electronically excited state that the species is in. These term symbols follow specific rules which are related to the spin angular momentum and the overall electron arrangement of the species. For the purposes of this, it is necessary to understand that different term symbols indicate the different excited states a species can exist in, with different energies shown in Figure 2.3.

As discussed in Section 2.2.3, $\gamma_- = \gamma_n = 0$. $\gamma_e = \gamma_+ = \gamma_* = 1$ and $f = 1$ where the species return in the uncharged, ground state. For the nitrogen chemistry set, the exceptions to this generalisation are for the vibrationally excited states and the atomic ground state nitrogen. For vibrational states, wall loss fractions are assumed to be $\gamma_{N_2(v)} = 4.5 \times 10^{-4}$ (calculated in Morgan and Schiff [142], further discussed in Black et al. [143]). However, these calculations were not performed using plasmas, and surfaces may react differently when a plasma is

Table 2.2: Nitrogen Species included in chemistry set. [1] Species considered as one

Particle	State
N_2	$X(v = 0 - 58), A, B, C, (a, a', w)^1$
N	${}^4S, {}^2P, {}^2D$
N_2^+	X, B
N^+	X
N_4^+	X
e^-	—

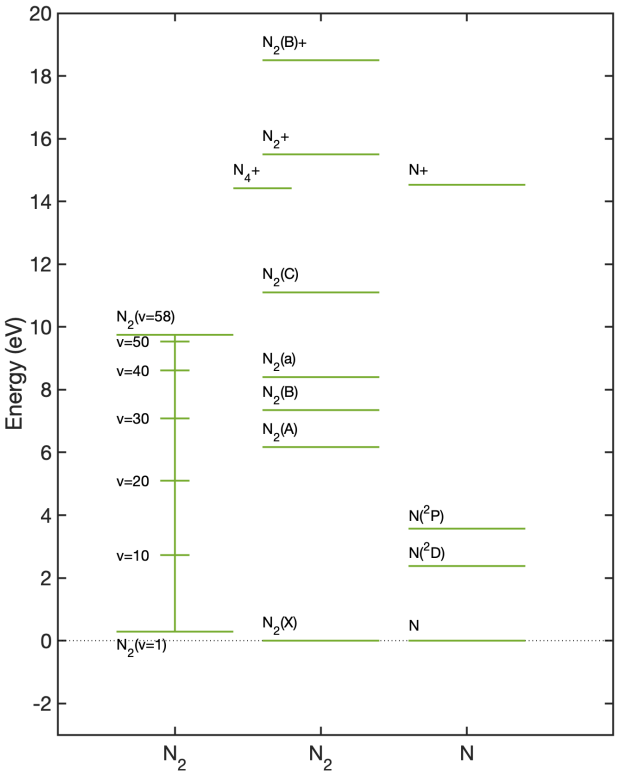

Figure 2.3: Energy level diagram for all species included in the nitrogen chemistry set. The energies shown are relative to the ground state plotted at 0 eV, and stated on the x axis. The range of energies for vibrationally excited nitrogen species are shown, with levels v=1, 10, 20, 30, 40, 50, 58 marked.

ignited or not. Therefore, wall loss fractions remain a source of error in these models. The returning fraction is considered to be $f_{vib} = 1$, where the returning species is $N_2(v-1)$ [102, 122]. For atomic nitrogen the assumption is made that $\gamma = 1 \times 10^{-4}$ and $f_N = 1$, returning as $N_2(X)$, based on the range of wall loss fractions for N from $1 \times 10^{-3} - 3 \times 10^{-6}$, given in [113].

2.3.2. Electron Impact Reactions

Electron impact reactions are an important part of a reaction chemistry set as they have a large influence on the energy of electrons in the plasma. Cross sectional data for all of these reactions is required to build up a complete set of cross sections, and there are a number of different sources for the data. All the electron impact reactions for the nitrogen chemistry set are shown in Appendix A, Table A.1, with the original reference for the cross sectional data.

The ability to assess whether the cross section set is realistic is important for accurate simulations, and one way of making this assessment is to use another model, called BOLSIG+ [144]. In principle, the Boltzmann solver in GlobalKin could also be used for these investigations, however, BOLSIG+ is a much more convenient tool for comparing different sets of cross sections. This is because the input files are simpler, and easier to adapt between cases.

2.3.3. BOLSIG+ and Reaction Cross Section Validation

BOLSIG+ is a two-term Boltzmann equation solver (similar to that used in GlobalKin), developed by Hagelaar and colleagues, and reported in [144]. When provided with sets of cross sectional data, it will calculate EEDFs and electron transport coefficients, as a function of reduced electric field (E/N). How cross section sets affect electron transport coefficients, such as electron mobilities, diffusion coefficients and ionisation coefficients, is a really useful way of validating cross sectional data. This is because these transport coefficients can also be measured experimentally, and data from such experiments (known as swarm data) is available in the LXCat online database [138]. Through this comparison

of BOLSIG+ outputted electron transport coefficients and swarm data, the best cross sectional data can be chosen to include in models.

Electron impact cross sectional data for excitation of vibrational states of nitrogen (reaction 2.7, NE2 in Appendix Table A.1) from the ground state have recently been calculated by Laporta et al. [141]. These cross sections were of particular interest to this study to accurately model the effects of vibrational excitation on electron energies in the plasma, as they are the most recent calculations of the excitation cross sections, and were calculated using an accurate potential energy curve for the N2 molecule, rather than using Morse-like energy curves as in previous works [141, 145].

$$e^- + N_2(X, v = 0) \rightarrow N_2(X, v = 1 - 58) + e^- \tag{2.7}$$

For this work, cross sectional data for vibrational excitation were compared through the use of BOLSIG+. The comparison was done between the cross sections used previously in GlobalKin, largely coming from [146], and those calculated by Laporta *et al* in [141]. In Figure 2.4, electron mobilities for each set are compared to each other (solid lines), and to the reference swarm data (points, error bars showing 10 % error), across a range of electric fields (E/N). Swarm data was obtained from the LXCat database, using the IST-Lisbon database [147]. Above an E/N value of ≈ 3, both the sets of cross sections fall within the 10 % of the swarm data. Below 3, both sets are outside 10 % of the swarm data values, but using the cross sections from [141] improve the agreement in the low E/N range. The effects of the different cross section sets on other electron parameters such as the mean electron energy and reduced ionisation coefficient were also compared to swarm data, and showed that the vibrational excitation cross sections from [141] were suitable.

In light of this comparison, the cross sections calculated by Laporta *et al* are used for all the vibrational states in the chemistry set.

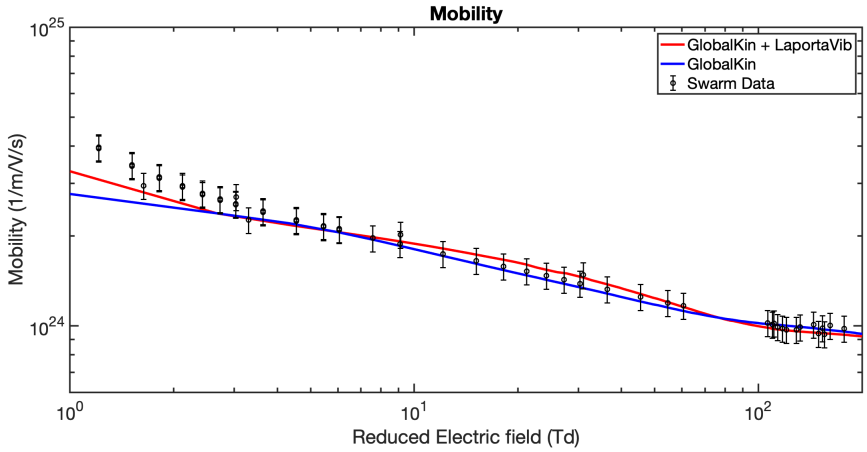

Figure 2.4: Graph showing the electron mobilities output from BOLSIG+ when different cross section sets are used. The blue line shows the GlobalKin cross section sets and the red line shows the GlobalKin cross section set where the vibrational excitation cross sections have been substituted for those published in [141]. The black points are the measured electron mobilities from LXCat [147], and the error bars show ± 10 % error.

2.3.4. Dissociation Reactions

Mechanisms of dissociation in nitrogen plasmas usually vary, particularly with dependence on the discharge pressure [112, 113]. Historically, the dissociation in nitrogen plasmas was believed to be solely electron impact mediated, through reaction 2.8 (NE8 in Appendix Table A.1).

$$e^- + N_2 \rightarrow N + N + e^- \tag{2.8}$$

This process occurs as electrons can excite ground state molecular nitrogen to an upper singlet state (such as $N_2(a)$ (among others), which causes predissociation and then dissociation. The cross section for electron impact dissociation used in this chemistry set for this process is the sum of all the cross sections for excitation into these predissociative upper singlet states [101, 148].

However, it was noticed that models were not able to accurately represent the measured atomic nitrogen concentrations seen in experimental settings, there-

fore more dissociation processes were proposed and discussed in [112]. These new processes have a reliance on both vibrationally and electronically excited states of N_2, and are described in reactions 2.9 and 2.10.

$$N_2(X, v = n) + N_2(X, v = n) \rightarrow N_2(X, v = 0) + N + N, \qquad \text{where} \quad n = 10 - 25 \tag{2.9}$$

$$N_2(X, 14 \leq v \leq 19) + N_2(A) \rightarrow N_2(X) + N_2(B) \rightarrow N_2(X) + N + N \tag{2.10}$$

All studies so far for the dissociation mechanisms in nitrogen discharges have been carried out at low pressures (relative to atmospheric pressure), and therefore, it is not known exactly how important each of these processes are at atmospheric pressure [104, 112]. Pressure variations in the few Torr range have shown previously that the dominant N_2 dissociation pathways change as a function of pressure [112]. In particular, that as the pressure of the discharge increases, the contribution of the electron mediated process decreases, and processes 2.9 and 2.10 become increasingly important. However, whether these trends will still hold at much higher pressures (1 atm $\approx$ 760 Torr) is not known.

There is concern over whether or not equation 2.9 is actually possible in a real plasma, and the reason for this comes when considering the enthalpies of formation of the different reactants and products, and the resulting strong endothermicity of the reaction. The enthalpy of formation of two N atoms equates to 9.80 eV. The enthalpy of formation of $N_2(X, v = 10)$ equals 2.73 eV [141]. Therefore, to produce two N atoms, a further 7.07 eV of energy would be required from another reactant, and from the gas temperature. Taking the upper limit of the vibrational state for this reaction, $N_2(X, v = 25)$, which has 6.14 eV of energy, this still leaves a deficit of 0.93 eV which would need to be overcome to allow the reaction to occur. Roughly, this means the gas temperature would need to be approximately 10000 K to provide sufficient energy. For this reason,

these reactions have not been included in this reaction chemistry set as this gas temperature is unrealistically high for the conditions considered here.

2.3.5. Vibrational Kinetics

As mentioned previously, vibrational kinetics are important to include in plasma chemistries, due to their influence on the electron energy distribution function (EEDF) through population of vibrationally excited states by electron impact (electrons losing energy, equation 2.11), and superelastic collisions between electrons and vibrationally excited states (electrons gaining energy, equation 2.12) [113].

$$e^- + N_2(X, v = 0) \rightarrow N_2(X, v = 1) + e^- \tag{2.11}$$

$$e^- + N_2(X, v = 1) \rightarrow N_2(X, v = 0) + e^- \tag{2.12}$$

Reactions involving vibrationally excited states are also believed to have an impact on nitrogen dissociation and gas heating, therefore, should be included to make the model as realistic as possible [106].

The first type of reactions to include are those which transfer vibrational energy (V) to translational energy (T), through so-called V-T reactions. These are particularly important for gas heating and are when vibrationally excited states collide with either ground state molecular (V-Tm) or atomic nitrogen (V-Ta) as follows:

$$N_2(X, v) + N_2 \rightleftharpoons N_2(X, w) + N_2, \qquad \text{where} \quad w = v - 1 \tag{2.13}$$

$$N_2(X, v) + N \rightleftharpoons N_2(X, w) + N, \qquad \text{where} \quad v - w =\leq 5 \tag{2.14}$$

where v and w are vibrational quantum numbers.

V-Tm collisions (Reaction 2.13, N32, Appendix Table A.2) are considered only as single quantum transitions. However, for V-Ta collisions (equation 2.14, N33, Appendix Table A.2), multi-quantum transitions are likely, therefore, transitions

where $v - w \leq 5$ are considered in this reaction chemistry set, with the rate remaining constant for all transitions from a particular value of v [113, 148, 149].

The second type are vibration-vibration (V-V) reactions (N34 in Table A.2), where two vibrationally excited states collide and vibrational energy is transferred between molecules, as follows:

$$N_2(X, v) + N_2(X, w - 1) \rightleftharpoons N_2(X, w) + N_2(X, v - 1) \tag{2.15}$$

where v and w are the vibrational quantum numbers of the collision partners.

V-V reactions are a mechanism for vibrationally excited states to climb the energy ladder, through so called vibrational up-pumping [101]. V-V reactions always favour the increase in vibrational state for the collision partner with the highest initial vibrational state. This is due to the anharmonicity of the potential curve used to model the energy levels, which means that the energy spacing between vibrational levels decreases with increasing vibrational energy. This is shown in Figure 2.3, where the energy difference between $N_2(X, v = 10)$ and $N_2(X, v = 20)$ is much greater than the difference between $N_2(X, v = 40)$ and $N_2(X, v = 50)$ [101]. This is the process which brings about the nitrogen pink afterglow seen in low pressure nitrogen discharges, and will be discussed again later in Chapter 3.

V-V Reaction Rate Coefficients

Rate coefficients for vibration-vibration (V-V) reactions are not widely available, other than for $v = 1 \rightarrow 0$ and the reverse reaction ($v = 0 \rightarrow 1$). Mainly, prior publications use data from Billing and Fisher [150], where rate coefficients are given for V-V reactions involving $N_2(X, v \leq 9)$. Then, using this data, authors either limit their studies to include only 9 vibrational states, or apply a scaling law [151]. Alves et al. [149] uses the latter approach and have published an expression for calculating the V-V reaction rate coefficient for any value of v. However, when using these expressions and comparing the rate coefficients obtained, to those published for v=1 in Pintassilgo and Guerra [106], there are significant discrepancies. Therefore, through personal communication with Vasco

Guerra, the expressions in [149] have been corrected, and are shown below in Equations 2.16. These expressions were used to calculate forward ($Q_{forward}$) and reverse ($Q_{reverse}$) V-V reaction rate coefficients all 58 vibrational states at 300 K (approximate temperature of a low temperature plasma), which are in agreement with the rate coefficients presented in [106].

$$Q_{forwards} = \left(\frac{v}{1 - v\chi_e^{N_2}}\right)\left(\frac{w}{1 - w\chi_e^{N_2}}\right) \times dif \times \frac{F(Y_{v,v-1}^{w-1,w})}{F(Y_{1,0}^{0,1})} \times Q_{1,0}^{0,1} \tag{2.16a}$$

$$Q_{reverse} = Q_{forwards} \times exp\left[\frac{2\hbar\omega_{N_2}}{k_B T_g} \times \chi_e^{N_2} \times (w - v)\right] \tag{2.16b}$$

$$Y_{v,v-1}^{w-1,w} = \frac{\pi L_{N_2-N_2}}{\hbar}\left(\frac{M}{4k_B T_g}\right)^{1/2} \Delta E_{v,v-1}^{w-1,w} \tag{2.16c}$$

with the normalisation:

$$Q_{1,0}^{0,1}(cm^3 s^{-1}) = \frac{6.35 \times 10^{-17} T_g^{3/2}}{\zeta} \tag{2.16d}$$

where $dif = 1$ when $w \leq v$.

For $w > v$;

$dif =$

$$exp\left(\frac{\hbar\omega_{N_2}}{k_B T_g}(w - v)\right), \qquad w > v, \tag{2.16e}$$

and $\zeta =$

$$39.0625 - 1.5625 max[v, w], \qquad max[v, w] < 10, \tag{2.16f}$$

$$25.2 + 24.1\left(\frac{max[v, w] - 10}{30}\right)^3, \qquad max[v, w] \geq 10 \tag{2.16g}$$

$F(Y) =$

$$\frac{1}{2}\left[3 - exp\left(-\frac{2Y}{3}\right)\right]exp\left(-\frac{2Y}{3}\right), \qquad 0 \leq Y \leq 20, \tag{2.17a}$$

$$8\left(\frac{\pi}{3}\right)^{1/2} Y^{7/3} exp(-3Y^{2/3}), \qquad Y > 20, \tag{2.17b}$$

Where v and w are the vibrational states of the collision partners, and all other constants are shown in Table 2.3. The forward and reverse V-V rates at 300 K for $v = 1$ are shown in Figure 2.5.

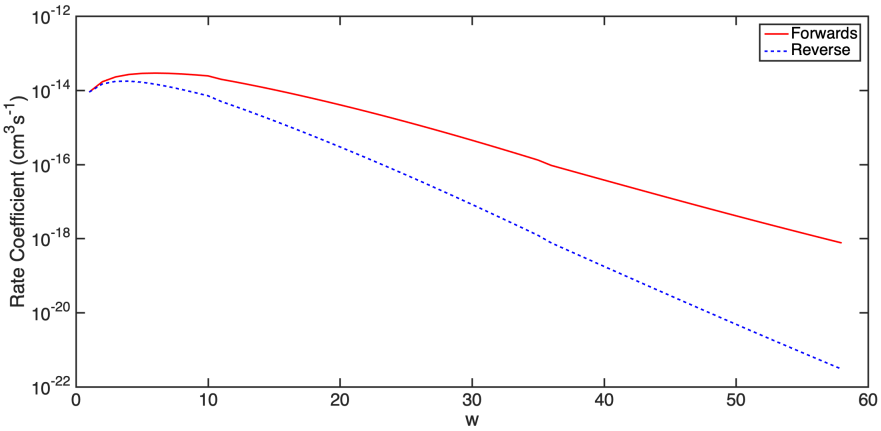

Figure 2.5: Figure showing the V-V rate coefficient as a function of vibrational quantum number w, when $v = 1$ in the reaction $N_2(X, v) + N_2(X, w-1) \rightleftharpoons N_2(X, w) + N_2(X, v-1)$. Coefficients are calculated using equations 2.16, at 300 K.

Table 2.3: Constants for equations 2.16 and 2.19 to calculate V-V and V-Tm reaction rate coefficients in nitrogen

Constant	Value	Description
$\chi_e^{N_2}$	6.073×10^{-3}	Morse's operator parameter
h	6.63×10^{-34} m² kg s⁻¹	Planck's constant
$\hbar$	1.055×10^{-34} m² kg s⁻¹	$\hbar \equiv \frac{h}{2\pi}$
ω_{N_2}	4.443×10^{14} s⁻¹	Morse's operator parameter
k_B	1.38×10^{-23} m² kg s⁻² K⁻¹	Boltzmann's Constant
$L_{N_2-N_2}$	2×10^{-11} m	Range of intermolecular forces in $N_2 - N_2$ collisions
M	4.65×10^{-26} kg	Mass of nitrogen molecule
$\Delta E_{v,v-1}^{w-1,w}$	$\hbar\omega_{N_2} 2\chi_e^{N_2} \lvert w - v \rvert$	Energy difference with transition between level v to $v-1$, and $w-1$ to w
$\Delta E_{v,v-1}$	$\hbar\omega_{N_2}(1 - 2\chi_e^{N_2} v)$	Energy difference between v and $v-1$

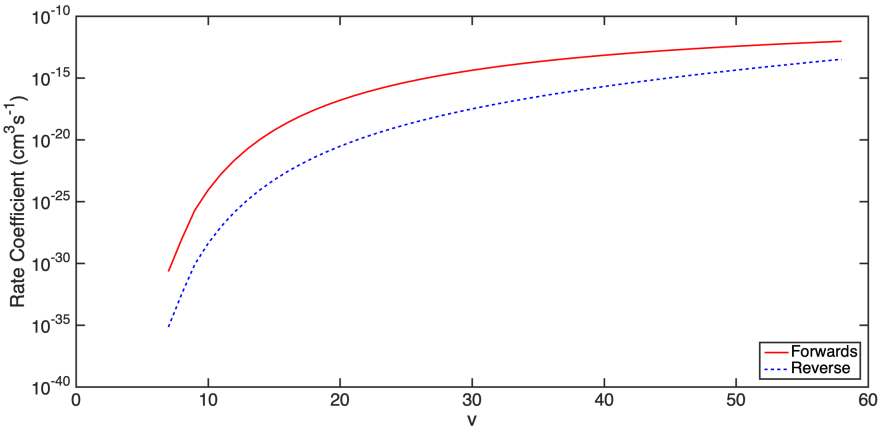

Figure 2.6: Figure showing the forwards and reverse atomic V-T rate coefficients as a function of vibrational quantum number v, calculated at 300 K, using equations 2.18

V-T Reaction Rates

V-Ta reaction rates come from Equation 2.18 found in [113]. The V-Ta process can either be a reactive process (where the molecule reactant becomes the atomic product and the atom combines with the remaining atom, at a vibrational level one less than the original vibrationally excited molecule), or a non-reactive process (where the molecule remains molecular and just drops down a vibrational level) [110]. The constants used in Equation 2.18 are different for these two instances, and the total V-Ta rate is the sum of the two processes (N33 in Appendix Table A.2). There is also a threshold, v_{thresh} for the vibrational state, above which the V-Ta processes can occur.

$$K_{v,v-1}^{N_2-N} = \left(A_0 \times exp\left(-\frac{A_1}{v} + \frac{A_2}{v^2} \right) \right) \times \frac{1}{5 \times 10^{10}} \tag{2.18}$$

Where $K_{v,v-1}^{N_2-N}$ is the rate coefficient for the de-excitation of $N_2(v)$ to $N_2(v-1)$ upon collision with atomic nitrogen in $cm^3\ s^{-1}$, v is the vibrational state, and A_0, A_1 and A_2 are constants given in Table 2.4. The V-Ta rates at 300 K are shown in Figure 2.6. As mentioned in Section 2.3.5, multi-quantum transitions are highly likely in V-Ta collisions, and the rate coefficient is assumed to be the same for changes of up to 5 vibrational levels.

Table 2.4: Constants for equation 2.18 to calculate V-Ta reaction rate coefficients in nitrogen. T_g is gas temperature in K.

	Reactive	Non-reactive
A_0	$2.21 \times 10^4 / T_g^{1.43}$	$9.24 \times 10^4 / T_g^{1.63}$
A_1	$3.21 \times 10^4 / T_g^{0.80}$	$1.82 \times 10^4 / T_g^{0.70}$
A_2	$2.50 \times 10^5 / T_g^{1.04}$	$9.89 \times 10^3 / T_g^{0.44}$
v_{thresh}	7	9

For V-Tm reaction rates, Equations 2.19 also in [149] was used. Equation 2.19a gives the expression for the forwards reaction coefficient, where 2.19b gives the rate for the reverse reaction rate coefficient (N32 in Appendix Table A.2).

$$K_{v,v-1} = v\left(\frac{1-\chi_e^{N2}}{1-\chi_e^{N2}v}\right)\frac{F(Y_{v,v-1})}{F(Y_{1,0})}P_{1,0} \tag{2.19a}$$

$$K_{v-1,v} = K_{v,v-1}exp\left(-\frac{\Delta E_{v,v-1}}{k_B T_g}\right) \tag{2.19b}$$

$$Y_{v,v-1} = \frac{\pi L_{N_2-N_2}}{\hbar}\left(\frac{M}{4k_B T_g}\right)^{\frac{1}{2}}\Delta E_{v,v-1} \tag{2.19c}$$

where the $F(Y)$ term uses equation 2.17 and the normalisation is as follows:

$$P_{1,0}(\mathrm{cm^3 s^{-1}}) = \frac{1.07 \times 10^{-12} T_g^{3/2}}{0.2772 T_g - 80.32 + 35.5(\frac{v-1}{39})^{0.8}}F(Y_{1,0}) \tag{2.19d}$$

The V-Tm rate coefficients for the forward and reverse process at 300 K are shown in Figure 2.7. As mentioned earlier in Section 2.3.5, only single quantum transitions are considered for V-Tm collisions.

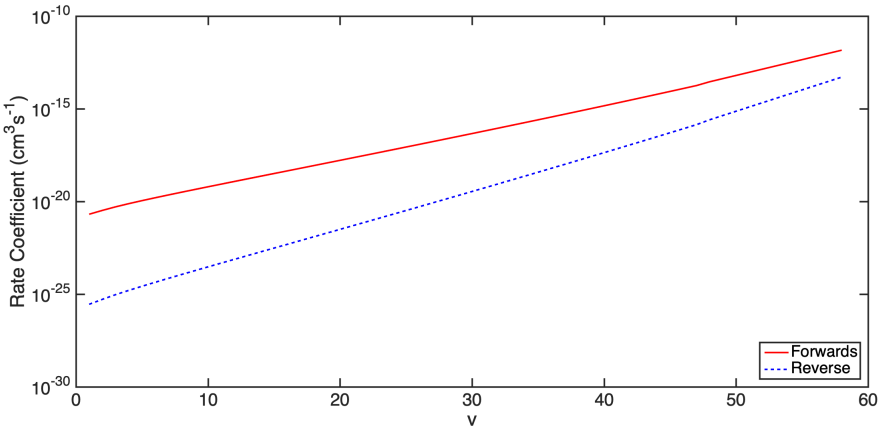

Figure 2.7: Figure showing the forwards and reverse molecular V-T rate coefficients as a function of vibrational quantum number v, calculated at 300 K, using equations 2.19.

2.4. Air Chemistry Set Development

Air chemistry is becoming increasingly important, as more and more applications are using air feed gases for plasmas. Importantly, the use of air plasmas in the field of plasma medicine is gaining interest due to the reduced need for infrastructure capable of handling expensive bottled, noble gases. Air is also readily available across the globe, opening up new opportunities for air plasma applications in developing countries for a variety of biomedical applications such as skin infections and chronic wounds [152].

To advance the understanding of air plasmas, in particular for their molecular interactions with biological targets, the complex chemical kinetics occurring in them are of particular interest [152]. Specifically, how different biorelevant species are produced and can be controlled in the active plasma, and delivered to the biological target.

Here, a detailed air chemistry set has been developed, by extending the nitrogen chemistry set above. Using the nitrogen chemistry set as a starting point, the extension to a dry, synthetic air (80 : 20, N_2 : O_2) chemistry set requires the addition of oxygen species, and the resulting nitrogen oxygen species. The oxygen and nitrogen/oxygen chemistry comes mostly from the sets used in

Table 2.5: Species included in the air chemistry set, in addition to those in Table 2.2

Type	Species
Neutral Molecules	$O_2(X, a, b), O_3(X), NO(X, A, B), NO_2(X)$
Neutral Atoms	$O(^3P), O(^1D), O(^1S)$
Positive Ions	O^+, O_2^+, NO^+, NO_2^+
Negative Ions	O^-, O_2^-, O_3^-

[99, 102, 110, 122, 132].

2.4.1. Species

Species included in addition to those in Table 2.2 are shown in Table 2.5, and in the energy level diagram Figure 2.8. These include ground state molecular and atomic oxygen, as well as the molecular, $O_2(a)$ (also known as singlet delta oxygen) and $O_2(b)$, and atomic $O(^1D)$ and $O(^1S)$, electronically excited states. Both the positive and negative ions of O and O_2, are included in their ground state, as well as O_3^-.

Vibrationally excited oxygen is not included specifically as individual species, as the formation of an oxygen VDF is not particularly important for determining species concentrations and plasma dynamics in mixtures of air and nitrogen [153]. However, the inclusion of a single "pseudo vibrationally excited state" of $O_2(X, v = 1)$ will be discussed in Section 2.4.4 because of its role in mediating the highly important nitrogen vibrational kinetics.

Exceptions to the generalised case for surface losses of plasma species (see Section 2.2.3) in the oxygen system are ground state atoms $O(^3P)$, and electronically excited molecules $O_2(a)$, and $O_2(b)$. These species have sticking coefficients of $\gamma = 0.02, 0.0004$ and 0.02, respectively, to return as $O_2(X)$ with $f = 1$ for the molecules and $f = 0.5$ for the atoms [99].

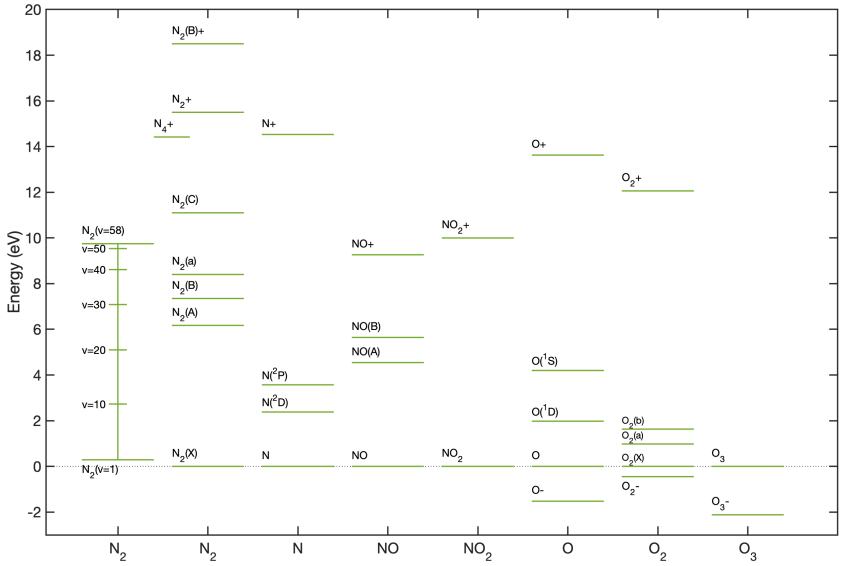

Figure 2.8: Energy level diagram for all species included in the air chemistry set. The energies shown are relative to the ground state plotted at 0 eV, and stated on the x axis. The range of energies for vibrationally excited nitrogen species are shown, with levels $v = 1, 10, 20, 30, 40, 50, 58$ marked.

2.4.2. Electron Impact Reactions

Electron impact reactions are included in the model for collisions with all ground state and excited states. Unless otherwise stated, the reaction rates are determined in GlobalKin as a function of the appropriate electron impact reaction cross section and the electron energy, calculated using the internal Boltzmann solver. A subset of the electron impact reactions used in this work, that will be discussed in more detail in this section, is shown in Table 2.6. The table shows the reactions, grouped by the type of electron impact process, the threshold energy at which the cross section becomes non-negligible, and information regarding the choice or calculation of the cross section.

Unlike the nitrogen system, positive oxygen ion production is mediated only by electron impact ionisation (OE1, OE2, Table 2.6), as Penning processes causing ionisation by collisions between metastable excited states do not occur [102]. Similarly, negative ions produced in plasmas containing oxygen are produced

Table 2.6: Important electron impact reactions in oxygen, discussed in more detail in the text

No.	E_{Thr} (eV)	Reaction	Rate	Reference
Electron Impact Ionisation				
OE1	13.62	$e^- + O > O^+ + e^- + e^-$	$f(E)$	[154]
OE2	12.06	$e^- + O_2 > O_2^+ + e^- + e^-$	$f(E)$	[155]
Dissociative Electron Attachment				
OE3	0.00	$e^- + O_2 > O + O^-$	$f(E)$	[155]
OE4	3.50	$e^- + O_2(a) > O + O^-$	$f(E)$	[156]
OE5	2.85	$e^- + O_2(b) > O + O^-$	$f(E)$	[99, 156]
OE6	0.00	$e^- + O_3 > O_2 + O^-$	$f(E)$	[157]
OE7	0.25	$e^- + O_3 > O_2^- + O$	$f(E)$	[157]
Electron Impact Vibrational Excitation				
OE8	0.19	$e^- + O_2 > O_2 + e^-$	$f(E)$	[155]
OE9	0.38	$e^- + O_2 > O_2 + e^-$	$f(E)$	[155]
OE10	0.57	$e^- + O_2 > O_2 + e^-$	$f(E)$	[155]
OE11	0.75	$e^- + O_2 > O_2 + e^-$	$f(E)$	[155]

through dissociative electron attachment, another electron impact mediated process (OE3-7, Table 2.6). Alongside these important processes for ionisation and electron attachment, electron impact reactions for momentum transfer and dissociation are also included to describe the electron kinetics in the plasma.

In order for the Boltzmann solver to accurately determine electron energy in the plasmas, electron impact reactions which produce excited species (which are not modelled as discrete species in the simulation) are also included. These reactions have the appropriate reaction cross section and thresholds, and therefore, affect the electron energy correctly, however, the reactions just show the production of the ground state species. Examples of these are OE8-11, Table 2.6, where the reaction is actually denoting the excitation into a vibrationally excited state of O_2, with the threshold energy denoting the energy of the vibrational state. However, since vibrational states of oxygen are not included as individual species, these reactions will just affect the electron energies. This contribution to the EEDF calculations will have effects on the simulation as if vibrational

states were included, but does not allow the tracking of specific vibrational state densities, or their chemical effects on other plasma species.

2.4.3. $N_2 - O_2$ Chemical Kinetics

There are $\approx$ 5500 reactions included in the presented air chemistry set, which includes $\approx$ 4800 reactions which form the standalone nitrogen chemistry set (when all the reactions with all the possible vibrational states are included). The reaction scheme for air is made up of the nitrogen and nitrogen/oxygen chemistry reaction schemes shown in full in the Appendix, in tables A.1, A.2, A.3, A.4 and A.5. The reaction scheme for pure oxygen, not included in the Appendix is presented in full in [99]. All the reactions and rate coefficients are chosen to describe as accurately as possible the species kinetics in an oxygen/nitrogen plasma. The reactions include the interactions between ions and neutrals as charge exchange reactions, recombination reactions between positive and negative ions, and neutral chemistry involving ground and excited states.

The production of nitric oxide is of particular interest to biomedical plasmas, because of its relevance in a wide variety of physiological process occurring in the body. The production of nitric oxide in air plasmas has been investigated previously, and of particular interest is the Zeldovich reaction as follows:

$$N_2(v) + O \rightarrow NO + N \tag{2.20}$$

Equation 2.20 (NO49 in Appendix Table A.5) is known to become exothermic at $N_2(X, v = 13)$ and is assumed to not be possible when a lower vibrational state is involved [110]. For this reason, for $N_2(X, 0 \leq v < 13)$ the rate is assumed to be zero, whereas for $N_2(X, v \leq 13)$, the rate coefficient is assumed to be constant at 1×10^{-13} cm^3 s^{-1} for all values of v, due to the lack of available experimental or theoretical data to explain how the rate is affected by v [102, 110].

Another important point to make about the Zeldovich equation is that, in the low pressure case, this reaction is also the major mechanism for dissociation of N_2 in the $N_2 - O_2$ system [110]. Whether or not this is the case at atmospheric pressure is not known.

2.4.4. Nitrogen-Oxygen Vibrational Kinetics and Rate Coefficients

V-V reactions

As stated earlier, the individual vibrational states of oxygen have not been included in this reaction set in their own right, as they should not have a significant effect on plasma kinetics in these gas mixtures [153]. However, they do have a role as a collision partner in V-V reactions involving $N_2(X, v)$ as per reaction 2.21, therefore, they can contribute to the evolution of the nitrogen vibrational distribution function, VDF, known to be potentially important in $N_2 - O_2$ plasmas.

$$N_2(X, v+1) + O_2(X, v=0) \rightleftharpoons N_2(X, v) + O_2(X, v=1) \tag{2.21}$$

As a result, $N_2 - O_2$ V-V reactions have been included for the $O_2(X, v=0) \rightleftharpoons O_2(X, v=1)$ transition as per equation 2.21 (NO63 in Appendix Table A.5), using the appropriate rate for the quantum vibrational numbers of N_2 and O_2. As mentioned previously, $O_2(X, v=1)$ will be included as a pseudo vibrational state, to affect the nitrogen VDF, but its density will not be calculated by GlobalKin.

The rate coefficients for these reactions were obtained from Guerra and Loureiro [110], and are shown in Figure 2.9.

V-Ta and V-Tm reactions

As per reactions 2.22 and 2.23 (NO64 and NO65 in Appendix Table A.5), oxygen species O and O_2 can also influence the VDF of $N_2(X, v)$ by acting as a

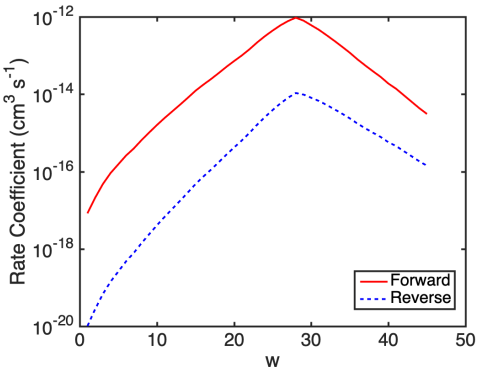

Figure 2.9: Reaction rate coefficients for $N_2 - O_2$ V-V reactions $N_2(X, v = w+1) + O_2(X, v = 0) \rightarrow N_2(X, v = w) + O_2(X, v = 1)$ [110], as a function of N_2 vibrational quantum number at 500 K.

quenching species in V-Ta and V-Tm reactions.

$$N_2(X, v) + O \rightleftharpoons N_2(X, v-1) + O \tag{2.22}$$

$$N_2(X, v) + O_2 \rightleftharpoons N_2(X, v-1) + O_2 \tag{2.23}$$

In order to determine the reaction rate coefficients for these reactions, expressions published in [110] were used.

For $N_2 - O$ V-Ta reactions, the rate scales with the value of v as stated in [110], as per equation 2.24:

$$K_{v,v-1} = v \times K_{1,0} \tag{2.24}$$

where $K_{1,0}$ is the rate coefficient for $N_2(v = 1) + O \rightarrow N_2(v = 0) + O$, stated in [158], as follows:

$$K_{1,0} = \left[2.3 \times 10^{-13} exp\left(-\frac{1280}{T_g}\right)\right] + \left[2.7 \times 10^{-11} exp\left(-\frac{10840}{T_g}\right)\right] \tag{2.25}$$

For molecular V-T rates, the scaling expression in [110] is used to determine the ratio between the rate of depopulation of $N_2(v)$ by N_2 and of $N_2(v)$ by O_2. This scaling factor for each value of v is then applied to the rates for the $N_2(v) - N_2$ V-Tm rate coefficients to determine the new rate coefficient for collisions with molecular oxygen.

For V-Tm reactions, the reaction rate coefficients for $N_2 - N_2$ V-Tm reactions can be scaled using the formula shown in equation 2.26 as discussed in [110].

$$\frac{P_{v,v-1}^{N_2-O_2}}{P_{v,v-1}^{N_2-N_2}} = \frac{P_{1,0}^{N_2-O_2}}{P_{1,0}^{N_2-N_2}} exp[(\delta_{VT(N_2-O_2)} - \delta_{VT(N_2-O_2)})(v-1)] \tag{2.26}$$

where

$$\frac{P_{v,v-1}^{N_2-O_2}}{P_{v,v-1}^{N_2-N_2}} = \left(\frac{\mu_{v,v-1}^{N_2-O_2}}{\mu_{v,v-1}^{N_2-N_2}}\right)^{0.5} \left(\frac{d_{N_2-O_2}}{d_{N_2}}\right)^2 \frac{F(Y_{v,v-1}^{N_2-O_2})}{F(Y_{v,v-1}^{N_2-N_2})} \tag{2.27}$$

and where $\delta_{VT(N_2-O_2)}$ and $\delta_{VT(N_2-N_2)}$ are given by:

$$\delta_{VT} = 4\chi_e^{N_2}(\hbar\omega_{N_2})^{2/3} \left(\frac{\pi L}{\hbar}\right)^{2/3} \left(\frac{\mu}{2k_B T_g}\right)^{1/3} \tag{2.28}$$

Here, d is the distance of closest approach between the two particles ($d_{N_2-O_2} = \frac{d_{N_2}+d_{O_2}}{2}$) and μ is the reduced mass of the colliding particles. The $F(Y)$ terms are calculated as per equations 2.19c and 2.17, exchanging L for either $L_{N_2-N_2}$ or $L_{N_2-O_2}$ and M for $\mu_{N_2-N_2}$ or $\mu_{N_2-O_2}$ for the $N_2 - N_2$ or $N_2 - O_2$ reactions, respectively. Values for these equations are given in Table 2.7.

For all V-T reactions, the reverse reaction rate coefficient can be obtained by detailed balancing, as per equation 2.19b, where the forward rate coefficient is multiplied by the term $exp(-\frac{\Delta E_{v,v-1}}{k_B T_g})$.

Reaction rates for the forward and reverse V-T reactions are shown in Figure 2.10, as a function of the vibrational quantum number of $N_2(X)$.

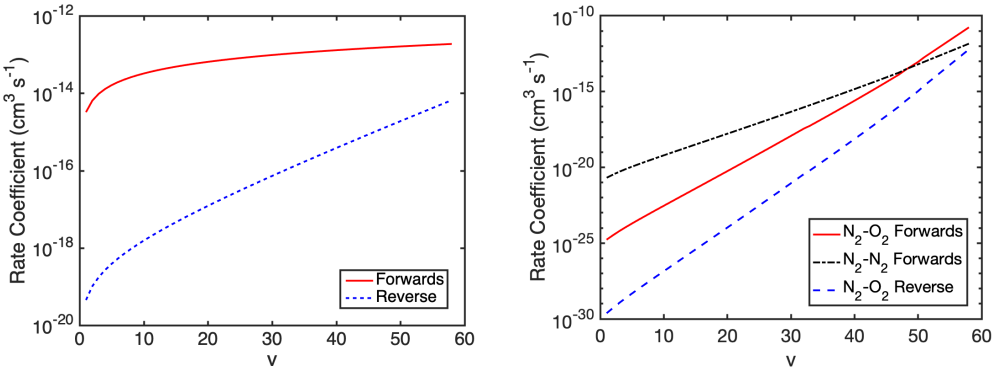

(a) Forward and reverse reaction rate coefficients for $N_2 - O$ V-Ta reactions.

(b) Forward and reverse reaction rate coefficients for $N_2 - O_2$ V-Tm reactions.

Figure 2.10: Graphs to show V-Ta and V-Tm reaction rate coefficients in the nitrogen-oxygen system, as a function of vibrational quantum number of $N_2(X)$. All rates are calculated for 300 K using equations 2.24 and 2.26 for the V-Ta and V-Tm reactions, respectively. Figure 2.10b also shows the V-Tm rates for $N_2 - N_2$ collisions from which the $N_2 - O_2$ V-Tm reaction rates are calculated.

Table 2.7: Constants for Equation 2.26 to calculate $N_2 - O_2$ V-Tm reaction rate coefficients. Constants are in addition to those in Table 2.3

Constant	Value	Description
$L_{N_2-N_2}$	2×10^{-11} m	Range of intermolecular forces in $N_2 - N_2$ collisions
$L_{N_2-O_2}$	3×10^{-11} m	Range of intermolecular forces in $N_2 - O_2$ collisions
$\mu_{N_2-N_2}$	2.33×10^{-26} kg	Reduced mass of nitrogen-nitrogen collision
$\mu_{N_2-O_2}$	2.48×10^{-26} kg	Reduced mass of nitrogen-oxygen collision
d_{N_2}	3.75×10^{-10} m	Distance of closest approach (N_2)
d_{O_2}	3.50×10^{-10} m	Distance of closest approach (O_2)
$d_{N_2-O_2}$	3.63×10^{-10} m	Distance of closest approach ($N_2 - O_2$)

2.5. Summary

Molecular plasmas have extremely complex chemical kinetics, and the understanding of them is vital for the potential tailoring of LTP RONS compositions for biomedical applications. Here, a novel chemistry set for atmospheric pressure, pure nitrogen discharges has been developed, with particular attention paid to the vibrational kinetics. Care has been taken to include the most accurate electron impact reaction cross sections, and expressions for the calculation of V-V and V-T reaction rate coefficients have been presented. Further to this, the nitrogen reaction scheme has been extended to include oxygen species and the resulting nitrogen/oxygen species. Once again, particular attention has been paid to the nitrogen vibrational kinetics, and the influence of oxygen species on the nitrogen VDF. These reaction schemes will be used in the following chapters to interrogate the chemical kinetics occurring in nitrogen and air plasmas.

Results I - Simulations of Nitrogen LTPs

3.1. Motivation

The chemical kinetics taking place in nitrogen plasmas have been under investigation for a long time, and there is extensive literature dedicated to the understanding of them. Until recently, studies were limited to low pressure situations (up to $\approx$ 10 Torr [113]), due to the applications for which nitrogen plasmas were used, such as modification of a variety of surfaces [104]. However, with the advent of the field of plasma medicine, and the development of atmospheric pressure plasma sources, the use of nitrogen as a feed gas is now extending to atmospheric pressure ($\approx$ 760 Torr $\approx$ 100000 Pa) applications, requiring new understanding of how these high pressures affect the chemical plasma kinetics.

In Chapter 1, Section 1.6, the overall aim of developing an air chemistry set to help with the understanding of the chemical kinetics occurring in these chemically complex LTPs was presented. Nitrogen forms $\approx$ 80 % of air, and is known to be very chemically complex in its own right, therefore as a first step to developing an air chemistry model, a nitrogen reaction scheme was developed and presented in Chapter 2. To test the scope of the nitrogen model, and to gain some insight into how nitrogen alone may be useful for medical therapeutics, the chemical kinetics were investigated using GlobalKin.

Nitrogen is a particularly interesting diatomic molecule, existing not only in the ground state, but also multiple electronically excited states. On top of this, vibrational excitation has been shown to play a huge role in determining kinetics in nitrogen plasmas at low pressure, acting to mediate the appearance of a well-documented phenomenon known as the nitrogen pink afterglow [101, 159]. The nitrogen pink afterglow is a phenomenon first described many years ago, when it was noticed that downstream from low pressure DC nitrogen discharges, there was a region of pink light in the afterglow [159]. This afterglow region has been the subject of many experiments and modelling studies for many years [101, 159, 160], and has since been shown to be the result of local ionisation in the afterglow region, after an initial decay of the electrons produced in the active plasma region [161]. This local ionisation has been attributed to Penning ionisation processes such as $N_2(A) + N_2(a) \rightarrow N_4^+ + e^-$ and $N_2(a) + N_2(a) \rightarrow N_4^+ + e^-$ involving the $N_2(A)$ and $N_2(a)$ metastable states, produced as a result of longer-lived vibrationally excited nitrogen species carrying energy downstream from the active plasma [101].

Vibrationally excited states of nitrogen can carry large amounts of energy, up to almost 10 eV [141], and in certain situations can be long lived. Therefore, these could potentially become a mechanism of transferring energy to biological settings, by a mechanism that has not yet been considered. Importantly, these energies are similar to the energies of bonds found in many organic molecules, and therefore, the delivery of these energies to biological targets by vibrationally excited states may have consequences, either positive or negative, that have not been considered previously.

At atmospheric pressure, molecular plasmas require large amounts of energy to cause breakdown, due to the ability of molecules to absorb energy in their bonds and exist in many vibrational states. These vibrational states have a high propensity to collide with other species, and release this energy into translational, heat, energy through vibration-translation (V-T) collisions [106]. Therefore, to prevent excessive gas heating that would be harmful in biomedical applications, these plasmas require pulsing. With pulsing, the time when the

plasma is on, and power is being applied, is relatively small compared to the whole period of the pulse frequency, therefore, the majority of time that plasma is in contact with biological tissue, the tissue will be effectively subjected to the plasma afterglow. Since certain species are also able to build up during this off time, the simulation of afterglows at atmospheric pressure is highly important, and has not been investigated in atmospheric pressure nitrogen discharges previously.

The atmospheric pressure nitrogen plasma afterglow has not been investigated before. In this chapter, a novel investigation into the chemical kinetics of atmospheric pressure nitrogen discharges will be presented, through an in-depth study using a global plasma chemistry model, GlobalKin. In particular, due to a lack of prior research, the nitrogen electron and heavy particle species concentrations will be interrogated throughout the afterglow region, with particular interest being paid to vibrationally excited states of $N_2(X)$. To achieve this, a detailed reaction chemistry set introduced in Chapter 2, has been used, based on reaction sets presented in [104, 113, 140] to highlight some fundamental, novel findings regarding the afterglow region of atmospheric pressure nitrogen discharges.

3.2. Aims

The aims of this chapter are:

1. To determine the scope of the novel nitrogen chemistry set presented in Chapter 2
2. To determine whether complex afterglow kinetics are seen in atmospheric pressure discharges, as in the low pressure case of the pink afterglow
3. To determine the importance of vibrationally excited nitrogen species at atmospheric pressure

Using the work presented in this chapter, the next step would be to validate the

findings experimentally. Unfortunately, this was not possible here due to a lack of appropriate equipment and experimental setups.

3.3. Methods

3.3.1. GlobalKin

As described more fully in Chapter 2, GlobalKin is a zero-dimensional global plasma chemistry model. For this chapter, the simulations will be carried out using the nitrogen reaction scheme also discussed in Chapter 2.

3.3.2. Test Case Plasma

Geometry

The geometry used in the test case is that of a volume dielectric barrier discharge used at York Plasma Institute, and described in [40]. Briefly, the powered electrode has a diameter of 1 cm, and is held a fixed distance from the grounded electrode, giving a discharge gap of 1 mm. In keeping with a realistic situation, this plasma is simulated to have a pulsed power applied, and in most cases, a single pulse and associated afterglow will be investigated. The plasma, unless otherwise stated, will be simulated at atmospheric pressure, with an initial gas temperature of 310 K as this is close to room temperature.

Power Pulse Characteristics

A single power pulse is used for the test case plasma. The pulse has a rise time of 100 ns, remains on for 100 μs, falls for 100 ns, then remains off for the rest of the 1 ms period, in keeping with a 1 kHz pulse frequency. Throughout these test situations, the pulse characteristics remain the same, with only the magnitude of the power being varied as described in the following sections. The pulse shape used is shown in Figure 3.1, for a number of different pulse powers. Throughout this chapter, when a power is mentioned, it relates to the

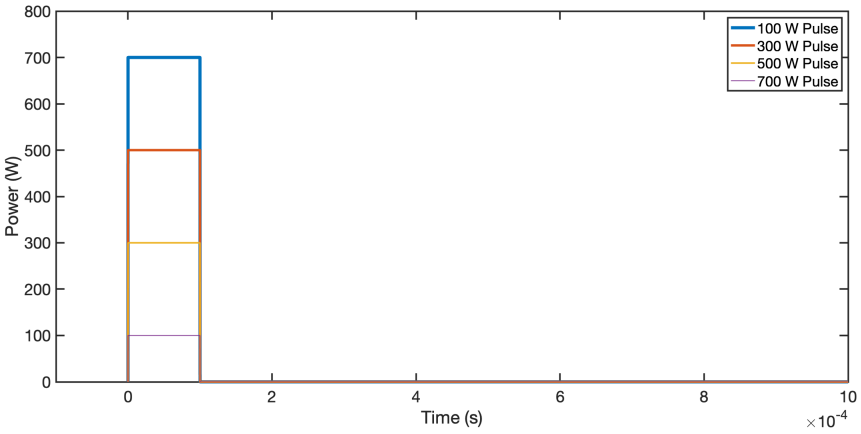

Figure 3.1: Pulses used for simulations of a pure N_2 DBD plasma

peak pulse power. For example a 900 W situation, means that the pulse power was 900 W, then the power returns to 0 W at the end of the fall time.

Initial Molar Fractions

As an initial input, GlobalKin requires the setting of the initial molar fraction for each of the considered species. For pure nitrogen simulations, the fraction of molecular nitrogen was set to 1, with atomic nitrogen and electronically excited states set at 10^{-15}, and electrons and ions at 10^{-20}. To GlobalKin, these values essentially mean that the species are not present at the beginning of the simulation.

For each of the vibrational states, their initial molar fraction has been calculated by setting a vibrational distribution function (VDF) to a Boltzmann distribution at 310 Kelvin.

Absolute Reaction Rate Analysis

As well as outputting time-evolved species densities, GlobalKin is also able to output all of the absolute reaction rates for every reaction as a function of time.

To calculate these absolute rates, GlobalKin uses equation 3.1 as follows:

$$AbsoluteRate = k \times N_i \times N_j \tag{3.1}$$

Where k is the rate coefficient in $cm^3\ s^{-1}$ and N_i and N_j are the species densities of the reactants in cm^{-3}. Equation 3.1 is for a two-body reaction. For three-body reactions, the principle is the same, but the units of k become $cm^6\ s^{-1}$, and there would be a third species density to multiply by.

The calculation of absolute reaction rates allows the determination of the dominant reactions which produce and destroy a species of interest. Therefore, because generally there are hundreds of reactions which may contribute to the densities of each species, a threshold absolute reaction rate can be set to only consider reactions with rates greater than this threshold. This threshold is usually $\approx 10^{15}\ cm^{-3}\ s^{-1}$ / $cm^{-6}\ s^{-1}$.

3.4. Results

3.4.1. Pulse Power Variation

To test the model with the novel chemistry set, and determine the energy input to ignite a plasma, a power variation was performed. From here, the term power refers to the peak pulse power. Peak pulse powers from 10 W to 900 W were tested, and the resulting electron densities within the plasma bulk and afterglow of each pulse are shown in Figure 3.2a. The simulation time for investigating electron kinetics in the afterglow had to be extended, as the decay times were noted to be extremely long, on the order of $\approx$ 10 - 20 milliseconds for the higher power cases ($\geq$ 300 W). However, after confirming that the electron density does eventually fall to zero if the simulation is allowed to run for sufficient time (Figure 3.2a), shorter times were then used (1 - 2 ms, Figure 3.2b), as this was sufficient to look at the interesting kinetics as described below.

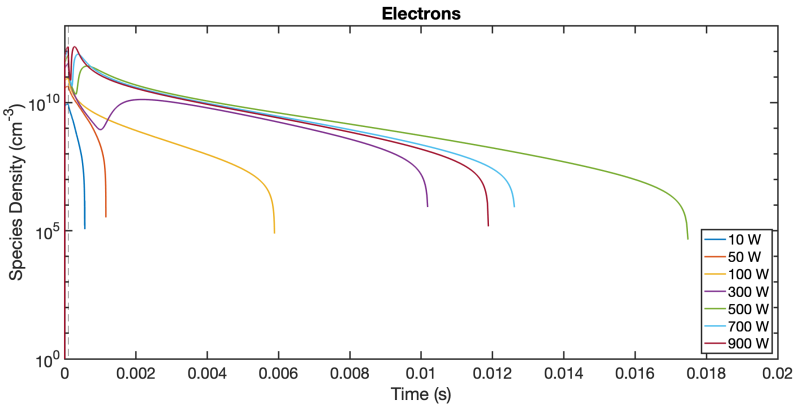

(a) Electron density - full time

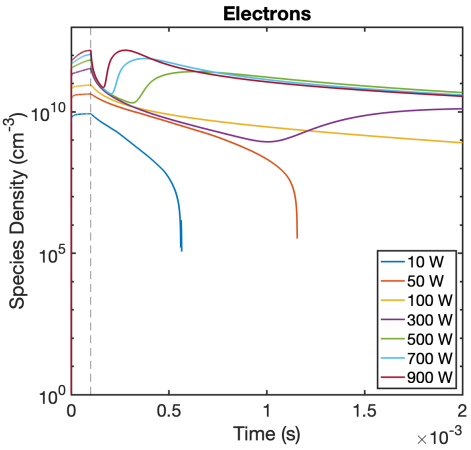

(b) Electron density - AEP region

Figure 3.2: Changing the pulse power affects electron densities in the powered plasma region (0 - 0.1 ms), and the afterglow (0.1 ms - 20 ms). 3.2a shows the species densities over the full simulation time of 20 ms. 3.2b shows the densities over the early afterglow region containing the afterglow electron peak (AEP), if present. The black vertical dashed line indicates the end of the powered region.

What is striking when looking at the first 2 ms of simulation time, shown more clearly in Figure 3.2b, is that for powers of 300 W and above, there is an electron density of approximately 10^{11} cm^{-3} in the powered plasma region, which decays when the power is turned off at 0.1 ms, but then begins to increase again in the afterglow. This Afterglow Electron Peak (AEP) seems to be influenced in appearance time and duration by the plasma pulse power, with high power cases resulting in an earlier and shorter AEP, compared to the lower power cases. Below 300 W, no AEP is seen. The electron density in these low power cases just decays to zero.

This result was unexpected due to the high collisionality of atmospheric pressure plasmas, and the assumption that after the initial plasma region, all excited states would be quenched by the background gas [162]. What this work shows is that the atmospheric pressure case may be more similar to the low pressure case than might be expected as the low pressure nitrogen pink afterglow is also characterised by an AEP in the afterglow region, and electron densities have been measured showing such electron kinetics [161]. The power dependence of the appearance time of the AEP has also been demonstrated experimentally in the low pressure pink afterglow in [163].

Mentioned previously, Penning processes are vital for local ionisation occurring in the nitrogen pink afterglow. Here, it is hypothesised that at atmospheric pressure, when the applied power is sufficient, the same Penning processes may be occurring to cause the appearance of the AEP seen in Figure 3.2b. Therefore the $N_2(A)$ and $N_2(a)$ metastable states were also investigated to see if this is the case. Figure 3.3a and Figure 3.3b shows how the $N_2(A)$ and $N_2(a)$ densities evolves over time. Interestingly, the early afterglow kinetics of $N_2(A)$ and $N_2(a)$ show similar features to that of electrons, with cases where the power is $\geq$ 300 W showing peaks in the metastable densities after an initial decay when the power turns off. When investigated further, Figure 3.4 shows that the afterglow metastable densities peak before the afterglow electron density peaks, further suggesting that the increase in metastables could contribute to the increase in electron density. As with the electron kinetics, similar $N_2(A)$ dynamics and

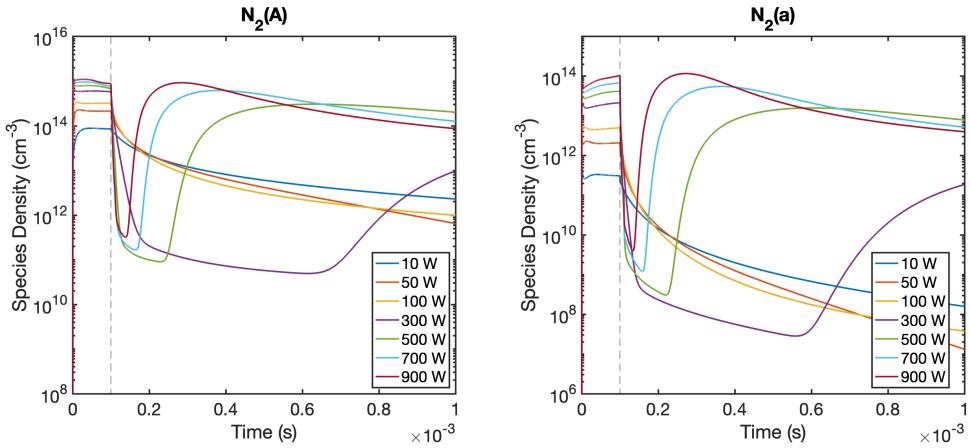

(a) $N_2(A)$ (b) $N_2(a)$

Figure 3.3: Simulated densities of metastables $N_2(A)$ and $N_2(a)$ as a function of pulse power in the powered plasma region (0 - 0.1 ms) and the afterglow (0.1 ms onwards). The black vertical dashed line indicates the end of the powered region.

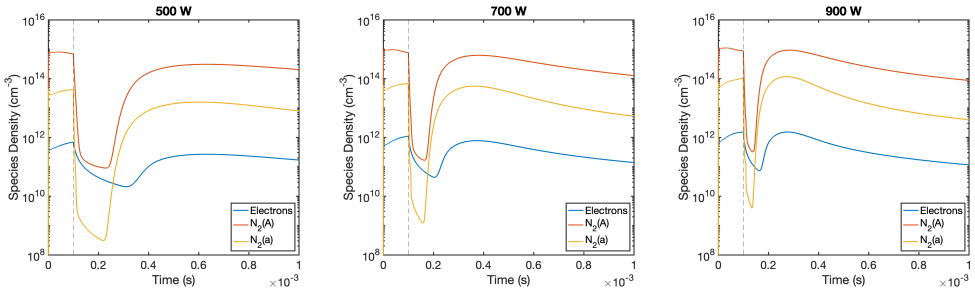

(a) 500W (b) 700W (c) 900W

Figure 3.4: The simulated metastable peaks of $N_2(A)$ and $N_2(a)$ occur prior to the AEP, at different pulse powers of 500 W, 700 W and 900 W. The power specified is applied for the first 0.1 ms then turned off. The black vertical dashed line indicates the end of the powered region.

timings with respect to the AEP are seen in the low pressure experimental characterisation of Sadeghi et al. [161], where they particularly investigated the kinetics of $N_2(A)$ metastable in a flowing nitrogen microwave discharge displaying a pink afterglow, at a pressure of 3.3 Torr.

To check that the nitrogen afterglow effects of the AEP and metastable peaks were not due to the power input being unphysically high and therefore giving erroneous results, the densities of ground state atomic nitrogen were com-

pared to the measurements taken by Es-Sebbar et al. [95]. In their work, a plane parallel plasma source was used for an atmospheric pressure nitrogen plasma. The plasma was powered by a sinusoidal waveform to produce a homogeneous discharge, or square wave pulses to produce a filamentary discharge. Due to the large differences in experimental setup, it is not possible to relate the plasma parameters of the published work to the simulated data presented here. However, due to the lack of other published data which gives an indication of feasible N atom densities in atmospheric pressure nitrogen plasmas, the data from Es-Sebbar et al. [95] provides way of checking that the simulated densities may be of a reasonable order of magnitude. Since N density seems to scale with power, this is also a way of checking whether or not, the powers used in the simulations are physically possible or not. In the work of Es-Sebbar et al. [95], they used two-photon laser induced fluorescence (TALIF), and present N densities of the order of 10^{14} cm^{-3} in an atmospheric pressure pure nitrogen discharge. This is the same order of magnitude as the densities obtained from the present simulations, and shown in Figure 3.5. This suggests that the powers used, resulting in these N densities can be reasonable. The long lifetime of N atoms seen in Figure 3.5 is also believed to be reasonable as it is consistent with the findings of Es-Sebbar et al. [95], who suggest that the lifetime of N in their experiments is approximately 8 ms. It can also be seen in Figure 3.5 that there is an increase in N density during the afterglow, which coincides with the AEP, suggesting that the locally produced electrons are also contributing to dissociation of N_2.

3.4.2. Vibrational Distribution Functions

It is known that the nitrogen pink afterglow occurs due to local ionisation in a region downstream of the plasma [101]. Since electrons cannot be carried from the active plasma region to where the pink afterglow is observed as they are confined to the electric field of the powered region, the ionisation must occur as a result of longer-lived energy carrying particles [161]. It is known that in the low pressure situation, this requirement is fulfilled by vibrationally excited

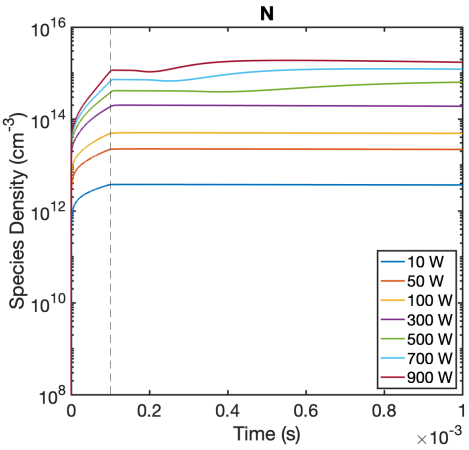

Figure 3.5: Simulated atomic nitrogen density in the powered plasma region (0 - 0.1 ms) and the afterglow (0.1 ms onwards) as a function of pulse power. Power specified in the legend is the peak pulse power. The black vertical dashed line indicates the end of the powered region.

nitrogen, $N_2(X, v)$ [101].

The fact that the time point at which the AEP appears in this present work is power dependent, suggests that it may also be reliant on some form of energy carrying plasma species whose density/production is dependent on the input power in the plasma. The group of species that would fit this idea, and would show consistency with the low pressure situation, are the $N_2(X, v)$ species which are produced in the plasma and a have a longer lifetime than electrons, meaning that they can mediate chemical processes in the time between power pulses. The higher the pulse power, the more highly populated the higher vibrational states are. To show these vibrational population dynamics, vibrational distribution functions (VDFs) can be plotted, where densities of vibrational states are normalised to the ground state density, $N_2(X, v = 0)$. In Figure 3.6, VDFs are plotted for the same afterglow time points across all the different pulse powers investigated, to show the time-evolution of VDFs in atmospheric pressure nitrogen discharges. The solid blue line indicates the VDF in each case at the last powered time point in the simulated plasma. This time point indicates the populations of vibrational states left in the plasma as the power turns off, and, thus, the initial VDF for the afterglow. Importantly, between 100 W

and 300 W, the interval when the AEP begins to appear, there is a significant difference in this initial VDF. In particular, the states where $N_2(X, v > 10)$ start to become appreciably populated at 300 W, whereas at 100 W, this does not seem to be the case.

The main mechanism for altering vibrational state densities are vibration-vibration (V-V) reactions as discussed in Chapter 2 in equation 2.16, where:

$$N_2(X, v) + N_2(X, w-1) \rightleftharpoons N_2(X, w) + N_2(X, v-1)$$

Importantly, the molecule with the highest initial vibrational state will be the molecule that increases its vibrational quantum number in the collision, and the other will decrease vibrational quantum number [101]. This can be explained when considering the vibrational state energy levels in Figure 2.3. Here it can be seen that as the vibrational state increases, the energy spacing between states decreases, therefore, if $w - 1 > v$, it requires less energy to increase $w - 1$ to w, than v to $v + 1$. This allows for the process of up-pumping, where the higher vibrational states become populated through a series of ladder-climbing collisions.

Figure 3.6 shows VDFs for time points throughout the afterglow, and show that there is indeed up-pumping occurring in this atmospheric pressure situation. After the initial VDF (blue line), for all the powers where an AEP appears, there is a significantly populated plateau in the VDF between approximately v=10 and v=40, suggesting that this region may be crucial for the appearance of an AEP. The time taken to reach this maximum plateau is power dependent, which may account for the power dependence of the appearance of the AEP. As the initial VDF becomes more highly populated at higher vibrational states with increasing pulse power, the amount of up-pumping required to reach the plateau is less, since the initial population of vibrational states are already higher on the VDF climbing ladder. Therefore, fewer step-wise vibrational increases are required to reach the plateau.

This up-pumping of the VDF is in keeping with work by Colonna et al. [127]. Here they present a study on using different electron impact cross section data,

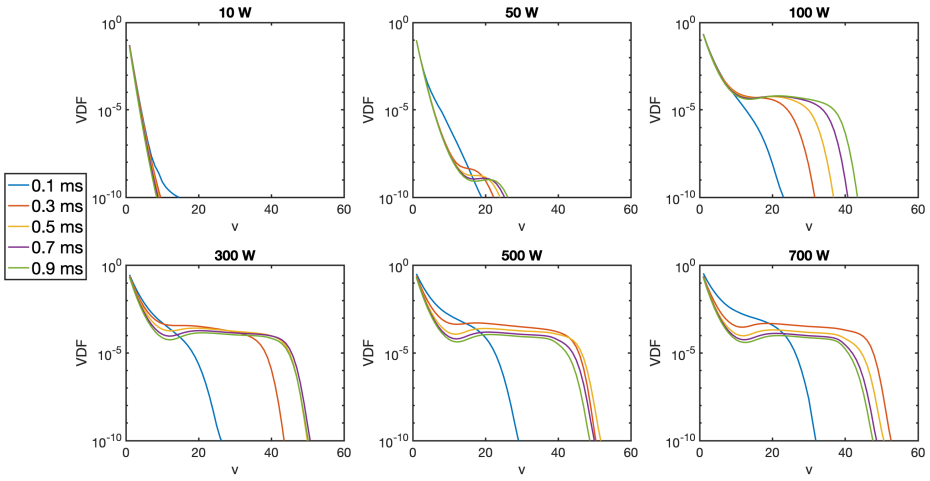

Figure 3.6: Time evolution of nitrogen vibrational distribution functions in nitrogen plasmas with different power inputs. The power is specified at the top of each VDF, and the time points for each of the lines is shown in the legend. 0.1 ms corresponds to the final powered time point and taken to be the initial VDF of the afterglow. 0.3 ms, 0.5 ms, 0.7 ms and 0.9 ms correspond to subsequent time points in the simulation.

and how it can affect the EEDFs and VDFs in atmospheric pressure nitrogen plasmas powered with different pulse characteristics. In their work they show that there is some up-pumping of the VDF following the powered plasma region at atmospheric pressure. They also see a plateau region, but this is between $\approx$ v=12-25 so at lower energies than the plateau regions seen in Figure 3.6. However, in their work, they use nanosecond pulses (orders of magnitude shorter than the ones in this present study), and the assessment of the VDF stops at 1 μs. Therefore, their work cannot be directly compared to the work presented here.

On closer inspection, the dynamics of the VDFs in Figure 3.6 may be more nuanced than first thought. In particular, the time point at which the VDF reaches maximal population of high vibrational states for the different power cases is different, and seems to correlate with the time point at which the AEP is seen. At 300 W, the VDF is always becoming more populated throughout the 0.9 ms period shown. However, in the 900 W case, the maximum up-pumping is seen by the 0.3 ms time point, and the VDFs beyond this point are depopulating,

suggesting that the maximally populated VDF may coincide with the AEP appearance.

Showing the VDF over more finely resolved time frames, specifically chosen around the time point that the AEP appears at that power, it is seen that that maximum VDF does appear at the same time as the AEP. Figure 3.7 shows the time points for which VDFs are plotted, corresponding to particular features of the AEP, shown in the representative example at 900 W in Figure 3.7b. The time points shown in Figure 3.7a were chosen to be:

- T_{min} - the time of the minimum electron density after the powered plasma region and before the AEP
- T_{slope} - the mid point of the electron density increase for the AEP
- T_{max} - the time point at which the electron density was maximal in the AEP
- T_4 - 1×10^{-4} s after T_{max}
- T_5 - 2×10^{-4} s after T_{max}
- T_6 - 3×10^{-4} s after T_{max}

VDFs plotted for each of these time points for the 500 W, 700 W and 900 W cases are shown in Figure 3.8. These powers are chosen as these are the instances where the whole AEP is seen in the electron dynamics in the 1 ms time frame. The 900 W case clearly shows the dynamics of the VDF surrounding the time of the AEP, with an increasing VDF between T_{min} up to T_{max}, after which the VDF begins to depopulate, and the plateau region decays.

The 500 W and 700 W cases show the same VDF evolution, with the VDFs becoming increasingly populated from T_{min} up to T_{max}. However, due to the longer lifetime of the AEP dynamics at lower powers, the changes are less pronounced.

This suggests that the AEP is somehow related to the VDF in the afterglow, however, it is not clear whether the VDF is responding to the increase in electron

Time Point	500 W	700 W	900 W
T_{min}	3.1×10^{-4}	2.0×10^{-4}	1.6×10^{-4}
T_{slope}	4.1×10^{-4}	2.6×10^{-4}	2.0×10^{-4}
T_{max}	6.3×10^{-4}	3.8×10^{-4}	2.8×10^{-4}
T_4	7.3×10^{-4}	4.8×10^{-4}	3.8×10^{-4}
T_5	8.3×10^{-4}	5.8×10^{-4}	4.8×10^{-4}
T_6	9.3×10^{-4}	6.7×10^{-4}	5.8×10^{-4}

(a) Individual time points for plotting the evolution of the VDF in each of the power cases

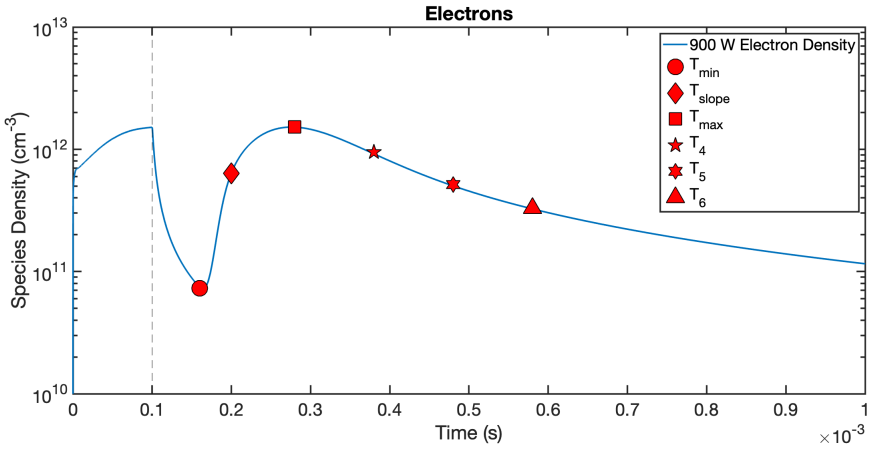

(b) 900 W representative example of where T_{min}, T_{slope}, T_{max}, T_4, T_5 and T_6 are on the electron density curve. The vertical dashed line represents the time when the power is turned off at 0.1 ms.

Figure 3.7: Time points for VDF plotting around the region of the AEP, for different plasma powers, and a representative example of AEP features that correspond to the chosen time points.

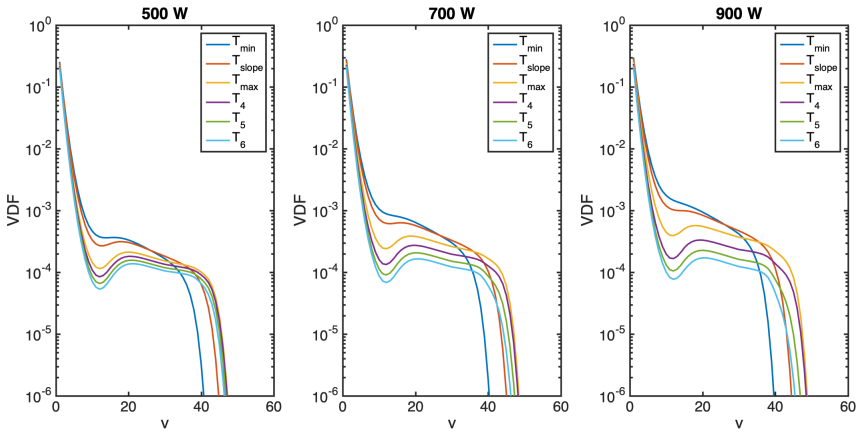

Figure 3.8: Evolution of the vibrational distribution functions surrounding the afterglow electron peaks at different simulated plasma powers, indicated above each of the graphs. The legend indicates the time points for each of the plotted VDFs, corresponding to the data in Figure 3.7.

density (though electron impact excitation), or whether the VDFs are causing the increase in electron density (V-V reactions causing metastable production and subsequent electron production). To determine this, simulations were performed with and without including vibrational states.

3.4.3. The Importance of Vibrational States

Vibrational states are known to be crucially important in low pressure nitrogen discharges [113]. However, it is not clear how important these species are in discharges operating at atmospheric pressure. To investigate this, a series of simulations were carried out. Starting with the full manifold of 58 states included, each simulation systematically removed a number of vibrational states, until only the first 5 states were included in the chemistry set. It is important to note that the electron impact cross sections involving vibrationally excited N_2 were still included, to make sure that the electron transport parameters were still correct (as discussed in Chapter 2). Therefore, the vibrational states could still affect the electron energies in the plasma, but not the chemical kinetics.

Using these simulations, the effects of vibrational states on other plasma species, such as electrons, can be determined. Figure 3.9a shows the electron densities

in 700 W power case, with respect to the number of vibrational states included, throughout the powered plasma region and the afterglow. The 700 W case was chosen as it shows a strong AEP, therefore, if the number of vibrational states included affects the AEP appearance, it would be seen. The power is deposited into the plasma up to 0.1 ms, after which, the power is turned off, and the simulation is concerned with afterglow effects only.

The first thing to note from Figure 3.9a, is that the appearance of the AEP and $N_2(A)$ metastable peak is dependent on the number of vibrational states included. If the intermediate case is considered, where 5-35 vibrational states are included in the chemistry set, it can be seen from Figure 3.9a that the electron density, and the afterglow kinetics are very similar, showing a consistent decrease throughout the afterglow, without any evidence of an AEP. However, if 40 or more vibrational states are included, an AEP appears, and seems to be unaffected as to whether there are 40 or 58 states included. This gives evidence for the fact that the AEP depends on vibrationally excited N_2, and more specifically, on having a sufficient number of states being considered.

Therefore, it appears that the presence of the AEP is dependent on:

1. Vibrationally excited ground state nitrogen molecules

2. Having a sufficient amount of power deposited in the powered plasma region, which will sufficiently populate the intermediate energy states of the VDF at the start of the afterglow, to allow adequate up-pumping of the high energy states.

Since similar kinetics were seen for both electrons and metastable $N_2(A)$ for the power variation in Figure 3.2 and Figure 3.3, it was wondered whether the same could be said when differing numbers of vibrational states are included in the chemistry set. As shown in Figure 3.9b, the $N_2(A)$ kinetics follow the same trends as electrons for different numbers of vibrational states. Specifically, for cases including 5-35 vibrational states, there is a general decay of $N_2(A)$ throughout the afterglow, whereas for cases including at least 40 vibrational

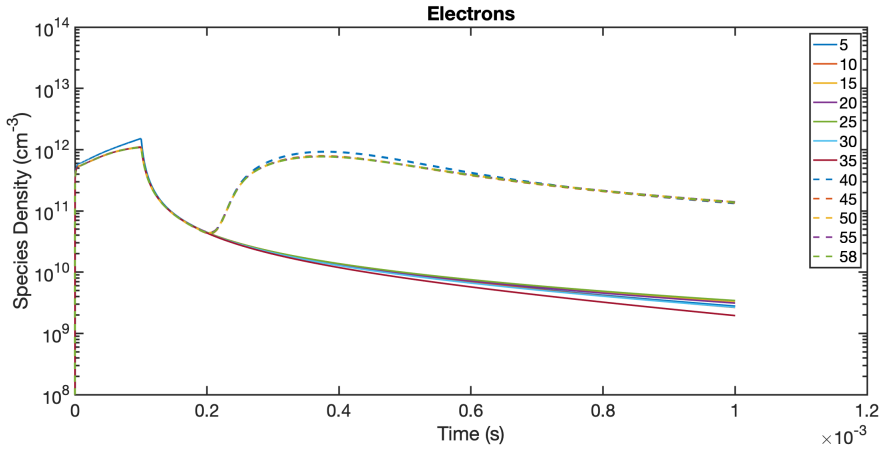

(a) Electrons

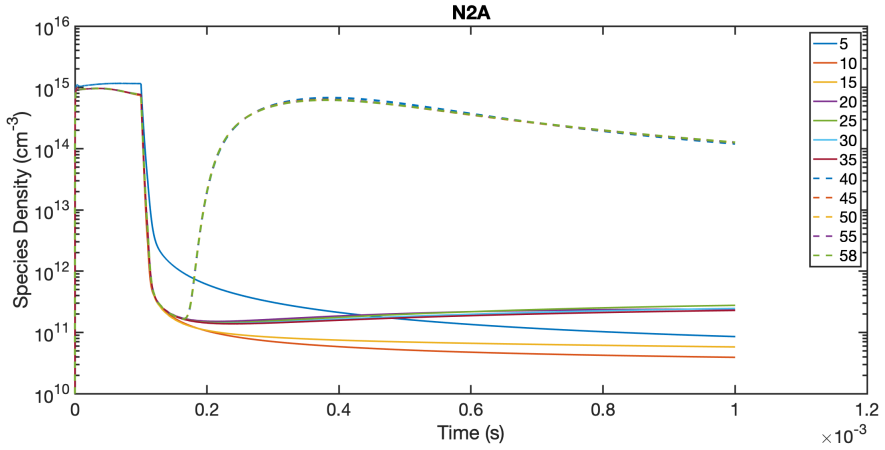

(b) $N_2(A)$

Figure 3.9: Electron and $N_2(A)$ densities in the active plasma and afterglow as a function of number of vibrational states included in the chemistry set. The legend states how many vibrational states are included for each line. Pulse power is 700 W up to 0.1 ms, then 0 W in the afterglow.

states, the $N_2(A)$ afterglow peak occurs.

To understand these different kinetics more fully, the VDFs were plotted for each case when a different number of vibrational states was included. These VDFs are shown in Figure 3.10, and here it can be seen how the shape of the VDF changes as more vibrational states are included. From Figure 3.9 it is recalled that there were two trends in electron and $N_2(A)$ kinetics. Firstly, when 5-35 vibrational states are included there is a steady decay of electrons in the

afterglow. Secondly, when 40 or more vibrational states are included, the AEP appears in the early afterglow. Therefore, the intention is to see if these trends can be explained by the VDFs for the different cases. Looking at the VDFs in Figure 3.10, it is clear that there is a distinct change in VDF shape when either 35 or 40 vibrational states are included. For $\leq$ 35 states, there is a U shape VDF formed most probably due to an excessive production of higher vibrational states through V-V up-pumping reactions, and a lack of V-T reactions and other destruction processes to balance this out. The change in shape above v=35 suggests that above this level there are extra destruction processes for the vibrational states, concurrent with V-T reaction rate coefficients reaching their maximal values (as shown in Figure 2.6), which results in an overall decay of the higher end of the VDF.

3.4.4. Electron Chemical Kinetics

It is thought that the production of electrons in the low pressure nitrogen pink afterglow is due to collisions between metastable nitrogen states [105, 113]. To determine whether a similar mechanism was applicable at atmospheric pressure, the absolute rates of electron producing or consuming reactions were calculated in GlobalKin, as per Section 3.3.2. Using these rates, the dominant reactions for producing and consuming electrons were compared across different power cases when an AEP occurred or not. For these analyses, the representative cases are the 100 W and 700 W ones, displaying the absence and presence of the AEP, respectively.

Figure 3.11 shows the absolute rates of electron production (left hand panel) and consumption (right hand panel) in the afterglow in the 100 W (Figure 3.11a) and 700 W (Figure 3.11b) cases. Since the dominant electron producing or destroying reactions have absolute rates on the order of 10^{14} cm^{-3} s^{-1} and above, a threshold was chosen at 10^{12} cm^{-3} s^{-1} to make analysis clearer. Rates for important reactions are shown as a function of time, from the beginning of the afterglow region at 0.1 ms, through the afterglow. From this figure it can be seen that for the 100 W case (Figure 3.11a), the rates of electron producing re-

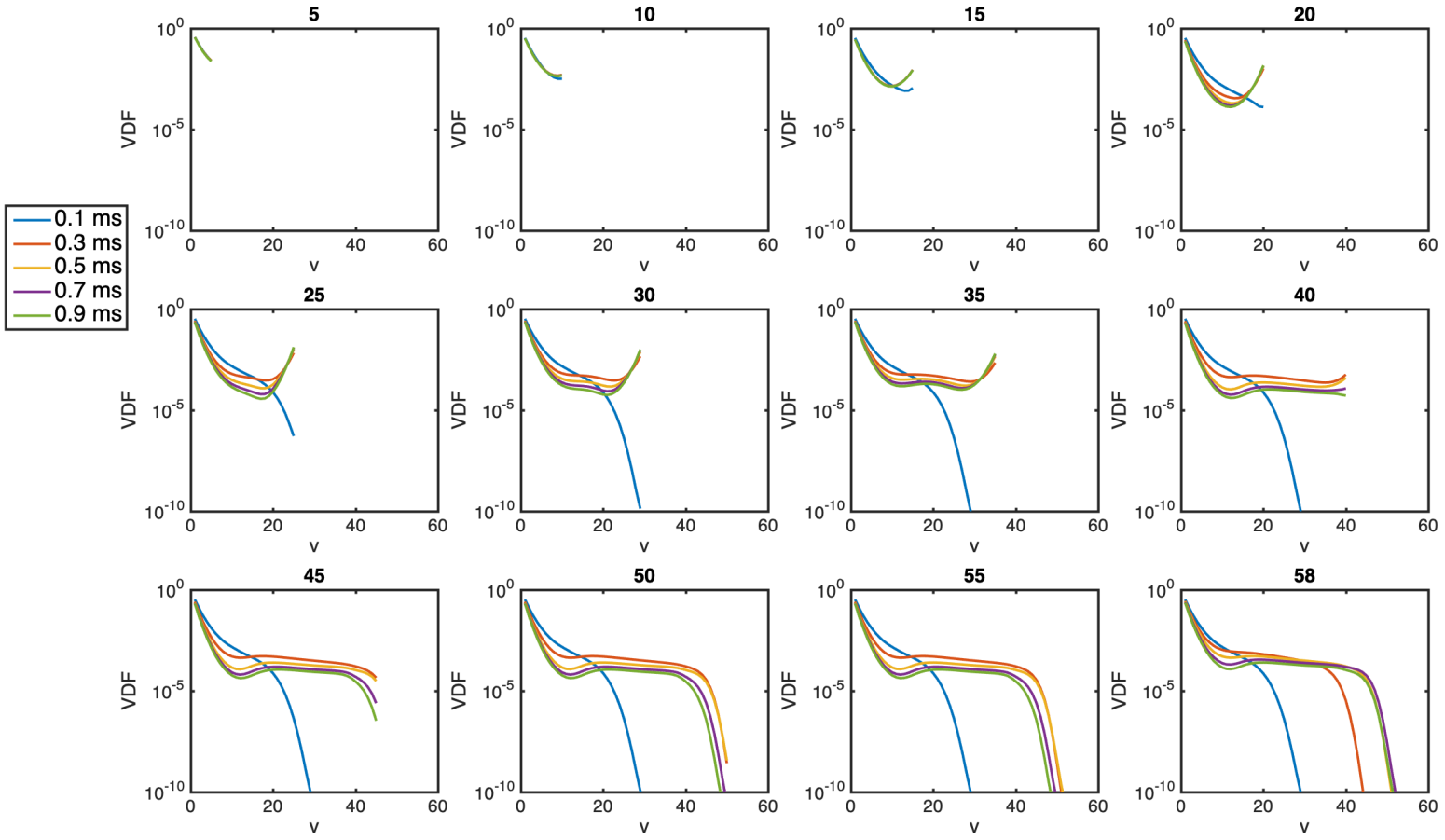

Figure 3.10: Time-evolved VDFs for simulations where different numbers of vibrational states were included in the chemistry set. The title of each subplot gives the number of vibrational states included in each case and the legend indicates the time point for the VDF. The pulse power is 700 W for 0.1 ms, for each of the simulations using different numbers of vibrational states. The blue line (0.1 ms) corresponds to the very end of the powered region, and is taken as the initial VDF of the afterglow.

actions in the afterglow are continually decreasing. Alongside this, the rates of the destruction mechanisms are orders of magnitude larger than the production reactions. This is consistent with a lack of AEP in the afterglow region, as there are no peaks in production, and destruction always outweighs productions.

However, in the higher power cases (Figure 3.11b), what can be seen is that electron-producing reactions decrease in rate after the active plasma region but at a time point corresponding to the time period of the AEP appearance, the rates increase once more. The rates of electron destruction reactions also increase, however, there is a lag between the increase in production and destruction rates (because the increase in the destruction rate is dependent on the electron density, therefore, the electron density has to first increase for the destruction rate to begin to increase), which means that the electron density can rise (to show an AEP), before the electron destruction rates start to outweigh production once more.

To understand the AEP kinetics, the specific reactions causing electron production can be determined, and from Figure 3.11, the dominant reactions are as follows:

$$N_2(a) + N_2(a) \rightarrow e^- + N_4^+ \tag{3.2}$$

$$N(^2P) + N(^2P) \rightarrow e^- + N_2^+ \tag{3.3}$$

$$N(^2D) + N(^2P) \rightarrow e^- + N_2^+ \tag{3.4}$$

$$N_2(A) + N_2(a) \rightarrow e^- + N_4^+ \tag{3.5}$$

Interestingly, these reactions do not directly involve vibrational states, however, if the production kinetics of $N_2(a)$ are investigated, a different story is seen. $N_2(a)$ is the reactant of the most dominant electron producing reaction in the AEP as per equation 3.2, and the absolute rates for its production and

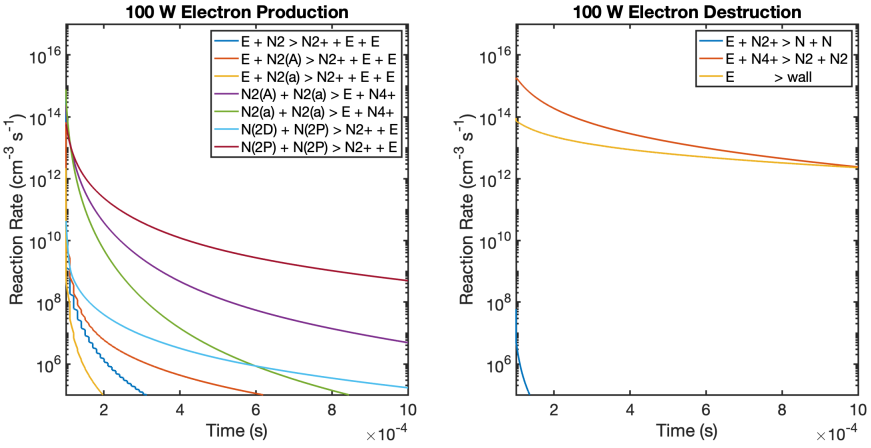

(a) 100W

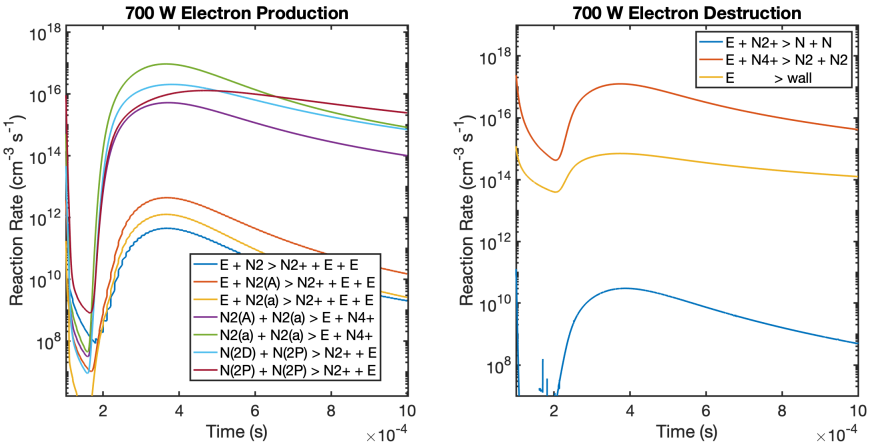

(b) 700W

Figure 3.11: Absolute reaction rates of dominant electron production and destruction mechanisms in the afterglow of nitrogen plasmas at 100 W (3.11a when no AEP occurs, and 700 W (Figure 3.11b) where an AEP does occur. The threshold for analysis of reaction rates is 10^{12} cm^{-3} s^{-1}. Only the afterglow period is shown on the figure (0.1 ms - 1 ms).

destruction are shown in Figure 3.12. Once again, the low and high power cases are considered and the $N_2(a)$ production reactions and rates can be compared between the two. In the 100 W (Figure 3.12a) case, there are only two $N_2(a)$ production reactions above the designated 10^{12} cm^{-3} s^{-1} threshold chosen, and both of these are decreasing in rate throughout the afterglow and are outweighed by the destruction processes. This explains the decay of $N_2(a)$ throughout the afterglow. However, in the 700 W case, the main production reaction for $N_2(a)$ involves highly vibrationally excited states of N_2, as per the following reaction:

$$N_2(39 \leq v \leq 53) + N \rightarrow N_2(a) + N \tag{3.6}$$

This suggests that as vibrational up-pumping occurs, population of the VDF above $v = 39$ allows increased production of $N_2(a)$ and consequently, increased electron production by Penning ionisation. This chemical pathways analysis also helps to explain the switch in species densities trends, and appearance of the AEP in Figure 3.9 when at least 40 vibrational states were included.

As stated in equation 3.5, $N_2(A)$ is also involved in one of the dominant electron production reactions. The absolute production and consumption reaction rates are, therefore, of interest and are plotted as a function of time in Figure 3.13. The main production process of $N_2(A)$ by $N_2(B)$ is as follows:

$$N_2(B) + N_2 \rightarrow N_2(A) + N_2 \tag{3.7}$$

However, the main loss process of $N_2(A)$ is through production of $N_2(B)$ as follows:

$$N_2(A) + N_2(5 \leq v \leq 14) \rightarrow N_2(B) + N_2 \tag{3.8}$$

These processes, therefore, do not form an efficient mechanism of depopulation of either state. This is the same as the process seen in low pressure cases, as discussed in [105] and [161], where it suggests, in agreement with the data shown in Figure 3.13, that in fact the most important $N_2(A)$ loss reaction is as follows:

$$N_2(A) + N \rightarrow N_2(6 \leq v \leq 9) + N(^2P) \tag{3.9}$$

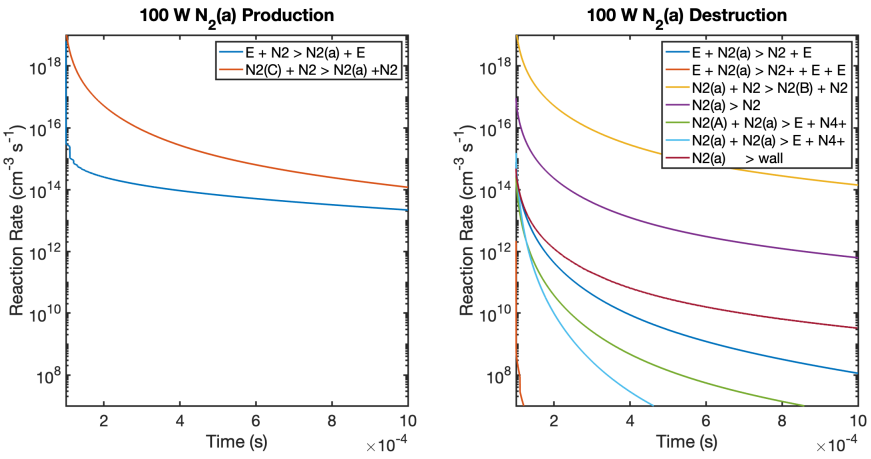

(a) 100W

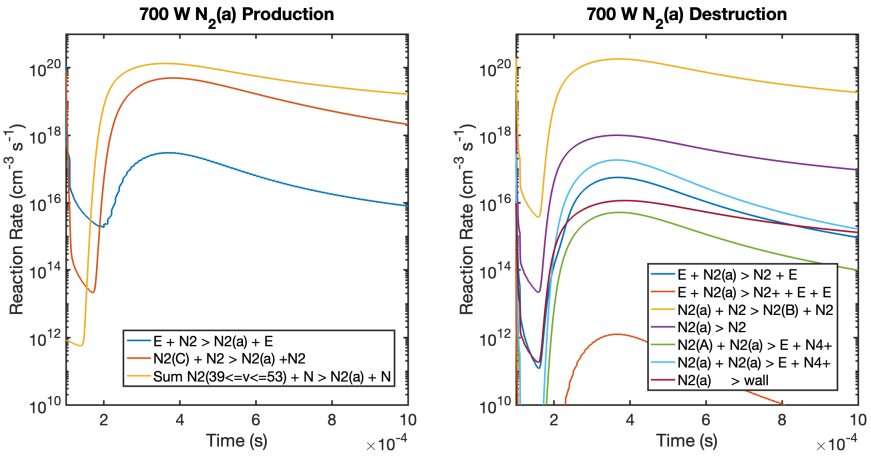

(b) 700W

Figure 3.12: Absolute reaction rates of dominant $N_2(a)$ production and destruction mechanisms in the afterglow of nitrogen plasmas at 100 W (3.12a when no AEP occurs, and 700 W (Figure 3.12b) where an AEP does occur. The threshold for analysis of reaction rates is 10^{12} cm^{-3} s^{-1}. Only the afterglow period is shown on the figure (0.1 ms - 1 ms).

By disregarding the reactions involving $N_2(B)$ as main production or loss processes, once again, the importance of vibrational states are highlighted, and the dominant production mechanisms become reactions 3.10 and 3.11 as follows:

$$N_2(40 \leq v \leq 48) + N \rightarrow N_2(A) + N \tag{3.10}$$

$$N_2(10 \leq v \leq 46) + N(^2P) \rightarrow N_2(A) + N \tag{3.11}$$

In the 700 W case (Figure 3.13b), an increase in production reaction rates can be clearly seen in the region of the AEP time point, and in particular, reactions 3.10 and 3.11 (aside from the recycling reaction 3.7). The 100 W case (Figure 3.13a), however, does not show this rate increase, and instead just shows how the reaction rates decrease throughout the afterglow.

This dominance of reactions 3.10 and 3.11 is in agreement with the low pressure situation presented in [103], where modelling results were presented alongside experimental data. As a study, they altered the rates of of these reactions, and compared the resulting $N_2(A)$ densities to experimental data from [161], and found that including this reaction, with a rate of 10^{-11} cm^3 s^{-1} gave the best agreement. This gives further evidence that the atmospheric pressure nitrogen discharge acts in a similar way to low pressure nitrogen pink afterglows.

3.4.5. Potential for Experimental Validation - The 'Species S' Approach

To validate computational models it is vital to carefully benchmark the simulated output data, against experimental data. For cases such as pure nitrogen, the complication is the fact that in a real life situation, it is extremely difficult to have an environment containing only nitrogen, with no impurities. As shown above, vibrational states are crucial mediators of the AEP and associated chemical kinetics, therefore, vibrational quenching by impurities could have serious implications for experimental validation of the model. Therefore, to determine

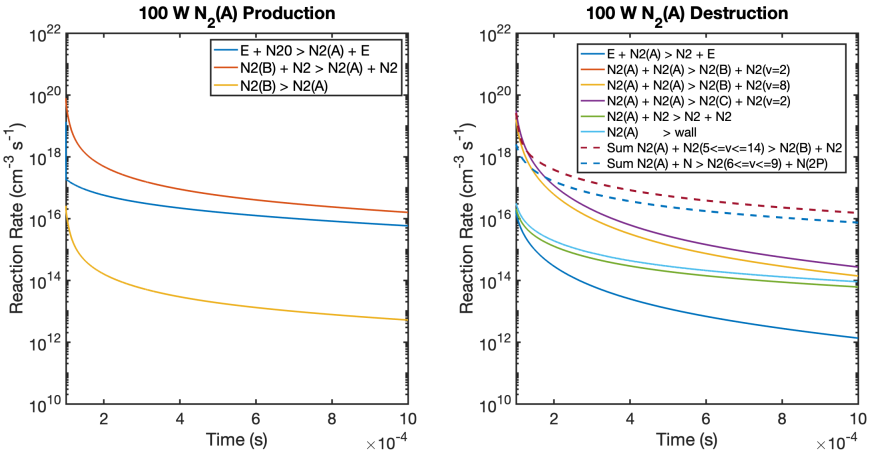

(a) 100W

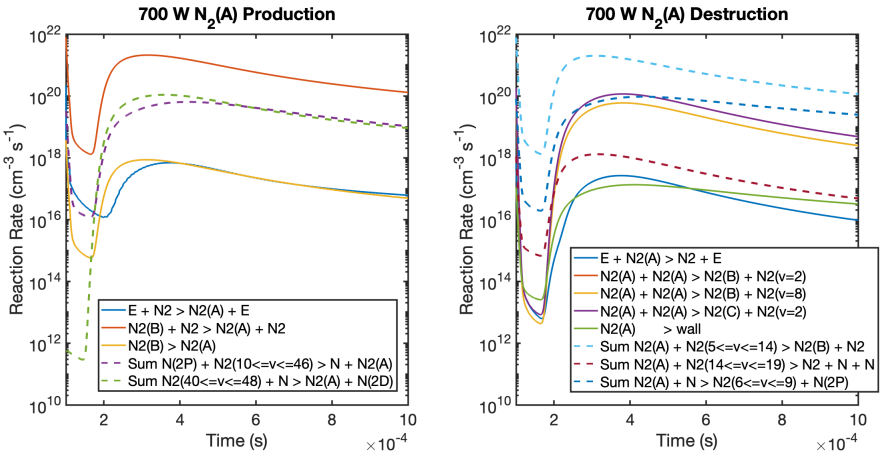

(b) 700W

Figure 3.13: Absolute reaction rates of dominant $N_2(A)$ production and destruction mechanisms in the afterglow of nitrogen plasmas at 100 W (3.13a when no AEP occurs, and 700 W (Figure 3.13b) where an AEP does occur. The threshold for analysis of reaction rates is 10^{12} cm^{-3} s^{-1}. Only the afterglow period is shown on the figure (0.1 ms - 1 ms).

how pure the environment would need to be in order to see the afterglow effects described in this chapter, simulations were performed which included an artificial quenching species which acts as a virtual impurity.

In an experimental situation, it is likely that there would be some level of impurities in the plasma region. These would more than likely be water or oxygen species, which are known to be able to act as quenching partners to $N_2(X, v)$, causing their depopulation through V-T and V-V collisions [110, 164]. Therefore, in the simulated setting, species S has been added to the model, as a proxy for all the possible impurities that could cause vibrational quenching in this way.

Species S was added into the model as a quenching species for vibrational states as follows:

$$N_2(X, v) + S \rightarrow N_2(X, w = v - 1) + S \tag{3.12}$$

The rate coefficient for quenching by species S, K_q, was varied, as well as the initial molar fraction MF_S, in order to see how much of the impurities the model could tolerate before afterglow effects, such as the AEP, were lost. Figure 3.14a shows how the quenching rate coefficients and molar fractions were varied in each of the cases, and the case letter corresponds to that shown in the legends of the species density plots in Figure 3.14.

Figure 3.14 shows the densities of electrons, $N_2(A)$ and $N_2(a)$ when species S is included in the simulations. These data show that the main parameter affecting the influence of S is the quenching reaction rate, k_q. When k_q is set to 10^{-20} cm^3 s^{-1} (solid lines), changing the initial molar fraction makes no difference to any of the species densities. This is because the rate coefficient is too low, so the chance of reactions happening is very small. The same can be said when k_q is set to a much larger value of 10^{-10} cm^3 s^{-1}. Here, changing the molar fraction also makes no difference, as the rate coefficient is so high, the chance of a reaction happening, even with low reactant densities is still high. However, at the intermediate k_q of 10^{-15} cm^3 s^{-1}, changing the molar fraction can affect the species densities slightly, suggesting that this value of k_q is very close to

$K_q(cm^3s^{-1}) \rightarrow$	10^{-20}	10^{-15}	10^{-10}
$MF_S \downarrow$	(solid)	(dash)	(dot)
10^{-1}	A	E	I
10^{-2}	B	F	J
10^{-3}	C	G	K
10^{-4}	D	H	L

(a) Table showing the molar fraction of (MF_S), and vibrational quenching rate with (K_q) species S and line style and colour for each case.

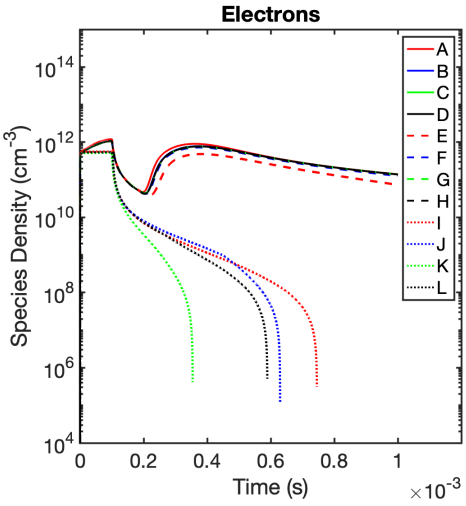

(b) Electrons

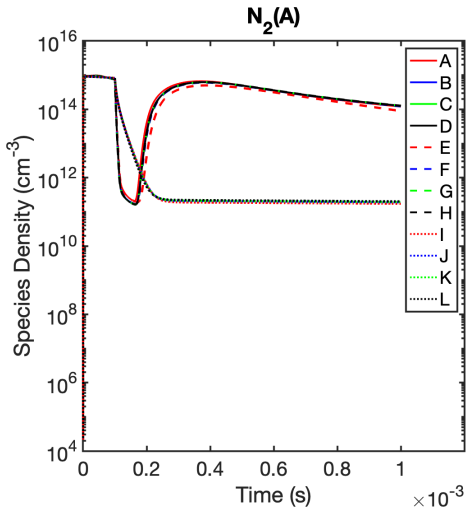

(c) $N_2(A)$

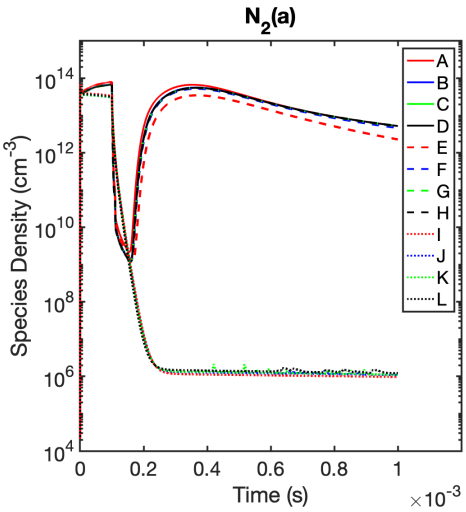

(d) $N_2(a)$

Figure 3.14: The effects of addition of an artificial $N_2(X, v)$ quenching species, S, on electron and metastable densities. Conditions for the different lines in 3.14b, 3.14c and 3.14d are shown in 3.14a.

the threshold reaction rate coefficient, where the reactant densities might start to have an effect. This is shown by case E (red dash line), which has moved away from the rest slightly, showing a lower species density in the afterglow. In a real life situation, this means that anything with a reaction rate coefficient of the order 10^{-15} cm^3 s^{-1} or higher could affect the species densities, if the densities of the impurity are high enough.

To investigate the idea of a reaction threshold more, an intermediate reaction rate coefficient of $k_q = 10^{-13}$ cm^3 s^{-1} was chosen for S, to see if the species dynamics could be wholly controlled by MF_S. This would indicate a true threshold reaction rate for any impurities, that would dictate the exact density of impurity allowed in an experimental setup. The results are shown in Figure 3.15, with the parameters for each case shown in Figure 3.15a. These data suggest that at this threshold reaction rate, whether or not the afterglow effects of the AEP and metastable peaks are abolished, depends wholly on the MF_S. For $MF_S = 10^{-4}$ the AEP and metastable peaks are unchanged. However for $MF_S = 10^{-3}$, the AEP and metastable peaks are slightly diminished, showing lower species densities. For $MF_S = 10^{-2}$ and $MF_S = 10^{-1}$, the AEP and metastable peaks are lost totally, and the species just decay when the power is turned off. In practical terms, this means that the concentrations of impurity species that quench $N_2(X, v)$ with a reaction rate of the order of 10^{-13} cm^3 s^{-1} must be kept small so as not to lose the nitrogen afterglow effects observed in the pure nitrogen simulations.

In summary, these data suggest that for experimental characterisation of an AEP in atmospheric pressure N_2 plasmas, the impurities in the nitrogen gas must be controlled. Impurities that react with $N_2(X, v)$ species with reaction rate coefficients of $\approx 10^{-15}$ cm^3 s^{-1} or lower, can be present in the nitrogen feed gas at up to 10%. This is because the rate coefficient is too low to cause appreciable quenching of $N_2(X, v)$ species, irrelevant of the quenching species density. Conversely, impurities that react with $N_2(X, v)$ species with reaction coefficients of $\approx 10^{-10}$ cm^3 s^{-1} cannot be present even small quantities, as the reaction rate, even with a small amount of reactant, is high enough to abolish the afterglow effects. The impurity species that require more consideration are any which have a $k_q \approx 10^{-13}$ cm^3 s^{-1}, as their effects would be strongly dependent on their densities.

$K_q(cm^3s^{-1}) \rightarrow$	10^{-13}
$MF_S \downarrow$	(dash dot)
10^{-1}	M
10^{-2}	N
10^{-3}	O
10^{-4}	P

(a) Table showing the molar fraction of (MF_S), and vibrational quenching rate with (K_q) species S and line style and colour for each case.

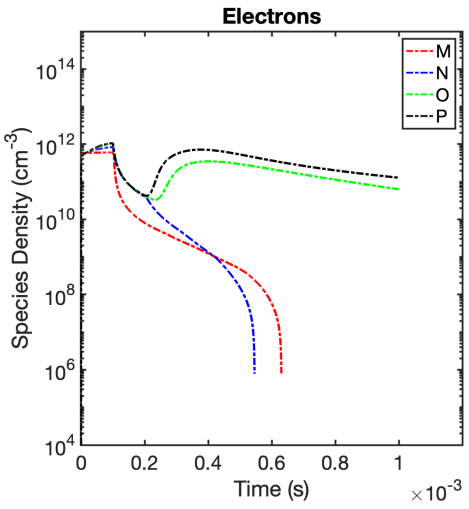

(b) Electrons

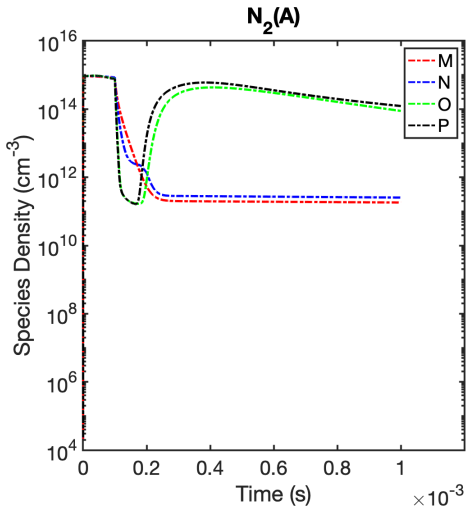

(c) $N_2(A)$

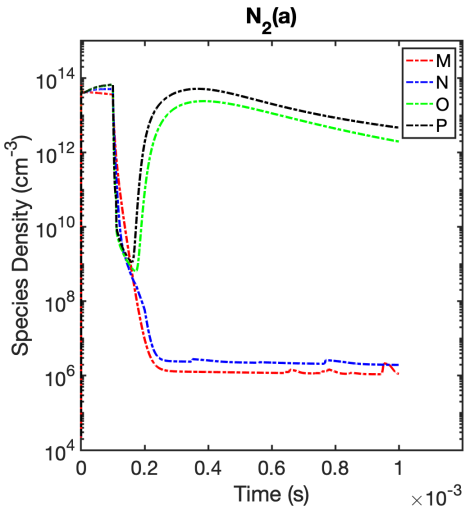

(d) $N_2(A)$

Figure 3.15: Effects of molar fraction of artificial $N_2(X, v)$ quenching species, S, at a threshold reaction rate coefficient on electron and metastable densities. Conditions for the different lines in 3.15b, 3.15c and 3.15d are shown in 3.15a.

3.4.6. Putting the 'Species S' Approach into Practical Terms

Using these results, and by drawing on information in the literature, it is possible to determine what stringency of conditions would be required in an experimental setup, in order to investigate the effects described above. Species that often act as impurities are molecules such as water vapour (H_2O) and oxygen from air (O_2). Therefore, it is of interest to consider the reaction rates for water and oxygen with $N_2(X, v)$ species, to see what levels of these impurities would be tolerable to still see the nitrogen afterglow effects of AEP and metastable peaks.

Firstly, considering depopulation of $N_2(X, v)$ by H_2O by the reaction:

$$N_2(X, v = 1) + H_2O \rightleftharpoons N_2(X, v = 0) + H_2O^* \tag{3.13}$$

Has an experimentally determined reaction rate coefficient of 1.2×10^{-14} cm^3 s^{-1} at 293 K [164], where H_2O^* is a vibrationally excited water molecule. This rate was measured as the depopulation rate of $N_2(X, v = 1)$, and has been accepted to be the rate for the V-V reaction, rather than the V-T rate. The V-T reaction rate is much smaller than the V-V reaction rate coefficients [165]. This V-V rate coefficient is smaller than the equivalent reaction between H_2O^* and $O_2(X, v)$ as the reaction is more resonant between $O_2(X, v = 1)$ and H_2O^*, than $N_2(X, v = 1)$ and H_2O^* [165].

In terms of the effect of water impurities in nitrogen experiments, the reaction rate coefficient of 1.2×10^{-14} cm^3 s^{-1} stated for reaction 3.13 is close to the threshold reaction rate coefficient of 10^{-13} cm^3 s^{-1} presented in Figure 3.15. It is slightly lower than the threshold reaction rate coefficient, therefore, may allow slightly higher initial concentrations of water before the nitrogen afterglow effects of AEP and metastable peaks are lost. However, it is definitely likely that the initial MF of water impurity would need to be kept below 10^{-2}, probably closer to 10^{-3}. This would suggest that any water impurity would need to be kept ideally below 1 % of nitrogen gas used.

Secondly, oxygen species are likely to be present in impurities and are known to act as quenching partners for the depopulation of $N_2(X, v)$ in both V-V and V-T processes [102]. The ones with the greatest magnitude and therefore likely to have the greatest effect are V-T processes for the depopulation of $N_2(X, v)$ by atomic oxygen (See Chapter 2). It can be recalled that these rates are presented in Chapter 2 and are shown to have a magnitude of approx $10^{-14} - 10^{-13}$ cm^3 s^{-1} [110]. In terms of this process causing the loss of the nitrogen afterglow effects of AEP and metastable peaks, these reaction rates for V-Ta processes are very close to the threshold rate coefficient, at which point the influence of the impurity of the afterglow effects is controlled by the impurity concentration. Similarly, $N_2 - O_2$ V-V reaction rate coefficients are shown in Chapter 2 Figure 2.9, and vary from $\approx 10^{-17}$ cm^3 s^{-1} to $\approx 10^{-12}$ cm^3 s^{-1} at the resonant peak of collisions between $N_2(X, v = 29)$ and $O_2(X, v = 1)$ [110]. Once again, many of these reactions are close to the threshold reaction, therefore, concentrations of oxygen are important to control for nitrogen afterglow effects. Once again, using the data from species S in Figure 3.15, this would suggest that the concentration of oxygen species would also be controlling whether the nitrogen afterglow effects were allowed in the experimental setting.

3.4.7. Limitations of the 'Species S' Approach

Modelling an artificial quenching species such as species S is a useful method for determining approximate parameters for which the nitrogen afterglow effects would still be present in an experimental setting. However, there are definite limitations to these investigations.

Firstly, species S assumes a constant reaction rate coefficient for quenching of every vibrational state of $N_2(X, v)$ for any quenching partner. This is clearly a very simplistic approach, however, comparing rate coefficients of known quenching partners with the species S data, could give an idea of whether the average reaction rates of the species of interest with $N_2(X, v)$ are close to the threshold or not. Thus, could give an indication of the levels of impurity allowed.

Secondly, the species S simulations only take into account the effect of impurities directly on vibrational states of nitrogen. They do not take into account the effect of impurities on densities of other species in the plasma, such as metastables which can indirectly affect electron afterglow dynamics. Further to this, the species S approach does not take into account the formation of negative ions with the impurities. This would be particularly important for oxygen species, which can combine with electrons in the nitrogen plasma, or indeed the nitrogen afterglow, to produce species such as O^- and O_2^-. This loss mechanism for electrons, if occurring in the afterglow, could also act to diminish the AEP.

However, if used with caution, the species S data suggests the limits of impurities that could potentially be present when experimentally assessing the nitrogen afterglow effects of the AEP and metastable peaks. Specifically, it suggests that O_2 and H_2O impurity levels must be below 1 %, for the nitrogen afterglow effects to be present.

3.5. Discussion

Low pressure nitrogen discharges have been the centre of research efforts for many years, however, the interest in atmospheric pressure discharges is now increasing. The advent of plasma medicine as a field is driving research into plasmas which could have potential medical benefit, therefore, plasma operating at atmospheric pressures are vital. Here, data is presented to aid the understanding of the nitrogen afterglow in an atmospheric pressure nitrogen plasma. The afterglow region is of particular interest in biomedical applications for molecular plasmas as these plasmas are pulsed to limit gas temperature, therefore, biological tissues are subjected to short bursts of plasma, and relatively, much longer periods of afterglow. Here, a chemistry set for modelling atmospheric pressure nitrogen discharges has been developed, including the full manifold of 58 vibrational states of the ground state nitrogen molecule, and tested through a series of studies. The chemical kinetics presented here using a reaction scheme based on sets used in [104, 113, 140], has highlighted some fundamental, novel

findings regarding the afterglow region of atmospheric pressure nitrogen discharges.

The nitrogen pink afterglow is a phenomenon that has been well researched in the past [101], and the mechanisms for its formation are described. Here, novel data is presented to suggest that similar mechanisms are occurring in nitrogen plasmas at atmospheric pressure. In particular, vibrational up-pumping has been shown, which leads to a peak in metastable $N_2(A)$ and $N_2(a)$ densities, which is turn produce electrons through Penning ionisation.

It has also been shown that the inclusion of different numbers of vibrational states of ground state nitrogen in the chemistry reaction scheme can influence the results, particularly the electron dynamics. It has been suggested that at least 40 vibrational states must be included in order to show the afterglow effects of the AEP and metastable peaks presented here. This threshold for numbers of vibrational states included can be explained by looking at the VDF up-pumping around the time of an AEP, and also the chemical kinetics occurring in the afterglow. In particular, the production of $N_2(a)$, a vital metastable state for formation of the AEP, is produced mainly by collision of $N_2(X, v \geq 39)$ and N, thus showing how these high vibrational states mediate the AEP.

This computational study gives this evidence for the existence of these afterglow effects, however, experimental validation would be the next step. The obvious first step for this would be to use fast imaging of the atmospheric pressure discharge, to determine if there was any pink light being emitted, suggesting the decay of $N_2(B)^+$ ion to $N_2(X)^+$ ion. This could be done using Optical Emission Spectroscopy to look for the first negative band of nitrogen ($N_2(B)^+ \rightarrow N_2(X)^+$) which is responsible for the pink light emitted in the so-called pink afterglow.

Of course, the nitrogen afterglow effects of the AEP and metastable peaks may also be influenced by impurities, and the levels of these impurities allowed before the afterglow effects are lost have been discussed. The advantages and disadvantages of the species S approach mentioned above have already been

discussed in the relevant sections, however, the approach suggests that impurities should be kept to less than 1 % for species such as water and oxygen.

3.6. Future Outlook and Application

Moving forward with this work, experimental validation of the simulated results is crucial. It is also necessary to consider how these findings could influence the development of potential medical devices, for example, for wound healing.

Przekora et al. [166] present the use of a low temperature nitrogen plasma for the influence of preosteoblast cells (cells which differentiate to form bone-producing osteoblasts). Here they showed that for specific treatment times, they could increase the proliferation and differentiation of preosteoblasts, whilst maintaining cellular health. Further to this, Kang et al. [167] used low temperature nitrogen plasmas and showed that it could promote the wound healing process in a rat model. This suggests that nitrogen may provide a potential new feed gas for medical plasmas, and therefore, the understanding of the chemical kinetics and how they can be controlled is paramount.

It is likely that for biomedical treatments, energy delivery to the target such as a chronic wound, may be important [168], therefore species that can carry energy over relatively long periods are of particular interest. Once again, vibrational states and metastables provide a source of interest, as they may hold biological effect potential in their own right, as well as contributing to overall plasma dynamics such as electron density.

In summary, this body of work presents new understanding of the chemical kinetics occurring in atmospheric pressure nitrogen discharges. The importance of vibrationally excited states of nitrogen has been highlighted, in particular, for mediating the species dynamics in the plasma afterglow region. The importance of vibrationally excited states in plasma/biology interactions is not known, but these species may present a new mechanism by which plasmas can induce biological effects at target sites.

Results II - Simulations and Experimental Characterisation of Air LTPs

4.1. Motivation

In recent years, low temperature plasmas have been showing significant promise for aiding skin wound healing. This effect is believed to be due to the fact that reactive oxygen and nitrogen species (RONS) produced in abundance by LTPs are the same as reactive species produced normally inside the body to mediate many different cellular process such as the immune response, wound healing processes and cell-cell signalling [46]. Many of the reactive species functioning in the body are derived from nitrogen and oxygen, for example, nitric oxide (NO), superoxide (O_2^-) and singlet delta oxygen ($^1O_2$). Therefore, there is increasing interest in the use of air plasmas for medical treatments, not only due to the reduced need for expensive infrastructure and bottled gases, but also for their efficient production of biorelevant RONS.

The ultimate aim for the field of plasma medicine is to design LTP treatments that can be tailored to specific patient needs. For this to be achievable, there needs to be an understanding of how different RONS produced by LTPs influence biological tissues, meaning that the flux of LTP-produced RONS reaching

biological targets needs to be determined. Experimental diagnostics at atmospheric pressure in molecular gases are extremely challenging, and while it is possible to measure some species using highly sophisticated methods such as Picosecond Two-Photon Absorption Laser-Induced Fluorescence (psTALIF, for atomic species such as N and O) and Ultraviolet Absorption Spectroscopy (for molecules such as O_3 and NO), there remains a significant number of species that cannot be quantified [96, 98]. These species, including the electronically and vibrationally excited molecular states, could be important for biological applications, as mentioned in Chapter 2 with reference to the vibrationally excited states of nitrogen.

To circumvent these experimental challenges, it is beneficial to develop a suitable air plasma chemistry model which can be benchmarked against experimental data. Models such as these allow determination of plasma species concentrations, and can predict what physical plasma parameters may be the most influential to different plasma species. Importantly, these simulations allow quantification of species that may not be easily measured experimentally, such as vibrationally excited states and metastables. They also allow the dominant production and destruction mechanisms for each of the species to be interrogated. Once benchmarked, chemistry modelling also allows relatively quick understanding of how different plasma species can be controlled through various inputs, such as the power deposition. Therefore, this may also allow the guidance of experimental treatments of cells, for example, by informing which parameters would be best to change to alter the plasma composition in contact with the cells being treated.

To date, air plasma chemistry modelling has been carried out for a number of different applications, such as space re-entry [169] or nitrogen fixation [126], and has mainly been concerned with either low pressure or high temperature situations [109, 110, 125]. There appears to be little on low temperature atmospheric pressure air plasmas suitable for biomedical applications [128, 170]. Therefore, in this work, an air chemistry model discussed in Chapter 2 is used to quantify species densities in such a plasma, taking particular care to invest-

igate nitrogen vibrational states.

Of particular interest for biomedical applications is the delivery of important species such as nitric oxide, NO. NO is known to be crucial in normal physiology for the regulation of vascular tone, maintenance of blood pressure, neurotransmission and the immune response [49], as well as mediating wound healing processes [171]. This gives evidence to suggest that NO delivery by plasmas may be beneficial in aiding wound healing, and therefore, warrants further investigation. NO delivery as a therapeutic strategy has been considered previously, and in fact there are devices claiming to be able to deliver high quantities of NO to biological targets [172, 173]. However, their NO production and destruction mechanisms are not well presented. Therefore, the control of NO, and the mechanisms by which it is produced and destroyed will be investigated in this work in order to inform how it could be controlled in future biomedical plasma devices.

The production and destruction of ozone, O_3, is also of interest to any studies involving LTPs and biology. Due to the toxic nature of the species [174], it is of interest for both determining safety limits for its concentration, but also, it is an effective species for killing bacteria. Therefore, it may be useful to be able to increase this species density in the case of infected wounds, but reduce it in the absence of infection.

4.2. Aims

The overall aims of this chapter are as follows:

1. Develop an air chemistry set for use in global plasma chemistry models, including vibrationally excited states, to be able to quantify more air plasma species than is possible using experiments alone

2. Begin the benchmarking process of the air simulations, using basic diagnostics on an air DBD plasma source

3. Using the simulations, determine important production and destruction reaction mechanisms for different biorelevant species, with the aim of using this information in the future to guide how different RONS could be independently controlled in the plasma

4.3. Methods

4.3.1. The Experimental Plasma Source

For this work a dielectric barrier discharge, described fully in [40], will be used. The cylindrical copper electrode is 8 mm in diameter, covered by a 1 mm thick aluminium oxide (Al_2O_3) layer, giving an overall diameter of 1 cm. This electrode is powered by high voltage ($\approx$ 10 - 17 kV amplitude) square wave pulses, at kilohertz frequencies ($\approx$ 1 - 5 kHz). The voltage is generated by a DC power supply (Technix SR20KV-600W), which is converted to pulses via a fast switching box, with pulse characteristics set using a function generator (TTi, TG5012A, 50 MHz). The voltage is measured by a high voltage probe (LeCroy, PPE 20kV high voltage probe), and the current is measured by a current probe (Ion Physics Corporation, CM-100-L). The driven electrode is placed on the order of 1-3 mm from the ground, to allow breakdown of the air. Since the breakdown of the air depends on having a strong enough field over a small enough distance, addition of extra spacing can prevent breakdown. In order to be in keeping with the requirements for future experiments to be able to involve biological targets, the plasma is always ignited in a well of a 24 well plate. The well plate has an extra ground plate to fill the space between the base of the wells and the table, and decrease the gap width, thus allowing easier breakdown over a wider range of pulse voltages.

A diagram of the full experimental setup is shown in Figure 4.1. Figure 4.2 shows annotated photographs of the experimental setup, and Figure 4.3 shows the DBD plasma ignited.

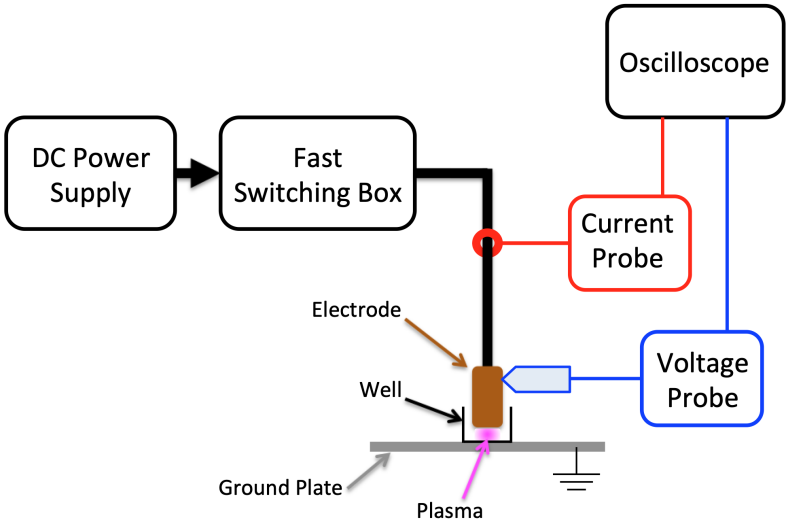

Figure 4.1: The overall setup of the DBD Source

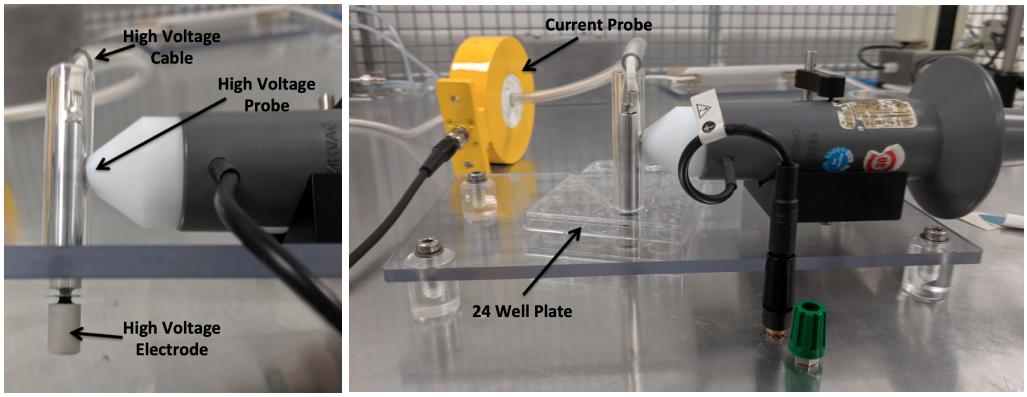

(a) Plasma Source (b) Whole Plasma Setup

Figure 4.2: The DBD plasma setup. 4.2a shows the plasma electrode covered with an Al_2O_3 dielectric coating and the high voltage probe integrated into the plasma source housing. 4.2b shows how the electrode and voltage probe fits in to the overall setup, with the electrode inside a well of a 24 well plate used to treat cells, and the current probe around the high voltage cable.

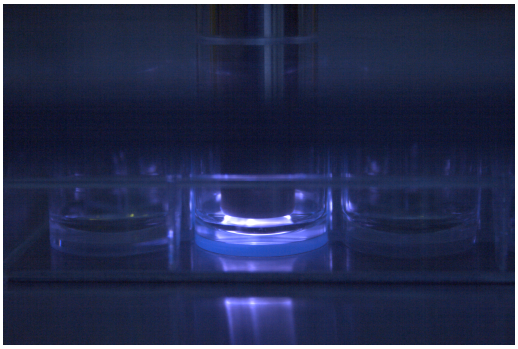

Figure 4.3: Photograph of DBD plasma ignited in a well of a 24 well plate

4.3.2. Power Measurements

For characterisation of a particular plasma operation, and to be able to translate the experimental parameters to simulations, it is necessary to measure the power dissipated in the plasma. To vary the energy being dissipated into the plasma, the applied voltage was varied using the DC power supply. Voltage and current waveforms were measured using the voltage probe (LeCroy, PPE 20kV high voltage probe) and the current probe (Ion Physics Corporation, CM-100-L, 5 ns useable risetime) connected to an oscilloscope (Teledyne Lecroy Wavesurfer 10, 500 kS per second), then the waveforms were analysed using Matlab. Further details on the methods will be described in the following results sections.

4.3.3. Ozone Measurements

Ozone densities in the plasma were measured using a commercially available ozone monitor (2 B Technologies, Model 106 Ozone Monitor). The monitor uses Ultraviolet Absorption Spectroscopy to determine the absolute densities of ozone in gas drawn in from the plasma at $\approx$ 1 litre per minute. The wavelength for absorption spectroscopy is 254 nm, corresponding to the Hartley continuum system of O_3 [98]. A switching mechanism in the monitor either sends the sample gas straight to the absorption cell, or sends it firstly through an ozone scrubber and then the absorption cell. The light is passed through the samples and the intensity of light passing through the sample gas that has been through

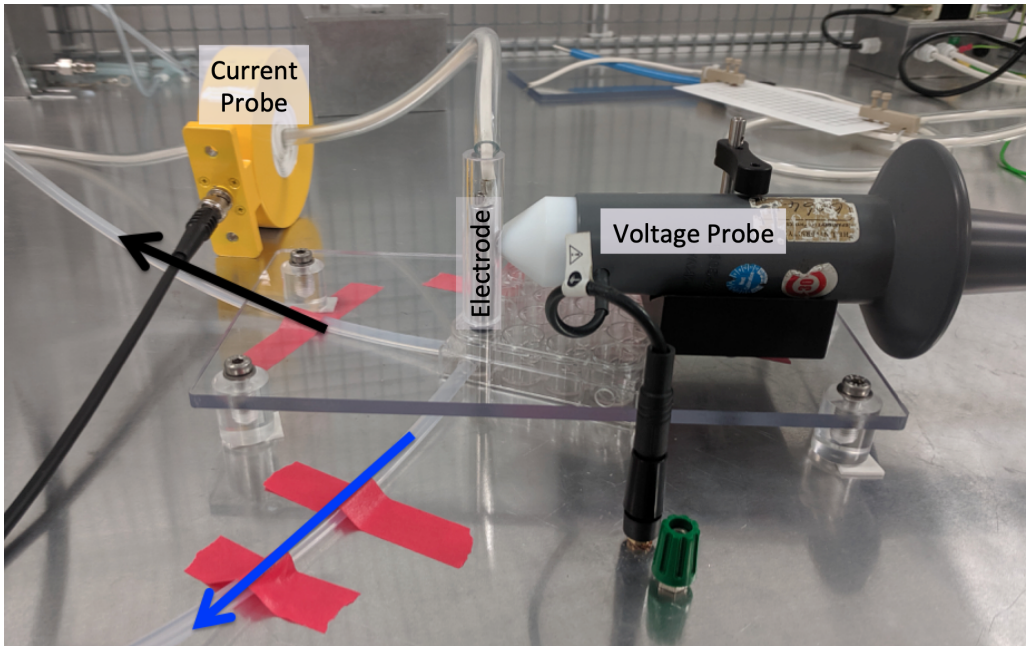

Figure 4.4: Annotated photo showing the setup of the plasma source with two gas lines going to the ozone monitor (blue arrow) and NOx monitor (black arrow).

the scrubber, I_0, and not, I, is measured. The values for I and I_0 can then be compared and the overall concentration of O_3 calculated using the Beer-Lambert Law as follows:

$$C_{O_3} = \frac{1}{\sigma l} ln(\frac{I_0}{I}) \tag{4.1}$$

where C_{O_3} is the concentration of O_3, σ is the absorption cross section and l is the absorption path length, which in this case is 14 cm.

During measurements, the plasma was ignited in a modified 24 well plate, with a hole drilled into the side of one of the wells to allow a 6.5 mm diameter gas line to be placed right next to the discharge to sample the plasma. A photograph of the setup is shown in Figure 4.4. Data was obtained over a prolonged time period, with measurements being taken and recorded every 5 seconds, by connecting the monitor to a laptop via a serial cable.

4.3.4. NO_x Measurements

NO_2, NO and NO_x densities in the plasma are measured using a commercially available NO_x monitor (2 B Technologies, Model 405 nm). NO_2 is measured

by absorption spectroscopy at 405 nm, because NO_2 absorbs strongly at this wavelength [175]. Similar to the ozone monitor, the NO_x monitor passes sample gas either straight to the absorption cell, or through an NO_2 scrubber then the absorption cell, in order to calculate the difference in absorbance between the two. NO_2 densities are then obtained using the Beer-Lambert Law.

NO is measured within the monitor through the addition of O_3 to the sample gas. This ozone reacts with any NO present to produce NO_2 as follows in reaction 4.2:

$$NO + O_3 \rightarrow NO_2 + O_2 \tag{4.2}$$

The absorption spectroscopy measurements are then performed again to measure the amount of NO_2 with and without the addition of ozone. This allows the calculation of NO concentrations. Total NO_x densities are determined by adding together the concentrations of NO_2 and NO. One potential weakness of this measurement method is that O_3 is also produced by the plasma and may interfere with the measured concentrations of NO.

The monitor setup was the same as described above for the ozone monitor and also shown in Figure 4.4.

4.3.5. GlobalKin

The zero-dimension global plasma chemistry model, GlobalKin was used for this work with the air chemistry set, both of which were presented and discussed in Chapter 2. The geometry for the plasma is that of the experimental source introduced above, with a diameter of 1 cm, and a gap of $\approx$ 1.5 mm, giving a plasma volume of 7.85 cm^3. The power input to the GlobalKin simulations will be discussed in the following results sections.

4.3.6. Absolute Reaction Rate Analysis

Analysis of the dominant production and destruction reactions for different plasma species was carried out as described in Chapter 3, Section 3.3.2, using the thresholds stated in the following text.

4.4. Results and Discussion

4.4.1. Experimental Quantification of Ozone and NO_x densities in an air DBD

Quantities of O_3 and NO_x were determined experimentally using the commercially available monitors. Measurements were taken continuously, measuring for a specific applied voltage for 2.5 minutes, then turning off the plasma for 2.5 minutes, then measuring at a new voltage for 2.5 minutes, as shown in Figure 4.5. Measurements are recorded every 5 seconds, and were taken for ascending and descending voltages. The densities for each voltage were averaged after the initial settling time while the voltage was changing.

Figure 4.6a shows that the density of O_3 increases almost linearly with applied voltage, reaching a maximum of $\approx 1 \times 10^{15}$ cm^{-3}. In Baldus et al. [40], the average ozone densities in a plasma source the same as the one used in this work are presented, and the average is given as 2×10^{16} cm^{-3}. This density is an order of magnitude greater than the maximum presented in this work, and could be explained by the fact the authors use Optical Absorption Spectroscopy (OAS) to measure absolute densities within the plasma bulk. This contrasts with the measurements taken here using the ozone monitor, where the densities are measured by flowing gas from the plasma to the monitor, which in itself will allow mixing with ambient air and cause the plasma species densities to be altered by this additional chemistry.

Figure 4.6b shows that the densities of NO_x species also increase linearly with increasing applied voltage. Here, NO_x denotes the densities of $NO + NO_2$ combined, as the two species are strongly dependent on each other through their

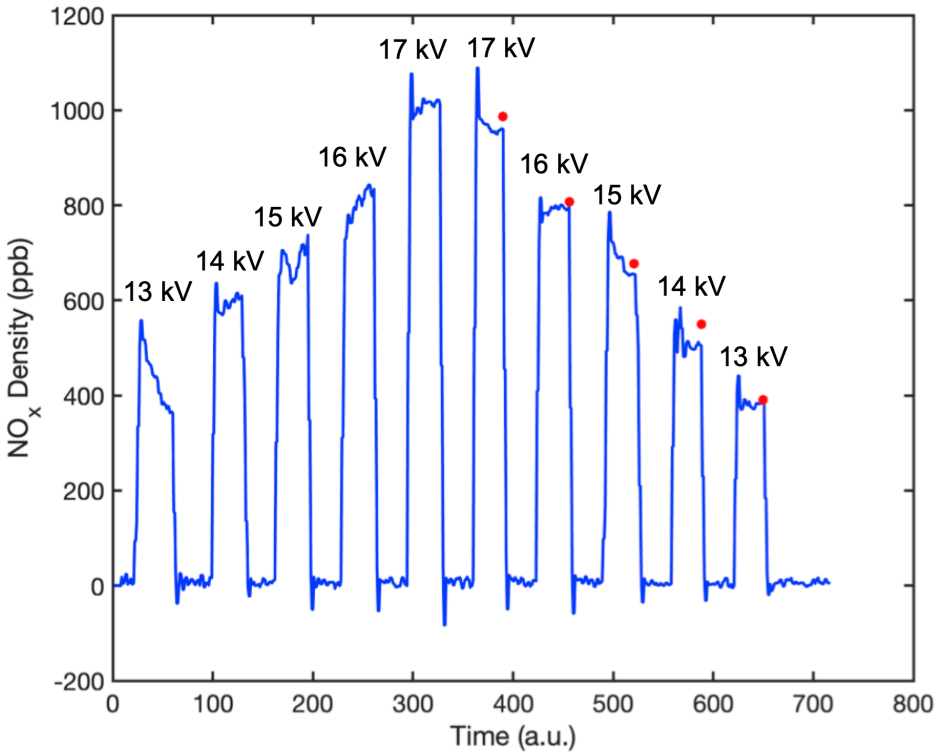

Figure 4.5: Raw NO_x densities in an air DBD showing the species measurement protocol. The plasma was set to a specific applied voltage as shown in the figure, and measurements are taken every 5 seconds for 2.5 minutes. After the densities had settled, the average densities for each voltage were calculated, and are marked by the red points. The plasma was turned off for 2.5 minutes between measurements at different applied voltages.

chemical interactions, particularly through reaction 4.2 above, where NO_2 is formed by the reaction between NO and O_3. This is an important process to consider, particularly in light of the results in Figure 4.6a which shows that there are high densities of O_3, which can be causing production of NO_2, and destruction of NO in the tube between the plasma and the monitor. Therefore, this can skew the result of the ratios of NO and NO_2 in the plasma, compared to that measured in the monitor. For this reason, the NO_x density is considered, rather than NO and NO_2 separately.

The distance between the plasma and the monitor, and the fact that there will be reactions between species occurring in the tube to alter the measured plasma

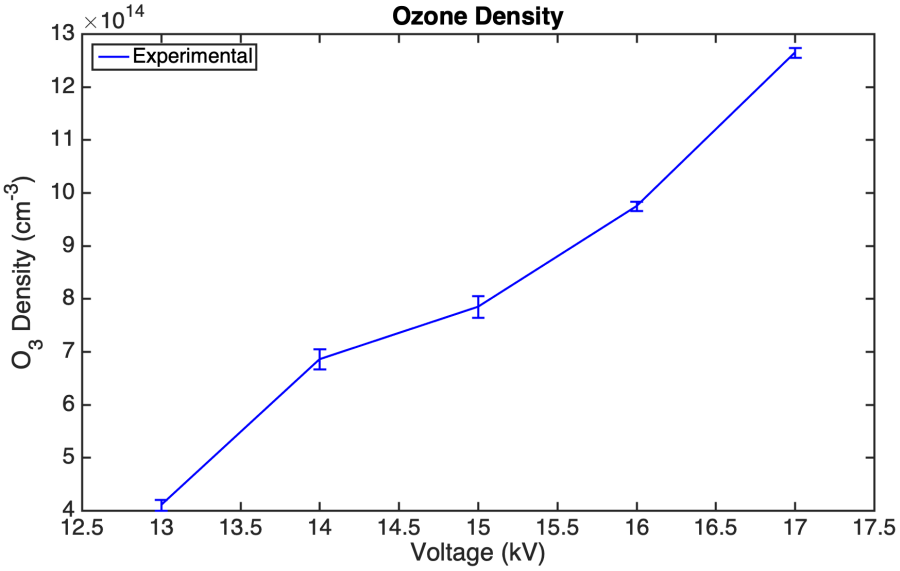

(a) O_3 densities as a function of applied voltage

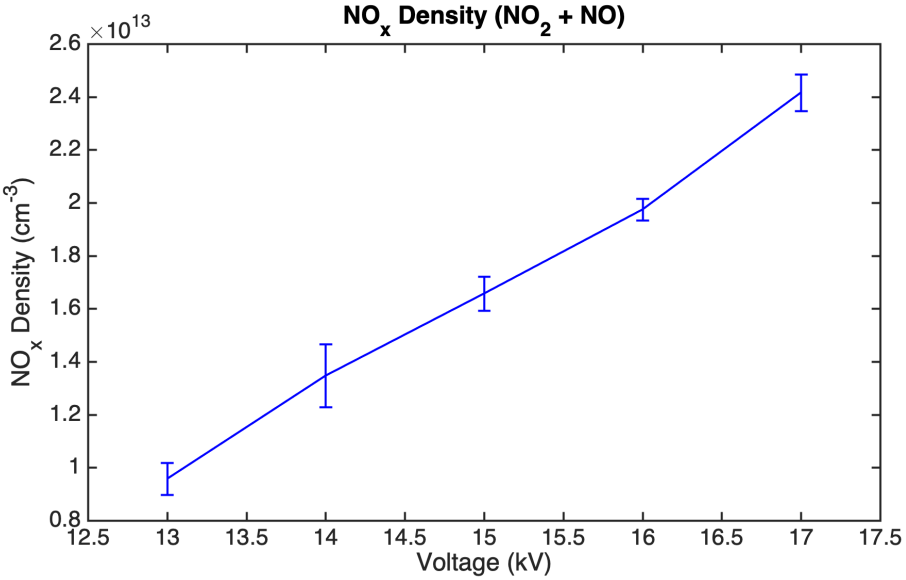

(b) NO_x densities as a function of applied voltage

Figure 4.6: Experimentally determined O_3 and NO_x densities in an air DBD as a function of applied voltage. Average densities of O_3 and NO_x were obtained as stated in the text, using the measurement protocol in Figure 4.5. The applied voltage was set using the DC power supply.

species densities, is the major drawback of this type of diagnostic. In essence, the measurement is being taken in a far effluent region of the plasma, which is not necessarily representative of the species densities in the plasma bulk. Future work would greatly benefit from more sophisticated diagnostic techniques to measure densities of species directly in the plasma bulk. Types of diagnostics to use would be Picosecond-scale Two-Photon Absorption Laser-Induced Fluorescence (PsTALIF), which can measure absolute densities of atomic species such as atomic nitrogen (N) and atomic oxygen (O) at atmospheric pressure. Atmospheric pressure plasma diagnostics are always complicated by extremely fast quenching rates of species, due to the high plasma collisionality [118]. Therefore, to overcome this challenge, PsTALIF makes use of extremely short laser pulses to excite the ground state atoms to an excited state, and very fast imaging techniques to capture the fluorescence from the atoms' radiative decay processes. This allows resolution of the lifetime of species such as N and O at atmospheric pressure. For measurements of molecules, other techniques such as Ultraviolet Broadband Absorption Spectroscopy can also be used to measure O_3 and NO, as well as other species produced in humid air such as hydroxyl radicals [40, 98, 99].

While experimental diagnostics are vital, they are complex and species-specific, only yielding information about the specific species being measured. Therefore, to aid plasma characterisation, the use of global models discussed previously is invaluable to investigate other aspects of the plasma. For example, other species densities, particularly those that are challenging or impossible to measure, and electron dynamics. However, for a model to be valid, it requires careful benchmarking to ensure it can represent the experimental situation. To do this, the experimental plasma operating conditions, such as the geometry, power input and feed gas composition need to be translated as accurately as possible into the simulated setting. GlobalKin, the model of choice discussed in Chapter 2, requires the plasma power as an input parameter, whereas in the experimental setting, the energy in the plasma is set by altering the applied pulse voltage. Therefore, the power in the experimental source needs to be determined for

input to GlobalKin.

4.4.2. Power Measurements

Principles of power measurements

As mentioned above, the experimental plasma power needs to be determined for inputting to GlobalKin for the simulations. To do this, the applied current and voltage waveforms need to be measured during experiments. However, it is not reasonable to assume that the applied current and voltage waveforms are the same as those that would be seen if it were possible to measure them directly within the plasma gap.

The whole plasma setup consists of a DC power supply, and fast switch box, cables and the plasma source, all of which contain various electrical components with their own capacitances and resistances. To try and reduce the influence of the power supply, switch box and cables, the voltage and current are measured as close as possible to the actual plasma discharge. However, the plasma source itself is not electrically simple. A DBD plasma source consists of a metal electrode covered by a dielectric layer, which prevents conduction current flowing through the system, and a gas gap where the discharge occurs [176]. The voltage and current waveforms can be measured at the electrode, but the capacitances given by the dielectric layer results in a displacement current. The system can be modelled as discussed in [176, 177], using the circuit shown in Figure 4.7.

The presence of a dielectric in an electrical circuit results in a displacement current, meaning that in this plasma situation, the measured current, I_a, is the sum of the conductive plasma current, I_p, and the displacement current, I_d, as follows in equation 4.3.

$$I_a = I_p + I_d \tag{4.3}$$

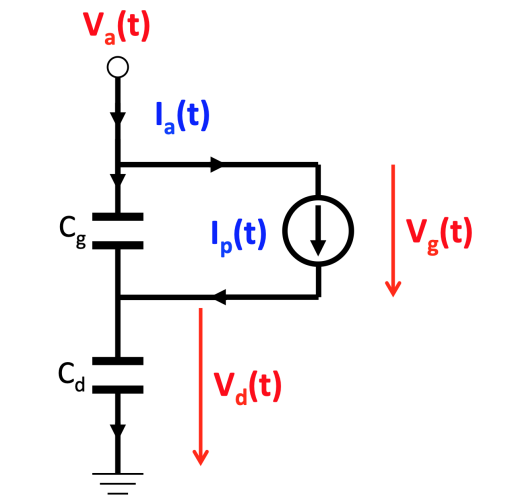

Figure 4.7: Circuit diagram for representing the DBD plasma source

Similarly, the measured voltage, V_a, is the sum of the voltage across the plasma gap, V_g, and the voltage across the dielectric barrer, V_d, as follows in Equation 4.4.

$$V_a = V_g + V_d \tag{4.4}$$

In order to calculate the plasma current and voltage, expressions in [178–180] can be used as follows:

$$I_p(t) = \left(1 + \frac{C_g}{C_d}\right) I_a(t) - C_g \frac{dV_g(t)}{dt} \tag{4.5}$$

C_g and C_d are the capacitances of the gas gap and the Al_2O_3 dielectric, respectively. To calculate the capcitance of the air gap and the dielectric, Equation 4.6 was used, as follows:

$$C = \frac{\epsilon_r \epsilon_0 A}{d} \tag{4.6}$$

Where C is the capacitance, ϵ_r is the dielectric constant of the material, ϵ_0 is the permittivity of free space, A is the area and d is the thickness of the material.

As the capacitances of C_g and C_d in Figure 4.7 will be different, there will be a different voltage across each of them in the circuit, before the plasma ignites. This is known as a voltage divide, and is accounted for in the power equations by the preterm multiplier in the first term on the right hand side of Equation 4.5.

Once I_p is known, the integral of I_p can be used to find the total charge transferred, $Q(t)$, using Equation 4.7, and this can then be put into Equation 4.8 to calculate the voltage across the dielectric barrier.

$$Q(t) = \int_0^t I_p(t) \tag{4.7}$$

$$V_d(t) = \frac{1}{C_d} Q(t) \tag{4.8}$$

The voltage across the plasma gap, V_g, can then be calculated as follows in Equation 4.9 [179].

$$V_g(t) = V_a(t) - V_d(t) = \frac{C_d}{C_g + C_d} V_a(t) - \frac{1}{C_g + C_d} Q(t)dt \tag{4.9}$$

The first term on the right hand side relates to the initial voltage across the gap, with the $\frac{C_d}{C_g + C_d}$ term arising due to the initial voltage divide across the different capacitances in the circuit, before the plasma ignites. When the conduction current I_p begins to flow, it causes charge to build up (Equation 4.7), which serves to reduce the gap voltage, hence the negative term for the displacement current in Equation 4.9 [179].

Once the plasma current and voltage have been obtained, the instantaneous power dissipated into the plasma, P_p, can then be determined as follows:

$$P_p(t) = I_p(t) \times V_p(t) \tag{4.10}$$

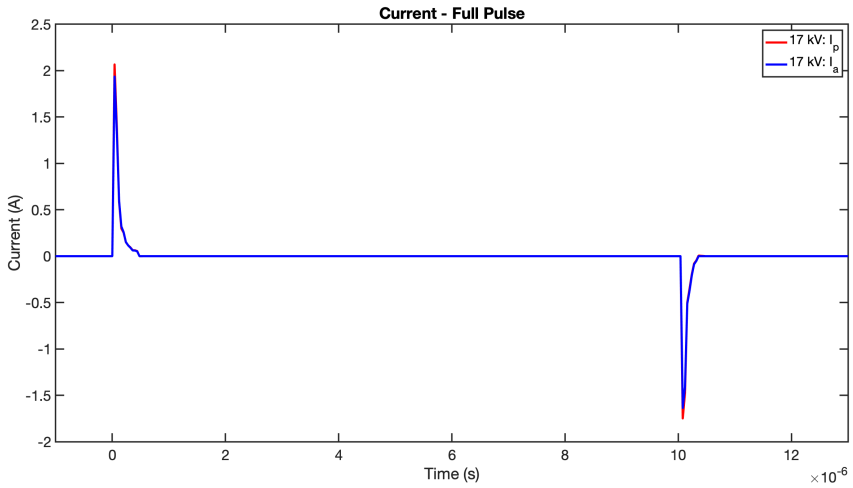

(a) Full Pulse

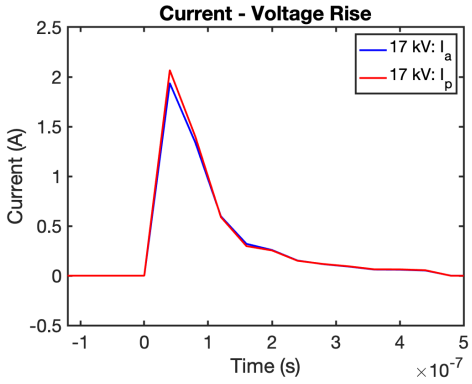

(b) Voltage Rise

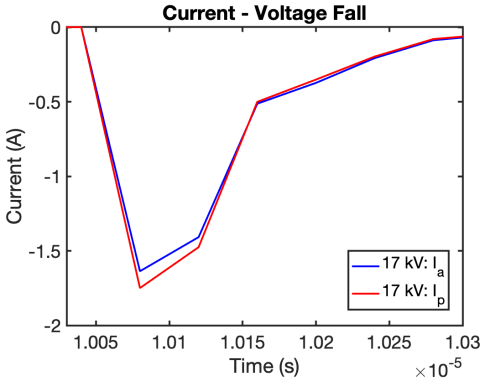

(c) Voltage Fall

Figure 4.8: Figure showing the measured total current in the DBD, and the plasma current, calculated using equation 4.5. Current peaks correspond to the rising and falling edges of the measured voltage waveform at 17 kV. 4.8a shows the current across the full voltage pulse, and Figure 4.8b and Figure 4.8c show the currents for the voltage rise and fall times, respectively.

Calculations of the power dissipated into the DBD plasma source were attempted out over a range of input voltages. Experimentally, the maximum voltage of the pulses applied to the high voltage electrode was set manually on the DC power supply, and from here, any voltages mentioned will refer to this maximum pulse voltage. The plasma reliably ignites for voltages ranging from approximately 13 kV to 17 kV, therefore, the calculated powers are for this voltage range.

Figure 4.8 shows the total measured current trace for the 17 kV experimental situation (I_a, solid line) and the calculated plasma current (I_p, dashed line). It can be seen here that the peak values of I_p are in fact greater than those of I_a, which is not physically possible, suggesting that there is an issue with the calculations of I_p.

This procedure relies on the fact that the the capacitances of the gap, and the dielectric are known, and that accurate dimensions of the plasma, and the dielectrics in direct contact with the plasma, are known [181]. Here, this is a problem, as the plasma is not a perfect cylinder, with definite edges, therefore, the plasma volume may not be exactly what is calculated using dimensions specified in Section 4.3.1. On top of this, the exact dielectric constants of the Al_2O_3 dielectric, the thickness of it, and the exact area in contact with the plasma is not known. The dielectric covers the bottom of the electrode, but also extends up the sides, meaning that if the plasma ignites around the edges of the electrode, this could have an influence. Also, if the plasma is not fully uniform, and contains filaments, then these will have a much smaller cross section, and the relevant areas of the dielectric and the gap would be impossible to measure. If the capacitances of the gap and the dielectric are not correct, or at least the ratio between them is not correct, then the preterm multiplier in the first term of Equation 4.5, as well as the capacitance used to calculate the displacement current in the same equation will be incorrect. This will skew the calculations of I_p, and result in a value for I_p, that is greater than I_a, which is not physically possible. Since the calculation of I_p is the first step for calculating the power, if this does not work, then the whole calculation, unfortunately, does not hold. Further to this, in order to calculate the plasma current, it is necessary to have a measured current waveform of high enough resolution to be able to see additional currents as a result of plasma breakdown and this may also be a contributing factor in this case if the resolution is not sufficient.

For future work an alternative approach would have to be taken. In order to circumvent the potential issues with obtaining high enough resolution current waveforms, it may be preferable to instead measure the total charge across the

system, by placing a capacitor in series with the plasma source, with a significantly larger capacitance than that of the system (usually a factor of 1000 times greater) [180]. Using the information on the charge and voltage, a charge-voltage (V-Q) plot can be drawn to infer the associated capacitances of the system, as well as total energy dissipation, total power and breakdown voltage [180]. This approach would also have the advantage of not requiring a knowledge of the capacitances in the system to input to equation 4.5. and therefore, may offer a good alternative experimental approach to power measurements. Unfortunately, due to time constraints, this alternative method could not be attempted.

Power For GlobalKin

Since the plasma power in the experimental situation cannot be measured using the methods described above, an alternative approach was taken for estimating the plasma power. Since the applied voltage and total current waveforms have been obtained, the applied power to the system (P_a) can be calculated as follows in equation 4.11.

$$P_a(t) = I_a(t) \times V_a(t) \tag{4.11}$$

The waveforms for I_a and V_a, and the resulting P_a using equation 4.11 are shown in Figure 4.9. It is important to remember that this power is NOT the same as the power that is dissipated into the plasma, however, it is a real physical quantity to start from.

Translating Experimental Power into GlobalKin

To find a more suitable power for GlobalKin, for which simulations can be qualitatively compared, a power variation was performed, with the aim of comparing the resulting electron densities to published data, and species densities to the experimental diagnostics in Section 4.4.1. From now, the power in the simulation will relate to the experimental applied power, and will be termed P_a[value], where the value is the applied experimental voltage. For example P_a17 is the 17 kV experimental case and P_a13 is the 13 kV experimental case.

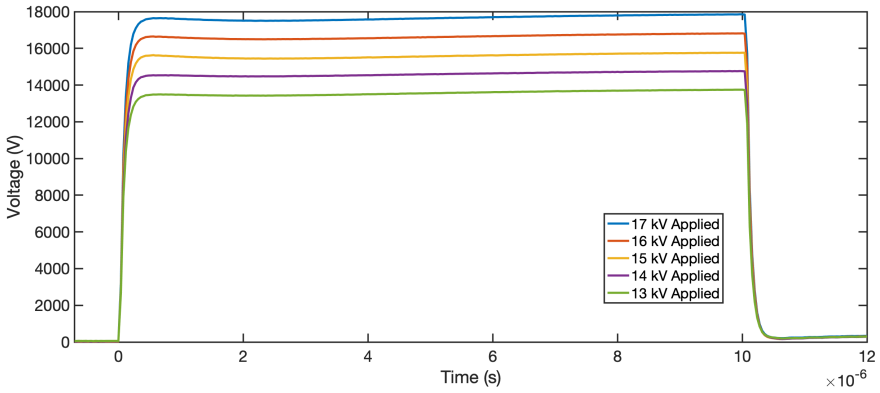

(a) Voltage

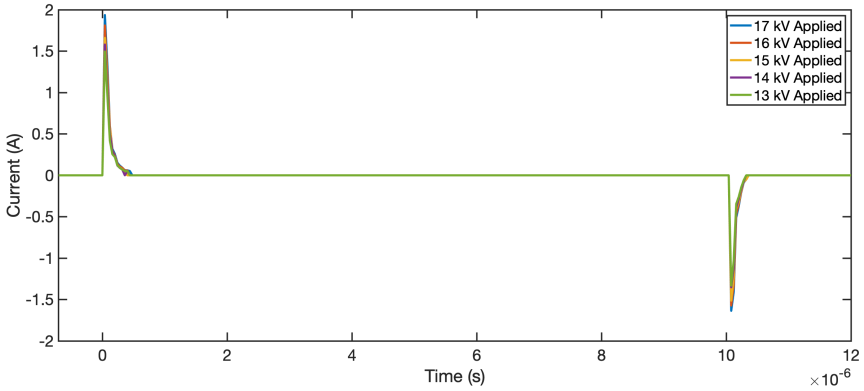

(b) Current

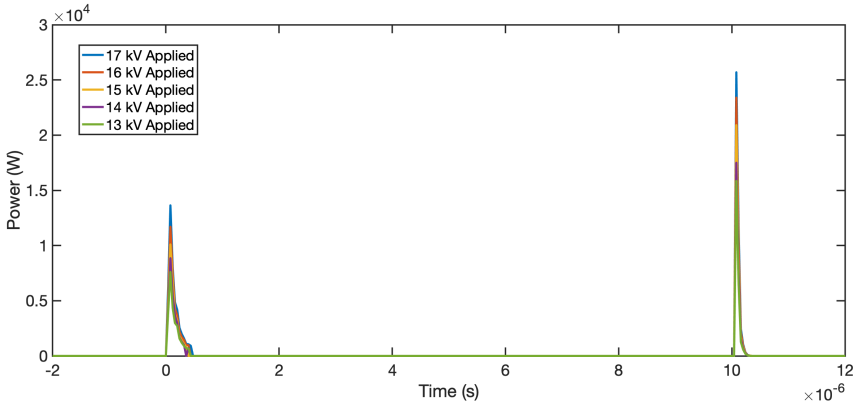

(c) Power

Figure 4.9: Graph to show voltage and current waveforms for different applied voltages in the experimental setup. Equation 4.11 was then used to calculate the applied power shown in 4.9c.

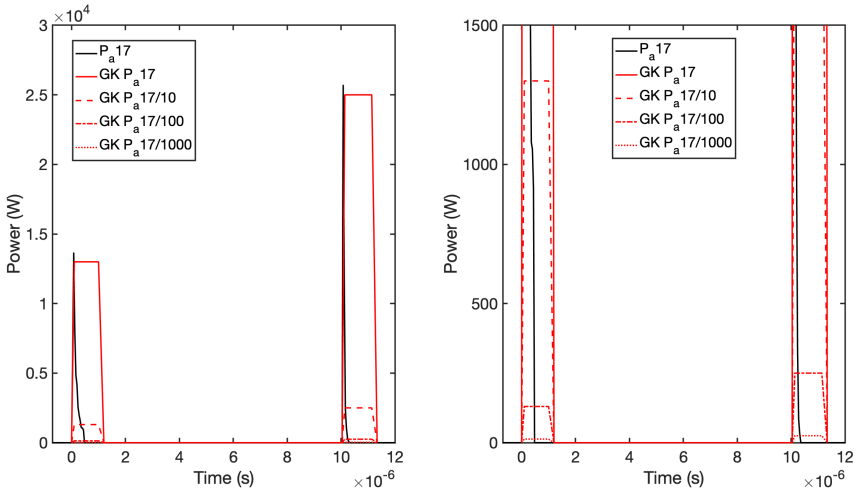

Figure 4.10: Comparing GlobalKin power pulse shape to the applied power pulse shape. The experimental applied power for the 17 kV experimental situation is shown in the black line (P_a17). For the simulations, the experimental applied power for 17 kV situation is the starting point (GK P_a17), then the power is decreased by factors of 10. GK in the legend indicates the pulses used in GlobalKin.

For the power variation, the starting power was the applied power for experiment, then the power was sequentially decreased by a factor of 10, until the power was $\frac{1}{10000}$ of the original. The power pulses also had to be lengthened in GlobalKin, compared to the experimental power pulses, due to the fact that the simulations were too computationally intensive, meaning that GlobalKin was unable to resolve all of the pulses and skipped some out when run for multiple pulses. Therefore, a less intensive pulse shape was chosen, and is compared to the experimental pulses in Figure 4.10. Similarly to the experimental pulse, the power pulses coincide with the rise and fall times of the voltage.

Figure 4.10 (left panel) shows that the two peaks in power corresponding to the rise and fall of the voltage pulse have a different maximum power, with the second peak being up to a factor of 2 greater than the first. This is due to the fact that the current spike is not exactly in phase with the voltage rise, therefore, this reduces the power for this time period. For the voltage fall time, the current spike directly overlies the voltage fall, so the maxima of the two traces line up. This is shown in Figure 4.11.

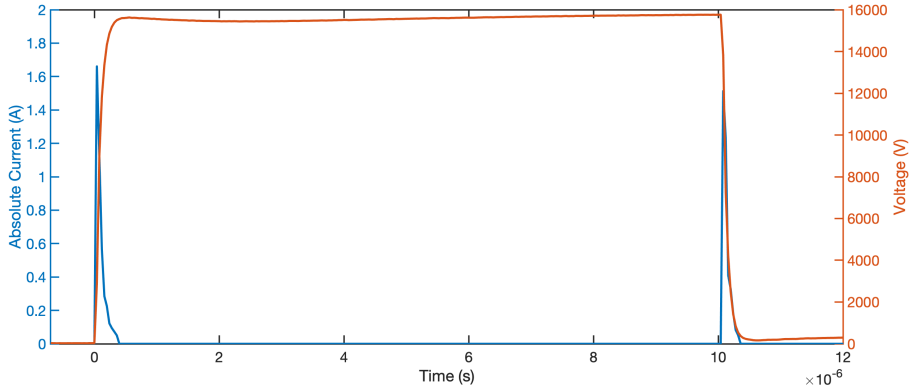

Figure 4.11: Graph to show timing of the applied voltage rise and fall time compared with the measured current. The current shown is the absolute magnitude of the current to show the relative times of the current spike with the voltage rise and fall. The current peaks actually have opposite signs, with a positive peak for the voltage rise, and a negative peak for the voltage fall, as shown in Figure 4.9b. The traces shown are for representative waveforms taken in the 15 kV situation.

4.4.3. Benchmarking air simulations to experimental O_3 and NO_x densities

Quantities of O_3 and NO_x were determined experimentally using the commercially available monitors, as discussed in Section 4.4.1, and shown in Figure 4.6. To begin the process of model benchmarking, the power variations shown in Figure 4.10 were performed, for the different experimental applied voltages, and the simulated densities of NO_x and O_3 were compared to the experimental densities. Simulations were run for 20 ms, at 1 kHz, to ensure equilibrium was reached for species densities. Densities of NO_x ($NO_2 + NO$) and O_3 were then averaged over the final 10 ms when equilibrium was reached. These average densities for the different fractions of the experimental applied power are shown in Figure 4.12a and Figure 4.12b.

From Figure 4.12 it can be seen that the **simulated** densities of NO_x and O_3 scale with the power fraction used, particularly for O_3, where a factor of 10 increase in power results in roughly a factor of 10 increase in density ($P_a/10000 \rightarrow n_{O_3} \approx 10^{14}$ cm^{-3}, $P_a/1000 \rightarrow n_{O_3} \approx 10^{15}$ cm^{-3} and $P_a/100 \rightarrow n_{O_3} \approx 10^{16}$ cm^{-3}). up to $P_a17/10$ and P_a17, where the densities seem to become less responsive to

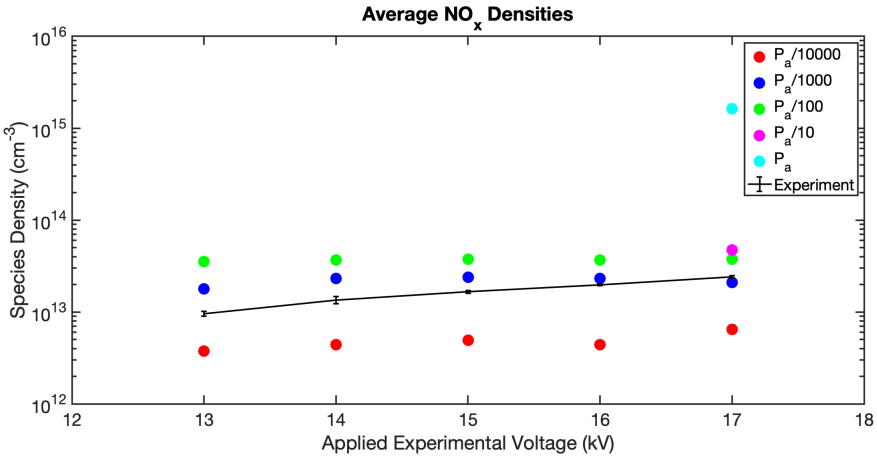

(a) NO_x

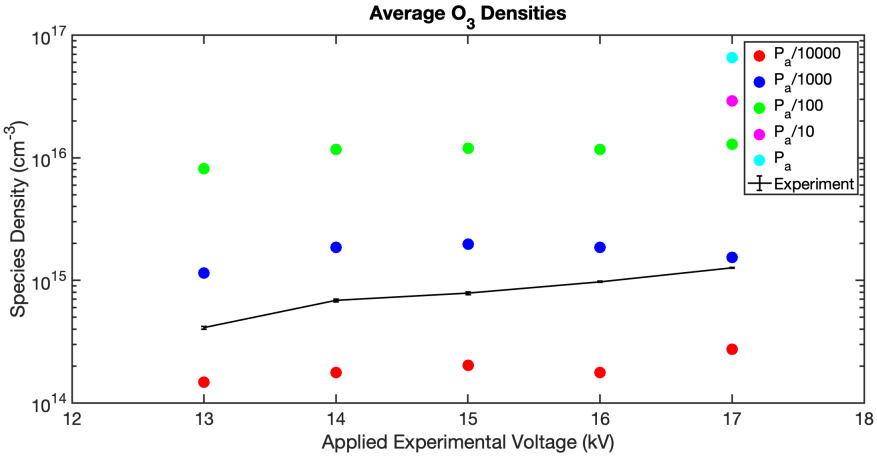

(b) O_3

Figure 4.12: Average simulated densities of NO_x and O_3 as a function of GlobalKin input power. Power was varied starting at the original P_a value for the experimental voltage, then decreased sequentially by a factor of 10. The simulated species densities were averaged over 10 ms once the densities had reached equilibrium in the simulation. The experimental results are shown by the black line, and the error bars show the standard deviation.

increasing power. This is in keeping with results published by Lietz and Kushner [129] who also found that O_3 densities only increase up to a certain applied voltage. Above this voltage, O atoms that at low voltages produce O_3 instead are quenched by longer-lived NO_2 [129]. When comparing the **simulated** species densities in Figure 4.12 to the **experimental** species densities, it can be seen that the **simulated** densities when the power is $P_a/1000$ shows good qualitative agreement with the experiment. This trend is consistent for both NO_x and O_3, where the same power input gives a similar level of agreement for the different species. This is positive, as it suggests the model is able to qualitatively match the trends for more than one species.

Of course, the same problems stand as mentioned in Section 4.4.1, as the **experimental** data is taken in the plasma effluent, whereas the **simulated** data is for within the plasma bulk. Therefore, it would not be expected that the densities would necessarily match perfectly, even if the power input was exactly correct. However, from this comparison, it is possible to say that using a plasma power that is 1000 times smaller than the applied power, with the pulse shape shown in Figure 4.10 is reasonable for further investigations using the model. As further validation that this is the case, the average maximum electron density (occurring when the power is on and maximal) for the power fractions was calculated. It was found that for $P_a/10000 \Rightarrow n_e \approx 10^{10}$ cm^{-3}, for $P_a/1000 \Rightarrow n_e \approx 10^{11}$ cm^{-3} and for $P_a/100 \Rightarrow n_e \approx 10^{12}$ cm^{-3}. Using this information, combined with the NO_x and O_3 data above, the $P_a/1000$ values will be used from now on. An electron density of $n_e \approx 10^{11}$ cm^{-3} is a realistic value for a plasma of these conditions, and is in agreement with that published in [40]. These powers equate to approximately 7-25 W, for the length of each of the power pulses shown in Figure 4.10.

Since the model is able to produce similar to trends to the experimental data, it is reasonable to being using it to investigate aspects of the plasma that are hard or impossible to measure experimentally. In particular:

1. Investigate pathways for species production and destruction

2. Quantify other species present in the plasma - other potential biorelevant species

3. Probe how the plasma is working, and how it might be possible to alter the running parameters to alter the chemical kinetics.

4.4.4. Pathways analysis for *NO* production and destruction using GlobalKin

One of the motivations for using a global chemistry plasma model alongside experimental diagnostics for plasma characterisation is to allow the interrogation of the dominant production and destruction mechanisms for different species in the plasma. Of particular interest in this work is the production and destruction mechanisms of biorelevant RONS that are present in the plasma, such as nitric oxide. *NO* is known to be important for many physiological processes such as wound healing and blood pressure regulation in many different tissues in the body [65, 171, 182]. Due to its far reaching effects in the body, and the potential for use as a therapeutic agent, there are some plasma devices which are designed to specifically produce *NO* as discussed above [172, 173]. However, mechanisms describing the production and destruction of *NO* that could potentially inform how to control this species density in a plasma is not well understood. Therefore, to more fully understand *NO* kinetics in the plasma in this work, analysis of *NO* production and consumption pathways was performed.

For this, the intermediate P_a15/1000 power values were used with the pulses outlined above in Figure 4.10, and a simulation was run for 20 ms so that equilibrium was reached. A threshold of 10^{10} cm^{-3} s^{-1} was set for analysis of the important production and destruction rates. Figure 4.13a shows sets of reactions contributing to *NO* production which all have similar trends in terms of absolute rates during and between pulses. As follows:

1. Group 1 Reactions - Reaction rates increase during the power pulse, then decreases again between pulses. These reactions are shown in Table 4.1, Group 1 reactions.

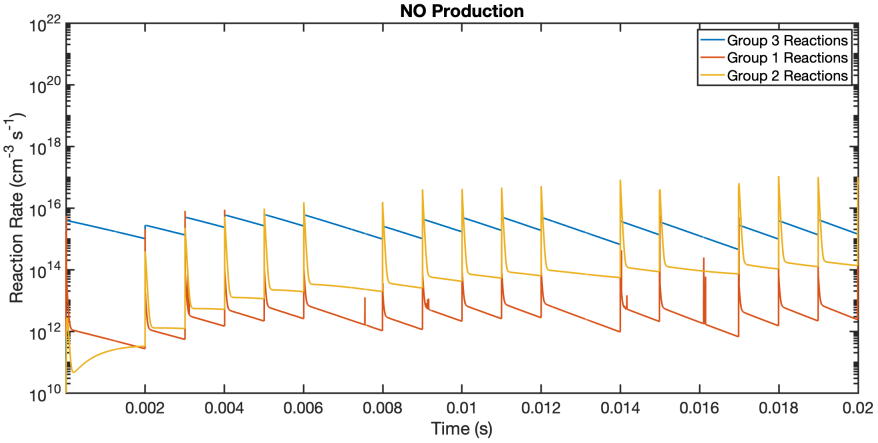

(a) Total absolute reaction rates for groups of reactions contributing to *NO* production.

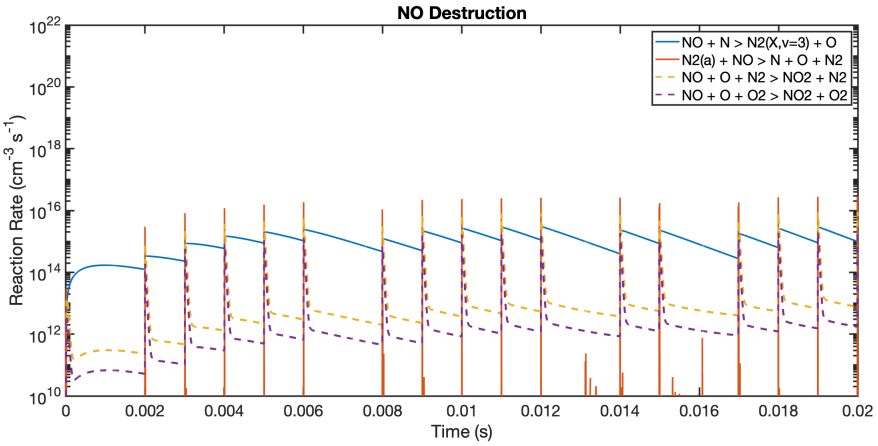

(b) Destruction

Figure 4.13: *NO* Production and destruction mechanisms as a function of time in the 20 ms time period simulated. This is for the $P_a/1000$ power case. All reactions are shown for *NO* destruction, however, for clarity, *NO* production reactions are grouped as per Table 4.1. Threshold for analysis was 10^{10} cm^{-3} s^{-1}.

Table 4.1: A subset of Appendix Table A.5 showing the dominant NO production reactions. [a] Rate coefficient is $cm^3\ s^{-1}$ for 2-body reactions, $cm^6\ s^{-1}$ for 3-body reactions and s^{-1} for radiative decay processes.

No.	Reaction	Rate Coefficient [a]	Reference
Group 1 Reactions			
NO11	$N_2(A) + O \rightarrow NO + N(^2D)$	7×10^{-12}	[110]
NO13	$O_2 + N(^2D) \rightarrow NO + O$	$1.5 \times 10^{-12}(T_g/300)^{0.5}$	[183]
NO14	$O_2 + N(^2D) \rightarrow NO + O(^1D)$	$6 \times 10^{-12}(T_g/300)^{0.5}$	[183]
NO15	$O_2 + N(^2P) \rightarrow NO + O$	2.6×10^{-12}	[183]
NO16	$O_2(a) + N \rightarrow NO + O$	$2 \times 10^{-14} exp(-600/T_g)$	[183]
NO20	$N + O + O_2 \rightarrow NO + O_2$	$1.02 \times 10^{-32}\ cm^6\ s^{-1}$	[183]
NO23	$NO(A) + N_2 \rightarrow NO + N_2$	1×10^{-13}	[114]
NO24	$NO(A) + O_2 \rightarrow NO + O_2$	1.5×10^{-10}	[114]
NO25	$NO(A) + NO \rightarrow NO + NO$	2×10^{-10}	[114]
NO26	$NO(B) + N_2 \rightarrow NO + N_2$	6.1×10^{-13}	[114]
NO27	$NO(B) + O_2 \rightarrow NO + O_2$	1.5×10^{-11}	[114]
NO36	$NO(A) \rightarrow NO$	4.5×10^6	[184]
NO37	$NO(B) \rightarrow NO$	3×10^5	[185]
NO61	$O^- + N \rightarrow NO + e^-$	2×10^{-10}	[31]
NO49	$N_2(X, v \geq 13) + O \rightarrow NO + N$	1×10^{-13}	[110]
Group 2 Reactions			
NO47	$NO_2 + N \rightarrow NO + NO$	2.3×10^{-12}	[183]
NO48	$NO_2 + O \rightarrow NO + O_2$	$6.51 \times 10^{-12} exp(998/T_g)$	[114]
Group 3 Reactions			
NO12	$O_2 + N \rightarrow NO + O$	$3.3 \times 10^{-12} exp(-3150/T_g)$	[183]

2. Group 2 Reactions - Reaction rates may be increased by the pulse, but also increase in the 'off time'. These reactions are shown in Table 4.1, Group 2 reactions.

3. Group 3 Reactions - Reaction rates stay relatively constant throughout the simulation time, compared to Group 1 and Group 2 reactions. This reaction is shown in Table 4.1, Group 3 reactions.

The reasons for the different trends in reaction rates for the different groups

become clear when looking at the kinetics of the different reactant species. Figure 4.14 shows the densities of the different reactants for group 1, 2 and 3 reactions in Table 4.1. Here it can be seen that there are also different trends in in the species dynamics. Group 1 reactions generally have at least one reactant that is a metastable state such as $N_2(A)$, $N(^2D)$, $N(^2P)$, $NO(A)$ and $NO(B)$. These species only exist at significant densities for a very short time, coincident with the power pulse. Other reactants such as N and O are longer lived, and consistently at higher densities than the metastables. However, since the absolute reaction rate is determined by product of the densities of the reactants and reaction rate coefficient, the reaction rate outside the pulse time will always be low when at least one of the reactant densities becomes negligible.

On the other hand, group 2 reactions have the same reactant of NO_2 which is a very long-lived species, that increases over time in the plasma. The second reactant of N or O also have consistently significant densities. Therefore, the group 2 reaction rates increase in the pulse (coincident with increases in NO_2, N and O densities), but also increase over time between pulses, due to the overall increasing concentrations of NO_2. The increasing concentration of NO_2 is mainly due to the fact that the total destruction rate is approximately an order of magnitude lower than its production rate. Therefore, for NO production, the group 2 reactions are more important for longer term NO production, as the destruction of NO_2 is slower than its production. This means that while N and O densities remain fairly constant throughout the whole simulation time, the NO_2 density is always increasing, thus increasing NO production over time.

Two reactions of note are NO49 and NO20, whose absolute rates are shown in Figure 4.15. NO20 is a 3-body recombination reaction for N and O, with O_2 acting as a third body. Therefore, since all these species are longer lived as shown in Figure 4.14, it may be expected that this reaction should belong in group 3, rather than group 1. However, due to having an extremely low reaction rate coefficient (1.02×10^{-32} cm^6 s^{-1}, [183]), the densities of the reactants need to be very high to make the reaction significant. Since N and O do increase in the pulse, the overall reaction rate increases in the pulse, but then decreases again.

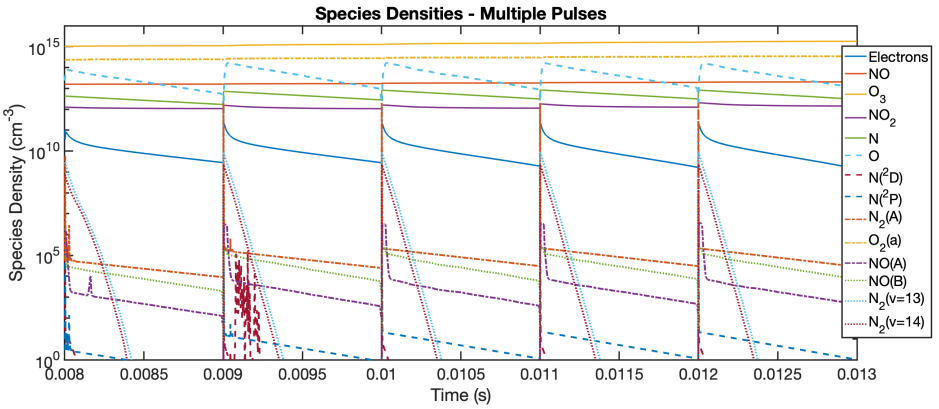

(a) Multiple Full Pulse Periods

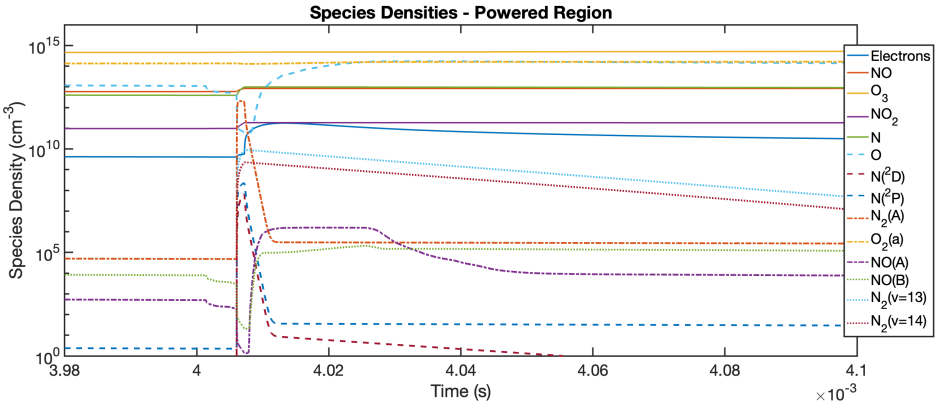

(b) Powered Region only

Figure 4.14: Species densities as a function of time in a simulated air plasma. 4.14a shows the species dynamics across multiple full pulse periods that are representative of all the pulses in the simulation time. 4.14b shows the species dynamics in the powered region of a representative pulse. The species shown are reactants in the main *NO*-producing reactions shown in Table 4.1.

Secondly reaction NO49 is the Zeldovich equation, believed to be one of the main *NO* production mechanisms in some types of plasma sources [126]. However, for these reactions to become significant, the VDF needs to be significantly populated for $N_2(X, v \geq 13)$, and from the absolute rates of these reactions in Figure 4.15 (maximum of $\approx 10^{11}$ cm^{-3}s^{-1}) compared to the overall absolute rates of each of the groups in Figure 4.13a (minimum $\approx 10^{12}$ cm^{-3}s^{-1}), this does not appear to be the case for these plasma conditions.

Finally the group 3 reaction shown in Table 4.1 shows a relatively consistent,

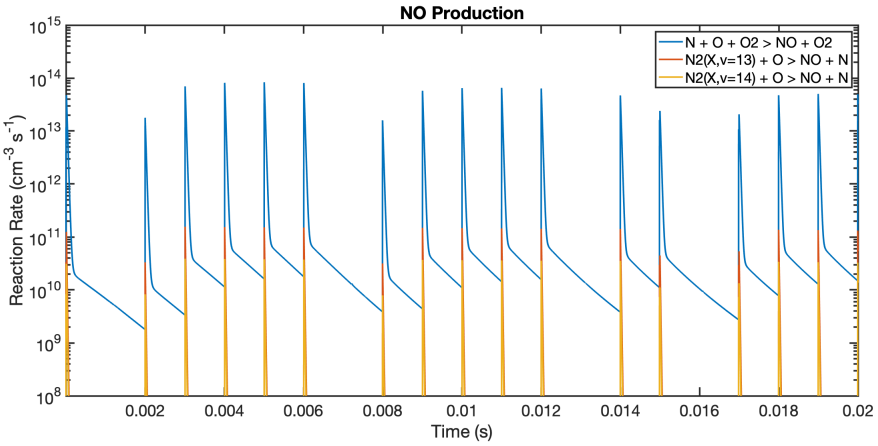

Figure 4.15: A subset of reactions contributing to NO production.

high reaction rate for production of NO. This is because one of the reactants is O_2, a main constituent of the background gas and therefore, always in abundance. N is also a a relatively stable species as mentioned before, meaning that overall, while the reaction rate increases slightly in the pulse, is remains high throughout most of the simulation time. Figure 4.13a suggests that the production of NO is mainly from Group 3, reaction NO12, $O_2 + N \rightarrow NO + O$. However, when looking at the main destruction pathways of NO in Figure 4.13b, the NO destroying reaction, $NO + N \rightarrow N_2(X, v = 3) + O$ occurs at a very similar rate to NO12. This suggests that these reactions do not actually result in a net increase in NO density.

Overall it appears that it is a combination of Group 1 and Group 2 reactions that cause the increasing densities of NO throughout the simulation.

4.4.5. Pathways analysis for O_3 production using GlobalKin

Conversely to NO, O_3 is a molecule that is not produced endogenously within the body to partake in normal physiological functions. Instead, it is known to be a toxic molecule [186, 187]. However, it is also of interest as it is extremely effective for killing bacteria. This means that the control of ozone in a biomedical plasma treatment could be valuable, for example, to increase O_3 concentrations delivered in the context of infected chronic wounds, but decreased concentra-

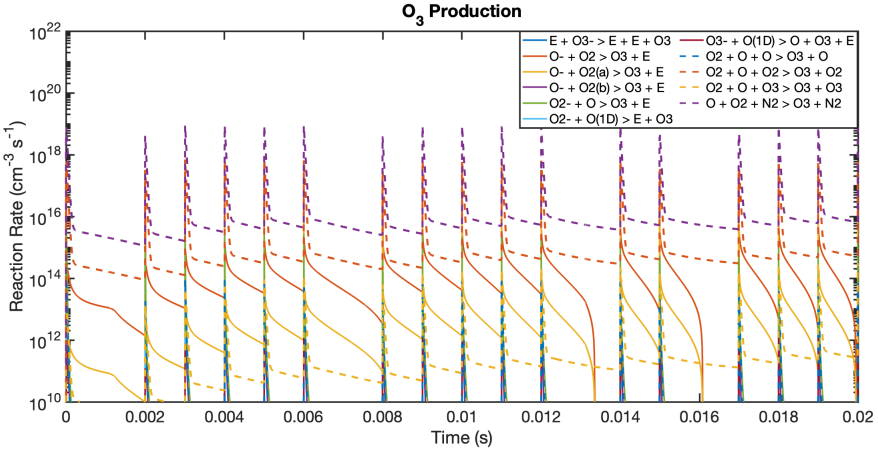

(a) Production

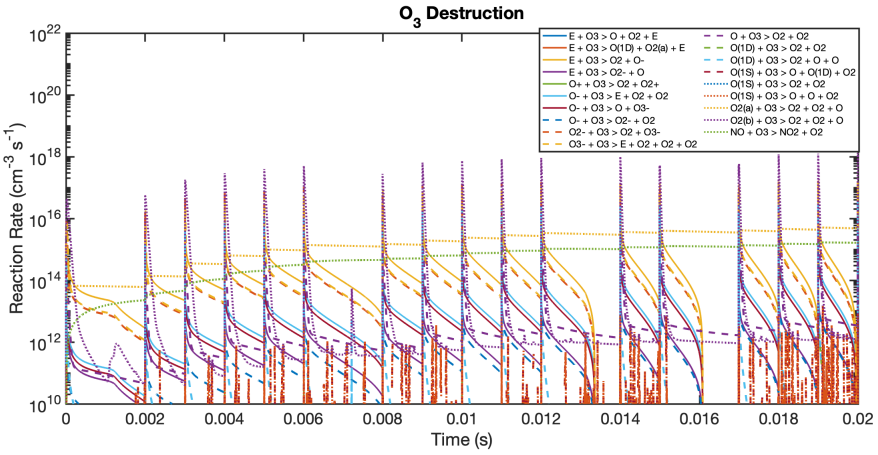

(b) Destruction

Figure 4.16: All production and destruction mechanisms for O_3 as a function of simulation time. The threshold rate for the reaction rate analysis is set at 10^{10} cm^{-3} s^{-1}.

tions in the absence of infection.

Therefore, to understand how the concentrations of O_3 are controlled in the plasma, first of all, the main production and destruction mechanisms for it in the plasma need to be determined [98, 119].

The main production and destruction processes for ozone over the full 20 ms simulation time are shown in Figure 4.16. Here it can be seen that there are two different types of reactions, showing different magnitudes, but similar dynamics. Firstly, there are two-body reactions which are involving ions which

Table 4.2: A subset of the total reaction scheme showing the dominant O_3 production reactions. [a] Rate coefficient is cm^3 s^{-1} for 2-body reactions and cm^6 s^{-1} for 3-body reactions.

No.	Reaction	Rate Coefficient [a]	Reference
2-body Reactions			
OE12	$e^- + O_3^- > e^- + e^- + O_3$	$2.12 \times 10^{-8} T_e^{0.51} exp(\frac{-5.87}{T_e})$	[188]
O8	$O^- + O_2 \rightarrow O_3 + e^-$	1×10^{-12}	[132]
O9	$O^- + O_2(a) \rightarrow O_3 + e^-$	6.1×10^{-10}	[132]
O10	$O^- + O_2(b) \rightarrow O_3 + e^-$	6.1×10^{-10}	[132]
O11	$O_2^- + O \rightarrow O_3 + e^-$	$8.5 \times 10^{-11} (T_g/300)^{-1.8}$	[189]
O12	$O_2^- + O(^1D) \rightarrow O_3 + e^-$	$8.5 \times 10^{-11} (T_g/300)^{-1.8}$	[132]
O13	$O_3^- + O(^1D) \rightarrow O + O_3 + e^-$	3×10^{-10}	[132]
3-body Reactions			
NO10	$O + O_2 + N_2 \rightarrow N_2 + O_3$	5.7×10^{-34}	[114]
O5	$O_2 + O + O \rightarrow O_3 + O$	$2.1 \times 10^{-34} exp(345/T_g)$	[190, 191]
O6	$O_2 + O + O_2 \rightarrow O_3 + O_2$	$2.11 \times 10^{-35} exp(663/T_g)$	[190, 191]
O7	$O_2 + O + O_3 \rightarrow O_3 + O_3$	$1.66 \times 10^{-34} (T_g/300)$	[192]

have significant contributions to O_3 production during the power pulses, but are negligible between them. Secondly, there are 3-body reactions where O and O_2 combine, with a third body to produce O_3. The most important of these reactions are those where the third body is either N_2 or O_2. The O_3-producing reactions are shown in Table 4.2, and the simplified O_3 production mechanism graph is shown in Figure 4.17.

When comparing O_3 production and destruction mechanisms in Figure 4.16, it appears that for the 3-body production mechanisms, there are destruction mechanisms with similar dynamics, but a slightly reduced absolute rate. Similarly, for the 2-body production mechanisms that are significant in the power pulses, there are destruction mechanisms also important in these time periods, but again, with a slightly lower reaction rate. Combined, this results in an overall slight increase in O_3 density over time, though it is difficult to conclude which reactions are specifically responsible.

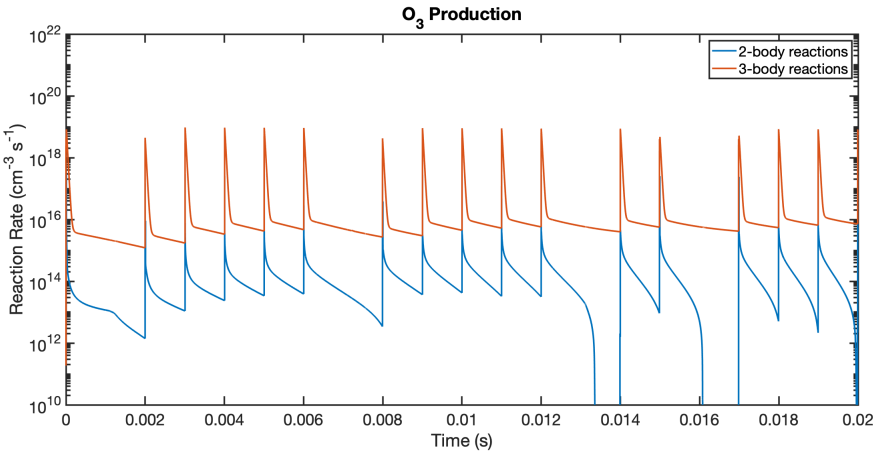

Figure 4.17: Contribution of 2- and 3-body reactions to O_3 production as a function of time.

4.4.6. Electron density as a function of power

In Chapter 3, the presence of an afterglow electron peak (AEP) was discussed, and the mechanisms by which it was formed were presented. Therefore, using the air chemistry set, and the experimental applied and plasma powers obtained as per the power variation above, whether or not an AEP would be present in the experimental situation was investigated. This is also of interest for whether or not the VDF is populated in these plasma conditions, and able to contribute to NO production as mentioned above.

To investigate this, a single pulse 15 ms into the 20 ms simulation was chosen, as the simulation was at equilibrium by this point and, therefore, is most representative of the overall situation. The electron density for this peak is shown in Figure 4.18a, for the different powers ($P_a/1000$). Importantly, the overall shape of the electron dynamics in Figure 4.18a is the same, and there is no sign of an AEP for any of the powers used. After the pulse, the electrons decay away continuously. Therefore, to investigate this further, the VDFs for different time points across the pulse period were determined, as the population of the higher levels of the VDF determine whether or not an AEP is formed (see Chapter 3). The time points chosen were during the maximum power peak, and subsequent time points of 1×10^{-4}, 3×10^{-4}, 5×10^{-4} and 7×10^{-4} s later. These time points are shown in Figure 4.18a by the vertical black dashed lines, to indicate

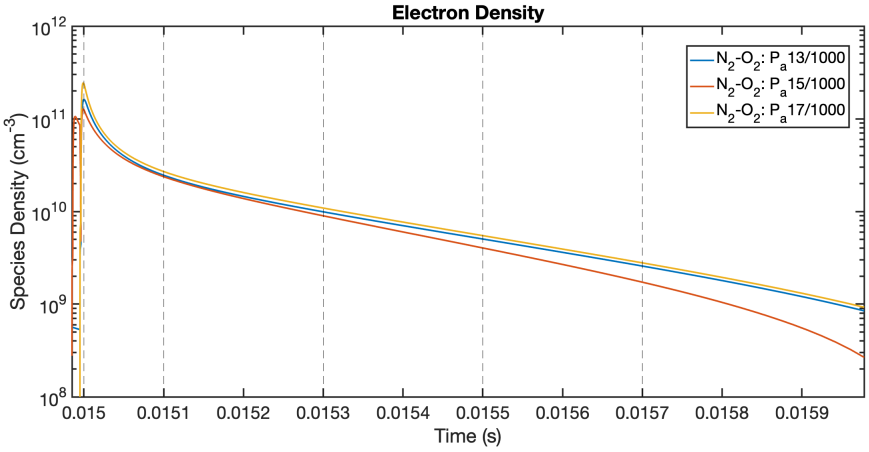

(a) Time points for air VDFs (80% N_2/20% O_2)

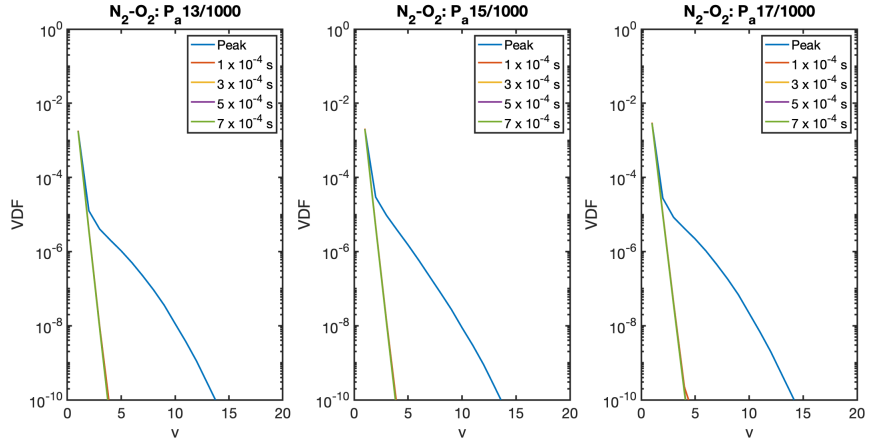

(b) Air VDFs (80% N_2/20% O_2) as a function of power input and time point in the pulse

Figure 4.18: Electron density and vibrational distribution functions in a simulated air plasma as a function of plasma power. VDFs are plotted at the time points specified after taking the 'Peak' to be 0 s, and corresponding to the dashed vertical lines in 4.18a. The pulse at 15 ms was chosen for the analysis as it was after the point at which the simulations reach equilibrium.

the state of the electron density at each point. The time points were chosen as they would have a high enough resolution to see very fast up-pumping (as in the 700 W case in Chapter 3, Figure 3.2), but cover a large enough time scale to see slower up-pumping of high vibrational states, should it occur (such as in the 300 W case in Figure 3.2). Figure 4.18b shows the VDFs at the different time points, as a function of power. What can be seen is a lack of any sort of up-pumping during the afterglow (all the VDFs for time points outside the peak overlie each other), and a poorly populated VDF at the end of the power pulse (blue line). As presented in Chapter 3, the underpopulated VDF at the end of the power pulse, means that there are insufficient vibrationally excited species to allow up-pumping to occur by V-V processes, therefore, no metastables can be produced by Reactions 3.6, 3.10 and 3.11 (Section 3.4.4) to cause ionisation by Penning processes. Thus, no AEP is seen.

4.4.7. Comparison with Nitrogen

In order to determine if this lack of VDF population is due to oxygen species quenching $N_2(X, v)$ species, or whether it is due to the specific plasma parameters, i.e. the power input, the same power inputs were used, but all the oxygen species were removed from the chemistry set. This results in the same chemistry set as was used in Chapter 3, but the power input shape and magnitude is different (in Chapter 3 the power was 100-900 W for a single 0.1 ms pulse). The electron densities from these simulations are shown in Figure 4.19a, and also show a lack of an AEP. VDFs plotted for each of the time points indicated in Figure 4.19a by the vertical dashed lines also show no increasing population of the higher vibrational states, meaning there is no up-pumping occurring. Therefore, this suggests that the specific characteristics of the power input are not appropriate for allowing population of the highly vibrationally excited nitrogen species. The poorly populated VDFs in Figure 4.19a are in contrast to the results in Chapter 3, where the nitrogen VDFs were highly populated. However, in those cases, the power input was a single pulse, in which power was being deposited for a much longer time period (0.1 ms) , rather than being

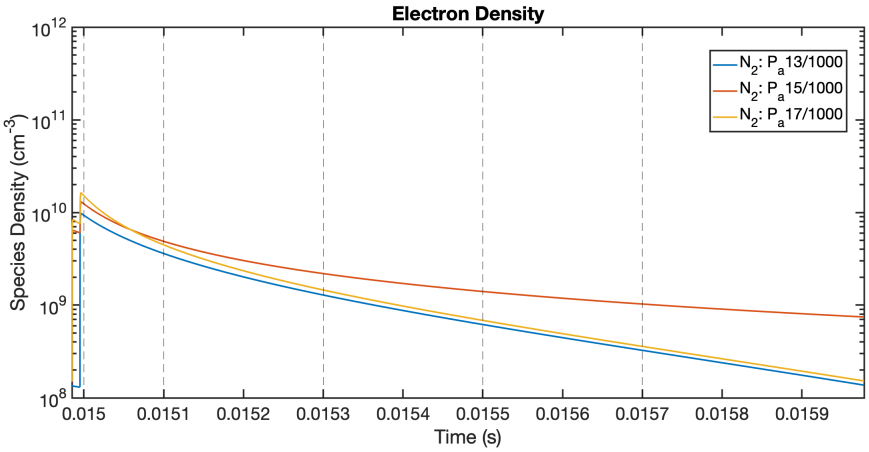

(a) Time points for N_2 VDFs

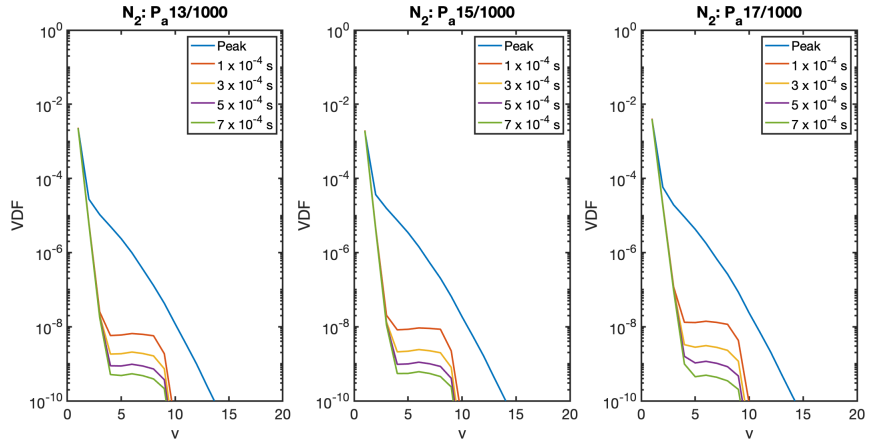

(b) N_2 VDFs as a function of power input and time point in the pulse

Figure 4.19: Electron density and vibrational distribution functions in a simulated nitrogen plasma as a function of plasma power. VDFs are plotted at the time points specified, taking the time of the electron peak as 0, and corresponding to the dashed vertical lines in 4.18a. The pulse at 15 ms was chosen for the analysis as it was after the point at which the simulations reach equilibrium.

two pulses (each approximately 1 μs) corresponding to the rise and fall time of the voltage. This is further evidence for the power dependence of the AEP discussed in Chapter 3.

Comparing the electron densities seen in the air situation (Figure 4.18a) and the N_2 only situation (Figure 4.19a), the maximum electron density in the pulse in air is 10^{11} cm^{-3}, whereas in the pure nitrogen case it is 10^{10} cm^{-3}. This can

be explained by comparing the electron production mechanisms in the different gases in Table 4.3. In air, electrons can be produced from negative ions colliding with neutral species and producing electrons, and this mechanism of associative detachment ($A^- + B \rightarrow AB + e^-$) is one of the major loss processes for negative ions in electronegative plasmas. These processes involve negative ions (O^-, O_2^-, O_3^-) colliding with both ground state O_2 or O_3, or electronically excited O_2, $O_2(a)$ or $O_2(b)$. This is due to the long lifetimes of the electronically excited states of O_2 [107]. However, in pure nitrogen discharges, no negative ions are formed, so this mechanism does not occur.

This is an interesting effect as it suggests that by adding oxygen to nitrogen, the electron density can be increased. However, in a real life situation, there are likely to be impurities in the air, in particular water vapour. In this case it may be that these effects are lost as it is known that O^- and O_2^-, two of the major reactions in the electron producing reactions in air, over time form water clusters and are lost [129]. This competing reaction mechanism would reduce the number of negative ions in the plasma available to produce electrons.

It would be valuable to understand exactly how the addition of oxygen contributes to the electron density seen in the plasma, and this could be done by varying the oxygen/nitrogen ratio. This could provide interesting insight into not only the electron density, but also the resulting effects of changing the electron densities and gas mixtures on other RONS densities.

Table 4.3: Electron production mechanisms in air and nitrogen plasmas. Threshold for analysis was taken to be 10^{15} cm^{-3} s^{-1}.

Air	Nitrogen
$e^- + N_2 \rightarrow N_2^+ + e^- + e^-$	$e^- + N_2 \rightarrow N_2^+ + e^- + e^-$
$e^- + O_2 \rightarrow O_2^+ + e^- + e^-$	
$e^- + O_2 \rightarrow O + O^+ + e^- + e^-$	
$O^- + O \rightarrow O_2 + e^-$	
$O^- + O_2 \rightarrow O_3 + e^-$	
$O^- + O_2(a) \rightarrow O_3 + e^-$	
$O^- + O_3 \rightarrow O_2 + O_2 + e^-$	
$O_2^- + O \rightarrow O_3 + e^-$	
$O_2^- + O_2(a) \rightarrow O_2 + O_2 + e^-$	
$O_2^- + O_2(b) \rightarrow O_2 + O_2 + e^-$	
$O_3^- + O_3 \rightarrow O_2 + O_2 + O_2 + e^-$	

4.5. Discussion

Low temperature air plasmas are gaining interest in the field of plasma medicine, due to their efficient production of a wide range of RONS, and their ability to make use of ambient air as a feed gas. RONS produced include those of particular biological importance, such as nitric oxide, ozone, singlet delta oxygen, superoxide and hydrogen peroxide, which are known to have physiological importance in the body under normal conditions [49, 52, 65, 171, 182]. The use of ambient air for biomedical plasmas is also attractive as it reduces the need for complex infrastructure and costs that are related to the use of expensive bottled gases. This could open up opportunities for using air LTPs across the globe in both developed and developing countries, where conditions such as chronic wounds cause a large problem [193].

However, whilst it is believed that plasma-produced RONS can have therapeutic benefit in a wide range of medical conditions [46], the individual contribution of different RONS to specific biological outcomes is not well understood. In order to investigate this, it is necessary to be able to fully understand the RONS composition being applied to a biological target during plasma treat-

ment. Using this knowledge, and by altering the composition in a known way, it is then hoped that species densities delivered could be correlated with any biological outcomes seen. This would require the ability to control RONS composition, ideally with independent control of individual species. Here, a chemistry set for dry air has been developed to use with global models, in particular GlobalKin, to investigate the time evolution of species densities in the plasma, as well as helping to understand the chemical kinetics occurring therein.

Firstly, as discussed above, the benchmarking of the air chemistry model is crucial to ensure that the model is representative of the true physical situation. Initial benchmarking is shown above, and would benefit in the future from more in-depth diagnostics both of the chemical and electrical properties of the plasmas. However, the qualitative agreement shown in Figure 4.12 is good and allows the use of the model for determining important reaction mechanisms driving the production and destruction of NO and O_3.

The work here begins to highlight the intricacies of chemical kinetics occurring in plasmas, and in particular, the interlinked nature of different species. For example, it is suggested above that there is a cycling process for NO (Group 3 reactions), whereby there are reactions producing and destroying NO at a very similar rate, resulting in no net increase in NO, but the absolute rate will depend on the density of NO. However, these reactions do serve to consume N, and produce O. This can then lead to promoting the production of O_3 by 3-body processes, of which most will be controlled by the O density. This serves to show how the densities of NO and O_3 are strongly connected, and highlights how independent control of individual species will be challenging.

With the particular case of NO and O_3, where NO is known to be a useful species in the body, and O_3 is thought to be more toxic, independent control of these two species would be useful. Therefore, it is useful to consider NO production mechanisms in different situations. In particular, in more thermal plasmas, it is thought that the Zeldovich reaction, producing NO from vibrationally excited N_2 is very important ($N_2(X, v \geq 13) + O \rightarrow NO + N$). In the

conditions described in this work, this reaction has a very small contribution, and involves only $N_2(X, v = 13 - 14)$, due to the VDF being very poorly populated throughout the simulation time. However, if it became possible to increase the population of the VDF, potentially by altering power input mechanisms such as frequency or waveform, the contribution of the Zeldovich reaction could be increased. By increasing this reaction, the densities of NO could potentially be increased, without increasing atomic oxygen density and subsequent O_3. Interestingly, in Gentile and Kushner [170], the control of an air plasma to remove NO as efficiently as possible was investigated, and parameters such as power and frequency were altered to find optimum conditions where NO was removed, but O_3 was not excessively produced. The work in [170] shows the importance of using modelling tools to help guide plasma operation.

Altering the power input to control the plasma components has been used in the past, in particular by varying the shape of the voltage waveform to control electron and ion fluxes to surfaces. This approach of tailoring waveforms allows the control of electron densities and ion bombardment for plasmas used in technology [194, 195], but the effects on RONS densities has not been investigated. Considering the different responses of different RONS in Figure 4.14 to the powered and non-powered regions, different species may be affected differently by changing the shape of the input pulse, and may add an element of differential control to different species. Therefore it would be interesting to determine whether a similar approach could be used to control the chemical kinetics in the plasma.

Many studies involving the plasma treatment of biological targets vary treatment time as the main investigation (for example [89, 90, 196]) which would just increase the flux of species to a target indiscriminately. Whilst this is an interesting measure of the plasma treatment as a whole, it does not allow identification of contributions from specific RONS. Schmidt et al. [197] have attempted correlations between species densities and biological outcomes using the kINPen with shielding gas flows of nitrogen or oxygen. However, this study used only indirect treatment of skin cells (where the culture medium is treated

and then applied to the cells), and the measured species were the liquid species resulting from treatment such as nitrate and nitrite. Whilst the understanding of the liquid composition is also important for treatments where liquids are involved, the initial understanding of the plasma RONS composition as described in this present work is still crucial.

To understand the actions of specific RONS in inducing biological actions, it would be preferable to be able to change species densities independently. This would provide information about the actions of specific RONS that would be valuable not just to the field of plasma medicine, but to the field of Redox biology as a whole.

4.6. Future Outlook and Application

Using a novel synthetic air chemical reaction scheme, the production and destruction mechanisms for specific RONS that have biomedical interest have been investigated. Specific reactions, or groups of reactions have been highlighted that have particular importance for the production and destruction of ozone and nitric oxide - both of which have far-reaching consequences in a biological setting. This work has shown how benchmarked global plasma chemistry models can provide valuable insights, not only into plasma-produced species densities, but also the dominant mechanisms for species production and destruction. Further to this, it has shown how these production and destruction mechanisms for different species of biomedical interest in synthetic air plasmas are strongly connected and provide a challenge to achieving independent control of different plasma-produced species. However, this still remains an important area of study, and the global modelling data and pathways analysis methods presents a useful tool for investigating the chemical kinetics and, with further benchmarking, the model could be used to guide the study of how input parameters could be changed to alter RONS compositions specifically.

Future efforts should be to first build on the experimental data for model benchmarking, paying particular attention to plasma diagnostics on the plasma bulk,

using methods such as absorption spectroscopy for molecular species, and Picosecond TALIF for atomic species. Using a fully benchmarked model will then be valuable for determining specific RONS compositions of plasma treatments applied to biological targets. In the context of wound healing, this would be cells such as keratinocytes, fibroblasts and immune cells, and the model data may be able to show how different cell types have different tolerances and responses to different RONS compositions that are applied to them. This would allow the process of plasma treatment design for wound healing applications, based on specific effects of specific components, rather than the composition as a whole.

Results III - Towards Correlation of Plasma Species Densities and Skin Cell Viability

5.1. Motivation

As discussed in Chapter 1, RONS play a vital part of normal cellular functioning, though their production and actions have to be highly regulated to prevent RONS mediated damage. The aim for LTP treatments for biomedical applications is to deliver high quantities of RONS which can act to mimic the functions of endogenous RONS, and enhance cell signalling mechanisms and activate specific pathways, or to selectively kill invading pathogens and cancerous cells [198]. However, to date, little research has been carried out to establish an understanding of how specific types and quantities of specific RONS equate to specific biological outcomes. This understanding is vital for the development of biomedical treatments, particularly when the aim is to be able to tailor LTP treatments to elicit specific biological effects.

In the past, research has been carried out to identify safety limits for other plasma characteristics, such as UV emission and temperatures [92]. However, this information is not available for RONS, and equally, there is no information available describing the relationship between RONS type and quantity de-

livered, and the cellular effects induced. Using the plasma RONS quantification techniques described in the previous chapters, as well as future experimental plasma diagnostics, the aim is to be able to correlate the species densities delivered to biological tissues with the biological effects observed.

To understand this relationship in the context of wound healing applications, a protocol is required where effects of LTP treatment can be monitored in skin cells for a time period following the treatment. Of particular interest is the basic effect of LTP treatment on skin cell viability, which can be monitored by assessing some of the functions which characterise healthy eukaryotic cells. These range from very non-specific activities, such as active proliferation and metabolism, through to more cell-specific traits, such as morphology and gene expression profile. Depending on the level of damage cells are subjected to, they can either i) undergo cell-cycle arrest, where they pause proliferation to allow time to repair damage using pathways such as the DNA damage response, ii) enter a long term non-replicative state known as scenescence, where they remain viable, but alter their gene expression, morphology and adhesion properties, or iii) if the damage is too great, they can die either by apoptosis or necrosis [199, 200].

In this study, the cells to be used are HaCaT cells, which are a keratinocyte cell line, first isolated and described by Boukamp et al. [201], which have a phenotype of the proliferating basal keratinocytes in the lower levels of the epidermis [202]. It is common practice to use a cell line (cells immortalised for laboratory use, derived originally from a donor) rather than primary cells (cells derived from donors) for initial studies such as these, as cell lines are more robust, cheaper, and less variable between passage numbers [203]. Futhermore, the use of human primary keratinocytes for *in vitro* skin cell studies is complicated by high donor-to-donor variability and high correlation between passage number and experimental outcome [202]. However, cell lines can also be considered to be less biologically relevant, as they are more removed from the true biological situation that would be in a human body, due to the cell practices required to immortalise them, and due to prolonged culture in laboratory conditions.

The methods discussed in this work will use HaCaT cells but will also be applicable for primary cells which should be used for subsequent future studies beyond this work.

5.2. Aims

The aims of this work are to investigate the methods of monitoring cellular health/viability after plasma treatment, at the population level. This can be done both qualitatively and quantitatively, and the mechanisms will be explored in the following sections. Generally, studies into the interactions of plasmas with biological targets involve liquids, either with the cells being treated directly in some form of media, or treating media which is then applied to cells. However, for this present study, of particular interest is the effects of treating HaCaT cells without a liquid layer. The reason for this is twofold. Firstly, treating the cells directly with plasma, without a layer of liquid between the plasma bulk and the cells results in a simpler environment with no intermediate species produced by the plasma-liquid interactions. This allows for more detailed characterisation of the whole RONS environment in contact with the biological target. Secondly, if plasmas are to be used on wounds, then they are likely to interact with surrounding healthy cells which may not be covered in any sort of liquid or wound exudate, therefore, understanding the effects of dry treatment is crucial for ensuring safe patient treatments.

Specifically, the aims are to:

1. Determine a method for investigating the macroscopic, static, population effects of plasma treatment

2. Develop a protocol for plasma treatment of skin cells which allows quantifiable monitoring of cell viability/health over time, that can be correlated with concentrations of species delivered by the plasma.

The long term goal is to have a robust protocol to use alongside the quantification of delivered plasma RONS, to help build up a picture of how specific

plasma RONS compositions can influence skin cell populations. This will help to inform the design of specific plasma treatments for wound healing applications in the future.

5.3. Methods

5.3.1. Cells and Cell Culture Methods

The immortalised keratinocyte HaCaT cell line, described in [201], was obtained from Caltag Medsystems, UK. HaCaTs were maintained in high glucose (4.5 g/L) Dulbecco's Modified Eagle Medium (ThermoFisher) supplemented with 10% Foetal Calf Serum (FCS), in a 37 °C, 5% CO_2 incubator. Passaging was performed at $\approx$ 60-70% confluency, using 0.25% trypsin-EDTA solution (Sigma), after PBS washing. For use in experiments, cells were counted using a haemocytometer, and plated in 24 well tissue-culture plates (Corning, Part number 3526), with 1 mL of culture medium.

5.3.2. Low Temperature Air Plasma Treatments

An air DBD described in Chapter 4 Section 4.3.1, Figure 4.3, and [40] was used for LTP treatments. The diameter of the electrode is 10 mm, and the diameter of wells in a 24 well tissue-culture plate is 15.6 mm, therefore, treatments were performed with the electrode inside the well, at a constant distance from the cells ($\approx$ 2 mm).

For treatments, cells had to be transported on a ten minute walk outside between departments. For transfer either side of the treatments, plates were parafilmed and placed in a polystyrene box alongside 15 mL Falcon tubes filled with warm water, to minimise the effects of a lower ambient temperature. Once travelled, the plates were put in the 37 °C, 5% CO_2 incubator to equilibrate before treatments or further processing of the plate.

Prior to treatments, cell culture medium was removed from treatment wells and

Table 5.1: Crystal Violet Stain Preparation for a 20 mL Staining Volume

Substance	Amount
Crystal Violet	0.01 g
Formaldehyde (10%)	2 mL
1X PBS	2 mL
Methanol (1%)	200 μL
Distilled Water	15.8 mL

appropriate controls, and either replaced with 250 μL of phosphate buffered saline (PBS), or left dry. The ignited plasma was then in direct contact with the cells (no liquid layer above cells) in the dry treatment situation, or in contact with the PBS layer in the wet situations. During treatments, all wells not being treated were parafilmed to prevent plasma species from entering non-target wells. Immediately after treatment, 1 mL of fresh media was replaced in each of the wells, and the plate was returned to the incubator.

5.3.3. Crystal Violet Staining

Crystal violet staining was performed using a 0.05% w/v crystal violet (Sigma) solution as shown in Table 5.1. 380 μL of staining solution was added to each well of a 24 well plate and left at room temperature for 20 minutes. Stain was removed using a pasteur pipette and discarded, then residual stain was washed off by dipping the plate in a container of water 5 times, with the tap continuing to run. Plates were air dried for 24 hours then imaged using a scanner (Epson Perfection V750 Pro) connected to a computer.

For the time course information from the crystal violet, the protocol in [204] was used. Briefly, stained plates were air dried for at least 24 hours, then the crystal violet was solubilised using 500 μL/well of methanol. Plates were rocked at 20 oscillations/minute for at least 20 minutes, then the optical density at 570 nm (OD_{570}) was measured using a BMG ClarioStar plate reader. Results were analysed using Microsoft Excel.

5.3.4. RealTime-Glo Assays

RealTime-Glo MT Cell Viability Assay (Promega) was used to determine the real-time cell viability up to approximately 70 hours after LTP treatment. The reagents was prepared as stated in the product protocol.

For RealTime-Glo experiments, 400 μL/well of 1X reagent was prepared in complete culture medium. The reagent was filtered using a 0.2 μm filter to ensure sterility. Cells were treated as described above, then immediately after treatment, the 400 μL of filtered RealTime-Glo 1X reagent was added to the wells (instead of the 1 mL of culture medium). Plates were kept in the incubator.

Luminescence readings of the RealTime-Glo signal were taken at regular intervals post-plasma treatment using a BMG Clariostar plate reader, with the temperature control set to 37 °C. Measurements were taken using an integration time of 0.5 s, and a 6 x 6 matrix scan was performed meaning that 36 readings were taken in each well. Plates were kept in the 37 °C, 5% CO_2 incubator between readings, as the RealTime-Glo reagent is sensitive to changes in temperature. Data was analysed using Microsoft Excel.

5.3.5. Treatment Temperature Measurement

Temperature of treated PBS in a 24 well plate was determined using a thermocouple (Tenma 72-7715 Thermometer) immersed in the liquid. The temperature was measured before and after a two minute plasma treatment and the temperature difference determined.

5.4. Results

5.4.1. Post-Treatment HaCaT Population Effects can be seen Using Crystal Violet Staining

Following plasma treatment, the macroscopic effects of plasma treatment on the whole cell population in a well can be visualised using crystal violet staining. If adherent cells, such as the HaCaT cells used here, become damaged, they can

detach from the plastic surface, and therefore, be lost from the population in the well. Crystal violet is a substance which stains the DNA and proteins present inside cells [204], meaning that overall population structure after treatment can be visualised, and any areas where cells have detached can be seen, indicating regions where damage may be most concentrated.

Figure 5.1 shows a representative plasma treated (Figure 5.1a) and control (Figure 5.1b) wells, containing HaCaT cells stained purple with crystal violet. The control well shows a consistent coverage of HaCaT cells, whereas the plasma treated well shows distinct areas where there are no cells, suggesting that the plasma treatment has resulted in the detachment of the cells in those areas. However, the reason for detachment cannot be determined by these methods, and the overall cell health in the population cannot be determined, as this is a static qualitative measure of the cell population.

Crystal violet is a useful way of determining which plasma treatments can be potentially damaging, because damaged cells are no longer able to adhere to the plastic plate [204]. For example, if large areas of wells are cleared of cells by the plasma treatment, this indicates high levels of plasma-induced damage, and would have two major implications for downstream cell analysis after the particular treatment. Firstly, the remaining population of cells to assay is greatly reduced, therefore, the applicability of any results may be reduced as the smaller population of surviving cells may not be representative of the initial whole population. Secondly, if there was a way of collecting the non-adhered cells then they could be assayed, however, then the spatial information would be lost. Therefore, with this in mind, this technique may allow the choice of a plasma treatment which does not result in the loss of adherence of the majority of the cell population, in a quick and easy way, without wasting expensive reagents. However, while this method has its uses, it does not allow the quantification of damage to the cell population, and as such, would not allow for the correlation of species densities delivered by plasma, to the viability of cells post-treatment.

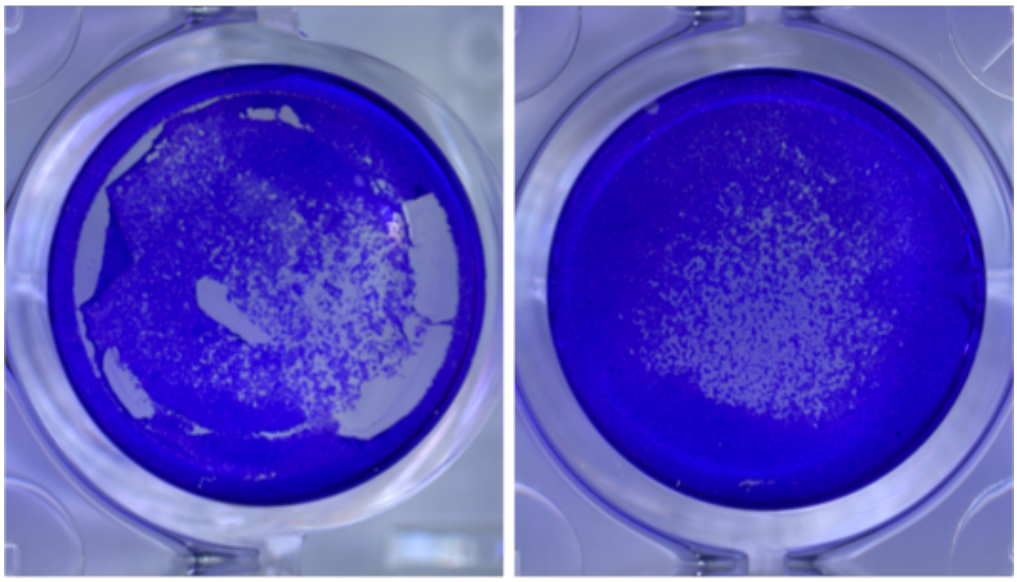

(a) Plasma Treated (b) Untreated Control

Figure 5.1: Representative image of the population effects of HaCaT cells treated with 1 minute plasma at 16 kV (5.1a) compared to untreated control (5.1b) HaCaT cells. Cells were plated at 2×10^5 cells/well the evening prior to treatment, then incubated overnight in a 37 °C, 5% CO_2 incubator. Staining with crystal violet was performed the same day as the plasma treatment.

5.4.2. Growth Curves Can be Obtained from Crystal Violet Stained Cells Post-Treatment

For a more dynamic, quantifiable measurement of the cell health, the crystal violet stain can be solubilised after drying, and the optical density determined. Since the amount of crystal violet is proportional to the cell mass present in the well, an increase in optical density of crystal violet is associated with cell proliferation. This method allows the determination of the relative number of cells in the control wells compared to the plasma treated wells. Using this technique, the growth rates of control and plasma treated wells was compared, by treating cells in triplicate 24 well plates. This gave three identical plates which could be crystal violet stained and the OD_{570} measured for the day of treatment, 1 day post treatment and 2 days post treatment. The use of an end-point assay on multiple occasions gives a time course assay.

Immediately before cell treatment, the culture media is removed from the treat-

ment cell groups, and then fresh media is replaced after treatment. This is to keep the treatment environment as simple as possible, removing any influence from the plasma species interacting with species present in the culture medium. To ensure that this period without media or any liquid was not detrimental to the cells, 'dry controls' were included. The media was also removed from these wells, so that the populations in the 'dry control' wells could be compared to the true untreated controls which remained in culture media for the whole time period of the experiment. Again, fresh media was replaced in the 'dry control' wells after the time period of the experiment.

Figure 5.2 shows the results of this time course experiment, when the treatment was 1 minute, at 16 kV. Cells were plated on day 0, with treatments being carried out on day 1. Plates were stained on day 1 (same day as treatment), day 2 and day 3. What can be seen from these data is that the 'dry controls' and the true untreated controls are very similar, and show that the period of dry does not harm the cells growth for at least 2 days post treatment (3 days post cell seeding). However, it can be clearly seen that the plasma treated wells do not grow as effectively, with less proliferation between day 1 and 2 compared to the controls. Further to this, they appear to stop growing from day 2, with no increase in OD_{570} on day 3. This suggests that the growth of cells is being stopped by the plasma treatment, but is not causing detachment of the cells from the plastic surface of the well.

This method of using a time course of crystal violet staining does begin to give a quantitative biological outcome associated with cell viability. However, it does not give any sort of information on the cell status. For example, it is not possible to tell whether the remaining cells are adhered due to being healthy, or whether they are there due to excessive adhesion often seen with cells in a scenescent state [200, 205]. Also, as with the single end-point crystal violet staining described above, unless the lost cells are collected and assayed, there is no way of knowing whether they are dead, or just detached temporarily then lost during media changing or staining processes.

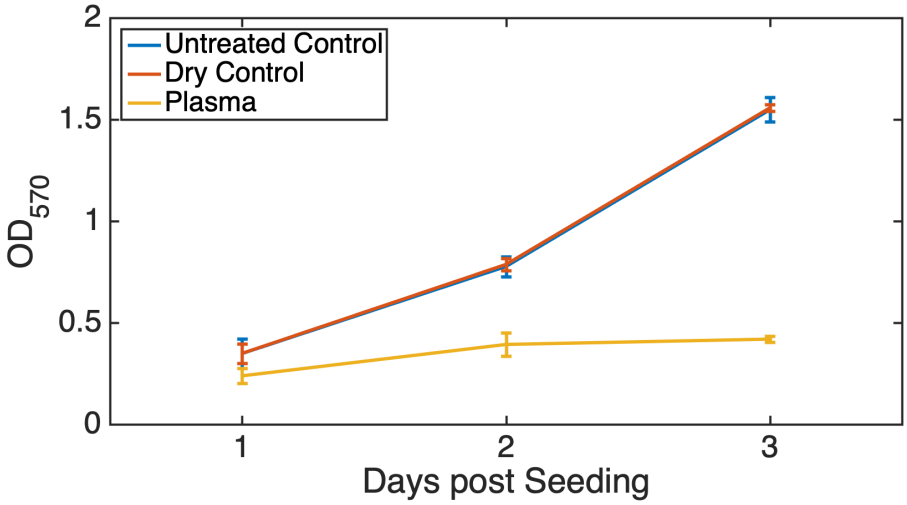

Figure 5.2: Cell growth curve using crystal violet staining. Multiple plates were plated identically at 5×10^4 cells per well on day 0, and treated identically on day 1. One plate was stained on day 1, one on day 2 and one on day 3. Each plate was allowed to air dry overnight, then the crystal violet was solubilised using methanol, and the OD_{570} was measured. Average OD_{570} is plotted, and error bars show the standard deviation across the triplicate wells.

There are also other major issues with this protocol, in terms of places where errors can be introduced. Firstly, the time course analysis relies on the cells and treatments being identical across duplicate plates, and also means that the number of time points that measurements can be taken depends purely on the number of plates prepared prior to the treatment. Secondly, the OD_{570} density of the crystal violet depends on how long the plates have been air dried, as if they are still damp, then the stain will be diluted and the OD_{570} lowered. If they are too dry, the methanol is unable to solubilise all of the crystal violet that is present, therefore, artificially lowering the OD_{570}. Finally, the OD_{570} is also highly dependent on the quality and consistency of the washing steps during the initial staining, as any stain that just sticks to the sides of the wells non-specifically, may also be solubilised, artificially increasing the OD_{570}.

In order to circumvent these problems, of lack of information on cell status, and reliance on multiple identical plates, RealTime-Glo MT Cell Viability Assay (Promega) was investigated to determine whether this would allow better post-

treatment monitoring.

5.4.3. Post-Treatment Viability Monitoring using RealTime-Glo MT Viability Assay

The RealTime-Glo MT Cell Viability Assay is a two part assay which determines cellular viability by making use of the reducing potential of cells [206]. Firstly, there is a pro-substrate which, when cells are healthy and have normal reducing potential, is reduced by the tested cells. This pro-substrate reduces to a substrate for the second reagent, a luciferase. The luciferase uses the substrate to produce a luminescent signal [207]. This results in an assay that produces a luminescence signal in the presence of viable cells, and the strength of the signal is proportional to the number of viable cells.

The RealTime-Glo Assay can be used over a number of days to assess longer term cell viability in response to drugs, chemicals or other substances [206]. Therefore, it should provide useful information on cells following plasma treatment.

5.4.4. Determination of Optimum Cell Seeding Densities for RealTime-Glo Assay

Since the luminescent signal produced by the RealTime-Glo assay is dependent on the viability substrate, and the viability substrate is used up by viable cells, the length of time that the signal can be measured for is dependent on the number of viable cells in culture. The more viable cells present, the quicker the substrate gets used up. Once the substrate has been used up, there can be no more luminescent signal produced.

To determine the best cell seeding density, based on the length of time a meaningful luminescence signal can be produced, a cell seeding density variation was performed. Cells were plated into 24-well plates at 0 hours, with the RealTime-Glo reagents, then incubated at 37 °C for an hour, before taking the first luminescence reading at time = 1 hour. Figure 5.3 shows the results of this variation for low cell seeding densities of 1×10^4 and 5×10^4 cells per well (Figure 5.3a) and high seeding densities of 1×10^5 and 2×10^5 cells per well (Figure 5.3b).

For the case of the 2×10^5 cells per well, it can be seen that the luminescence signal is continually decreasing for all measurement time points after seeding. For 1×10^5 cells per well, the signal initially rises slightly, however, only until $\approx$ 6 hours, before decaying, due to the reagent being used up by the viable cells. When considering using this reagent following plasma treatments of cells, it is important to note that sufficient time is required between cell plating and plasma treatment to allow the cells to fully adhere to the plate. As this adherence process takes a number of hours in itself, neither of the high seeding densities would be suitable for monitoring with RealTime Glo after plasma treatment, as the signal would be lost far too early. Thus, this would mean that for seeding densities of $\geq 1 \times 10^5$ cells per well, would not allow viability monitoring after plasma treatment for any meaningful length of time.

For the lower densities, the time scales for measuring are more useful. At 5×10^4 cells per well, the timescale for measuring is between 20-30 hours, however, the 1×10^4 cells per well situation is the most promising, showing the ability to measure the cell densities to over 60 hours post cell plating.

When treating cells with plasma, it is preferable to have as simple a system as possible, so that only the plasma is influencing cellular responses and there are minimal influences from the surrounding environment. Practically, this means either just treating cells adhered to a plate, or having cells with a thin layer of liquid above them. In either the wet or dry case, this requirement means that cells must be plated in media, then left to adhere to the well plate long enough that the culture medium can be removed without disrupting the cell layer. For this, cells are plated on the evening prior to plasma treatment, and incubated at 37 °C, 5% CO_2 overnight. Then, immediately prior to treatment, culture medium is removed, and cells are treated, either dry, or with a thin layer of PBS covering them. Immediately after treatment, culture medium containing the RealTime-Glo reagent is replaced, and the plate incubated for an hour before the first measurement can be taken. In terms of the RealTime-Glo reagents, this means that the first measurement point is actually many hours ($\approx$ 16 hours) after cell plating. Therefore, the RealTime-Glo reagent would need to be able

to still produce a good signal beyond the 16 hour time point. The only seeding density tested which fulfils this requirement is 1×10^4 cells per well.

5.4.5. Plasma Treatment is Detrimental to HaCaT Cell Growth

Using the predetermined 1×10^4 cells per well seeding density, cells were treated using two different plasma treatments and compared to control, untreated wells. Cells were treated for 45 s, at either 13 kV or 17 kV. Culture medium was removed prior to treatment as described previously, and then after treatment, media containing RealTime Glo was replaced into the wells. Plate readings for luminescence commenced $\approx$ 1 hour after the last treatment, after incubation in the 37 °C, 5% CO_2 incubator. Each treatment and control was done in triplicate, and the error bars show standard deviation across the triplicates.

Figure 5.4 shows the resulting luminescent signals for both treatment groups, and the untreated controls. It can be seen that the growth of the untreated controls is continuous from the first plate read, right through to almost 60 hours post-treatment. At this point it appears that the RealTime Glo substrate is being used up, and depleted. This is in keeping with what is seen in the cell seeding density curves in Figure 5.3. In comparison, the plasma treated cells show a much reduced growth rate between $\approx$ 0 - 25 hours compared to controls, and then the signal appears to flatten off. There does not appear to be any increase in signal for the treated cells beyond this point, suggesting that a small number of cells may be viable, but not proliferating, indicating the possibility of them entering a scenescent state following treatment. The signal also does not appear to particularly decrease from this point either, consistent with the idea that some cells may remain viable (the signal remains greater than that seen for the controls at 120 hours when the luminescent signal has vanished due to substrate depletion). To fully investigate this, it is important to include a true negative control of a population of true nonviable cells, to compare the signals in any future experiments.

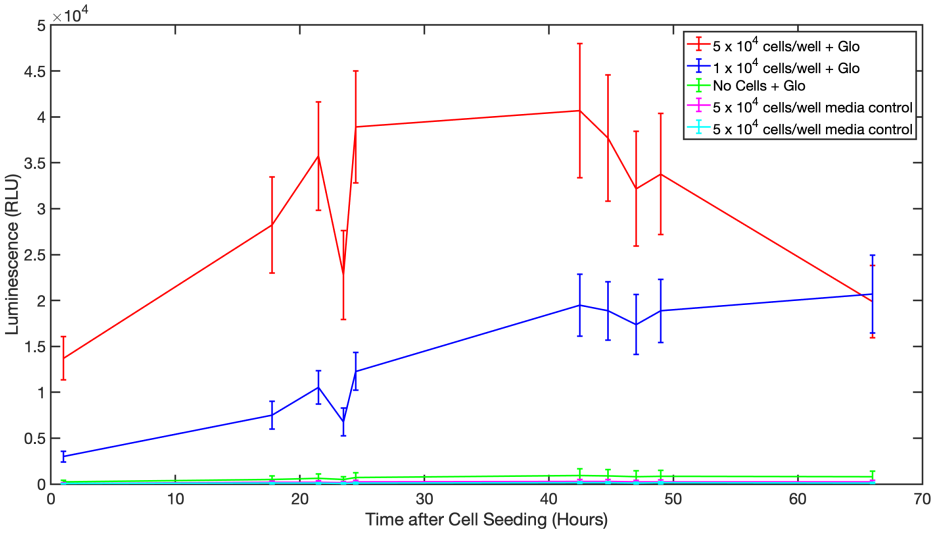

(a) Low Cell Densities

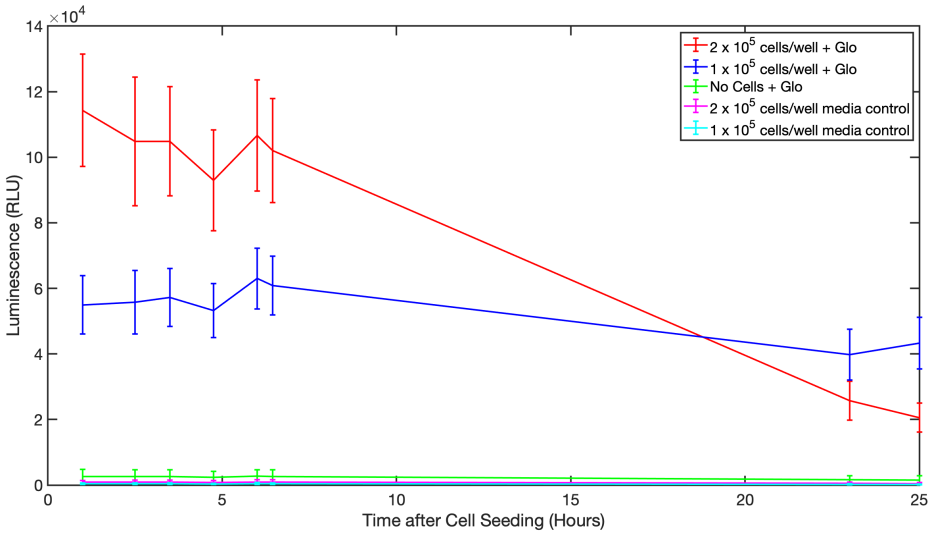

(b) High Cell Densities

Figure 5.3: Viability of cells as a function of time for different cell seeding densities. The luminescence signal is a marker of viability. Error bars show standard deviation from the triplicate wells. Media controls shown in the legend are for cells plated only in media, with no RealTime Glo reagent added, to indicate background luminescence from cells and media. No cells + Glo control gives the background luminescence from the RealTime Glo reagent alone. Cells were counted and adjusted to the correct concentration then plated in 24 well plates using media containing RealTime Glo (or just media for appropriate controls), then incubated for 1 hour in 37 °C, 5 % CO_2 incubator, before the first reading 1 hour later.

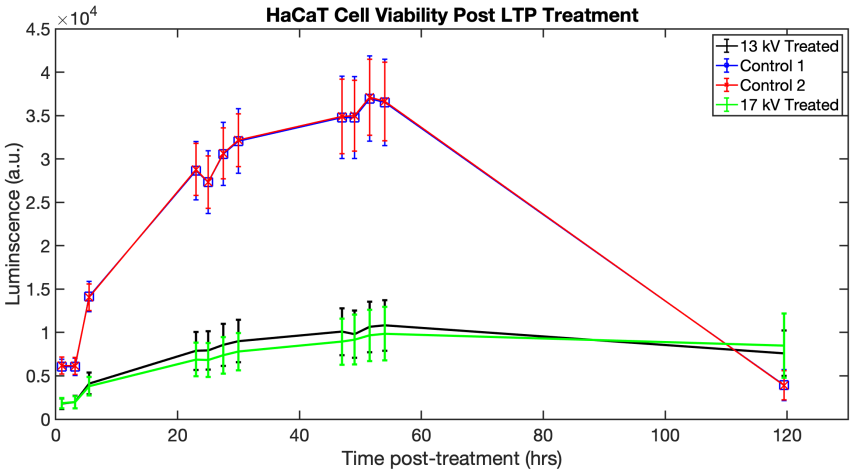

Figure 5.4: Realtime HaCaT cell viability monitoring after plasma treatment. An increase in luminescence is caused by an increase in number of viable cells. Cells were plated at 1×10^4 cells/well, and incubated overnight in a 37 °C, 5% CO_2 incubator, then treatments were performed in triplicate. The treatment time corresponds to time = 0 hours in the figure. Average luminescence of the triplicates is plotted, with error bars showing the standard deviation. Control 1 and control 2 are untreated controls.

It is important to note the different time points shown in Figure 5.3 and Figure 5.4, as they start at the cell plating time point, and the treatment time point respectively. Therefore, Figure 5.4 effectively starts at T = 14 hours after seeding in Figure 5.3, and would therefore, show luminescent signal still at over 60 hours post seeding. However, this is due to the fact that for the experiment, the RealTime Glo is only added after cell treatment, therefore, isn't being used up by viable cells in the initial time period between cell plating and plasma treatment. Further investigations would be needed to determine at what point the RealTime Glo signal saturates in the control cells. However, for the purpose of this experiment, it is clear that the plasma treated cells have a decreased growth rate in comparison to the untreated controls, independent of the treatment applied. Therefore, this experiment suggests that plasma treatment significantly hinders growth of HaCaT cells.

5.4.6. HaCaT Population Damage is Independent of Treatment Time

Overall, the outcome of this experiment suggests that plasma treatment significantly hinders growth of HaCaT cells. Therefore, it was hypothesised that the treatment time might be too long, and causing excessive damage to the cells, meaning that they cannot begin proliferating again. As a quick test, a treatment time variation was performed, from 5 to 45 seconds, at 15 kV (halfway between the two treatments chosen for Figure 5.4), and the cells were stained with crystal violet. The maximum of 45 seconds was chosen as this was the treatment time for the RealTime Glo investigation, which already showed significant growth reduction. A higher cell seeding density of 1×10^5 cells per well was chosen to make analysis of the crystal violet staining easier. Representative wells for each treatment time and the untreated control are shown in Figure 5.5. Interestingly, all of the treatment times show a significant reduction in cell population areas in comparison to control. The 5 second treatment well has greater coverage that the other treatment wells, but still shows an obvious reduction. In fact, for 15-45 second treatment wells appear largely independent of the treatment time.

Also of interest is the patterning of the cells in the wells. On close inspection, small rings of clear areas can be seen in the treatment wells, particularly for 25 - 45 seconds of treatment (Figure 5.5, red arrows). This ring appears to correspond to the shape of the plasma electrode, therefore suggesting that there may be some physical effects induced by the plasma, simply by turning it on. This could imply that potentially the strong electric field produced between the electrode and the ground plate below the well-plate is influencing the cell population, and potentially resulting in membrane permeabilisation and death of the cells in the immediate vicinity. This process has been discussed before in the context of bacterial killing by plasmas [208], therefore, with sufficient electric field, a similar process could be occurring in eukaryotic cells. On the other hand, it may be that the concentrations of RONS that are produced inside the plasma bulk, directly in contact with the cells causes rapid, excessive oxidative stress.

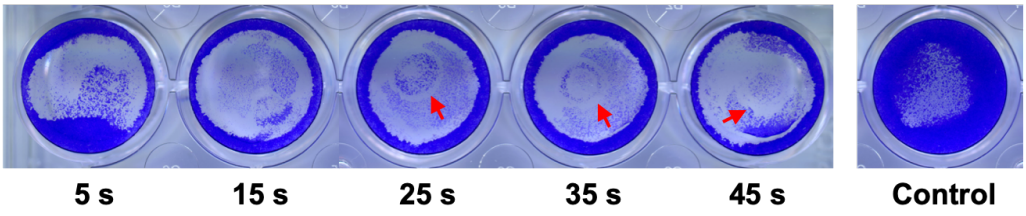

Figure 5.5: HaCat population effects of 15 kV plasma treatment as a function of treatment time. Treatments of each length were done in triplicate and a representative treated HaCaT population stained with crystal violet is shown, with the treatment time denoted below. The red arrows show the ring-like clear areas in the populations after treatment (see text). A representative untreated control well is also shown. Cells were seeded at 1×10^5 cells/well.

5.4.7. A Liquid Layer Protects HaCaT cells from Plasma-Induced Population Damage

Due to the data showing a disruption to HaCaT growth following plasma treatment, independent of treatment time, it was hypothesised that a liquid layer is required to protect the cells from harsh electric fields, ions and RONS in the plasma bulk in direct contact with the cell layer. Therefore, to test this hypothesis, prior to cell treatment, culture medium was removed from the cells and replaced with 250 μL of PBS, treated, then the PBS was removed and replaced with fresh culture medium. PBS was chosen as it is optimal to use as minimal a liquid as possible to prevent interactions between plasma species and the rich molecules present in liquids such as cell culture media [209]. The treatments varied in length, and the plates were stained with crystal violet after treatment.

The results of this treatment time variation are shown in Figure 5.6, and show that, unlike in the dry scenario, there are very little effects between the treated and untreated cells. This supports the idea that the liquid provides a protective layer to the cells, either by i) decreasing the electric field that is incident on them, ii) shielding them from excessive concentrations of RONS produced by the plasma bulk or iii) slowing down the time it takes for plasma-induced species to reach the cells as they have to negotiate the liquid barrier and form ions and new species that have to diffuse to the cell layer. This is also in agreement with what was found by Balzer et al. [196], who found that skin fibroblasts

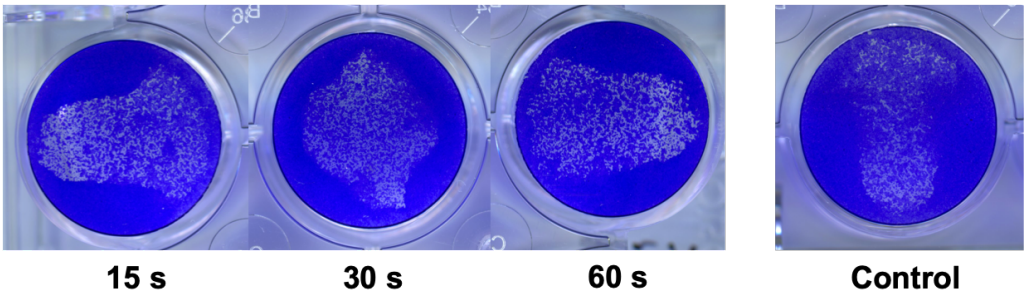

Figure 5.6: Effects of treatment time variation on HaCaT cells treated in 250 μL of PBS. Treatments of each length were done in triplicate and a representative treated HaCaT population stained with crystal violet is shown, with the treatment time denoted below. A representative untreated control well is also shown. Cells seeded at 1×10^5 cells per well.

require a liquid layer to survive.

5.4.8. PBS Temperature After Treatment

When using a liquid layer, it is important to determine any temperature changes in the liquid that have been induced by the plasma treatment. If the liquid were to heat too much, it could be detrimental to the cells, purely from a thermal perspective, therefore, any effects seen after plasma treatment could not be purely attributed to the plasma-produced species.

To check that the temperature of the PBS does not rise too much to cause thermal damage to the HaCaT cells, the temperature was measured after two minute treatments, at different applied voltages. The temperature of the PBS before treatment was measured to be $\approx$ 20 °C, then the temperature was measured immediately after a 2 minute treatment, at the stated voltage, using a thermocouple.

Figure 5.7 shows the results of this experiment. As expected, the higher the plasma voltage, the greater the increase in PBS temperature after 2 minutes of treatment. However, the maximum temperature increase is $\approx$ 2.2 °C, which, when starting at room temperature, should not have a big effect on the cells. The temperature does not become too high to become damaging to cell growth

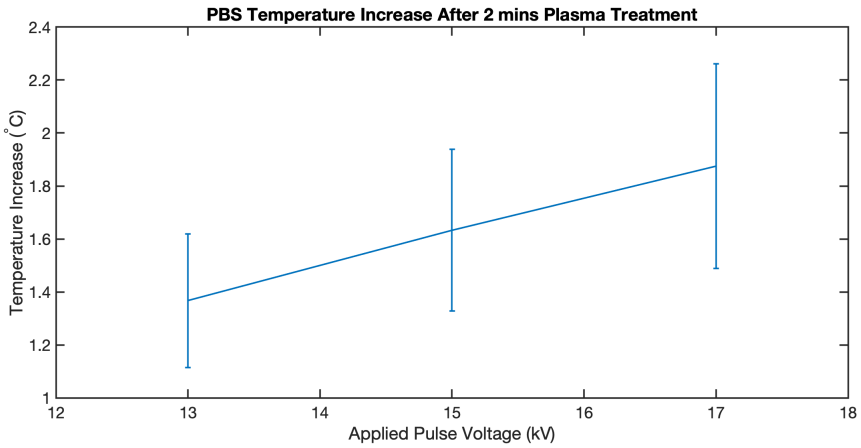

Figure 5.7: Temperature increase of PBS following plasma treatment as a function of applied voltage. All PBS started at room temperature (20 °C), then the temperature was measured immediately after two minutes of plasma treatment using a thermocouple. Each point is representative of 3 repeats, and the error bars show the standard deviation.

in vitro, or to human skin. This means that the effects of PBS temperature can be neglected when analysing any growth changes in skin cells following plasma treatment.

5.4.9. Correlation between Plasma Delivered Species Concentrations and Cellular Outcomes

In order to correlate between species densities delivered and biological outcomes, there is a requirement for a quantifiable outcome. The different methods of monitoring cells post-treatment are summarised in Table 5.2, showing the intended use for each, as well as their advantages and disadvantages. Shown here, the potential assays to use for correlative processes are either the time-course crystal violet or the RealTime-Glo assays. Due to the excessive errors inherent in the method for the crystal violet based assay, the RealTime-Glo assay is preferable.

Therefore, if this is to be used, quantification of species densities delivered to the cells to affect this assay output is required. To do this, simulations of the plasma will be used, as discussed in chapter 4.

Using the global model, it will be possible to determine the densities of all the plasma species in contact with the cells being treated, as a function of the plasma operating conditions. After performing a variety of different plasma treatments, for example, at different voltages, it will be possible to monitor the resulting cell viability over time using the RealTime-Glo assay. The species densities in each of these treatments can then be calculated, and it will be possible to see if there are any obvious correlations between species densities and cell viability. If independent control of specific species can be achieved, as discussed in Chapter 4, this would be particularly useful for the purpose of correlating species densities and biological effects.

When using the model, it would be important to consider the time period that would need to be simulated. Experimental treatments are usually on the scale of seconds to minutes, whereas simulations are often on the scale of milliseconds to seconds. This is important to consider if the kinetics of some species change on the timescales greater than those simulated. For example, some species may increase initially, but after multiple seconds begin to decrease as species that cause their quenching accumulate [129]. This suggests that short simulations and extrapolations for species densities may not always be sufficient. However, due to the relatively low computational power required for global chemistry models, it is possible to simulate plasma chemistry for extended periods of time.

Table 5.2: Summary of different techniques to monitor cells after plasma treatment

Method	Intended Use	Pros	Cons	Quantitative?
End-Point Crystal Violet Staining	Overall macroscopic population effects	– Quick and easy – Good for determining ranges of plasma operation to prevent excessive damage – Provides qualitative information on the whole cellular population	– Not quantifiable – No information on cell status – End point assay only	No
Time Course Crystal Violet	Cell growth post-treatment	– Quick and easy – Obtains quantifiable information on cell mass present post-treatment – Also provides end-point crystal violet staining population data before solubilising the stain	– No information on cell status – Many sources of errors - plating differences, staining differences, solubilising differences across duplicate plates	Yes
RealTime Glo	Cell viability post-treatment	– Realtime viability data – Multiple time data points from the same population of treated cells – Measures a cell activity, rather than just cell mass	– Length of time for monitoring is determined by the ratio of cells to reagent, therefore must be pre-determined before experiments	Yes

5.5. Discussion

RONS produced by low temperature plasmas are believed to be the basis for the biological effects that are seen in mammalian cells after treatment. Indeed, the application of low temperature plasmas to aid healing of chronic wounds is based on the premise that plasma-produced RONS can be delivered to a biological target, to mimic the functions of endogenous reactive species involved in wound healing processes, to enhance their effects. However, little is known about how specific quantities and types of particular RONS contribute to specific biological effects. Here a protocol has been presented that will allow introductory investigations for determining the effects of different plasma treatments on HaCaT cell viability. This is important, not only for the therapeutic intentions of plasma treatment, but also for determining safety limits for

treatments, similar to those already published for other aspects of the plasma composition, such as temperature and UV emission [92].

The protocol uses a cell viability assay which monitors cellular metabolism - something which is altered when cells enter a scenescent state, or die. Therefore, using this, alongside a range of plasma treatments, it should be possible to map how different treatments result in different viabilities. For future studies, it would also be beneficial to multiplex the RealTime-Glo reagent with a marker of cell death, such as CellTox Green (Promega), which gives real time information on membrane damage-induced cell death.This would allow the protocol to not only be sensitive to cellular viability, but also give more insight as to whether membrane damage may be a possible main effect of plasma treatment with certain RONS compositions.

The potential for membrane damage and subsequent cell death has been mentioned in Section 5.4.6 and Section 5.4.7, and it highlights the need for understanding the electric fields in the plasma environment, alongside the RONS produced. Electric fields can be used in biology for techniques such as electroporation, which can transiently induce pores in the cell membrane to allow entrance of otherwise membrane impermeable substances [210], however, they have also been implicated in the natural wound healing process. In healthy skin, there is a transepithelial potential (TEP) across the epidermis, which is maintained by ion transport across the cell membranes, and tight junctions between cells preventing an extracellular current. However, following wounding, the TEP is broken, and an extracellular current can flow, which has been shown to be important for guiding the healing process, though the actual mechanisms are poorly understood. It has also been shown that increase or loss of these extracellular wounding currents can lead to increased or decreased wound healing rates respectively, including in clinical trials [211]. Therefore, this suggests that the electric field component of plasma treatment should not be neglected when investigating the effects of treatment, and even warrants further, more specific investigation into its role. One potential way to begin this investigation is to use different plasma geometries where electric fields are either perpendicular to, or

incident on, the biological target being treated (See Chapter 1, Figure 1.2). This would also allow a distinction to be made between the effects of RONS and of electric fields, as mentioned in Section 5.4.6.

However, the main focus of this work was to present a method to correlate plasma-produced RONS with biological outcomes. As discussed in Section 5.4.9, species densities for the air plasma used in this work can be obtained using the GlobalKin global plasma chemistry model, which shows qualitative agreement with experimental data for trends in species densities. This allows the densities of all the different plasma species to be determined over time. In future investigations it would be valuable to begin to introduce spatial variations to the calculated species densities, either using experimental diagnostics or different plasma models. In this case, the experimental diagnostics could be limited to the specific species that have been highlighted as potentially important by the global model data alongside the cell viability data. Models that include spatial dimensions could also be used to determine how different species diffuse in the plasma and ambient air to see how different species could have differing contributions to cellular damage in different regions of the treated population [128]. This, coupled with methods such as the crystal violet staining could offer insight into how homogeneous a plasma treatment could potentially be across a whole chronic wound in the clinical setting.

The crystal violet staining method discussed in Section 5.4.1 can be used to show how there is spatial variation across the treated skin cell population, particularly relating to the effects that plasma has on the cell adhesion properties. The difference in crystal violet staining patterns in Figure 5.1 between plasma treated and control samples, indicates that the plasma treatment has caused a loss of cells in the treated sample. However, it is not clear whether the loss of cells is due to a complete loss of adhesion, and cell death, or whether plasma causes a reduction in adhesion, and then the harsh *in vitro* processes of media changing and staining results in the loss of these cells. This is an important distinction when considering the aims of plasma treatment for wound healing, as the adhesion properties of keratinocytes are required to alter in different phases

of the normal healing process. For example, to allow keratinocytes to begin migration into the wound area, they first of all have to loosen their attachment with the basal lamina and the neighbouring cells [18]. Therefore, it is critical to understand whether the plasma-induced alteration in cell adhesion seen in Figure 5.1a would be detrimental or beneficial to wound healing processes in the body. If beneficial, it may also inform how wounds should be managed immediately post plasma treatment, for example, ensuring that the wound area is disturbed as little as possible, so that fragile treated cells remain in situ. For future work, assays such as the scratch assay could provide useful information on how plasma treatment affects the adhesion and migration properties of cells.

As well as spatial variations, the inclusion of a liquid, and its effects on the overall plasma treatment, is an experimental and computational arm of plasma physics in its own right [212], and beyond the remit of this work. However, it cannot be ignored. For example, it has been shown that the liquid on which a plasma is incident can have a large impact on the types of ions and species produced in the liquid, and in turn, the availability of reactive species which can reach the cellular targets below [209]. This is one of the main reasons that the first cell treatments presented here were carried out without a liquid layer, as the system was designed for direct correlation between gas phase RONS and their cellular effects, without the added complication of liquid phase species. However, it was seen, in agreement with Balzer et al. [196] who investigated plasma treatment of fibroblasts, that a liquid layer was required to prevent excessive cell death. Unfortunately, due to time constraints this was not an area that could be investigated in more depth for this work.

When considering the role of liquid in plasma treatments, and the context of plasma treatments for chronic wounds, it is important to consider the fact that chronic wounds have wound exudates, which vary in amount and composition. Therefore, exudates could have a significant impact on the types and concentrations of RONS that could be delivered to a chronic wound during plasma treatment. Consequently, although it is already a cornerstone of chronic wound management [2], it may be necessary to ensure thorough washing and debridement

of any chronic wound to be treated, preferably using a well defined substance, such as saline, so the environment can be as controlled as possible for plasma treatment. This defining of the wound environment should allow greater confidence that the plasma species reaching the chronic wound target, is as close as possible to the RONS composition in a laboratory that gives the intended biological outcomes.

5.6. Conclusion and Future Work

Here a protocol has been discussed for determining viability of a skin cell line following defined plasma treatments. The protocol is quantifiable and in the future can be combined with quantitative measures of RONS delivered by plasmas, using plasma chemistry modelling data. This is a first step to being able to inform not only safety parameters for plasma-RONS delivery, but also begin the work for determining which plasma-produced species can induce particular biological effects in skin cells.

In the future, once basic viability data has been accumulated for different plasma RONS compositions, it will be necessary to investigate more refined cellular responses to plasma treatment. For example it would be beneficial to understand the activation of keratinocytes in response to different plasma RONS compositions. In particular, keratinocytes have a well-known activation pathway in response to injury, ranging from specific cytokine production profiles, through to cytoskeletal alterations [10]. In the process of wound healing, keratinocyte activation is important not only for keratinocyte mediated repair responses such as re-epithelialisation, but also for activation of other cells such as immune cells and fibroblasts [10, 15, 213, 214]. Thus, in the future, understanding of these keratinocyte activation processes as a function of plasma RONS composition using methods such as Enzyme Linked Immunosorbent Assays (ELISA) and flow cytometry will be highly valuable.

Conclusion

The field of plasma medicine has grown rapidly over the last decade or so, with growing interest into the potential use of LTPs in cancer treatments, sterilisation and wound healing [29]. With the ever increasing interest in the use of plasmas for biomedical applications comes the need to understand the mechanisms by which LTPs can induce biological effects. It is believed that LTPs exert their effects largely through the production of RONS, by mimicking the functions of endogenously produced reactive species which mediate a wide range of physiological processes, including cell-cell signalling, immune responses and wound healing [49–51]. Therefore, in order to aid the design of plasma treatments, and to tailor these treatments to specific applications, it is necessary to understand the contribution of different RONS species to different biological effects seen following LTP treatment. In Chapter 1 several aims for this work were outlined to begin to address the task of understanding the effects of different RONS on biological targets, using global plasma modelling, experimental plasma diagnostics, and biological assays. In particular the RONS produced by air plasmas were of interest, due to their prevalence in normal physiology in the human body, as well as the attractiveness of using air as a plasma feed gas to reduce the need for expensive bottled gases and associated infrastructure. The aims of this work were to develop reaction chemistry sets for nitrogen then air, to be used to interrogate the chemical kinetics occurring in these plasmas, then to use biological assays to develop a protocol for correlating species densities

delivered by plasmas, with biological effects.

As a first step to developing an air chemistry set for use in global plasma chemistry models, a detailed nitrogen chemistry set was developed. The reaction scheme was based on the multiple works of Volynets et al. [104], Guerra et al. [113], Colonna and Capitelli [140], due to their stringent reaction validation techniques, and range of pressures that the sets were designed to simulate. This chemistry set presented in this current work is important as it is designed for modelling atmospheric pressure nitrogen discharges, and paying particular attention to the highly important vibrationally excited states of nitrogen. To date, nitrogen plasma research has largely been restricted to low pressure applications and chemistry models. Vibrationally excited states of nitrogen in low pressure discharges are known to be crucial in mediating a phenomenon known as the nitrogen pink afterglow, through vibrational up-pumping mechanisms involving V-V reactions [101]. Using GlobalKin, a global plasma chemistry model, this work has shown that these processes occurring at low pressure can also been seen in the atmospheric pressure situation. Here, it has been demonstrated that, similar to the low pressure situation, vibrational up-pumping can increase the densities of energetic nitrogen metastables which, through Penning ionisation, causes local ionisation in the afterglow region of nitrogen discharges. This is seen as a peak in electron density in the afterglow, after an initial decay when power input to the plasma ceases, and is dependent on the power deposition.

Further to this, the importance of including vibrationally excited states in nitrogen discharges at atmospheric pressure was investigated, in particular to determine the effects on the electron kinetics seen in the plasmas, as well as the effects on vibrational distribution functions. This novel investigation showed that there is a threshold number of vibrational states that must be included in the model in order to give VDFs that appear possible. If less than 40 vibrational states are included in the model, this gives VDFs that appear unphysical. This highlights the importance of including the full manifold of vibrationally excited states of ground state nitrogen in any future atmospheric pressure nitrogen discharge modelling, as without these, the chemical kinetics in the model would be

strongly affected, and less correct. Overall this work pertaining to nitrogen discharges presents novel insight into modelling atmospheric pressure discharges in pure nitrogen, and is suggestive of a situation that is more similar to the low pressure case than was originally expected, due to the increased collisional quenching seen at atmospheric pressure. The next steps for this work should be to experimentally determine the presence of an afterglow electron peak in a pure nitrogen plasma, and this work discusses the potential thresholds for impurities in the nitrogen gas that would be tolerable, without losing the nitrogen afterglow effects. This was achieved by adding an artificial quenching species into the global model, to quench vibrationally excited states. By varying the amounts of quenching species, and the quenching reaction rate coefficients, the levels of impurities allowed in the nitrogen gas before the nitrogen afterglow effects were lost were discussed. This is useful information considering that the next steps for this work would be to experimentally characterise the afterglow electron peak in atmospheric pressure nitrogen discharges using a diagnostic technique such as Optical Emission Spectroscopy.

Using the nitrogen chemistry set as a starting point, oxygen species were then added.This provided a chemistry set for a plasma running in a dry air environment, which was benchmarked against initial plasma diagnostics for NO_x and O_3, and published electron densities for similar plasma conditions, in a volume DBD plasma source. Given good qualitative agreement between the model and experimental RONS concentrations, the model could then be used to determine dominant production and destruction pathways for the biorelevant RONS, O_3 and NO. This gives a method for beginning the process of delineating the different dynamics by which different RONS are produced and destroyed. For example, the production and destruction mechanisms for species such as NO and O_3 show varying dynamics, particularly with respect to the types of reactants involved, and how strongly their density is related to the power input. Reactions involving short lived species, such as ions, increase in density rapidly during the power pulse, but also decay rapidly when the power ceases, meaning that reactions involving these species have absolute rates that increase

and decrease with the power pulse. Conversely, some reactions involve longer lived species, therefore are less strongly linked to the power input. This work suggests that this may be a way of controlling different species densities independently. For example, there may be potential to alter species densities by changing the power input shape or frequency, to differentially affect species densities where their production or destruction is strongly linked to the power input. Thus, this work would help to inform how plasmas for biomedical applications could be designed to specifically enhance or suppress the formation of different species, depending on the desired biological effect.

However, in order to understand which RONS species should be enhanced or suppressed for particular treatments, it is first of all necessary to determine the effects of the different species on the target cells. Therefore, protocols to determine the overall spatial effects of plasma treatment, and the long term viability of cells post plasma treatment were also presented. Here different methods were investigated to develop a protocol which, in the future, could be used in combination with global modelling to correlate species densities delivered by plasma treatment, with the overall cellular effects observed. Of particular interest was the ability to monitor cellular viability post-treatment in real time, without interfering with the cells, allowing a time course study to be performed. The future aims would be to use the simulations and pathways analyses described above to guide how the physical plasma operating conditions should be adjusted to give specific RONS compositions which could then be used to treat the cells. The realtime cellular viability assay could then be used to assess how the treatment affected the cells viability over time. If plasma-produced species densities can be altered in a controlled, independent manner, this combination of modelling, experiment, and realtime cellular viability data would provide valuable insight into both therapeutic concentrations of different plasma-produced RONS, and into the safe concentrations that can be delivered without causing undue harm to the cells. This would add significant value to *in vitro* plasma/biological interaction studies, and would allow plasma device design built on evidence of the specific contribution of different plasma species.

Overall this work is leading towards the informed design of LTP treatments for clinical use. Chronic wounds have a huge incidence both in the UK and across the globe, and this is expected to rise in future years [1]. Therefore, the need to develop effective, reliable treatments is greater than ever. A significant amount of evidence already exists for the use of LTPs in clinical trials for wound healing. By combining this evidence with thorough investigation into the specific contribution of different RONS to biological outcomes, the goal is to develop LTPs further to establish their use as an evidence based, effective therapeutic for wound healing.

Appendix A

A.1. Nitrogen Chemistry

Table A.1: Electron Impact Reactions with Nitrogen Species.

No.	E_{Thr} (eV)	Reaction	Rate	Reference
NE1	0.0	$e^- + N_2 \rightarrow N_2 + e^-$	$f(E)$	[215]
NE2	E(v)	$e^- + N_2(X) \rightarrow e^- + N_2(X, v > 0)$	$f(E)$	[141]
NE3	6.17	$e^- + N_2(X) \rightarrow e^- + N_2(A)$	$f(E)$	[215]
NE4	7.35	$e^- + N_2(X) \rightarrow e^- + N_2(B)$	$f(E)$	[216]
NE5	8.4	$e^- + N_2(X) \rightarrow e^- + N_2(a)$	$f(E)$	[215]
NE6	11.1	$e^- + N_2(X) \rightarrow e^- + N_2(C)$	$f(E)$	[215]
NE7	15.5	$e^- + N_2(X) \rightarrow e^- + N_2^+ + e^-$	$f(E)$	[217]
NE8	12.25	$e^- + N_2(X) \rightarrow e^- + N + N$	$f(E)$	[218]
NE9	0.0	$e^- + N_2(A) \rightarrow e^- + N_2(A)$	$f(E)$	[219]
NE10	9.33	$e^- + N_2(A) \rightarrow e^- + e^- + N_2^+$	$f(E)$	[219]
NE11	0.0	$e^- + N_2(a) \rightarrow e^- + N_2(a)$	$f(E)$	[220]
NE12	8.80	$e^- + N_2(a) \rightarrow e^- + N_2^+$	$f(E)$	[220]
NE13	0.0	$e^- + N \rightarrow e^- + N$	$f(E)$	[221]
NE14	2.38	$e^- + N \rightarrow e^- + N(^2D)$	$f(E)$	[222]
NE15	3.57	$e^- + N \rightarrow e^- + N(^2P)$	$f(E)$	[222]
NE16	14.55	$e^- + N \rightarrow e^- + e^- + N^+$	$f(E)$	[215]
NE17	0.0	$e^- + N^+ \rightarrow N$	$f(E)$	[223]
NE18	0.0	$e^- + N_2^+ \rightarrow N_2^+ + e^-$	$f(E)$	[223]
NE19	0.0	$e^- + N_2^+ \rightarrow N + N$	$f(E)$	[223]
NE20	0.0	$e^- + N_4^+ \rightarrow N_4^+ + e^-$	$f(E)$	[223]
NE21	0.0	$e^- + N_4^+ \rightarrow N_2 + N_2$	$f(E)$	[223]

Table A.2: Heavy Particle Nitrogen Reactions. [a] Rate coefficient is $cm^3\ s^{-1}$ for 2-body reactions, $cm^6\ s^{-1}$ for 3-body reactions and s^{-1} for radiative decay procecsses.

No.	Reaction	Rate[a]	Reference
N1	$N_2(A) + N_2(A) \rightarrow N_2(B) + N_2(v = 2)$	7.7×10^{-11}	[224]
N2	$N_2(A) + N_2(A) \rightarrow N_2(B) + N_2(v = 8)$	7.7×10^{-11}	[224]
N3	$N_2(A) + N_2(A) \rightarrow N_2(C) + N_2(v = 2)$	1.5×10^{-10}	[225]
N4	$N_2(A) + N_2(v = 5 - 14) \rightarrow N_2(B) + N_2$	2×10^{-11}	[105]
N5	$N_2(A) + N_2(v = 14 - 19) \rightarrow N_2 + N + N$	5×10^{-14}	[104]
N6	$N_2(A) + N \rightarrow N_2(v = 6 - 9) + N(^2P)$	4×10^{-11}	[226]
N7	$N_2(B) + N_2 \rightarrow N_2(A) + N_2$	2.85×10^{-11}	[105, 227]
N8	$N_2(B) + N_2 \rightarrow N_2 + N_2$	1.50×10^{-12}	[105]
N9	$N_2(B) \rightarrow N_2(A) + h\nu$	2.0×10^{5}	[228]
N10	$N_2(C) \rightarrow N_2(B) + h\nu$	2.74×10^{7}	[104, 113]
N11	$N_2(a) + N_2 \rightarrow N_2(B) + N_2$	1.9×10^{-13}	[104]
N12	$N_2(a) \rightarrow N_2 + h\nu$	1.8×10^{4}	[229]
N13	$N(^2D) + N_2 \rightarrow N + N_2$	1.0×10^{-13}	[230]
N14	$N(^2P) + N \rightarrow N + N(^2D)$	6.0×10^{-13}	[231]
N15	$N(^2P) + N \rightarrow N + N$	1.8×10^{-12}	[231]
N16	$N(^2P) + N_2 \rightarrow N + N_2$	6.0×10^{-14}	[231]
N17	$N(^2P) + N_2(X, 10 \leq v \leq 58) \rightarrow N + N_2(A)$	1.0×10^{-10}	[231]
N18	$N + N_2(X, 40 \leq v \leq 58) \rightarrow N(^2D) + N_2(A)$	1.0×10^{-11}	[103]
N19	$N + N_2(X, 39 \leq v \leq 58) \rightarrow N + N_2(a)$	1.0×10^{-11}	[103]
N20	$N_2(A) + N_2(a) \rightarrow N_4^+ + e^-$	1.5×10^{-13}	[104]
N21	$N_2(a) + N_2(a) \rightarrow N_4^+ + e^-$	3.0×10^{-11}	[104]
N22	$N(^2D) + N(^2P) \rightarrow N_2^+ + e^-$	6.0×10^{-12}	[104]
N22	$N(^2P) + N(^2P) \rightarrow N_2^+ + e^-$	1.5×10^{-11}	[104]
N23	$N_2^+ + N_2 + N_2 \rightarrow N_4^+ + N_2$	6.8×10^{-29}	[232]
N24	$N_2(X, 12 \leq v \leq 17) + N_2^+ \rightarrow$ $N_2(B)^+ + N_2(X, v - 12)$	1.0×10^{-11}	[113]
N25	$N_2(B) \rightarrow N_2(A) + h\nu$	1.6×10^{7}	[113]
N26	$N + N + N_2 \rightarrow N_2(A) + N_2$	1.7×10^{-33}	[140, 233]
N27	$N + N + N \rightarrow N_2(A) + N$	1.4×10^{-32}	[140, 233]
N28	$N + N + N_2 \rightarrow N_2(B) + N_2$	2.4×10^{-33}	[140, 233]
N29	$N + N + N \rightarrow N_2(A) + N$	1.4×10^{-32}	[140, 233]
N30	$N_2(A) + N_2 \rightarrow N_2 + N_2$	3.0×10^{-18}	[140]
N31	$N_2(C) + N_2 \rightarrow N_2(a) + N_2$	1.0×10^{-11}	[140]

Nitrogen Vibrational Kinetics			
N32	$N_2(X,v) + N_2 \rightarrow N_2(X,v-1) + N_2$	*See Chapter 2, Section 2.3.5*	[149]
N33	$N_2(X,v) + N \rightarrow N_2(X,v-1) + N$	*See Chapter 2, Section 2.3.5*	[149]
N34	$N_2(X,v+1) + N_2(X,w) \rightarrow N_2(X,v) + N_2(X,w+1)$	*See Chapter 2, Section 2.3.5*	[149]

A.2. Oxygen Chemistry

The oxygen chemistry used in this work is taken from [99], with the addition of the 3-body reactions shown in Table A.3.

Table A.3: Heavy Particle Oxygen Reactions

No.	Reaction	Rate ($cm^6\ s^{-1}$)	Reference
O1	$O + O + O_2 \rightarrow O_2 + O_2$	3.6×10^{-33}	[234]
O2	$O + O + O_2 \rightarrow O_2(a) + O_2$	2.38×10^{-33}	[234]
O3	$O + O + O_2 \rightarrow O_2(b) + O_2$	1.23×10^{-33}	[234]
O4	$O + O + O \rightarrow O_2 + O$	9.9×10^{-34}	[109]
O5	$O_2 + O + O \rightarrow O_3 + O$	$2.1 \times 10^{-34} exp(345/T_g)$	[190, 191]
O6	$O_2 + O + O_2 \rightarrow O_3 + O_2$	$2.11 \times 10^{-35} exp(663/T_g)$	[190, 191]
O7	$O_2 + O + O_3 \rightarrow O_3 + O_3$	$1.66 \times 10^{-34}(T_g/300)$	[192]

A.3. Nitrogen-Oxygen Chemistry

Table A.4: Electron Impact Reactions with Nitrogen/Oxygen Species.

No.	E_{Thr} (eV)	Reaction	Rate	Reference
NOE1	0.0	$e^- + NO \rightarrow NO + e^-$	$f(E)$	[235]
NOE2	0.23	$e^- + NO \rightarrow NO + e^-$	$f(E)$	[235]
NOE3	0.46	$e^- + NO \rightarrow NO + e^-$	$f(E)$	[235]
NOE4	0.69	$e^- + NO \rightarrow NO + e^-$	$f(E)$	[235]
NOE5	0.91	$e^- + NO \rightarrow NO + e^-$	$f(E)$	[235]
NOE6	1.13	$e^- + NO \rightarrow NO + e^-$	$f(E)$	[235]
NOE7	5.48	$e^- + NO \rightarrow NO(A) + e^-$	$f(E)$	[236]
NOE8	6.50	$e^- + NO \rightarrow NO + e^-$	$f(E)$	[236]
NOE9	6.58	$e^- + NO \rightarrow NO(B) + e^-$	$f(E)$	[236]
NOE10	6.60	$e^- + NO \rightarrow N + O^-$	$f(E)$	[237]

NOE11	6.77	$e^- + NO \rightarrow N + O + e^-$	$f(E)$	[235]
NOE12	7.58	$e^- + NO \rightarrow NO + e^-$	$f(E)$	[236]
NOE13	9.26	$e^- + NO \rightarrow NO^+ + e^- + e^-$	$f(E)$	[238]
NOE14	20.17	$e^- + NO \rightarrow N + O^+ + e^- + e^-$	$f(E)$	[238]
NOE15	0.0	$e^- + NO_2 \rightarrow NO_2 + e^-$	$f(E)$	[239]
NOE16	13.00	$e^- + NO_2 \rightarrow NO^+ + O + e^- + e^-$	$f(E)$	[238]
NOE17	0.0	$e^- + NO^+ \rightarrow NO^+ + e^-$	$f(E)$	[223]
NOE17	0.0	$e^- + NO^+ \rightarrow N + O$	$f(E)$	[223]

Table A.5: Heavy Particle Oxygen and Nitrogen/Oxygen Reactions. Rate coefficient is $cm^3\ s^{-1}$ for 2-body reactions, $cm^6\ s^{-1}$ for 3-body reactions and s^{-1} for radiative decay procecsses. [b] is averaged rate coefficient for lumped state.

No.	Reaction	Rate[a]	Reference
NO1	$O_2(b) + N_2 \rightarrow O_2(a) + N_2$	$1.7 \times 10^{-15}(T_g/300)$	[109]
NO2	$N(^2D) + O \rightarrow N + O$	1.1×10^{-12}	[240]
NO3	$N_2(A) + O_2 \rightarrow N_2 + O_2(a)$	1.29×10^{-12}	[183]
NO4	$N_2(A) + O_2 \rightarrow N_2 + O + O$	$1.63 \times 10^{-12}(T_g/300)$	[191]
NO5	$N_2(B) + O_2 \rightarrow N_2 + O + O$	3×10^{-10}	[183]
NO6	$N_2(C) + O_2 \rightarrow N_2 + O + O$	3×10^{-10}	[183]
NO7	$N_2(a) + O_2 \rightarrow N_2 + O + O$	1.86×10^{-16}	[111, 191, 241][b]
NO8	$N + N + O_2 \rightarrow N_2 + O_2$	$8.27 \times 10^{-34} exp(-500/T_g)$	[183]
NO9	$O + O + N_2 \rightarrow N_2 + O_2$	$2.76 \times 10^{-34} exp(-720/T_g)$	[183]
NO10	$O + O_2 + N_2 \rightarrow N_2 + O_3$	5.7×10^{-34}	[114]
NO11	$N_2(A) + O \rightarrow NO + N(^2D)$	7×10^{-12}	[110]
NO12	$O_2 + N \rightarrow NO + O$	$3.3 \times 10^{-12} exp(-3150/T_g)$	[183]
NO13	$O_2 + N(^2D) \rightarrow NO + O$	$1.5 \times 10^{-12}(T_g/300)^{0.5}$	[183]
NO14	$O_2 + N(^2D) \rightarrow NO + O(^1D)$	$6 \times 10^{-12}(T_g/300)^{0.5}$	[183]
NO15	$O_2 + N(^2P) \rightarrow NO + O$	2.6×10^{-12}	[183]
NO16	$O_2(a) + N \rightarrow NO + O$	$2 \times 10^{-14} exp(-600/T_g)$	[183]
NO17	$N + O \rightarrow NO(A)$	1.18×10^{-17}	[185]
NO18	$N + O + N_2 \rightarrow NO(A) + N_2$	2.12×10^{-34}	[185]
NO19	$N + O + N_2 \rightarrow NO(B) + N_2$	3.09×10^{-34}	[185]
NO20	$N + O + O_2 \rightarrow NO + O_2$	1.02×10^{-32}	[183]
NO21	$N + O + O_2 \rightarrow NO(B) + O_2$	3.09×10^{-34}	[185]
NO22	$NO + N_2(A) \rightarrow NO(A) + N_2$	6.6×10^{-11}	[242]
NO23	$NO(A) + N_2 \rightarrow NO + N_2$	1×10^{-13}	[114]
NO24	$NO(A) + O_2 \rightarrow NO + O_2$	1.5×10^{-10}	[114]
NO25	$NO(A) + NO \rightarrow NO + NO$	2×10^{-10}	[114]

NO26	$NO(B) + N_2 \rightarrow NO + N_2$	6.1×10^{-13}	[114]
NO27	$NO(B) + O_2 \rightarrow NO + O_2$	1.5×10^{-11}	[114]
NO28	$NO(B) + NO \rightarrow NO + NO$	2×10^{-10}	[114]
NO29	$NO + N \rightarrow N_2(v = 3) + O$	1.82×10^{-11}	[183]
NO30	$NO + N(^2D) \rightarrow N_2 + O$	6.3×10^{-11}	[243]
NO31	$NO + N(^2P) \rightarrow N_2(A) + O$	3.4×10^{-11}	[183]
NO32	$NO + N_2(a) \rightarrow N_2 + N + O$	3.6×10^{-10}	[241]
NO33	$NO + N_2(B) \rightarrow N_2(A) + NO$	2.4×10^{-10}	[183]
NO34	$O_2(b) + NO \rightarrow O_2(a) + NO$	6×10^{-14}	[109]
NO35	$O_2(a) + NO \rightarrow O_2 + NO$	2.5×10^{-17}	[244]
NO36	$NO(A) \rightarrow NO$	4.5×10^{6}	[184]
NO37	$NO(B) \rightarrow NO$	3×10^{5}	[185]
NO38	$NO + O_3 \rightarrow NO_2 + O_2$	$4.3 \times 10^{-12} exp(-1560/T_g)$	[183]
NO39	$NO + O + N_2 \rightarrow NO_2 + N_2$	1×10^{-31}	[245]
NO40	$NO + O + N_2 \rightarrow NO_2 + N_2$	3.7×10^{-32}	[246]
NO41	$NO + O + O_2 \rightarrow NO_2 + O_2$	8.6×10^{-32}	[247]
NO42	$NO + O + O_2 \rightarrow NO_2 + O_2$	3.7×10^{-32}	[246]
NO43	$NO_2 + N_2 \rightarrow NO_2 + N_2$	6×10^{-11}	[248]
NO44	$NO_2 + O_2 \rightarrow NO_2 + NO_2$	6×10^{-11}	[114]
NO45	$NO_2 + N \rightarrow N_2 + O_2$	7×10^{-13}	[183]
NO46	$NO_2 + N \rightarrow N_2 + O + O$	9.1×10^{-13}	[183]
NO47	$NO_2 + N \rightarrow NO + NO$	2.3×10^{-12}	[183]
NO48	$NO_2 + O \rightarrow NO + O_2$	$6.51 \times 10^{-12} exp(998/T_g)$	[114]
NO49	$N_2(X, v \geq 13) + O \rightarrow NO + N$	1×10^{-13}	[110]
NO50	$N_2^+ + O_2 \rightarrow N_2 + O_2^+$	6×10^{-11}	[183]
NO51	$N_2^+ + O \rightarrow N_2 + O^+$	1×10^{-11}	[183]
NO52	$N_2^+ + O \rightarrow N + NO^+$	1.3×10^{-10}	[183]
NO53	$N_2^+ + NO \rightarrow N_2 + NO^+$	3.3×10^{-10}	[183]
NO54	$N_4^+ + O_2 \rightarrow N_2 + N_2 + O_2^+$	2.5×10^{-10}	[183]
NO55	$N_4^+ + O \rightarrow N_2 + N_2 + O^+$	2.5×10^{-10}	[183]
NO56	$N_4^+ + NO \rightarrow N_2 + N_2 + NO^+$	4×10^{-10}	[183]
NO57	$O_2^+ + N \rightarrow O + NO^+$	1.2×10^{-10}	[183]
NO58	$O_2^+ + NO \rightarrow O_2 + NO^+$	4.4×10^{-10}	[183]
NO59	$O^+ + N_2 + N_2 \rightarrow N_2 + N + NO^+$	6×10^{-29}	[183]
NO59	$O^+ + N_2 + O_2 \rightarrow O_2 + N + NO^+$	6×10^{-29}	[183]
NO60	$O^+ + NO \rightarrow O + NO^+$	2.4×10^{-11}	[183]
NO61	$O^- + N \rightarrow NO + e^-$	2×10^{-10}	[31]
NO62	$O^- + NO \rightarrow NO_2 + e^-$	5×10^{-10}	[31]

Nitrogen-Oxygen Vibrational Kinetics			
NO63	$N_2(X, v+1) + O_2(X, v=0) \rightarrow N_2(X, v) + O_2(X, v=1)$	*See Chapter 2, Section 2.4.4*	[110]
NO64	$N_2(X, v) + O \rightarrow N_2(X, v-1) + O$	*See Chapter 2, Section 2.4.4*	[110]
NO65	$N_2(X, v) + O_2 \rightarrow N_2(X, v-1) + O_2$	*See Chapter 2, Section 2.4.4*	[110]

Bibliography

[1] Abdul R Siddiqui and Jack M Bernstein. Chronic wound infection: facts and controversies. *Clin. Dermatol.*, 28(5):519–526, 2010.

[2] Robert G Frykberg and Jaminelli Banks. Challenges in the treatment of chronic wounds. *Advances in wound care*, 4(9):560–582, 2015.

[3] Anke Persoon, Maud M Heinen, Carien JM Van Der Vleuten, Michette J De Rooij, Peter Van De Kerkhof, and Theo Van Achterberg. Leg ulcers: a review of their impact on daily life. *J Clin Nurs*, 13(3):341–354, 2004.

[4] Krister Järbrink, Gao Ni, Henrik Sönnergren, Artur Schmidtchen, Caroline Pang, Ram Bajpai, and Josip Car. The humanistic and economic burden of chronic wounds: a protocol for a systematic review. *Systematic reviews*, 6(1):15, 2017.

[5] John Posnett and PJ Franks. The burden of chronic wounds in the uk. *Diabetic Medicine*, 14(5):S7–S85, 2008.

[6] Ceri J Phillips, Ioan Humphreys, Jacqui Fletcher, Keith Harding, George Chamberlain, and Steven Macey. Estimating the costs associated with the management of patients with chronic wounds using linked routine data. *International wound journal*, 13(6):1193–1197, 2016.

[7] Ehrhardt Proksch, Johanna M Brandner, and Jens-Michael Jensen. The skin: an indispensable barrier. *Experimental dermatology*, 17(12):1063–1072, 2008.

[8] Leah C Biggs, Christine S Kim, Yekaterina A Miroshnikova, and Sara A Wickström. Mechanical forces in the skin: Roles in tissue architecture, stability, and function. *Journal of Investigative Dermatology*, 140(2):284–290, 2020.

[9] Roland Moll, Markus Divo, and Lutz Langbein. The human keratins: biology and pathology. *Histochemistry and cell biology*, 129(6):705, 2008.

[10] Irwin M Freedberg, Marjana Tomic-Canic, Mayumi Komine, and Miroslav Blumenberg. Keratins and the keratinocyte activation cycle. *Journal of Investigative Dermatology*, 116(5): 633–640, 2001.

[11] Gopinathan K Menon. New insights into skin structure: scratching the surface. *Advanced drug delivery reviews*, 54:S3–S17, 2002.

[12] Mara Mancini, Anna Maria Lena, Gaelle Saintigny, Christian Mahé, Nicola Di Daniele, Gerry Melino, and Eleonora Candi. Micrornas in human skin ageing. *Ageing research reviews*, 17:9–15, 2014.

[13] Sabine Werner and Richard Grose. Regulation of wound healing by growth factors and cytokines. *Physiological reviews*, 83(3):835–870, 2003.

[14] Kenneth Murphy. *Janeway's Immunobiology*. Garland Science, 8th edition, 2011.

[15] Stephan Barrientos, Olivera Stojadinovic, Michael S Golinko, Harold Brem, and Marjana Tomic-Canic. Growth factors and cytokines in wound healing. *Wound repair and regeneration*, 16(5):585–601, 2008.

[16] T Velnar, T Bailey, and V Smrkolj. The wound healing process: An overview of the cellular and molecular mechanisms. *Journal of International Medical Research*, 37(5):1528–1542, 2009. doi: 10.1177/147323000903700531. URL `http://imr.sagepub.com/content/37/5/1528.abstract`.

[17] Stuart Enoch and David John Leaper. Basic science of wound healing. *Surgery (Oxford)*, 26 (2):31–37, 2008.

[18] Irena Pastar, Olivera Stojadinovic, Natalie C Yin, Horacio Ramirez, Aron G Nusbaum, Andrew Sawaya, Shailee B Patel, Laiqua Khalid, Rivkah R Isseroff, and Marjana Tomic-Canic. Epithelialization in wound healing: a comprehensive review. *Advances in wound care*, 3(7):445–464, 2014.

[19] Paul Martin and R Nunan. Cellular and molecular mechanisms of repair in acute and chronic wound healing. *British Journal of Dermatology*, 173(2):370–378, 2015.

[20] Andrew Stanley and Turner Osler. Senescence and the healing rates of venous ulcers. *Journal of vascular surgery*, 33(6):1206–1211, 2001.

[21] Deirdre Church, Sameer Elsayed, Owen Reid, Brent Winston, and Robert Lindsay. Burn wound infections. *Clinical Microbiology Reviews*, 19(2):403–434, 2006. doi: 10.1128/CMR.19.2.403-434.2006. URL `http://cmr.asm.org/content/19/2/403.abstract`.

[22] PG Bowler, BI Duerden, and David G Armstrong. Wound microbiology and associated approaches to wound management. *Clinical microbiology reviews*, 14(2):244–269, 2001.

[23] Taylor Johnson, Belinda Gómez, Matthew McIntyre, Michael Dubick, Robert Christy, Susannah Nicholson, and David Burmeister. The cutaneous microbiome and wounds: New molecular targets to promote wound healing. *International journal of molecular sciences*, 19(9):2699, 2018.

[24] Annette B Wysocki. Evaluating and managing open skin wounds: colonization versus infection. *AACN Advanced Critical Care*, 13(3):382–397, 2002.

[25] RS Howell-Jones, MJ Wilson, Katja E Hill, AJ Howard, Patricia Elaine Price, and David William Thomas. A review of the microbiology, antibiotic usage and resistance in chronic skin wounds. *Journal of Antimicrobial Chemotherapy*, 55(2):143–149, 2005.

[26] Philip G Bowler. Antibiotic resistance and biofilm tolerance: a combined threat in the treatment of chronic infections. *Journal of wound care*, 27(5):273–277, 2018.

[27] George Han and Roger Ceilley. Chronic wound healing: a review of current management and treatments. *Advances in therapy*, 34(3):599–610, 2017.

[28] KD Weltmann and Th Von Woedtke. Plasma medicine—current state of research and medical application. *Plasma Physics and Controlled Fusion*, 59(1):014031, 2016.

[29] A. Fridman and G. Friedman. *Plasma Medicine*. Wiley, 2013.

[30] Gregory Fridman, Gary Friedman, Alexander Gutsol, Anatoly B Shekhter, Victor N Vasilets, and Alexander Fridman. Applied plasma medicine. *Plasma Processes and Polymers*, 5 (6):503–533, 2008.

[31] Alexander Fridman. *Plasma chemistry*. Cambridge university press, 2008.

[32] N St J Braithwaite. Introduction to gas discharges. *Plasma sources science and technology*, 9 (4):517, 2000.

[33] Angela Privat-Maldonado, Deborah O'Connell, Emma Welch, Roddy Vann, and Marjan van der Woude. Spatial dependence of dna damage in bacteria due to low-temperature plasma application as assessed at the single cell level. *Scientific Reports*, 6:35646, 10 2016. ISSN 2045-2322. doi: 10.1038/srep35646. URL `http:https://dx.doi.org/10.1038/srep35646`.

[34] AM Hirst, MS Simms, VM Mann, NJ Maitland, D O'Connell, and FM Frame. Low-temperature plasma treatment induces dna damage leading to necrotic cell death in primary prostate epithelial cells. *British journal of cancer*, 112(9):1536–1545, 2015.

[35] E. Wagenaars, M. van der Woude, and R. Vann. An atmospheric-pressure low-temperature plasma jet for growth inhibition of escherichia coli. *IEEE Transactions on Plasma Science*, 39 (11):2346–2347, Nov 2011. ISSN 0093-3813. doi: 10.1109/TPS.2011.2153881.

[36] Sander Bekeschus, Anke Schmidt, Klaus-Dieter Weltmann, and Thomas von Woedtke. The plasma jet kinpen - a powerful tool for wound healing. *Clinical Plasma Medicine*, 4(1): 19 – 28, 2016. ISSN 2212-8166. doi: http://dx.doi.org/10.1016/j.cpme.2016.01.001. URL http://www.sciencedirect.com/science/article/pii/S2212816616300014.

[37] J Golda, J Held, B Redeker, M Konkowski, P Beijer, A Sobota, G Kroesen, N St J Braithwaite, S Reuter, MM Turner, et al. Concepts and characteristics of the 'cost reference microplasma jet'. *Journal of Physics D: Applied Physics*, 49(8):084003, 2016.

[38] Gregory Fridman, Marie Peddinghaus, Manjula Balasubramanian, Halim Ayan, Alexander Fridman, Alexander Gutsol, and Ari Brooks. Blood coagulation and living tissue sterilization by floating-electrode dielectric barrier discharge in air. *Plasma Chemistry and Plasma Processing*, 26(4):425–442, 2006. ISSN 1572-8986. doi: 10.1007/s11090-006-9024-4. URL http://dx.doi.org/10.1007/s11090-006-9024-4.

[39] Gregory Fridman, Alexey Shereshevsky, Monika M. Jost, Ari D. Brooks, Alexander Fridman, Alexander Gutsol, Victor Vasilets, and Gary Friedman. Floating electrode dielectric barrier discharge plasma in air promoting apoptotic behavior in melanoma skin cancer cell lines. *Plasma Chemistry and Plasma Processing*, 27(2):163–176, 2007. ISSN 1572-8986. doi: 10.1007/s11090-007-9048-4. URL http://dx.doi.org/10.1007/s11090-007-9048-4.

[40] Sabrina Baldus, Daniel Schroeder, Nikita Bibinov, Volker Schulz-von der Gathen, and Peter Awakowicz. Atomic oxygen dynamics in an air dielectric barrier discharge: a combined diagnostic and modeling approach. *Journal of Physics D: Applied Physics*, 48(27):275203, 2015.

[41] Junggil Kim, Kyong-Hoon Choi, Yunjung Kim, Bong Joo Park, and Guangsup Cho. Wearable plasma pads for biomedical applications. *Applied Sciences*, 7(12):1308, 2017.

[42] S Reuter, J Winter, A Schmidt-Bleker, D Schroeder, H Lange, N Knake, V Schulz-Von Der Gathen, and KD Weltmann. Atomic oxygen in a cold argon plasma jet: Talif spectroscopy in ambient air with modelling and measurements of ambient species diffusion. *Plasma Sources Science and Technology*, 21(2):024005, 2012.

[43] A Fridman, A Chirokov, and A Gutsol. Non-thermal atmospheric pressure discharges. *Journal of Physics D: Applied Physics*, 38(2):R1, 2005.

[44] Ulrich Kogelschatz, Baldur Eliasson, and Walter Egli. From ozone generators to flat televi-

sion screens: history and future potential of dielectric-barrier discharges. *Pure and Applied Chemistry*, 71(10):1819–1828, 1999.

[45] Halim Ayan, Gregory Fridman, Alexander F Gutsol, Victor N Vasilets, Alexander Fridman, and Gary Friedman. Nanosecond-pulsed uniform dielectric-barrier discharge. *IEEE transactions on plasma science*, 36(2):504–508, 2008.

[46] David B. Graves. Low temperature plasma biomedicine: A tutorial reviewa). *Physics of Plasmas*, 21(8):080901, 2014. doi: http://dx.doi.org/10.1063/1.4892534. URL `http://scitation.aip.org/content/aip/journal/pop/21/8/10.1063/1.4892534`.

[47] Thomas von Woedtke, Anke Schmidt, Sander Bekeschus, Kristian Wende, and Klaus-Dieter Weltmann. Plasma medicine: A field of applied redox biology. *in vivo*, 33(4):1011–1026, 2019.

[48] Denham Harman et al. Aging: a theory based on free radical and radiation chemistry. *Journal of Gerontology*, 1955.

[49] Ying Wang, Robyn Branicky, Alycia Noë, and Siegfried Hekimi. Superoxide dismutases: Dual roles in controlling ros damage and regulating ros signaling. *J Cell Biol*, 217(6):1915–1928, 2018.

[50] Michael Schieber and Navdeep S Chandel. Ros function in redox signaling and oxidative stress. *Current biology*, 24(10):R453–R462, 2014.

[51] Bernard M Babior. Nadph oxidase. *Current opinion in immunology*, 16(1):42–47, 2004.

[52] Claudia Lennicke, Jette Rahn, Rudolf Lichtenfels, Ludger A Wessjohann, and Barbara Seliger. Hydrogen peroxide–production, fate and role in redox signaling of tumor cells. *Cell Communication and Signaling*, 13(1):39, 2015.

[53] Jiří Kanta. The role of hydrogen peroxide and other reactive oxygen species in wound healing. *Acta Medica (Hradec Kralove)*, 54(3):97–101, 2011.

[54] Thomas Devasagayam and Jayashree P Kamat. Biological significance of singlet oxygen. 2002.

[55] Leanne B Josefsen and Ross W Boyle. Photodynamic therapy and the development of metal-based photosensitisers. *Metal-based drugs*, 2008, 2008.

[56] Marian Valko, Dieter Leibfritz, Jan Moncol, Mark T.D. Cronin, Milan Mazur, and Joshua Telser. Free radicals and antioxidants in normal physiological functions and human disease. *The International Journal of Biochemistry & Cell Biology*, 39(1):44 – 84, 2007.

ISSN 1357-2725. doi: http://dx.doi.org/10.1016/j.biocel.2006.07.001. URL http://www.sciencedirect.com/science/article/pii/S1357272506002196.

[57] Wulf Droge. Free radicals in the physiological control of cell function. *Physiological reviews*, 82(1):47–95, 2002.

[58] David B Graves. The emerging role of reactive oxygen and nitrogen species in redox biology and some implications for plasma applications to medicine and biology. *Journal of Physics D: Applied Physics*, 45(26):263001, 2012. URL http://stacks.iop.org/0022-3727/45/i=26/a=263001.

[59] Victor J. Thannickal and Barry L. Fanburg. Reactive oxygen species in cell signaling. *American Journal of Physiology - Lung Cellular and Molecular Physiology*, 279(6):L1005–L1028, 2000. ISSN 1040-0605. URL http://ajplung.physiology.org/content/279/6/L1005.

[60] Kelvin JA Davies. Oxidative stress, antioxidant defenses, and damage removal, repair, and replacement systems. *IUBMB life*, 50(4-5):279–289, 2000.

[61] Saowanee Jeayeng, Adisak Wongkajornsilp, Andrzej T Slominski, Siwanon Jirawatnotai, Somponnat Sampattavanich, and Uraiwan Panich. Nrf2 in keratinocytes modulates uvb-induced dna damage and apoptosis in melanocytes through mapk signaling. *Free Radical Biology and Medicine*, 108:918–928, 2017.

[62] Anke Schmidt, Stephan Dietrich, Anna Steuer, Klaus-Dieter Weltmann, Thomas von Woedtke, Kai Masur, and Kristian Wende. Non-thermal plasma activates human keratinocytes by stimulation of antioxidant and phase ii pathways. *J. Biol. Chem.*, 290(11):6731–6750, 2015.

[63] Antonio De Maio. Heat shock proteins: facts, thoughts, and dreams. *Shock*, 11(1):1–12, 1999.

[64] Miral Dizdaroglu. Oxidatively induced DNA damage: Mechanisms, repair and disease. *Cancer Letters*, 327(1–2):26 – 47, 2012. ISSN 0304-3835. doi: http://dx.doi.org/10.1016/j.canlet.2012.01.016. URL http://www.sciencedirect.com/science/article/pii/S0304383512000468.

[65] Angel Lanas. Role of nitric oxide in the gastrointestinal tract. *Arthritis Research & Therapy*, 10(2):S4, 2008.

[66] I Adamovich, Scott D Baalrud, A Bogaerts, PJ Bruggeman, M Cappelli, V Colombo, Uwe Czarnetzki, U Ebert, James Gary Eden, P Favia, et al. The 2017 plasma roadmap: Low temperature plasma science and technology. *Journal of Physics D: Applied Physics*, 50(32): 323001, 2017.

[67] Jin-Ren Liu, Gui-Min Xu, Xing-Min Shi, and Guan-Jun Zhang. Low temperature plasma promoting fibroblast proliferation by activating the nf-κb pathway and increasing cyclind1 expression. *Scientific reports*, 7(1):11698, 2017.

[68] Stephanie Arndt, Petra Unger, Eva Wacker, Tetsuji Shimizu, Julia Heinlin, Yang-Fang Li, Hubertus M Thomas, Gregor E Morfill, Julia L Zimmermann, Anja-Katrin Bosserhoff, et al. Cold atmospheric plasma (cap) changes gene expression of key molecules of the wound healing machinery and improves wound healing in vitro and in vivo. *PloS one*, 8(11): e79325, 2013.

[69] S Hasse, T Duong Tran, O Hahn, S Kindler, H-R Metelmann, Th von Woedtke, and K Masur. Induction of proliferation of basal epidermal keratinocytes by cold atmospheric-pressure plasma. *Clinical and experimental dermatology*, 41(2):202–209, 2016.

[70] Annemarie Barton, Kristian Wende, Lena Bundscherer, Sybille Hasse, Anke Schmidt, Sander Bekeschus, Klaus-Dieter Weltmann, Ulrike Lindequist, and Kai Masur. Nonthermal plasma increases expression of wound healing related genes in a keratinocyte cell line. *Plasma Medicine*, 3(1-2), 2013.

[71] Krishna Priya Arjunan, Gary Friedman, Alexander Fridman, and Alisa Morss Clyne. Non-thermal dielectric barrier discharge plasma induces angiogenesis through reactive oxygen species. *Journal of the Royal Society Interface*, 9(66):147–157, 2011.

[72] Stephanie Arndt, Petra Unger, Mark Berneburg, Anja-Katrin Bosserhoff, and Sigrid Karrer. Cold atmospheric plasma (cap) activates angiogenesis-related molecules in skin keratinocytes, fibroblasts and endothelial cells and improves wound angiogenesis in an autocrine and paracrine mode. *Journal of dermatological science*, 89(2):181–190, 2018.

[73] G. Isbary, J. Heinlin, T. Shimizu, J.L. Zimmermann, G. Morfill, H.-U. Schmidt, R. Monetti, B. Steffes, W. Bunk, Y. Li, T. Klaempfl, S. Karrer, M. Landthaler, and W. Stolz. Successful and safe use of 2 min cold atmospheric argon plasma in chronic wounds: results of a randomized controlled trial. *British Journal of Dermatology*, 167(2):404–410, 2012. ISSN 1365-2133. doi: 10.1111/j.1365-2133.2012.10923.x. URL `http://dx.doi.org/10.1111/j.1365-2133.2012.10923.x`.

[74] Staffan Vandersee, Heike Richter, Jürgen Lademann, Marc Beyer, Axel Kramer, Fanny Knorr, and Bernhard Lange-Asschenfeldt. Laser scanning microscopy as a means to assess the augmentation of tissue repair by exposition of wounds to tissue tolerable plasma. *Laser Physics Letters*, 11(11):115701, 2014.

[75] G. Isbary, W. Stolz, T. Shimizu, R. Monetti, W. Bunk, H.-U. Schmidt, G.E. Morfill, T.G. Klämpfl, B. Steffes, H.M. Thomas, J. Heinlin, S. Karrer, M. Landthaler, and

J.L. Zimmermann. Cold atmospheric argon plasma treatment may accelerate wound healing in chronic wounds: Results of an open retrospective randomized controlled study in vivo. *Clinical Plasma Medicine*, 1(2):25 – 30, 2013. ISSN 2212-8166. doi: http://dx.doi.org/10.1016/j.cpme.2013.06.001. URL `http://www.sciencedirect.com/science/article/pii/S2212816613000188`.

[76] F Brehmer, HA Haenssle, G Daeschlein, R Ahmed, S Pfeiffer, A Görlitz, D Simon, MP Schön, D Wandke, and S Emmert. Alleviation of chronic venous leg ulcers with a hand-held dielectric barrier discharge plasma generator (plasmaderm® vu-2010): results of a monocentric, two-armed, open, prospective, randomized and controlled trial (ncto1415622). *Journal of the European Academy of Dermatology and Venereology*, 29(1):148–155, 2015.

[77] Rutger Matthes, Ina Koban, Claudia Bender, Kai Masur, Eckhard Kindel, Klaus-Dieter Weltmann, Thomas Kocher, Axel Kramer, and Nils-Olaf Hübner. Antimicrobial efficacy of an atmospheric pressure plasma jet against biofilms of pseudomonas aeruginosa and staphylococcus epidermidis. *Plasma Processes and Polymers*, 10(2):161–166, 2013.

[78] Katja Fricke, Ina Koban, Helena Tresp, Lukasz Jablonowski, Karsten Schröder, Axel Kramer, Klaus-Dieter Weltmann, Thomas von Woedtke, and Thomas Kocher. Atmospheric pressure plasma: a high-performance tool for the efficient removal of biofilms. *PloS one*, 7 (8):e42539, 2012.

[79] Svetlana A Ermolaeva, Alexander F Varfolomeev, Marina Yu Chernukha, Dmitry S Yurov, Mikhail M Vasiliev, Anastasya A Kaminskaya, Mikhail M Moisenovich, Julia M Romanova, Arcady N Murashev, Irina I Selezneva, et al. Bactericidal effects of non-thermal argon plasma in vitro, in biofilms and in the animal model of infected wounds. *Journal of medical microbiology*, 60(1):75–83, 2011.

[80] Tetsuji Shimizu, Bernd Steffes, René Pompl, Ferdinand Jamitzky, Wolfram Bunk, Katrin Ramrath, Matthias Georgi, Wilhelm Stolz, Hans-Ulrich Schmidt, Takuya Urayama, et al. Characterization of microwave plasma torch for decontamination. *Plasma Processes and Polymers*, 5(6):577–582, 2008.

[81] Georg Daeschlein, Sebastian Scholz, Andreas Arnold, Sebastian von Podewils, Hermann Haase, Steffen Emmert, Thomas von Woedtke, Klaus-Dieter Weltmann, and Michael Jünger. In vitro susceptibility of important skin and wound pathogens against low temperature atmospheric pressure plasma jet (appj) and dielectric barrier discharge plasma (dbd). *Plasma Processes and Polymers*, 9(4):380–389, 2012.

[82] C Ulrich, F Kluschke, A Patzelt, S Vandersee, VA Czaika, H Richter, A Bob, J von Hutten,

C Painsi, R Hüge, et al. Clinical use of cold atmospheric pressure argon plasma in chronic leg ulcers: A pilot study. *Journal of wound care*, 24(5):196–203, 2015.

[83] Martin Klebes, Christin Ulrich, Franziska Kluschke, Alexa Patzelt, Staffan Vandersee, Heike Richter, Adrienne Bob, Johanna von Hutten, Jorien T Krediet, Axel Kramer, et al. Combined antibacterial effects of tissue-tolerable plasma and a modern conventional liquid antiseptic on chronic wound treatment. *Journal of biophotonics*, 8(5):382–391, 2015.

[84] G. Isbary, G. Morfill, H.U. Schmidt, M. Georgi, K. Ramrath, J. Heinlin, S. Karrer, M. Landthaler, T. Shimizu, B. Steffes, W. Bunk, R. Monetti, J.L. Zimmermann, R. Pompl, and W. Stolz. A first prospective randomized controlled trial to decrease bacterial load using cold atmospheric argon plasma on chronic wounds in patients. *British Journal of Dermatology*, 163(1):78–82, 2010. ISSN 1365-2133. doi: 10.1111/j.1365-2133.2010.09744.x. URL `http://dx.doi.org/10.1111/j.1365-2133.2010.09744.x`.

[85] Kristian Wende, Kati Landsberg, Ulrike Lindequist, Klaus-Dieter Weltmann, and Thomas von Woedtke. Distinctive activity of a nonthermal atmospheric-pressure plasma jet on eukaryotic and prokaryotic cells in a cocultivation approach of keratinocytes and microorganisms. *IEEE Transactions on Plasma Science*, 38(9):2479–2485, 2010.

[86] Anke Schmidt, Kristian Wende, Sander Bekeschus, Lena Bundscherer, Annemarie Barton, Katja Ottmüller, Klaus-Dieter Weltmann, and Kai Masur. Non-thermal plasma treatment is associated with changes in transcriptome of human epithelial skin cells. *Free radical research*, 47(8):577–592, 2013.

[87] Kristian Wende, Annemarie Barton, Sander Bekeschus, Lena Bundscherer, Anke Schmidt, Klaus-Dieter Weltmann, and Kai Masur. Proteomic tools to characterize non-thermal plasma effects in eukaryotic cells. *Plasma Medicine*, 3(1-2), 2013.

[88] Anke Schmidt, Sander Bekeschus, Katja Jarick, Sybille Hasse, Thomas von Woedtke, and Kristian Wende. Cold physical plasma modulates p53 and mitogen-activated protein kinase signaling in keratinocytes. *Oxidative Medicine and Cellular Longevity*, 2019, 2019.

[89] Sander Bekeschus, Julia Kolata, Anne Muller, Axel Kramer, Klaus-Dieter Weltmann, Barbara Broker, and Kai Masur. Differential viability of eight human blood mononuclear cell subpopulations after plasma treatment. *Plasma Medicine*, 3(1-2), 2013.

[90] Sander Bekeschus, Kai Masur, Julia Kolata, Kristian Wende, Anke Schmidt, Lena Bundscherer, Annemarie Barton, Axel Kramer, Barbara Bröker, and Klaus-Dieter Weltmann. Human mononuclear cell survival and proliferation is modulated by cold atmospheric plasma jet. *Plasma Processes and Polymers*, 10(8):706–713, 2013.

[91] Stephanie Arndt, Michael Landthaler, Julia L Zimmermann, Petra Unger, Eva Wacker, Tetsuji Shimizu, Yang-Fang Li, Gregor E Morfill, Anja-Katrin Bosserhoff, and Sigrid Karrer. Effects of cold atmospheric plasma (cap) on ß-defensins, inflammatory cytokines, and apoptosis-related molecules in keratinocytes in vitro and in vivo. *PLoS One*, 10(3):e0120041, 2015.

[92] J. Lademann, C. Ulrich, A. Patzelt, H. Richter, F. Kluschke, M. Klebes, O. Lademann, A. Kramer, K.D. Weltmann, and B. Lange-Asschenfeldt. Risk assessment of the application of tissue-tolerable plasma on human skin. *Clinical Plasma Medicine*, 1(1):5 – 10, 2013. ISSN 2212-8166. doi: http://dx.doi.org/10.1016/j.cpme.2013.01.001. URL `http://www.sciencedirect.com/science/article/pii/S2212816613000024`.

[93] K Wende, S Bekeschus, A Schmidt, L Jatsch, S Hasse, KD Weltmann, K Masur, and Th von Woedtke. Risk assessment of a cold argon plasma jet in respect to its mutagenicity. *Mutation Research/Genetic Toxicology and Environmental Mutagenesis*, 798:48–54, 2016.

[94] T Maisch, AK Bosserhoff, P Unger, J Heider, T Shimizu, JL Zimmermann, GE Morfill, M Landthaler, and S Karrer. Investigation of toxicity and mutagenicity of cold atmospheric argon plasma. *Environmental and molecular mutagenesis*, 58(3):172–177, 2017.

[95] Et-Touhami Es-Sebbar, Christian Sarra-Bournet, Nicolas Naudé, Françoise Massines, and Nicolas Gherardi. Absolute nitrogen atom density measurements by two-photon laser-induced fluorescence spectroscopy in atmospheric pressure dielectric barrier discharges of pure nitrogen. *Journal of Applied Physics*, 106(7):073302, 2009.

[96] K. Niemi, D. O'Connell, N. de Oliveira, D. Joyeux, L. Nahon, J. P. Booth, and T. Gans. Absolute atomic oxygen and nitrogen densities in radio-frequency driven atmospheric pressure cold plasmas: Synchrotron vacuum ultra-violet high-resolution fourier-transform absorption measurements. *Applied Physics Letters*, 103(3):034102, 2013. doi: http://dx.doi.org/10.1063/1.4813817. URL `http://scitation.aip.org/content/aip/journal/apl/103/3/10.1063/1.4813817`.

[97] J Dedrick, Sandra Schröter, Kari Niemi, Apiwat Wijaikhum, Erik Wagenaars, Nelson de Oliveira, Laurent Nahon, Jean-Paul Booth, Deborah O'Connell, and Timo Gans. Controlled production of atomic oxygen and nitrogen in a pulsed radio-frequency atmospheric-pressure plasma. *Journal of Physics D: Applied Physics*, 50(45):455204, 2017.

[98] Apiwat Wijaikhum, Daniel Schröder, Sandra Schröter, Andrew Robert Gibson, Kari Niemi, Jochen Friderich, Arthur Greb, Volker Schulz-von der Gathen, Deborah O'Connell, and Timo Gans. Absolute ozone densities in a radio-frequency driven atmospheric pressure plasma using two-beam uv-led absorption spectroscopy and numerical simulations. *Plasma Sources Science and Technology*, 26(11):115004, 2017.

[99] Sandra Schröter, Apiwat Wijaikhum, Andrew R Gibson, Andrew West, Helen L Davies, Nicolas Minesi, James Dedrick, Erik Wagenaars, Nelson de Oliveira, Laurent Nahon, et al. Chemical kinetics in an atmospheric pressure helium plasma containing humidity. *Physical Chemistry Chemical Physics*, 2018.

[100] M Capitelli, G Colonna, G D'Ammando, A Laricchiuta, and LD Pietanza. Non-equilibrium vibrational and electron energy distribution functions in mtorr, high-electron-density nitrogen discharges and afterglows. *Plasma Sources Science and Technology*, 26(3):034004, 2017.

[101] Vasco Guerra, Paulo A Sá, and Jorge Loureiro. Nitrogen pink afterglow: the mystery continues. In *Journal of Physics: Conference Series*, volume 63, page 012007. IOP Publishing, 2007.

[102] V Guerra, A Tejero-del Caz, C D Pintassilgo, and L. L. Alves. Modelling $n_2 - o_2$ plasmas: Volume and surface kinetics. *Plasma Sources Sci. Technol.*, 28:073001, 2019.

[103] PA Sá, V Guerra, J Loureiro, and N Sadeghi. Self-consistent kinetic model of the short-lived afterglow in flowing nitrogen. *Journal of Physics D: Applied Physics*, 37(2):221, 2004.

[104] AV Volynets, DV Lopaev, TV Rakhimova, AA Chukalovsky, Yu A Mankelevich, NA Popov, AI Zotovich, and AT Rakhimov. N2 dissociation and kinetics of n (4s) atoms in nitrogen dc glow discharge. *Journal of Physics D: Applied Physics*, 51(36):364002, 2018.

[105] V Guerra and JMAH Loureiro. Electron and heavy particle kinetics in a low-pressure nitrogen glow discharge. *Plasma Sources Science and Technology*, 6(3):361, 1997.

[106] Carlos D Pintassilgo and Vasco Guerra. Modelling of the temporal evolution of the gas temperature in N_2 discharges. *Plasma Sources Sci. Technol.*, 26(5):055001, 2017.

[107] RN Franklin. The role of $O_2(a)$ metastables and associative detachment in discharges in oxygen. *Journal of Physics D: Applied Physics*, 34(12):1834, 2001.

[108] Andrew Robert Gibson, Mickaël Foucher, Daniil Marinov, Pascal Chabert, Timo Gans, Mark J Kushner, and Jean-Paul Booth. The role of thermal energy accommodation and atomic recombination probabilities in low pressure oxygen plasmas. *Plasma physics and controlled fusion*, 59(2):024004, 2017.

[109] Boris F Gordiets, Carlos M Ferreira, Vasco L Guerra, Jorge MAH Loureiro, Jacimar Nahorny, Daniel Pagnon, Michel Touzeau, and Marinette Vialle. Kinetic model of a low-pressure N_2-O_2 flowing glow discharge. *IEEE Transactions on Plasma Science*, 23(4):750–768, 1995.

[110] V Guerra and J Loureiro. Non-equilibrium coupled kinetics in stationary N_2 - O_2 discharges. *Journal of Physics D: Applied Physics*, 28(9):1903, 1995. URL http://stacks.iop.org/0022-3727/28/i=9/a=018.

[111] V Guerra and J Loureiro. Self-consistent electron and heavy-particle kinetics in a low-pressure $N_2 - O_2$ glow discharge. *Plasma Sources Science and Technology*, 6(3):373, 1997. URL http://stacks.iop.org/0963-0252/6/i=3/a=014.

[112] V Guerra, E Galiaskarov, and J Loureiro. Dissociation mechanisms in nitrogen discharges. *Chem Phys Lett*, 371(5):576–581, 2003.

[113] V Guerra, PA Sá, and J Loureiro. Kinetic modeling of low-pressure nitrogen discharges and post-discharges. *Eur. Phys. J. Appl. Phys.*, 2004.

[114] C D Pintassilgo, J Loureiro, and V Guerra. Modelling of a N_2-O_2 flowing afterglow for plasma sterilization. *Journal of Physics D: Applied Physics*, 38(3):417, 2005. URL http://stacks.iop.org/0022-3727/38/i=3/a=011.

[115] SE Babayan, G Ding, GR Nowling, X Yang, and RF Hicks. Characterization of the active species in the afterglow of a nitrogen and helium atmospheric-pressure plasma. *Plasma Chemistry and Plasma Processing*, 22(2):255–269, 2002.

[116] Ihor Korolov, Zoltan Donko, Gerrit Hübner, Lena Bischoff, Peter Hartmann, Timo Gans, Yue Liu, Thomas Mussenbrock, and Julian Schulze. Control of electron dynamics, radical and metastable species generation in atmospheric pressure rf plasma jets by voltage waveform tailoring. *Plasma Sources Science and Technology*, 2019.

[117] C Lazarou, D Koukounis, AS Chiper, C Costin, I Topala, and George E Georghiou. Numerical modeling of the effect of the level of nitrogen impurities in a helium parallel plate dielectric barrier discharge. *Plasma Sources Science and Technology*, 24(3):035012, 2015.

[118] K Niemi, J Waskoenig, N Sadeghi, T Gans, and D O'Connell. The role of helium metastable states in radio-frequency driven helium–oxygen atmospheric pressure plasma jets: measurement and numerical simulation. *Plasma Sources Science and Technology*, 20(5):055005, 2011.

[119] Tomoyuki Murakami, Kari Niemi, Timo Gans, Deborah O'Connell, and William G Graham. Chemical kinetics and reactive species in atmospheric pressure helium–oxygen plasmas with humid-air impurities. *Plasma Sources Science and Technology*, 22(1):015003, 2013.

[120] W Van Gaens and A Bogaerts. Kinetic modelling for an atmospheric pressure argon plasma jet in humid air. *Journal of Physics D: Applied Physics*, 46(27):275201, 2013. URL http://stacks.iop.org/0022-3727/46/i=27/a=275201.

[121] Kinga Kutasi, Vasco Guerra, and Paulo Sá. Theoretical insight into ar–o2 surface-wave microwave discharges. *Journal of Physics D: Applied Physics*, 43(17):175201, 2010.

[122] Kinga Kutasi, Cédric Noël, Thierry Belmonte, and Vasco Guerra. Tuning the afterglow plasma composition in $Ar/N_2/O_2$ mixtures: characteristics of a flowing surface-wave microwave discharge system. *Plasma Sources Science and Technology*, 25(5):055014, 2016. URL `http://stacks.iop.org/0963-0252/25/i=5/a=055014`.

[123] C Lazarou, T Belmonte, AS Chiper, and GE Georghiou. Numerical modelling of the effect of dry air traces in a helium parallel plate dielectric barrier discharge. *Plasma Sources Science and Technology*, 25(5):055023, 2016.

[124] J Hugill and T Saktioto. A simplified chemical kinetic model for slightly ionized, atmospheric pressure nitrogen plasmas. *Plasma Sources Science and Technology*, 10(1):38, 2001.

[125] L Prevosto, H Kelly, and B Mancinelli. Modelling of an atmospheric pressure nitrogen glow discharge operating in high-gas temperature regimes. *Plasma Chemistry and Plasma Processing*, 36(4):973–992, 2016.

[126] Weizong Wang, Bhaskar Patil, Stjin Heijkers, Volker Hessel, and Annemie Bogaerts. Nitrogen fixation by gliding arc plasma: Better insight by chemical kinetics modelling. *ChemSusChem*, 10(10):2145–2157, 2017.

[127] Gianpiero Colonna, Vincenzo Laporta, Roberto Celiberto, Mario Capitelli, and Jonathan Tennyson. Non-equilibrium vibrational and electron energy distributions functions in atmospheric nitrogen ns pulsed discharges and μs post-discharges: the role of electron molecule vibrational excitation scaling-laws. *Plasma Sources Science and Technology*, 24(3): 035004, 2015.

[128] Natalia Yu Babaeva and Mark J Kushner. Reactive fluxes delivered by dielectric barrier discharge filaments to slightly wounded skin. *Journal of Physics D: Applied Physics*, 46(2): 025401, 2012.

[129] Amanda M Lietz and Mark J Kushner. Air plasma treatment of liquid covered tissue: long timescale chemistry. *J. Phys. D: Appl. Phys.*, 49(42):425204, 2016.

[130] LL Alves, A Bogaerts, V Guerra, and MM Turner. Foundations of modelling of nonequilibrium low-temperature plasmas. *Plasma Sources Science and Technology*, 27(2):023002, 2018.

[131] Andrew Hurlbatt, Andrew Robert Gibson, Sandra Schröter, Jérôme Bredin, Alexander Paul Stuart Foote, Pascaline Grondein, Deborah O'Connell, and Timo Gans. Concepts, capabilities, and limitations of global models: a review. *Plasma Processes and Polymers*, 14 (1-2):1600138, 2017.

[132] Miles M Turner. Uncertainty and error in complex plasma chemistry models. *Plasma Sources Science and Technology*, 24(3):035027, 2015. URL http://stacks.iop.org/0963-0252/24/i=3/a=035027.

[133] D. Shane Stafford and Mark J. Kushner. $O_2(^1\Delta)$ production in He/O_2 mixtures in flowing low pressure plasmas. *J. Appl. Phys.*, 96(5):2451–2465, 2004. doi: http://dx.doi.org/10.1063/1.1768615. URL http://scitation.aip.org/content/aip/journal/jap/96/5/10.1063/1.1768615.

[134] Peter N Brown, George D Byrne, and Alan C Hindmarsh. Vode: A variable-coefficient ode solver. *SIAM journal on scientific and statistical computing*, 10(5):1038–1051, 1989.

[135] AV Phelps. The diffusion of charged particles in collisional plasmas: Free and ambipolar diffusion at low and moderate pressures. *Journal of research of the National Institute of Standards and Technology*, 95(4):407, 1990.

[136] Chang Sung Moon, Keigo Takeda, Seigo Takashima, Makoto Sekine, Yuichi Setsuhara, Masaharu Shiratani, and Masaru Hori. Surface loss probabilities of h and n radicals on different materials in afterglow plasmas employing h 2 and n 2 mixture gases. *Journal of Applied Physics*, 107(10):103310, 2010.

[137] Sandra Schröter, Andrew R Gibson, Mark J Kushner, Timo Gans, and Deborah O'Connell. Numerical study of the influence of surface reaction probabilities on reactive species in an rf atmospheric pressure plasma containing humidity. *Plasma Physics and Controlled Fusion*, 60(1):014035, 2017.

[138] https://fr.lxcat.net/. Accessed: 13/09/2019. URL https://fr.lxcat.net/.

[139] https://users.ba.cnr.it/imip/cscpal38/phys4entry/index.html. Accessed: 13/09/2019.

[140] G Colonna and M Capitelli. Self-consistent model of chemical, vibrational, electron kinetics in nozzle expansion. *J Thermophys Heat Transfer*, 15(3):308–316, 2001.

[141] V Laporta, DA Little, R Celiberto, and J Tennyson. Electron-impact resonant vibrational excitation and dissociation processes involving vibrationally excited n2 molecules. *Plasma Sources Science and Technology*, 23(6):065002, 2014.

[142] JE Morgan and HI Schiff. The study of vibrationally excited n2 molecules with the aid of an isothermal calorimeter. *Canadian Journal of Chemistry*, 41(4):903–912, 1963.

[143] Graham Black, Henry Wise, Samuel Schechter, and Robert L Sharpless. Measurements of vibrationally excited molecules by raman scattering. ii. surface deactivation of vibrationally excited n2. *The Journal of Chemical Physics*, 60(9):3526–3536, 1974.

[144] GJM Hagelaar and LC Pitchford. Solving the boltzmann equation to obtain electron transport coefficients and rate coefficients for fluid models. *Plasma Sources Science and Technology*, 14(4):722, 2005.

[145] V Laporta, CM Cassidy, J Tennyson, and R Celiberto. Electron-impact resonant vibration excitation cross sections and rate coefficients for carbon monoxide. *Plasma Sources Science and Technology*, 21(4):045005, 2012.

[146] Winifred M Huo, Thomas L Gibson, Marco AP Lima, and Vincent McKoy. Schwinger multichannel study of the π g 2 shape resonance in n 2. *Phys. Rev. A*, 36(4):1632, 1987.

[147] www.lxcat.net IST-Lisbon Database. Accessed: 29/03/18.

[148] B Gordiets, CM Ferreira, MJ Pinheiro, and A Ricard. Self-consistent kinetic model of low-pressure-flowing discharges: I. volume processes. *Plasma Sources Science and Technology*, 7 (3):363, 1998.

[149] Luís Lemos Alves, L Marques, Carlos D Pintassilgo, Gaëtan Wattieaux, ET Es-Sebbar, Johannes Berndt, E Kovacević, Nathalie Carrasco, Laïfa Boufendi, and Guy Cernogora. Capacitively coupled radio-frequency discharges in nitrogen at low pressures. *Plasma Sources Sci. Technol.*, 21(4):045008, 2012.

[150] Gert Due Billing and ER Fisher. Vv and vt rate coefficients in n2 by a quantum-classical model. *Chem. Phys.*, 43(3):395–401, 1979.

[151] EG Thorsteinsson and JT Gudmundsson. A global (volume averaged) model of a nitrogen discharge: I. steady state. *Plasma Sources Science and Technology*, 18(4):045001, 2009.

[152] Klaus-Dieter Weltmann, Juergen F Kolb, Marcin Holub, Dirk Uhrlandt, Milan Šimek, Kostya Ostrikov, Satoshi Hamaguchi, Uroš Cvelbar, Mirko Černák, Bruce Locke, et al. The future for plasma science and technology. *Plasma Processes and Polymers*, 16(1):1800118, 2019.

[153] Adriana Annušová, Daniil Marinov, Jean-Paul Booth, Nishant Sirse, Mário Lino da Silva, Bruno Lopez, and Vasco Guerra. Kinetics of highly vibrationally excited o2 (x) molecules in inductively-coupled oxygen plasmas. *Plasma Sources Science and Technology*, 27(4):045006, 2018.

[154] Russ R Laher and Forrest R Gilmore. Updated excitation and ionization cross sections for electron impact on atomic oxygen. *Journal of Physical and Chemical Reference Data*, 19(1): 277–305, 1990.

[155] SA Lawton and AV Phelps. Excitation of the b 1σ+ g state of O_2 by low energy electrons. *The Journal of Chemical Physics*, 69(3):1055–1068, 1978.

[156] PD Burrow. Dissociative attachment from the o2 (a 1δ g) state. *The Journal of Chemical Physics*, 59(9):4922–4931, 1973.

[157] S Matejcik, A Kiendler, P Cicman, J Skalny, P Stampfli, E Illenberger, Y Chu, A Stamatovic, and TD Märk. Electron attachment to molecules and clusters of atmospheric relevance: oxygen and ozone. *Plasma Sources Science and Technology*, 6(2):140, 1997.

[158] B Gordiets and A Ricard. Production of n, o and no in n2-o2 flowing discharges. *Plasma Sources Science and Technology*, 2(3):158, 1993.

[159] GE Beale Jr and HP Broida. Spectral study of a visible, short-duration afterglow in nitrogen. *The Journal of Chemical Physics*, 31(4):1030–1034, 1959.

[160] PA Sa and J Loureiro. A time-dependent analysis of the nitrogen afterglow in and-ar microwave discharges. *Journal of Physics D: Applied Physics*, 30(16):2320, 1997.

[161] N Sadeghi, C Foissac, and P Supiot. Kinetics of $N_2(A)$ molecules and ionization mechanisms in the afterglow of a flowing N_2 microwave discharge. *J. Phys. D: Appl. Phys.*, 34(12): 1779, 2001.

[162] Tomoyuki Murakami, Kari Niemi, Timo Gans, Deborah O'Connell, and William G Graham. Afterglow chemistry of atmospheric-pressure helium oxygen plasmas with humid air impurity. *Plasma Sources Science and Technology*, 23(2):025005, 2014.

[163] František Krčma, Věra Mazánková, Ivo Soural, and Vasco Guerra. Power dependence of the pink afterglow in flowing postdischarge in pure nitrogen. *IEEE Transactions on Plasma Science*, 42(10):2384–2385, 2014.

[164] ME Whitson Jr and RJ McNeal. Temperature dependence of the quenching of vibrationally excited N_2 by NO and H_2O. *The Journal of Chemical Physics*, 66(6):2696–2700, 1977.

[165] Atsushi Komuro, Ryo Ono, and Tetsuji Oda. Kinetic model of vibrational relaxation in a humid-air pulsed corona discharge. *Plasma Sources Science and Technology*, 19(5):055004, 2010.

[166] Agata Przekora, Joanna Pawlat, Piotr Terebun, David Duday, Cristina Canal, Sophie Hermans, Maïté Audemar, Cédric Labay, Jean-Sébastien Thomann, and Grazyna Ginalska. The effect of low temperature atmospheric nitrogen plasma on MC3T3-E1 preosteoblast proliferation and differentiation in vitro. *Journal of Physics D: Applied Physics*, 52(27):275401, 2019.

[167] Sung Un Kang, Jae Won Choi, Jae Won Chang, Yeon Soo Kim, Ju Kyeong Park, Yang Eun Kim, Yun Sang Lee, Sang Sik Yang, Chul-Ho Kim, et al. N2 non-thermal atmospheric pressure plasma promotes wound healing in vitro and in vivo: Potential modulation of adhesion molecules and matrix metalloproteinase-9. *Experimental dermatology*, 26(2):163–170, 2017.

[168] A. Kramer, J. Lademann, C. Bender, A. Sckell, B. Hartmann, S. Münch, P. Hinz, A. Ekkernkamp, R. Matthes, I. Koban, I. Partecke, C.D. Heidecke, K. Masur, S. Reuter, K.D. Weltmann, S. Koch, and O. Assadian. Suitability of tissue tolerable plasmas (ttp) for the management of chronic wounds. *Clinical Plasma Medicine*, 1(1):11 – 18, 2013. ISSN 2212-8166. doi: http://dx.doi.org/10.1016/j.cpme.2013.03.002. URL `http://www.sciencedirect.com/science/article/pii/S2212816613000048`.

[169] Arnaud Bultel, Bruno G. Chéron, Anne Bourdon, Ousmanou Motapon, and Ioan F. Schneider. Collisional-radiative model in air for earth re-entry problems. *Physics of Plasmas*, 13(4):043502, 2006. doi: http://dx.doi.org/10.1063/1.2194827. URL `http://scitation.aip.org/content/aip/journal/pop/13/4/10.1063/1.2194827`.

[170] Ann C Gentile and Mark J Kushner. Reaction chemistry and optimization of plasma remediation of n x o y from gas streams. *Journal of applied physics*, 78(3):2074–2085, 1995.

[171] Stefan Frank, Heiko Kämpfer, Christian Wetzler, and Josef Pfeilschifter. Nitric oxide drives skin repair: novel functions of an established mediator. *Kidney international*, 61(3):882–888, 2002.

[172] Anatoly B Shekhter, Vladimir A Serezhenkov, Tatiana G Rudenko, Alexander V Pekshev, and Anatoly F Vanin. Beneficial effect of gaseous nitric oxide on the healing of skin wounds. *Nitric oxide*, 12(4):210–219, 2005.

[173] Alexander V Pekshev, Anatoly B Shekhter, Andrey B Vagapov, Nikolay A Sharapov, and Anatoly F Vanin. Study of plasma-chemical no-containing gas flow for treatment of wounds and inflammatory processes. *Nitric Oxide*, 73:74–80, 2018.

[174] Georg Isbary, Tetsuji Shimizu, Yang-Fang Li, Wilhelm Stolz, Hubertus M Thomas, Gregor E Morfill, and Julia L Zimmermann. Cold atmospheric plasma devices for medical issues. *Expert review of medical devices*, 10(3):367–377, 2013.

[175] John W Birks, Peter C Andersen, Craig J Williford, Andrew A Turnipseed, Stanley E Strunk, Christine A Ennis, and Erick Mattson. Folded tubular photometer for atmospheric measurements of no 2 and no. *Atmospheric Measurement Techniques*, 11(5):2821–2835, 2018.

[176] AV Pipa, J Koskulics, R Brandenburg, and T Hoder. The simplest equivalent circuit of a

pulsed dielectric barrier discharge and the determination of the gas gap charge transfer. *Review of Scientific Instruments*, 83(11):115112, 2012.

[177] Andrei V Pipa and Ronny Brandenburg. The equivalent circuit approach for the electrical diagnostics of dielectric barrier discharges: The classical theory and recent developments. *Atoms*, 7(1):14, 2019.

[178] Shuhai Liu and Manfred Neiger. Excitation of dielectric barrier discharges by unipolar submicrosecond square pulses. *Journal of Physics D: Applied Physics*, 34(11):1632, 2001.

[179] Shuhai Liu and Manfred Neiger. Electrical modelling of homogeneous dielectric barrier discharges under an arbitrary excitation voltage. *Journal of Physics D: Applied Physics*, 36 (24):3144, 2003.

[180] Ronny Brandenburg. Dielectric barrier discharges: progress on plasma sources and on the understanding of regimes and single filaments. *Plasma Sources Science and Technology*, 26 (5):053001, 2017.

[181] AV Pipa, T Hoder, and R Brandenburg. On the role of capacitance determination accuracy for the electrical characterization of pulsed driven dielectric barrier discharges. *Contributions to Plasma Physics*, 53(6):469–480, 2013.

[182] Amit Soneja, Magdalena Drews, and Tadeusz Malinski. Role of nitric oxide, nitroxidative and oxidative stress in wound healing. *Pharmacol. Rep.*, 57:108, 2005.

[183] IA Kossyi, A Yu Kostinsky, AA Matveyev, and VP Silakov. Kinetic scheme of the non-equilibrium discharge in nitrogen-oxygen mixtures. *Plasma Sources Science and Technology*, 1(3):207, 1992.

[184] P Coche, V Guerra, and LL Alves. Microwave air plasmas in capillaries at low pressure I. self-consistent modeling. *Journal of Physics D: Applied Physics*, 49(23):235207, 2016.

[185] Kinga Kutasi, Bachir Saoudi, Carlos D. Pintassilgo, Jorge Loureiro, and Michel Moisan. Modelling the low-pressure N_2-O_2 plasma afterglow to determine the kinetic mechanisms controlling the uv emission intensity and its spatial distribution for achieving an efficient sterilization process. *Plasma Processes and Polymers*, 5(9):840–852, 2008. ISSN 1612-8869. doi: 10.1002/ppap.200800085. URL `http://dx.doi.org/10.1002/ppap.200800085`.

[186] Giuseppe Valacchi, V Fortino, and V Bocci. The dual action of ozone on the skin. *British Journal of Dermatology*, 153(6):1096–1100, 2005.

[187] Farrukh Afaq, Mohammad Abu Zaid, Edward Pelle, Naghma Khan, Deeba N Syed,

Mary S Matsui, Daniel Maes, and Hasan Mukhtar. Aryl hydrocarbon receptor is an ozone sensor in human skin. *Journal of Investigative Dermatology*, 129(10):2396–2403, 2009.

[188] Klaus Seiersen, J Bak, Henrik Bluhme, MJ Jensen, S Brøndsted Nielsen, and LH Andersen. Electron-impact detachment of O_3^-, NO_3^- and SO_2^- ions. *Physical Chemistry Chemical Physics*, 5(21):4814–4820, 2003.

[189] Shaun G Ard, Joshua J Melko, Bin Jiang, Yongle Li, Nicholas S Shuman, Hua Guo, and Albert A Viggiano. Temperature dependences for the reactions of O_2^- and O^- with N and O atoms in a selected-ion flow tube instrument. *The Journal of chemical physics*, 139(14): 144302, 2013.

[190] B Eliasson and U Kogelschatz. Electron impact dissociation in oxygen. *Journal of Physics B: Atomic and Molecular Physics*, 19(8):1241, 1986.

[191] V Guerra and J Loureiro. Kinetic model of a low-pressure microwave discharge in $O_2 - H_2$ including the effects of O^- ions on the characteristics for plasma maintenance. *Plasma Sources Science and Technology*, 8(1):110, 1999.

[192] T Belmonte, T Czerwiec, J Gavillet, and H Michel. Synthesis of zirconia thin films by RPECVD: modeling of $Ar - O_2$ post-discharge and comparison between $Ar - -O_2$ and $Ar - -O_2 - -H_2$ post-discharges processes. *Surface and Coatings Technology*, 97(1-3):642–648, 1997.

[193] Chandan K Sen, Gayle M Gordillo, Sashwati Roy, Robert Kirsner, Lynn Lambert, Thomas K Hunt, Finn Gottrup, Geoffrey C Gurtner, and Michael T Longaker. Human skin wounds: a major and snowballing threat to public health and the economy. *Wound Repair and Regeneration*, 17(6):763–771, 2009.

[194] Andrew R Gibson and Timo Gans. Controlling plasma properties under differing degrees of electronegativity using odd harmonic dual frequency excitation. *Plasma Sources Science and Technology*, 26(11):115007, 2017.

[195] Andrew R Gibson, Zoltán Donkó, Layla Alelyani, Lena Bischoff, Gerrit Hübner, Jérôme Bredin, Scott Doyle, Ihor Korolov, Kari Niemi, Thomas Mussenbrock, et al. Disrupting the spatio-temporal symmetry of the electron dynamics in atmospheric pressure plasmas by voltage waveform tailoring. *Plasma Sources Science and Technology*, 28(1):01LT01, 2019.

[196] Julian Balzer, Kiara Heuer, Erhan Demir, Martin A Hoffmanns, Sabrina Baldus, Paul C Fuchs, Peter Awakowicz, Christoph V Suschek, and Christian Opländer. Non-thermal dielectric barrier discharge (DBD) effects on proliferation and differentiation of human fibroblasts are primary mediated by hydrogen peroxide. *PLoS One*, 10(12):e0144968, 2015.

[197] Anke Schmidt, Sander Bekeschus, Helena Jablonowski, Annemarie Barton, Klaus-Dieter Weltmann, and Kristian Wende. Role of ambient gas composition on cold physical plasma-elicited cell signaling in keratinocytes. *Biophysical Journal*, 112(11):2397–2407, 2017.

[198] Adam M Hirst, Fiona M Frame, Manit Arya, Norman J Maitland, and Deborah O'Connell. Low temperature plasmas as emerging cancer therapeutics: the state of play and thoughts for the future. *Tumor Biology*, pages 1–11, 2016.

[199] Bennett G Childs, Darren J Baker, James L Kirkland, Judith Campisi, and Jan M van Deursen. Senescence and apoptosis: dueling or complementary cell fates? *EMBO reports*, 15(11):1139–1153, 2014.

[200] Ittai Ben-Porath and Robert A Weinberg. The signals and pathways activating cellular senescence. *The international journal of biochemistry & cell biology*, 37(5):961–976, 2005.

[201] Petra Boukamp, Rule T Petrussevska, Dirk Breitkreutz, Jurgen Hornung, Alex Markham, and Norbert E Fusenig. Normal keratinization in a spontaneously immortalized aneuploid human keratinocyte cell line. *The Journal of cell biology*, 106(3):761–771, 1988.

[202] Irma Colombo, Enrico Sangiovanni, Roberta Maggio, Carlo Mattozzi, Stefania Zava, Yolanda Corbett, Marco Fumagalli, Claudia Carlino, Paola Antonia Corsetto, Diletta Scaccabarozzi, et al. Hacat cells as a reliable in vitro differentiation model to dissect the inflammatory/repair response of human keratinocytes. *Mediators of Inflammation*, 2017, 2017.

[203] Gurvinder Kaur and Jannette M. Dufour. Cell lines. *Spermatogenesis*, 2(1):1–5, 2012. doi: 10.4161/spmg.19885. URL `https://doi.org/10.4161/spmg.19885`. PMID: 22553484.

[204] Maria Feoktistova, Peter Geserick, and Martin Leverkus. Crystal violet assay for determining viability of cultured cells. *Cold Spring Harbor Protocols*, 2016(4):pdb–prot087379, 2016.

[205] L Liu, H Xie, X Chen, W Shi, X Xiao, D Lei, and J Li. Differential response of normal human epidermal keratinocytes and hacat cells to hydrogen peroxide-induced oxidative stress. *Clinical and Experimental Dermatology: Experimental dermatology*, 37(7):772–780, 2012.

[206] Sarah J Duellman, Wenhui Zhou, Poncho Meisenheimer, Gediminas Vidugiris, James J Cali, Prson Gautam, Krister Wennerberg, and Jolanta Vidugiriene. Bioluminescent, nonlytic, real-time cell viability assay and use in inhibitor screening. *Assay and drug development technologies*, 13(8):456–465, 2015.

[207] Terry L Riss, Richard A Moravec, Andrew L Niles, Sarah Duellman, Hélène A Benink, Tracy J Worzella, and Lisa Minor. Cell viability assays. In *Assay Guidance Manual [Internet]*. Eli Lilly & Company and the National Center for Advancing Translational Sciences, 2016.

[208] D. A. Mendis, M. Rosenberg, and F. Azam. A note on the possible electrostatic disruption of bacteria. *IEEE Transactions on Plasma Science*, 28(4):1304–1306, Aug 2000. ISSN 0093-3813. doi: 10.1109/27.893321.

[209] Angela Privat-Maldonado, Yury Gorbanev, Deborah O'Connell, R Vann, Victor Chechik, and MW van der Woude. Non-target biomolecules alter macromolecular changes induced by bactericidal low-temperature plasma. *IEEE Transactions on Radiation and Plasma Medical Sciences*, 2017.

[210] James C Weaver. Electroporation of cells and tissues. *IEEE Transactions on plasma science*, 28(1):24–33, 2000.

[211] Mark A Messerli and David M Graham. Extracellular electrical fields direct wound healing and regeneration. *The Biological Bulletin*, 221(1):79–92, 2011.

[212] PJ Bruggeman, Mark J Kushner, Bruce R Locke, Johannes GE Gardeniers, WG Graham, David B Graves, RCHM Hofman-Caris, Dragana Maric, Jonathan P Reid, Elisa Ceriani, et al. Plasma–liquid interactions: a review and roadmap. *Plasma sources science and technology*, 25(5):053002, 2016.

[213] Sabine Werner, Thomas Krieg, and Hans Smola. Keratinocyte–fibroblast interactions in wound healing. *Journal of Investigative Dermatology*, 127(5):998–1008, 2007.

[214] Charles W Wyble, Karen L Hynes, Jaya Kuchibhotla, Benjamin C Marcus, Dennis Hallahan, and Bruce L Gewertz. Tnf-α and IL-1 upregulate membrane-bound and soluble E-selectin through a common pathway. *Journal of Surgical Research*, 73(2):107–112, 1997.

[215] Tatsuo Tabata, Toshizo Shirai, Masao Sataka, and Hirotaka Kubo. Analytic cross sections for electron impact collisions with nitrogen molecules. *Atomic Data and Nuclear Data Tables*, 92(3):375–406, 2006.

[216] RT Brinkmann and S Trajmar. Electron impact excitation of N_2. 1970.

[217] Yukikazu Itikawa, M Hayashi, A Ichimura, K Onda, K Sakimoto, K Takayanagi, M Nakamura, H Nishimura, and T Takayanagi. Cross sections for collisions of electrons and photons with nitrogen molecules. *Journal of physical and chemical reference data*, 15(3):985–1010, 1986.

[218] PC Cosby. Electron-impact dissociation of nitrogen. *The Journal of chemical physics*, 98(12): 9544–9553, 1993.

[219] L Vriens. Calculation of absolute ionisation cross sections of $He, He*, He^+, Ne, Ne*, Ne^+, Ar, Ar*, Hg$ and Hg. *Physics letters*, 8(4):260–261, 1964.

[220] D Ton-That and MR Flannery. Cross sections for ionization of metastable rare-gas atoms ($Ne*, Ar*, Kr*, Xe*$) and of metastable N_2*, $CO*$ molecules by electron impact. *Physical Review A*, 15(2):517, 1977.

[221] Sydney Geltman. Free-free radiation in electron-neutral atom collisions. *Journal of Quantitative Spectroscopy and Radiative Transfer*, 13(7):601–613, 1973.

[222] Ronald JW Henry, PG Burke, and A-L Sinfailam. Scattering of electrons by C, N, O, N+, O+, and O++. *Physical Review*, 178(1):218, 1969.

[223] J Brian and A Mitchell. The dissociative recombination of molecular ions. *Physics Reports*, 186(5):215–248, 1990.

[224] Lawrence G Piper. State-to-state $N_2(A)$ energy pooling reactions. ii. the formation and quenching of $N_2(B, v = 1 - 12)$. *The Journal of chemical physics*, 88(11):6911–6921, 1988.

[225] Lawrence G Piper. State-to-state $N_2(A)$ energy-pooling reactions. i. the formation of $N_2(C)$ and the herman infrared system. *The Journal of chemical physics*, 88(1):231–239, 1988.

[226] Lawrence G Piper. The excitation of n (2 p) by n2 (a 3 σ + u, v'= 0, 1). *The Journal of Chemical Physics*, 90(12):7087–7095, 1989.

[227] Lawrence G Piper. Energy transfer studies on n2 (x 1σ+ g, v) and n2 (b 3π g). *The Journal of chemical physics*, 97(1):270–275, 1992.

[228] Lawrence G Piper. The excitation of n2 (b 3π g, v= 1–12) in the reaction between n2 (a 3σ+ u) and n2 (x, v $\geq$ 5). *The Journal of chemical physics*, 91(2):864–873, 1989.

[229] William J Marinelli, William J Kessler, Byron David Green, and William AM Blumberg. Quenching of N_2 (a 1π g, v = 0) by N_2, O_2, CO, CO_2, CH_4, H_2, and ar. *The Journal of Chemical Physics*, 90(4):2167–2173, 1989.

[230] TG Slanger and G Black. Quenching of $N(^2D)$ by N_2 and H_2O. *The Journal of Chemical Physics*, 64(11):4442–4444, 1976.

[231] KA Vereshchagin, VV Smirnov, and VA Shakhatov. Cars study of the vibrational kinetics of nitrogen molecules in the burning and afterglow stages of a pulsed discharge. *Technical Physics*, 42(5):487–494, 1997.

[232] H Böhringer and F Arnold. Temperature dependence of three-body association reactions from 45 to 400 k. the reactions $N_2^+ + 2N_2 \rightarrow N_4^+ + N_2$ and $O_2^+ + 2O_2 \rightarrow O_4^+ + O_2$. *The Journal of Chemical Physics*, 77(11):5534–5541, 1982.

[233] Mario Capitelli, Carlos M Ferreira, Boris F Gordiets, and Alexey I Osipov. *Plasma kinetics in atmospheric gases*, volume 31. Springer Science & Business Media, 2013.

[234] VA Feoktistov, AV Mukhovatova, AM Popov, and TV Rakhimova. Self-consistent modelling of low-pressure rf discharges in oxygen plasma. *Journal of Physics D: Applied Physics*, 28(7):1346, 1995.

[235] L Josić, T Wróblewski, Z Lj Petrović, J Mechlińska-Drewko, and GP Karwasz. Influence of resonant scattering on electron-swarm parameters in no. *Chemical physics letters*, 350(3-4): 318–324, 2001.

[236] Michael James Brunger, L Campbell, DC Cartwright, AG Middleton, B Mojarrabi, and PJO Teubner. Electron-impact excitation of rydberg and valence electronic states of nitric oxide: Ii. integral cross sections. *Journal of Physics B: Atomic, Molecular and Optical Physics*, 33(4): 809, 2000.

[237] Donald Rapp and Donald D Briglia. Total cross sections for ionization and attachment in gases by electron impact. ii. negative-ion formation. *The Journal of Chemical Physics*, 43(5): 1480–1489, 1965.

[238] BG Lindsay, MA Mangan, HC Straub, and RF Stebbings. Absolute partial cross sections for electron-impact ionization of NO and NO_2 from threshold to 1000 eV. *The Journal of Chemical Physics*, 112(21):9404–9410, 2000.

[239] Y Sakai, T Okumura, and H Tagashira. Measurement of electron impact ionisation and attachment coefficients in NO_2/He gas mixtures and estimated electron collision cross sections for NO_2. *Australian Journal of Physics*, 48(3):419–426, 1995.

[240] Lawrence G Piper. The rate coefficient for quenching N (2D) by o (3P). *The Journal of Chemical Physics*, 91(6):3516–3524, 1989.

[241] Lawrence G Piper. Quenching rate coefficients for $N_2(a')$. *The Journal of chemical physics*, 87(3):1625–1629, 1987.

[242] Lawrence G Piper, Lauren M Cowles, and Wilson T Rawlins. State-to-state excitation of $NO(A, v = 0, 1, 2)$ by $N_2(A, v = 0, 1, 2)$. *The Journal of chemical physics*, 85(6):3369–3378, 1986.

[243] Keith Schofield. Critically evaluated rate constants for gaseous reactions of several electronically excited species. *Journal of physical and chemical reference data*, 8(3):723–798, 1979.

[244] M Yaron, A Von Engel, and PH Vidaud. The collisional quenching of o2*(1δg) by no and co2. *Chemical Physics Letters*, 37(1):159–161, 1976.

[245] R Atkinson, DL Baulch, RA Cox, R Ft Hampson Jr, JA Kerr, and J Troe. Evaluated kinetic and photochemical data for atmospheric chemistry: supplement iii. iupac subcommittee on gas kinetic data evaluation for atmospheric chemistry. *Journal of Physical and Chemical Reference Data*, 18(2):881–1097, 1989.

[246] A Ricard et al. Determination, through titration with no, of the concentration of oxygen atoms in the flowing afterglow of ar-02 and n2-02 plasmas used for sterilization purposes. *Journal of Physics D: Applied Physics*, 34(8):1203, 2001.

[247] Wing Tsang and John T Herron. Chemical kinetic data base for propellant combustion i. reactions involving NO, NO2, HNO, HNO2, HCN and N2O. *Journal of physical and chemical reference data*, 20(4):609–663, 1991.

[248] T Czerwiec, J Gavillet, T Belmonte, H Michel, and A Ricard. Determination of n and o atom density in ar-n 2-h 2 and ar-o 2-h 2 flowing microwave post discharges. *Journal de Physique III*, 6(9):1205–1212, 1996.